warwick.ac.uk/lib-publications

Fabrication and Characterisation of Self-healing Polymers and Nacre-like Films for Coatings

Mr Andrew James Smith

A thesis submitted in partial fulfilment of the requirements for the degree of

Doctor of Philosophy in Engineering

Warwick Manufacturing Group, University of Warwick

December 2020

Table of Contents

List of Figures

List of Schemes

List of Tables

List of Abbreviations

1HCPK	1-hydroxycyclohexylphenylketone
ACHN	1,1'-azobis(cyclohexanecarbonitrile)
AHMP	2-amino-4-hydroxy-6-methylpyrimidine
AIBN	2,2'-azobisisobutyronitrile
APT	Attached proton test
ATR	Attenuated total reflectance
ATRP	Atom transfer radical polymerisation
α-ZrP	alpha-Zirconium phosphate
BPO	Benzophenone
CO_2TR	Carbon dioxide transmission rate
COSY	Correlated spectroscopy
CTA	Chain-transfer agent
DA	Diels-Alder
DBA	Dibutylamine
DCPD	Dicyclopentadiene
DEPT	Distortionless enhancement by polarization transfer
DI	Deionised
DIW	Deionised water
DLS	Dynamic light scattering
DRI	Differential refractive index
DSC	Differential scanning calorimetry
E	Young's modulus
EBiB	Ethyl α-bromoisobutyrate
EBP	Ethyl 2-bromopropionate
EPA	Ethylphenylacetate

EPHP	1-ethylpiperidine hypophosphite
E_r	Reduced Young's modulus
FMA	Furfuryl methacrylate
f-MMA	Functionalised methyl methacrylate
FRP	Free-radical polymerisation
FTIR	Fourier-transform infrared spectroscopy
GO	Graphene oxide
GOx	Functionalised graphene oxide
GPC	Gel-permeation chromatography
H	Hardness
HDI	Hexamethylene diisocyanate
I500	Irgacure 500
IF	Intermolecular forces
JLR	Jaguar-Land Rover
L	Ligand
L-A	Less activated
LbL	Layer-by-layer
LDH	Layered double hydroxide
LRP	Living radical polymerisation
LS	Light scattering
M-A	More activated
MA	Methacrylate
MAS	Magic-angle spinning
MBPA	Methyl α-bromophenylacetate
Me$_6$TREN	*Tris*[2-(dimethylamino)ethyl]amine
MFC	Maleimide-furan coupling

MiMA	2-(1,3-dioxo-1,3,3a,4,7,7a-hexahydro-2H-4,7-epoxyisoindol-2-yl)ethyl
MMA	Methyl methacrylate
M_n	Number-averaged molecular weight
NMR	Nuclear magnetic resonance
O_2TR	Oxygen transmission rate
PA	Phenylacetate
PCDO	Pentacosadiyn-1-ol
PDA	Poly(dopamine)
PDDA	Poly(diallyldimethylammonium chloride)
PEA	Poly(ether amine)
PEG	Poly(ethylene glycol)
PET	Poly(ethylene terephthalate)
PMMA	Poly(methyl methacrylate)
PP	Poly(propylene)
PS	Poly(styrene)
PSD	Particle size distribution
PTFE	Poly(tetrafluoroethylene)
PU	Poly(urethane)
PVA	Poly(vinyl alcohol)
PVAy	Functionalised poly(vinyl alcohol)
RAFT	Reversible addition-fragmentation chain-transfer
rDA	Retro Diels-Alder
RDRP	Reversible-deactivation radical polymerisation
rGO	Reduced graphene oxide
RH	Relative humidity

ROMP	Ring-opening metathesis polymerisation
RT	Room temperature
SEM	Scanning-electron microscopy
SET-LRP	Single-electron transfer living radical polymerisation
SSNMR	Solid state nuclear magnetic resonance
T_g	Glass transition temperature
TGA	Thermo-gravimetric analysis
T_m	Melting transition temperature
TR	Transmission rate
TRDA	Thermally reversible Diels-Alder
UPy	2-Ureido-4[1H]-pyrimidinone
U_T	Tensile toughness
UV	Ultraviolet
UV-Vis	Ultraviolet-visible
VS	Viscometry
wsPU	Water-soluble polyurethane
WVTR	Water vapour transmission rate
XPS	X-ray photoelectron spectroscopy
XRD	X-ray diffraction
σ	Tensile strength
ε	Maximum strain

Acknowledgements

Firstly, I would like to extend my gratitude to my supervisors throughout my research project. I want to thank Dr Tara Schiller for offering me the opportunity to explore this PhD at the University of Warwick. Equally, Professor Tony McNally has continuously offered me support and guidance that I am hugely grateful for. I do not believe I would have carried my PhD to completion without his unwavering belief. To my secondary supervisors, Dr Łukasz Figiel and Dr Chaoying Wan, I want to express my gratitude for their advice and suggestions. The support I have received throughout my time at WMG has helped me break through multiple roadblocks, both mentally and practically, and their guidance has been a catalyst for achieving my goals.

Martin Worrall has been a rock for me during my research project and has provided me with technical guidance, but more importantly, has been a friend and a reliable source of emotional support. It would not be an understatement to say I would not be submitting this thesis without him. I also want to thank the multiple experts I have met and learned from, including Dr Daniel Lester, Dr Daniel Keddie, Dr David Walker, Dr Geoff West, Yujin Yang, Dr Sam Marks, Nicole Kelly, Dr John Hanna, Dr Ben Breeze, Dr Marc Walker, Paul Hadlum and Dr Alan Wemyss. Their knowledge and patience have been greatly appreciated.

The support of my colleagues has been unwavering. There are too many names to mention them all, but I'd like to specifically recognise Syeda, Tom, Sergio, Andy, Steve, and the entire McNally group. I have forged strong friendships with them all, and they thoroughly deserve every success in their future.

I want to thank my family and friends for listening to my problems and, at times, providing the necessary stimulant for me to carry on. I would like to specifically thank my partner, Chloe (and our dog, Lexie), who has been with me throughout my PhD, always cheering me on and believing in me. I love them all greatly, and, ultimately, this is for them.

Finally, I want to extend a mention to my GCSE and A-Level Chemistry teacher, Mrs Thompson. She ignited my interest and began me on this journey. I'm sure she would be proud to see me submit this thesis.

Declaration of Authorship

This thesis is submitted to the University of Warwick in support of my application for the degree of Doctor of Philosophy. It has been composed by myself and has not been submitted in any previous application for any degree to any other university or higher education institution or as any part of any other submission to the University of Warwick. It describes work carried out from October 2016 to December 2020.

The work presented (including data generated and data analysis) was carried out by the author except in the cases outlined below:

1. Solid-state nuclear magnetic resonance measurements were completed and the data processed by Nicole L. Kelly and Dr John V. Hanna, Department of Physics, University of Warwick.
2. X-ray photoelectron spectroscopy measurements were completed and the data processed by Dr Marc Walker, Department of Physics, University of Warwick.
3. Gas barrier analysis measurements were completed and the data processed by Dr Stefano Harris, Department of Food, Environmental and Nutritional Sciences, University of Milan.

Parts of this thesis have been published by the author:

1. Graphene Oxide Functionalized with 2-Ureido-4[1*H*]-pyrimidinone for Production of Nacre-Like Films, A. J. Smith, N. L. Kelly, Ł. Figiel, C. Wan, J. V. Hanna, S. Farris, T. McNally, *ACS Applied Nano Materials*, 2020, **7**, 7161-7171
2. Freestanding α-Zirconium Phosphate Based Nacre-like Composite Films Cast from Water, A. J. Smith, C. Wan, Ł. Figiel, S. Farris, T. McNally, *Composites Science and Technology*, 2020, **200**, 108443-108452

Journal Papers and Conference Presentations

Journal papers published and in progress

1. Graphene Oxide Functionalized with 2-Ureido-4[1H]-pyrimidinone for Production of Nacre-Like Films, A. J. Smith, N. L. Kelly, Ł. Figiel, C. Wan, J. V. Hanna, S. Farris, T. McNally, *ACS Applied Nano Materials*, 2020, **7**, 7161-7171 (1 citation)

2. Freestanding α-Zirconium Phosphate Based Nacre-like Composite Films Cast from Water, A. J. Smith, C. Wan, Ł. Figiel, S. Farris, T. McNally, *Composites Science and Technology*, 2020, **200**, 108443-108452 (0 citations)

3. Isocyanate-functionalized Graphene Oxide and Poly(vinyl alcohol) for Production of Nacre-Mimetic Materials, A. J. Smith, Ł. Figiel, C. Wan, T. McNally, (in progress)

4. Nacre-mimetic Materials: Masonry on the Molecular Level, A. J. Smith, Ł. Figiel, C. Wan, T. McNally, (in progress)

Conference presentations

1. Lightweight Memory Materials for Adaptive and Self-healing Automotive Structures, A. J. Smith, T. L. Schiller, Ł. Figiel, T. McNally. Poster presentation at *WMG Doctoral Research and Innovation Conference,* June **2017**, University of Warwick, Coventry, UK.

2. Nacre-mimetic Materials Produced via Chemical Functionalisation of Graphene Oxide Nanosheets, A. J. Smith, C. Wan, Ł. Figiel, T. McNally. Oral presentation at the 37th *Australasian Polymer Symposium*, 10-13th November **2019**, Sunshine Coast, Australia.

Abstract

Damage and wear of coatings represent a significant concern for both manufacturers and consumers in the automotive sector. As a result, it is critical to develop technologies that prolong the lifetime of these coatings, fundamentally increasing cosmetic longevity and customer satisfaction. This project explores two approaches to this problem that offer different mechanisms towards the ultimate goal of anti-wear coatings.

Firstly, substituting PMMA, currently used in automotive coatings, with self-healing analogues, would allow wear to be reversed by recovering the virgin material's mechanical and cosmetic properties. In this work, MMA monomers were successfully functionalised using a thermally reversible Diels-Alder coupling reaction. RAFT and Cu(0)-mediated LRP is used to control the molecular weight of the functional PMMA. Low dispersity functionalised polymers are reported that have potential for self-healing properties.

Second, this project explores the manufacture of nacre-mimetic films, with functionalised nanoplatelet and polymer components, to increase interfacial interactions. A GO-wsPU structure was produced and cross-linked via UV. Achieving homogeneous films proved challenging due to the micellar nature of the wsPU in that it did not readily disperse and distribute between GO layers. Equally, GO, and PVA is functionalised with UPy to encourage a strong hydrogen bonding network. Multiple characterisation techniques confirm the successful functionalisation of both components. Novel, uni-directional layered films are produced, and significant increases in E (392%), σ (535%), ε (598%), and U_T (1789%) were recorded.

Finally, innovative nacre-like films were produced containing α-ZrP and a PEA to produce the first freestanding nacre-mimetic films of their kind. Films with high PEA content are transparent. Static tensile testing yields 341%, 572%, 707% and 3981% increases to E, σ, ε and U_T, respectively, and nanoindentation measurements confirm a 200- and 44-fold increase in E_r and H when compared to the lowest PEA content film.

1. Introduction

1.1 Background

Coatings are widely used in various industries as a protective layer against several degradation mechanisms, including physical damage (scratches, dents, etc.), corrosion, and UV radiation. As a result, the improvement of these coatings' properties is of great interest to the scientific community and industry. Commonly, polymers are employed as surface coatings due to a range of properties that are often unrivalled by other materials and include transparency, gloss finish, and corrosion protection, to name a few. Critically, these properties depend on the choice of polymer, and thus, compromises are regularly made. For example, poly(methyl methacrylate) (PMMA) offers high gloss and transparency but poor resistance to scratch,[1] whereas poly(carbonate)s have good impact properties; however, they can display poor stability towards UV and visible light.[2]

1.2 Use of coatings in the automotive industry

Coatings have been widely used in the automotive industry since its inception. Due to the metallic nature of a number of components, paints were used to improve the vehicle's appearance and help protect against corrosion. More recently, specialised coatings have been developed that are applied above the paint layer to add further protection. These are most often polymer-based and applied as a clear-coat; however, ceramic alternatives have become more available in recent years. Polymer coatings utilised in the automotive industry experience weathering effects and micro-scale abrasions due to sand and other fine particulates. Therefore, micro-scale scratches are common during the lifetime of a component.[3, 4] Ceramic coatings are often lauded in the automotive community as the optimal choice for exterior coatings. High-gloss finish and protection against UV radiation are significant benefits of ceramics; nevertheless, they are still susceptible to scratching and swirl marks. Component micro-scratching can, in some cases, result in customers exercising warranty to receive a replacement at the cost of the product supplier. For this reason, companies are exploring approaches to extend the lifetime of the entire component by improving the cosmetic resilience of the coating.

1.3 The research problem

The lifetime of many of the coatings used in the automotive sector is limited, and their failure ultimately causes dissatisfaction for consumers. Extending the lifetime of the topcoat, in particular, would be extremely beneficial to both the manufacturer and consumer. Currently, no polymer system offers all the necessary properties for use over the entire car. Instead, polymers specific to the component are employed to achieve optimal properties. One of the main concerns expressed by consumers is the formation of micro-scratches and swirls in the topcoat, reducing the vehicle's aesthetic appearance. Other forms of degradation (such as corrosion and yellowing) occur on a longer time-scale and are less of a concern to new vehicle owners.

Extending the lifetime of coatings against scratch and mar may be achieved through multiple approaches; however, two strategies will be investigated in this project. Firstly, the polymer can be functionalised in such a way as to allow scratches and small-scale cracks to mend. Materials of this kind are known as 'self-healing' and are commonly produced using a reversible cross-linking agent and have seen significant interest within the research community. Multiple healing mechanisms have been reported thus far,[5-8] providing researchers with a plethora of options when designing polymers of this type. Despite the options available, not all are suitable for automotive coatings. Microcapsule technology is one example[5] where a monomer pool is encapsulated within the polymer matrix. This technique is not suitable as it only has the capacity to heal once at each site. It is essential for any self-healing materials used in automotive applications to have the capacity for multiple healing cycles due to the regularity of vehicle use and, consequently, the likelihood of repeated damage. By employing external stimuli to initiate self-healing, greater control is possible. This method does, however, have limitations. When heat is used as the stimulus, prudent selection of the reversible cross-linker is necessary. Globally, extreme temperatures are frequently observed in a number of climatic zones—for example, the heat of Saudi Arabia and extreme cold in Canada's northern regions. As a result, the temperature at which self-healing is initiated must be above that of the coating's highest temperature when in use, as high as 100 °C in the hottest climates. Simultaneously, the self-healing temperature needs to be at a practical level that can be reached with relative ease and creates no unnecessary hazard for consumers or

employees. Alternatively, UV active cross-linkers can be susceptible to degradation from ambient radiation absorbed from the Sun. There is currently very little reported on the large-scale manufacture of self-healing materials (see Chapter 2). The gap between academic and industrial interests in this field is significant, ultimately leading to the requirement for substantial optimisation of current technology towards use in industrial applications. This gap's bridging is a necessary yet time- and resource-heavy exercise and will likely take many years to achieve.

Second, the mechanical properties of the coating can be improved to prevent premature deformation. This method requires the development of new coatings that may contain additives or be of an innovative composition. Polymers have an inherent limit to the mechanical properties that can be achieved. The use of co-polymer systems can introduce reinforcing effects but often compromise other beneficial properties. The same is true for additives. Nanoparticle-polymer blends are widely proposed as a route to the improvement of the mechanical properties of polymers. These types of materials are known as 'nanocomposites.' It has been widely shown that the introduction of a minimal volume (<5%) of the nanoparticle can cause substantial improvements to mechanical properties. Most commonly, graphene, graphene oxide (GO), nanoclay, and boron nitride nanoplatelets are employed, but there are many more alternatives. Despite the improvement in mechanical properties, the introduction of nanoparticles often results in unwanted side effects. Graphene, for example, absorbs strongly in the visible region of the electromagnetic spectrum and thus produces polymer nanocomposites that are a black colour. Much work has focused on achieving homogeneous dispersion of nanoparticles within polymer matrices. It is often the case that the nanoparticle filler has relatively poor interactions with the polymer. This leads to the formation of agglomerations that result in highly concentrated nanoparticle regions. Consequently, inhomogeneous properties are obtained that can lead to premature deformation in mechanically weaker domains. The introduction of small-molecule additives can introduce instability towards UV or thermal radiation that would otherwise have minimal effect on a pure polymer.

Alternative compositions have much less description in the literature. Despite this, some biomimetic materials are receiving attention. One example is Nacre, which has a uni-directional layered structure with a very high nanoplatelet content (95%). In

these materials, the polymer content is very low (<5 vol%), but the contribution to mechanical properties is significant. Materials similar to Nacre can attain remarkable mechanical properties[9] that are impossible with traditional polymer materials.

Nonetheless, the production of suitable coatings with these materials is, at this point, a major technical challenge. As is observed with traditional nanocomposites, graphene- and GO-based films are opaque and black/brown in colour. It has been proven that clear and colourless examples of these films are possible; however, they are commonly less than 10 bilayers thick (one bilayer consists of one layer of nanoplatelet and one layer of polymer).[10] It is very difficult to achieve homogeneous coverage with coatings this thin without using intensive production methods that are unsuitable for large-scale manufacture. Other nanoplatelets can be used to produce transparent films but display weaker mechanical properties.[11] Production of nacre-mimetic films can be a complex process due to the high control needed over nanoplatelet morphology and polymer penetration. It is for this reason that a number of industrial-scale manufacturing techniques are not suitable.

Consequently, scale-up is an obstacle but is tackled by applying various techniques, including spray-coating, solvent casting, and hot pressing. Some nanoplatelets are produced on a large scale for a low cost (e.g., nanoclays); however, other nanoplatelets, including graphene and GO, are expensive to produce (although the cost continues to decrease). This is an important consideration when developing materials for use in large-scale applications. In most cases, avoiding the more expensive nanoplatelets is difficult due to the beneficial mechanical properties they display and the potential for further functionalisation of the nanoplatelet surface. Despite the expense, the extremely low thickness (typically 10-50 µm) of nacre-mimetic films reported in the literature greatly reduces the mass of nanoplatelet required. Finally, with materials of this nature, the interfacial interactions are essential to maintaining the mechanical properties and avoiding polymer aggregates within the structure. Therefore, the interaction between the polymer and nanoplatelet is of high importance. Weakly interacting components cause separation, preventing adequate penetration of the polymer between the nanoplatelet layers. This dramatically hinders the properties of the films produced.

Intelligent selection of nanoplatelet-polymer pairs allows production of high performing films that can exceed those of polymer coatings. This project seeks to develop suitable nacre-mimetic structures based on GO and alpha-Zirconium phosphate (α-ZrP) for scale-up in the future using compatible components. The compatibility will be improved through the chemical functionalisation of GO. To the best of my knowledge, at the time of writing this thesis, there have been no investigations into the direct functionalisation of GO with the 4-fold hydrogen-bonding moiety, 2-ureido-4[1H]-pyrimidinone (UPy), towards the production of nacre-mimetic materials. It is also believed there are no studies into UV-active water-soluble polyurethane (wsPU) and GO nacre-mimetic films that are covalently cross-linked following UV irradiation. Investigations into the production of freestanding α-ZrP nacre-mimetic films are also unreported prior to completing this project. The project also seeks to investigate the self-healing of functionalised PMMA. Exploring a zip-like approach to producing a reversibly cross-linked polymer is, to the best of my knowledge, a novel investigation.

1.4 Research strategy

The main goals of this project were two-fold. Firstly, it was intended that the synthesis of a self-healing material be studied with a direct focus towards specific automotive coatings. This will be achieved by functionalising monomer units with a reversible cross-linker that could later be included in polymerisation reactions towards self-healing polymers. In this work, PMMA coatings were targeted, and thus the functionalisation of methacrylate monomers is investigated. The polymerisation of these monomers into copolymers with MMA was studied to develop an understanding of their polymerisation. There is a plethora of literature on the polymerisation of MMA using a range of techniques.[12-14] Ultimately, a number of functionalised monomers were synthesised, and their polymerisation was studied to produce a PMMA-based self-healing material. Initially, the simplest approach was employed whereby a thermally reversible Diels-Alder (TRDA) dimer was end-capped with methacrylate groups. The polymerisation is theoretically possible through a range of radical techniques, including free-radical polymerisation (FRP), reversible addition-fragmentation chain-transfer (RAFT), and Cu(0)-mediated living radical polymerisation (LRP). It is also possible to synthesise DA active monomers for polymerisation into different polymers which can later be dimerised into a similar

cross-linked network. This method involved designing and synthesising monomers and methods with adequate protection from radical-induced branching and thermal degradation.

Second, this project also aimed to study the production of nacre-mimetic materials using a range of nanoplatelets and polymers. This will allow the properties and interactions of the two components to be studied towards understanding the effects of polymer-nanoplatelet interactions on mechanical properties. Multiple different nacre-mimetic structures are produced with varying success that provides insight into the self-assembly process mechanisms and the effect of adequate mixing of the two components. Interfacial interactions between the two components govern the properties of nacre-mimetic materials, so manipulating these interactions by covalent and non-covalent methods is explored.

Covalent cross-linking was the first method explored and can be achieved using a small molecule cross-linking agent or a polymer with the potential to react with the nanoplatelet. It is important for a reactive polymer that this cross-linking does not occur too readily to 'lock' the nanoplatelets together during self-assembly. Instead, a polyurethane was investigated with UV activity towards polymerisation through pendant acrylate groups. To achieve the desired structure, the polyurethane must have the following characteristics: it must be soluble in water as this was the ideal solvent for sample preparation, it must be unreactive towards the nanoplatelet prior to UV curing, and it must have a suitable structure and properties to facilitate effective penetration between the nanoplatelets during self-assembly. GO was employed as the nanoplatelet due to stable dispersion in water, polar functional groups on the surface, and vinylic regions within the structure that allow non-covalent binding and covalent cross-linking to the polyurethane, respectively. The literature on the use of polyurethanes in nacre-mimetic materials is limited, and furthermore, introducing UV cross-linking with this polymer-nanoplatelet combination is so far unreported. A highly cross-linked network was designed and expected to improve the material's mechanical properties through the UV initiated reaction.

The influence of non-covalent interactions was also examined through functionalisation of GO. The polar groups present on the surface of GO allow for hydrogen bonding to other GO sheets and the polymer component.[15] This can be

utilised to easily coat the GO with a suitable polymer during self-assembly to achieve excellent penetration and dispersion of the polymer component. This project looked to enhance the hydrogen bonding potential of the GO and polymer using poly(vinyl alcohol) (PVA). The GO and PVA were both functionalised with a 4-fold hydrogen bonding group, UPy, that greatly increases the interfacial interactions. The polar groups on the GO surface are highly reactive towards isocyanates, and so this was exploited to graft the UPy to the GO surface and, the same is true for the hydroxyl groups on PVA. The effect of this functional group on a range of properties was explored, as well as the potential for UPy to behave as a 'pseudo-polymer.'

Finally, a further target was to investigate the properties of a previously unreported nacre-mimetic material based on α-ZrP. Literature examples of α-ZrP based nacre-mimetic materials are very limited[16, 17] and freestanding film of this kind are, as yet, unreported. As a result, the aim was to explore the possibility of using similar experimental methods used in other investigations in this report to produce freestanding α-ZrP based films. The fundamental problem with using α-ZrP is it disperses poorly in water and many other solvents. Exfoliating agents are required to penetrate and separate the α-ZrP sheets[18] to allow adequate mixing in polymer materials. Polymeric exfoliating agents are widely available and often recommended for other applications,[19, 20] and so, in this work, investigations were made into the use of these polymers to achieve the two-fold effect of exfoliation and then reinforcement of an α-ZrP film. The properties of said materials were then explored and compared with the limited literature available to understand the polymer content's effects on the final material.

1.5 Thesis structure

Chapter 1 provides an introduction to the project, including a background of the current use of coatings in the automotive industry and the research problem addressed in this work. This chapter will also outline the aims of the project and the contribution to knowledge.

Chapter 2 outlines the current state of the art in the multiple disciplines explored in this project through a literature review. Key papers are presented that

provide an understanding of the concepts and prerequisite knowledge for focused research in these fields.

Chapter 3 provides a detailed report of the experimental methods and materials employed, including chemical syntheses, polymerisation reactions, sample preparation, and characterisation techniques and parameters.

Chapter 4 reports the results from testing the hypothesis that TRDA-functionalised methacrylate monomers can be polymerised with MMA and provide self-healing functionality following thermal treatment. It was anticipated that the functionalised monomers polymerise at a similar rate to MMA due to the methacrylate unit's similarity in each case. Polymerisation was achieved using FRP, RAFT, and Cu(0)-mediated LRP techniques and subsequently characterised using ^{1}H nuclear magnetic resonance (NMR) and size-exclusion gel permeation chromatography (GPC). The polymers' thermal properties are also analysed to determine suitability for self-healing if applied as an automotive coating. The final properties also determine suitability for processing on a large scale.

Chapter 5 describes the work done to prepare films where a wsPU can be adequately distributed within a GO dispersion to allow production of a homogeneous nacre-mimetic material through self-assembly. It was anticipated that this material could be cross-linked through UV irradiation to create a covalent network and greatly improve the mechanical properties of the films produced. Multiple conditions were explored including, different UV curing times, base stabilisers, and preparation methods. The morphological and mechanical properties of these materials were studied using scanning-electron microscopy (SEM) and static tensile testing to understand the relationship between film structure and properties. This section also discusses the development of a suitable film production method that was developed and then widely used in work described in the following chapters.

Subsequently, the work described in Chapter 6 covers the chemical modification of GO and PVA by functionalisation with a 4-fold hydrogen bonding group and the improvements in mechanical properties. It was expected that the enhanced interfacial interactions provided by the chemical modification would create a stronger network of non-covalently bound components and improve the film

properties. The films were characterised using a range of techniques whilst the morphological and mechanical properties were again examined using SEM, nanoindentation, and static tensile testing. The barrier properties of the films to oxygen, carbon dioxide, and water vapour are also reported.

Finally, Chapter 7 describes the study of using a poly(ether amine), Jeffamine M600 (PEA), for production of α-ZrP nacre-mimetic films. It was anticipated that improved exfoliation of the α-ZrP would facilitate a self-assembly process that has not yet been observed with α-ZrP. PEA is widely known to exfoliate α-ZrP through a cationic exchange process on the α-ZrP surface. It was expected that this exfoliation could be employed to improve the self-assembly of the α-ZrP into a uniform, uni-directional layered structure. The PEA also behaves as the polymer component in the nacre-mimetic structure, thus providing structural integrity and improved mechanical properties. Various PEA contents were explored, and the effect was followed by SEM, static tensile testing, nanoindentation, and other chemical characterisation techniques, including X-ray diffraction (XRD), Raman, and Fourier-transform infrared spectroscopy (FTIR). A visual representation of the thesis structure is outlined in Figure 1.1.
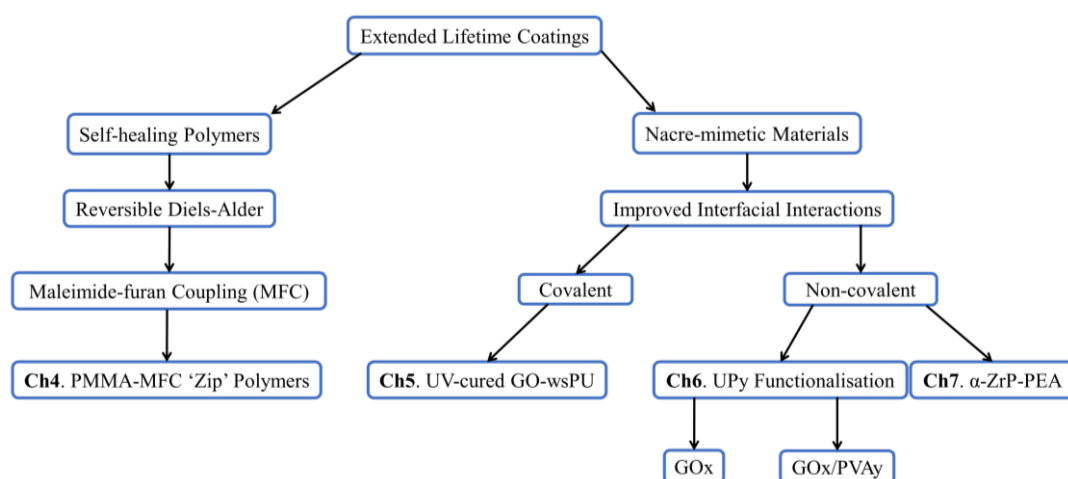
Figure 1.1 – Flow diagram depicting the development of the research strategy and thesis structure.

1.6 Contribution to knowledge

The work reported in this thesis makes a significant contribution to knowledge in the field of materials science. The content is beneficial to both the scientific community and society through the development of advanced materials for use in coatings that have the potential to prolong the lifetime of automotive coatings. The understanding of self-healing materials has greatly improved over the past two decades. Despite this, the use of RAFT polymerisation towards their synthesis has been very limited. The thermal stability of such polymers has thus far been unreported, with the literature to date focused on the synthesis of single polymers that contain both components for a reversible cross-link. Production of different polymers, each with one of the two cross-linking groups, towards a 'zip'-like cross-linking mechanism, is unexplored. Investigations into the design, synthesis, and characterisation of such polymers are reported, broadening the current conceptual approaches explored by the research community.

A significant contribution is made from the production of nacre-mimetic materials through design, synthesis, production, and analysis of a range of approaches towards increasing mechanical properties. Understanding the effects of interfacial interactions between the two key components is critical to the development of ever-stronger materials, ultimately towards their application in real-world products. Due to the recent interest in nacre-mimetic films, the understanding in this field is beginning to grow. Studies have encapsulated a number of components, with some work beginning to explore the functionalisation of the nanoplatelet component.[21-23] The work reported in this thesis describes further modification strategies. The self-assembly of micellar polymers with a nanoplatelet is widely unknown, and therefore, this work looks to explore this process to determine suitability for film production. The UV curing of such materials is also limited, and the use of pendant acrylate polymerisation as a form of covalent cross-linking has yet to be investigated.

Understanding of the chemical modification of GO used in nacre-mimetic materials is limited. This project explores the direct functionalisation of GO to increase interfacial interactions, and the effects this functionalisation has on a range of properties are explored. This then provides a foundation for the development of films with further increased properties using similar methods. Exploring surface

modification of GO towards the production of nacre-like films with a 'pseudo-polymer' component is yet to be studied. To the best of my knowledge, functionalisation of both the nanoplatelet and polymer components with complementary hydrogen bonding groups towards an increase in the mechanical properties of nacre-mimetic materials is as yet unreported.

Furthermore, α-ZrP based nacre-mimetic materials are studied. The production of freestanding films of this kind is yet to be reported. Nacre-mimetic films deposited on a substrate are described in the literature; however, this work is also very limited. Through investigations into improved exfoliation of α-ZrP, this project explores the potential towards freestanding nacre-mimetic films. This work has the potential to open a new field of research into freestanding α-ZrP films.

1.7 Aims and objectives

The **aims** of this project are to:

- Design and synthesise polymers based on PMMA with self-healing functionality using suitably functionalised monomers via radical polymerisation techniques.
- Disperse GO and wsPU and prepare nacre-mimetic films.
- Promote interfacial interactions of GO sheets through functionalisation with suitable hydrogen bonding isocyanate species.
- Prepare isocyanate-functionalised GO (GOx) for the production of nacre-like films with and without a functionalised PVA (PVAy) polymer component.
- Prepare via solvent casting and characterise α-ZrP freestanding nacre-mimetic films through adequate exfoliation assisted by a polymer component.

The **objectives** of this project are:

- Confirm synthesis of functionalised methyl methacrylate (*f*-MMA) monomers through ^{1}H NMR and FTIR.
- Polymerise MMA and *f*-MMA via FRP, RAFT, and Cu(0)-mediated LRP techniques and confirm the structure of the polymer with ^{1}H NMR and GPC and thermal properties from TGA and DSC studies.

- Characterise the purity, structure, size, and thermal stability of graphene oxide (GO) through solid-state NMR (SSNMR), X-ray photoelectron spectroscopy (XPS), Raman, FTIR, SEM, and TGA.

- Determine if a uni-directional layered structure within GO and wsPU films was produced from SEM imaging and measure the static mechanical properties by tensile testing.

- Prepare and characterise GOx using SSNMR, XRD, Raman, and FTIR. Determine the effect of functionalising GO by evaluating the morphological (SEM), mechanical (tensile testing), barrier, and chemical properties (XRD, Raman, and FTIR) of resulting films.

- Functionalise PVA (PVAy) with the 4-fold hydrogen bonding synthon, UPy, and confirm a successful reaction by FTIR. Prepare and characterise GOx/PVAy nacre-mimetic films through SEM, tensile testing, XRD, Raman, and FTIR.

- Characterise the purity, size, and structure of (α-ZrP) using SEM, XRD, Raman, and FTIR.

- Prepare and characterise α-ZrP films through exfoliation with an amine-functionalised polymer to determine the morphological (SEM), mechanical (tensile testing and nanoindentation), chemical (XRD, Raman, and FTIR), and moisture barrier properties.

1.8 References

1. E. Moghbelli, R. Banyay, and H.-J. Sue, *Tribology International*, 2014, **69**, 46-51.

2. M. Yazdan Mehr, W. D. van Driel, K. M. B. Jansen, P. Deeben, M. Boutelje and G. Q. Zhang, *Optical Materials*, 2013, **35**, 504-508.

3. R. R. Matheson, G. S. Blackman and L. Lin, *Progress in Organic Coatings*, 2000, **40**, 85-91.

4. J. Lin, in *Protective Coatings*, eds. K. Dušek and M. Wen, Springer International, New York, 2017, ch. 16, pp. 361-376.

5. S. R. White, N. R. Sottos, P. H. Geubelle, J. S. Moore, M. R. Kessler, S. R. Sriram, E. N. Brown and S. Viswanathan, *Nature*, 2001, **409**, 794-797.

6. X. Chen, M. A. Dam, K. Ono, A. Mal, H. Shen, S. Nutt, K. Sheran and F. Wudl, *Science*, 2002, **295**, 1698-1702.

7. K. S. Toohey, N. R. Sottos, J. A. Lewis, J. S. Moore and S. R. White, *Nature Materials*, 2007, **6**, 581-585.

8. Y. Zhang, B. Yang, X. Zhang, L. Xu, L. Tao, S. Li and Y. Wei, *Chemical Communications (Cambridge)*, 2012, **48**, 9305-9307.

9. S. Wan, J. Peng, Y. Li, H. Hu, L. Jiang and Q. Cheng, *ACS Nano*, 2015, **9**, 9830-9836.

10. R. Xiong, K. Hu, A. M. Grant, R. Ma, W. Xu, C. Lu, X. Zhang and V. V. Tsukruk, *Advanced Materials*, 2016, **28**, 1501-1509.

11. P. Podsiadlo, A. K. Kaushik, B. S. Shim, A. Agarwal, Z. Tang, A. M. Waas, E. M. Arruda and N. A. Kotov, *Journal of Physical Chemistry B*, 2008, **112**, 14359-14363.

12. Y. K. Chong, G. Moad, E. Rizzardo, M. A. Skidmore and S. H. Thang, *Macromolecules*, 2007, **40**, 9262-9271.

13. G. R. Jones, R. Whitfield, A. Anastasaki, N. Risangud, A. Simula, D. J. Keddie and D. M. Haddleton, *Polymer Chemistry*, 2018, **9**, 2382-2388.

14. L. Xue, U. S. Agarwal and P. J. Lemstra, *Macromolecules*, 2002, **35**, 8650-8652.

15. K. W. Putz, O. C. Compton, M. J. Palmeri, S. T. Nguyen and L. C. Brinson, *Advanced Functional Materials*, 2010, **20**, 3322-3329.

16. L. Zhang, L. Ling, M. Xiao, D. Han, S. Wang and Y. Meng, *Journal of Power Sources*, 2017, **352**, 111-117.

17. D. Han, Y. Luo, Q. Ju, X. Xiao, M. Xiao, N. Xiao, S. Chen, X. Peng, S. Wang and Y. Meng, *Polymers (Basel)*, 2018, **10**, 1082-1097.

18. H. Huang, M. Li, Y. Tian, Y. Xie, X. Sheng, X. Jiang and X. Zhang, *Progress in Organic Coatings*, 2020, **138**, 105390-105400.

19. H.-J. Sue, K. T. Gam, N. Bestaoui, N. Spurr and A. Clearfield, *Chemistry of Materials*, 2004, **16**, 242-249.

20. M. Wong, R. Ishige, K. L. White, P. Li, D. Kim, R. Krishnamoorti, R. Gunther, T. Higuchi, H. Jinnai, A. Takahara, R. Nishimura and H. J. Sue, *Nature Communications*, 2014, **5**, 3589-3601.

21. Y. Gao, L.-Q. Liu, S.-Z. Zu, K. Peng, D. Zhou, B.-H. Han and Z. Zhang, *ACS Nano*, 2011, **5**, 2134-2141.

22. Q. Cheng, M. Wu, M. Li, L. Jiang and Z. Tang, *Angewandte Chemie International Edition England*, 2013, **52**, 3750-3755.

23. K. Shahzadi, I. Mohsin, L. Wu, X. Ge, Y. Jiang, H. Li and X. Mu, *ACS Nano*, 2017, **11**, 325-334.

2. Literature Review

2.1 Introduction

Research into increasing the longevity of coatings has been explored for decades. Strong coatings protect the substrate against damage, including scratch, dent, and wear, whilst anti-corrosive properties are particularly important for metallic components. A coating is a thin layer of material applied to a substrate and has been revolutionary in the automotive industry in providing long-term resistance to heat, UV-radiation, physical damage, and corrosion. Despite this, there is greater demand for coatings with improved properties.[1, 2] Current coatings have limitations that ultimately result in premature failure and poor consumer satisfaction.

Self-healing materials have a high potential for protection against physical defects (most notably scratch) through a chemical reconstruction of the pre-damage assembly. The most popular techniques include microencapsulation, thermally reversible Diels-Alder (TRDA), and reversible intermolecular interactions (e.g., hydrogen bonding, π-π stacking, etc.). Each of these approaches has specific disadvantages that limit the options towards the target application; however, some literature reports exceptional recovery of mechanical and optical properties.

Alternatively, new materials yet to be explored in automotive applications could yield significant advances. Nacre-mimetic materials are one such example and have been shown to display remarkable properties, far exceeding current polymer composite alternatives. High impact toughness, tensile strength, and modulus can provide greater physical protection whilst anti-corrosive properties protect the substrate from chemical erosion. Extremely high nanoplatelet content ($\approx$95 vol%) forces manufacture through industrially unconventional methods; however, research has recently shifted towards more scalable techniques.[3, 4]

2.2 Self-healing polymers

2.2.1 Introduction

Materials with the ability to heal damage and recover properties offer more advanced, long-lasting, and higher performance alternatives to their traditional counterparts. In the natural world, it is vital for broken or damaged tissue to heal and

mend to maintain regular cell function.[5] Self-healing polymers aim to mimic this process to provide similar benefits to synthetic materials. Critically, research into these advanced polymers is in relative infancy, having been pioneered at the turn of the millennium[6] and as such, has significant potential for novel science. Currently, the manufacturing focus is on highly durable and chemically inert structures to maximise the lifetime of a material. Failure thus leads to significant downtime for repair or maintenance and negative environmental burden upon disposal. Extending the lifetime of the components through the incorporation of self-healing functionality has the potential to limit both of these criteria. Multiple healing techniques have been developed; however, they all aim to reverse the degradation of the material structure through a chemical transformation at a defect site. For almost a decade, the application of self-healing was limited to polymer systems, but, more recently, research has expanded to include nanocomposite materials.

2.2.2 Healing approaches and chemistries

Three main approaches to healing have received significant attention from research groups thus far. These are microencapsulation, TRDA, and intermolecular interactions. Microencapsulation employs micro-scale capsules loaded within the polymer matrix. The capsules contain unreacted monomer, and following crack or scratch propagation, the capsules are ruptured, and the monomer escapes. The monomer then fills the void before polymerising to recover the structure and properties of the original matrix. White *et al.* pioneered this work using an epoxide matrix and a dicyclopentadiene (DCPD) monomer.[6] The microcapsules and Grubb's catalyst were suspended in the epoxide structure that facilitated rapid contact-induced polymerisation (Figure 2.1 a)). The selection of the monomer and catalyst are required to meet a range of requirements including, long shelf-life allowing healing over long time scales, low monomer viscosity providing fast and complete filling of the crack void, low monomer volatility to prevent the monomer evaporating from the crack prior to polymerisation and finally, rapid polymerisation at RT to maintain the automatic healing mechanism. Ring-opening metathesis polymerisation (ROMP) fulfilled all of the associated requirements; however, the use of the expensive Grubb's catalyst provides issues for scale-up. Following the failure of samples under tensile load, the test specimens were allowed 48 hours to heal before fracture tests were repeated, and it was discovered that 75% of the original strength was recovered. The failure occurred

through the same crack plane, confirming a major drawback of the microcapsule technique.
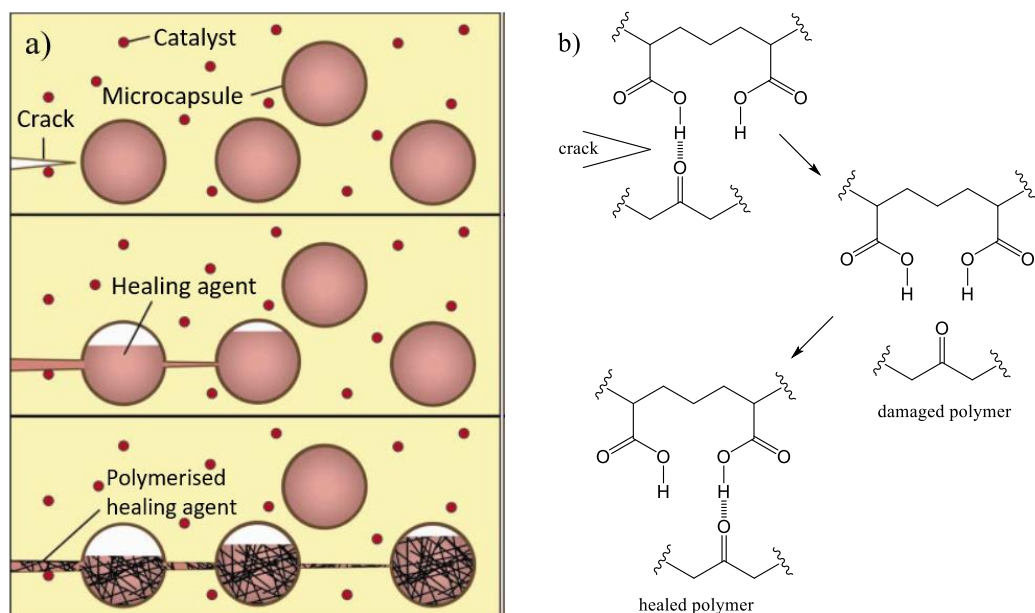
Figure 2.1 – Schematic representation of healing mechanisms for a) microencapsulation and b) reversible intermolecular interactions. Microcapsule figure reproduced from work by White *et al.*[6]

Due to the irreversible nature of the polymerisation, only one healing cycle can occur at each location. As was observed in the initial work by White *et al.*, recovery of the mechanical properties must be >100% if subsequent damage events are to propagate through alternate planes. Critically, the reduction in mechanical strength following healing attracts further stress failure to locations where healing is no longer possible. This greatly reduces the longevity of the material.

Other developments have produced matrices where the catalyst is contained within the microcapsule[7] and also examples where no catalyst is required.[8] It was found that the microcapsules could be infused with solvent, firstly chlorobenzene,[9] but later more environmentally friendly alternatives, phenylacetate (PA) and ethyl phenylacetate (EPA), recording similar healing properties.[8] A recovery of 82% was

reported with chlorobenzene, and when epoxy monomers and amine curing agents were included in tandem with the PA and EPA, 100% recovery was possible. In recent years, the focus has shifted away from microcapsule technology, most likely due to the limited applications of technology without multiple healing potential.

The reversibility of intermolecular forces (IF) can be exploited to create an infinite number of healing cycles (Figure 2.1 b)). Cracks are known to propagate through the weakest domains within a matrix and hence, IF are broken prior to cleavage of the covalent network. This can be used as a sacrificial mechanism to absorb stress before thermodynamically favourable intermolecular bonds are reformed. Multiple works have been published on π-π,[10] ionic,[11, 12] and metal-ligand coordination;[13, 14] however, the vast majority of research in this field focuses on hydrogen bonding interactions.

Early work by Cordier *et al*. reported a rubber elastomer with a large extension at the break, but minimal creep under load.[15] Through a complex mixture of functionalised fatty di- and tri-acids, a densely cross-linked network was produced through hydrogen bonding interactions (Figure 2.2). This work emphasises the importance of a large quantity of reversible interactions providing structural strength in non-covalently cross-linked materials. Without a covalently cross-linked network, it can be more challenging to produce materials with high mechanical strength. When a crack propagates through the network, the sacrificial hydrogen bonds are broken, protecting the covalent structure of the oligomers. Due to favourable hydrogen bonding, healing was achieved at RT but was not quantified.

Later work used similar chemistry to produce a range of elastomeric materials, in some cases quantifying the mechanical recovery of the healing process.[16-19] There are also a number of articles reporting hydrogel structures with similar healing chemistries.[20-22] It is, however, clear that the inclusion of high-density hydrogen bonding networks typically produces flexible, elastic materials.

Zhu *et al*. reported self-healing by including a hydrogen bonding polymer within a nacre-mimetic material (discussed in greater detail in Chapter 2.4).[23] The nacre-mimetic structure provides greater resistance to scratch and impact but is also highly rigid. As a result, the self-healing polymer is restricted in movement and

therefore cannot migrate easily to heal the damaged area. To remedy this, Zhu *et al.* used a low T_g polymer (-61 °C) to encourage high dynamics. Interestingly, the authors did not explore the mechanical recovery, instead focusing on alternative functionalities.
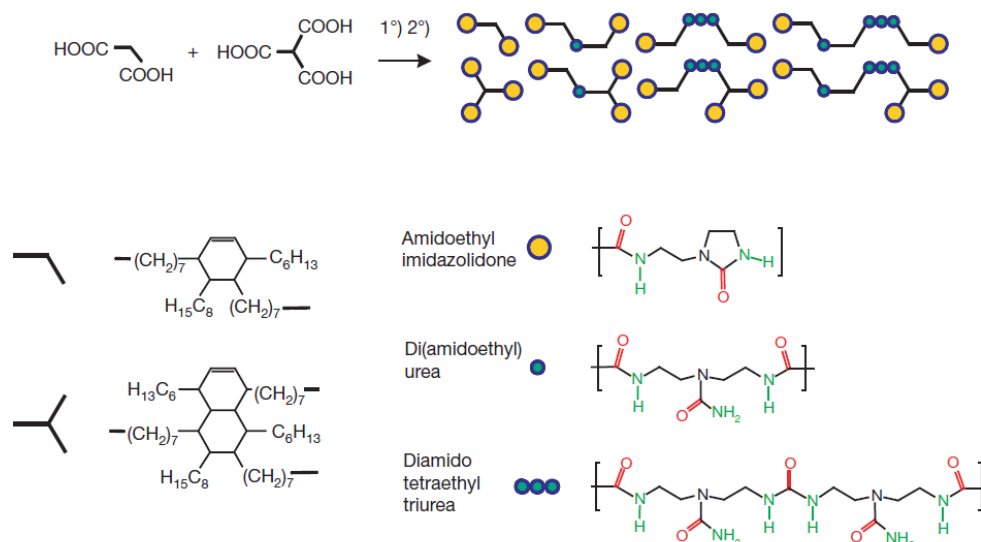
Figure 2.2 – Synthetic pathway towards a hydrogen bonded network of fatty acids as reported by Cordier *et al.*[15]

Ultimately, the use of hydrogen bonding as a self-healing mechanism is dependent on certain requirements. The key benefit of this type of chemistry is the ability to achieve healing at RT without the need for external stimuli. Critically, to facilitate efficient healing under these conditions, the hydrogen bonding groups must have a high level of dynamic freedom to migrate into a damaged site and couple to bonding partners. This favours elastomeric and flexible polymers, as the more rigid alternatives (e.g., epoxy, methacrylates, etc.) do not provide the same dynamic environment. As a result, the majority of polymers with this healing are not suitable for the coatings targeted in this project.

2.2.3 Thermally-reversible Diels-Alder (TRDA) functionality for self-healing polymers

The TRDA approach has been widely researched since its inception in 2002.[24] A polymer matrix is functionalised with diene and dienophile containing species that are able to undergo a Diels-Alder (DA) reaction to form cross-links. Following damage, the material can be heated to initiate a retro-Diels-Alder (rDA) reaction that breaks the cross-links. This increases the dynamic freedom of the matrix and allows migration into the crack or scratch. Once filled, the material is cooled to initiate the DA reaction to recover the properties of the virgin sample. This approach is more suitable for rigid polymers due to the strong cross-links created through the covalent coupling.

Chen *et al.* pioneered research into TRDA when they produced a macromolecular polymer through the DA reaction of tetrafuran and trimaleimide monomers (Figure 2.3).[24] The resulting material had similar mechanical properties to epoxy resins and unsaturated polyesters already used in the industry. Healing was quantified through fracture testing, and it was found that an average recovery of 50% and 41% were possible at 150 °C and 120 °C, respectively. Interestingly, the authors discovered that only 25% and 12% of the DA adducts were decoupled at these temperatures. No decoupling was observed below 120 °C. This would suggest that healing is achieved with minimal rDA reaction and the structural strength of the sample is unlikely to be significantly reduced during the healing treatment.
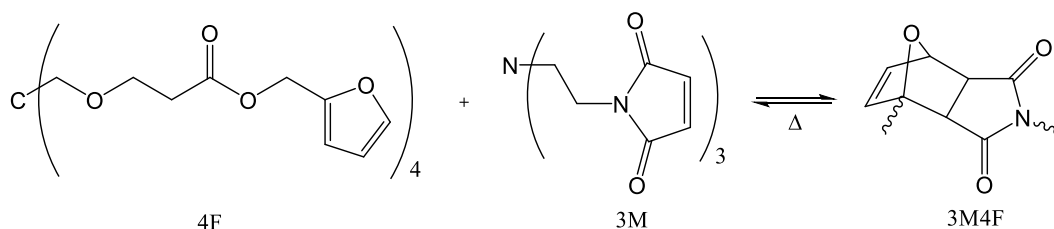
Figure 2.3 – Polymerisation reaction between tetrafuran (4F) and trimaleimide (3M) monomers reported by Chen *et al.*[24]

The maleimide-furan coupling (MFC) employed by Chen *et al.* is widely used in this field.[25-27] Furfuryl monomers and bis-maleimide compounds are commercially available, allowing for simple manufacture of polymer matrices, cross-linked by a MFC. Maleimide precursors are also widely available allowing for fast and efficient monomer/polymer functionalisation. Alternatively, a well understood synthetic route is available to produce a di-hydroxy-terminated MFC cross-linker that can undergo further functionalisation and monomer end-capping.[28, 29] The MFC undergoes rDA between 90 °C and 150 °C, proving critical for healing experiments in the laboratory and real-world conditions. When rDA occurs at close to ambient conditions, the matrix is in a constant state of DA/rDA exchange due to the equilibrium nature of the bonding. This results in incomplete cross-linking and weakening of the polymer structure. Equally, rDA at high temperature is impractical and hazardous in real-world applications, so is mostly avoided (unless for specific applications[30]).

Alternative DA couplings have been reported but are limited to very few examples. A one-component macromolecular polymer using DCPD couplings were reported by Murphy *et al.*[31] The one-component nature of the polymer was labelled as a significant advantage due to improved uniformity. Despite this, polymers having a wide range of fracture strengths post-healing were recorded. The DCPD linkage undergoes a further DA reaction to produce trimers allowing the formation of a cross-linked network that was healed at 120 °C. Healing recovery was found to range from 20% to 60%. It is likely that trimer formation is not uniform and therefore creates localised variations in the polymer structure. Ultimately, DCPD coupling was proven to facilitate self-healing; however, poor consistency and challenging synthesis have prevented significant further research.

The DA coupling of anthracene and a maleimide is theoretically stable to at least 250 °C. This was tested by Heo *et al.* who produced a polyurethane that was decoupled through mechanical stress and then mended via a thermally stimulated recombination.[30] It was found from TGA and DSC studies that the polymer degraded prior to the rDA reaction and thus could not be healed through the traditional heat-then-cool technique. Instead, the polymer was heated above T_g, and the improved dynamic freedom allowed for adequate recombination of the DA adduct. A tensile strength close to 90 MPa was reported with an average healing of 69% and 52% for

first and second healing cycles, respectively. This work represents an interesting alternative to the MFC; however, in most automotive applications, polymers rarely experience temperatures of >100 °C during general usage.

Protection of the maleimide can be useful in the preparation of di-functional self-healing polymers. Kötteritzsch *et al*. reported a poly(methyl methacrylate) (PMMA) containing both furfuryl and maleimide pendant groups.[32] Through synthesis of a maleimide methacrylate (MiMA), polymerisation was possible with furfuryl methacrylate (FMA) and methyl methacrylate (MMA). The MiMA monomer remained protected by a sacrificial furan group throughout preparation to prevent premature cross-linking with the furfuryl groups. When the polymer is processed, the application of heat initiates the rDA reaction, and furan is vaporised (boiling point = 30 °C), allowing a DA reaction to cross-link the polymer structure. Multiple co-monomers were studied with varying control of molecular weight and polydispersity. Mechanical properties were tested using nanoindentation and found to be weaker when compared to a poly(carbonate) control. This was believed to be beneficial as elastic deformation aids the healing process. Unfortunately, self-healing was not analysed via recovery of mechanical properties and so was not quantified. Instead, scanning-electron microscopy (SEM) was used to visualise the healing process. It can be seen from the images in Figure 2.4 that effective healing was possible after 3 minutes at 160 °C.

Syrett *et al*. used similar chemistry to synthesise TRDA acrylates through Cu(0)-mediated living radical polymerisation (LRP).[29] MFC initiators and monomers were produced that allowed great control over cross-link density. Anthracene-based couplings were also explored; however, only 20% of the linkages underwent rDA reactions at 200 °C. Gel-permeation chromatography (GPC) confirmed the MFC to be reversibly exchanging under heating cycles; however, the molecular weight was detected to decrease, suggesting incomplete recombination. Mechanical properties were not tested but the theoretical aspects of the synthesis and polymerisation techniques provide inspiration for this project and future research.
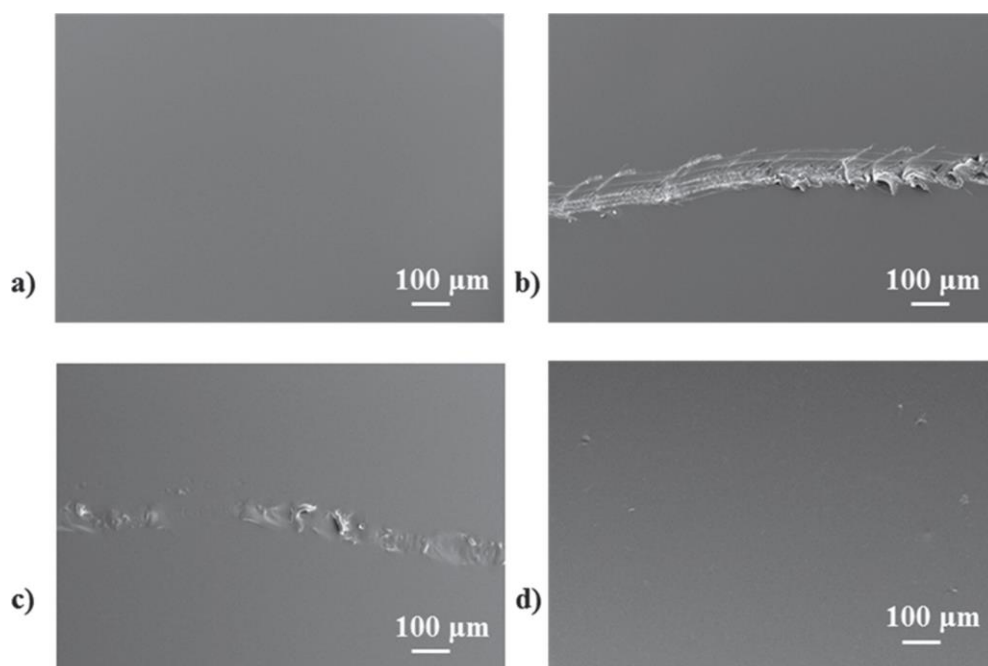
Figure 2.4 – SEM images of the self-healing process of the methacrylate based TRDA polymer where a) film post cross-linking, b) scratched surface prior to heat treatment, c) scratch following 1 minute annealing at 160 °C and d) scratch following 3 minutes annealing at 160 °C. Images are reproduced from Kötteritzsch *et al.*[32]

2.3 Polymerisation techniques

2.3.1 Introduction

Synthetic polymers have been produced for over a century, revolutionising materials science and finding a wide range of applications, including in automation and packaging.[33] More recent innovations have enabled high levels of control over the structure and molecular weight of the polymers produced. There are two classes of polymerisation: chain-growth and step-growth. Step-growth polymerisation utilises a reaction between complimentary functional groups on growing polymer chains, often releasing small molecule by-products during a condensation style reaction. Some step-growth polymers do not release by-products, e.g., polyurethanes, so proceed via an addition reaction. In these polymerisations, molecular weight remains low until the late stages of the reaction where the molecular weight begins to grow exponentially.

Chain-growth polymerisation proceeds through the addition of single monomer units to a polymer structure. As a result, molecular weight growth is linear. Chain-growth techniques are limited to a few synthetic processes, including anionic addition, cationic addition, and radical polymerisation. Of these, radical polymerisation is most widely used by researchers and industry alike. For many decades, free-radical polymerisation (FRP) was the only option available for the synthesis of a number of polymer structures. More recently, however, alternative techniques have been discovered that allow control over the polymerisation process yielding significant improvements in molecular weight control,[29] end group functionality[34] and block co-polymer structures.[35]

2.3.2 Free-radical polymerisation (FRP)

Widely used for many decades, FRP is a simple technique to produce polymeric materials. Monomers are combined with a radical initiator before either heat or light is applied to initiate polymerisation. Greater complexity is possible through combinations of different monomers or initiators. FRP is achieved when the radical initiator (e.g., 2,2'-azobisisobutyronitrile (AIBN)) decomposes from thermal or electromagnetic radiation. This produces a radical species that reacts with the alkene (or alkyne) bond of the monomer unit, creating a new covalent bond and transferring the radical onto the terminal carbon atom. The newly formed radical then reacts with another monomer unit in a repeating manner following a 'head to tail' mechanism. Ultimately, the polymerisation ends following exposure to diatomic oxygen or when the monomer pool is depleted. Termination occurs through recombination with another propagating polymer radical or through disproportionation, where the active chain removes hydrogen from the β-carbon and transfers it to a separate chain. This creates an alkene and alkane terminated polymer. The initiation step is very slow, and therefore new chains begin to grow throughout the polymerisation process. As a result, control of molecular weight is challenging, and end group fidelity is poor.[36]

2.3.3 Reversible-addition fragmentation chain-transfer (RAFT) polymerisation

Reversible-addition fragmentation chain-transfer (RAFT) polymerisation is a controlled living radical polymerisation (LRP) technique that is able to polymerise monomers containing a double bond through a radical propagation process. The key component of RAFT polymerisation is the chain-transfer agent (CTA) that is able to

reversibly bind to the propagating radical, temporarily forcing it into a dormant state. This allows the polymerisation to be regulated, narrowing the polydispersity of the final product. Essentially, the RAFT approach is equivalent to FRP in all ways except the presence of the CTA. The different RAFT polymerisation mechanisms are shown in Figure 2.5.
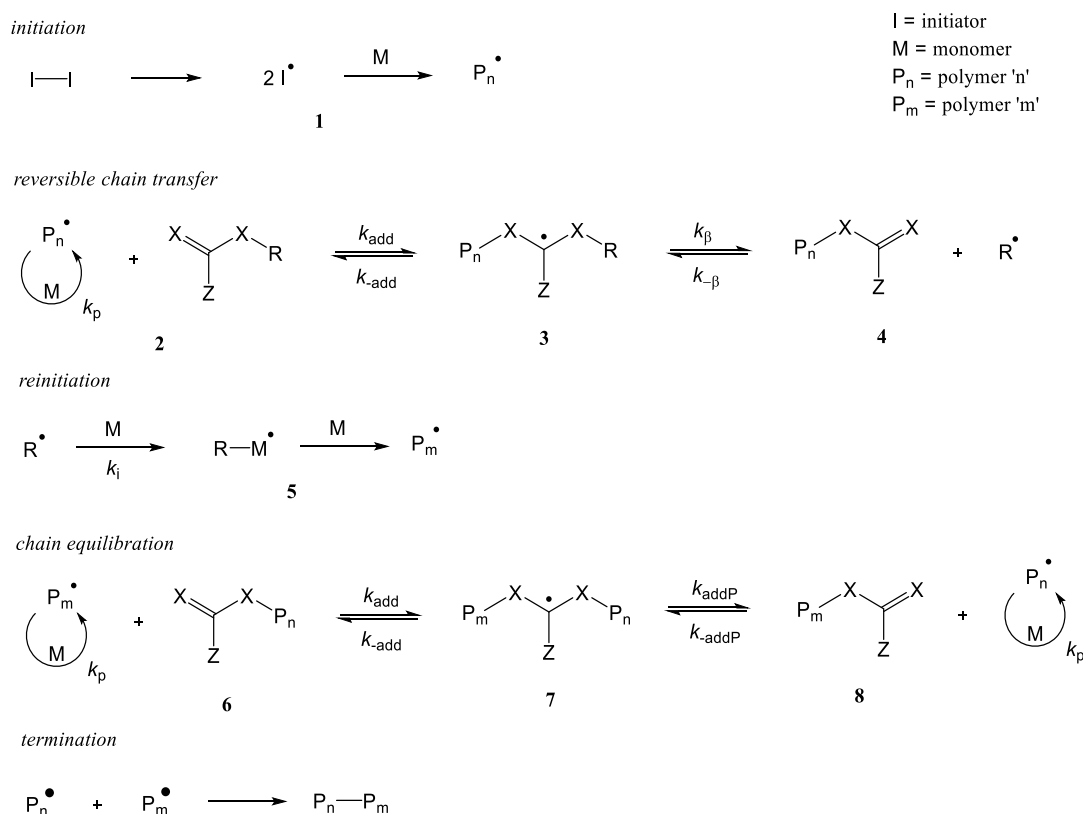
Figure 2.5 – Schematic mechanism for RAFT polymerisation.[37, 38]

The mechanism is initiated through the homolytic cleavage of the radical initiator by heat or light. The resulting initiator radicals begin to propagate with monomer units producing small molecular weight oligomers (**1**). After a short time, the oligomeric radical will interact with the CTA (**2**), whereby a reversible addition occurs, and the radical is stabilised at the tertiary carbon centre (**3**). At this point, the radical can either cleave the oligomer in a reverse of the binding process or can cleave the CTA leaving group, R (**4**). The R radical is then able to behave as a pseudo-initiator

and produce a new polymer chain (**5**). Meanwhile, chain equilibrium is established. The polymer radicals are temporarily and reversibly bound to the CTA, controlling the rate at which the chains can grow (**6**, **7**, **8**). The CTA prevents polymer chains from growing uncontrolled and narrows the molecular weight distribution. Commonly, the CTA remains bonded to the polymer following polymerisation; however, it is possible that two polymer radicals can combine in a termination reaction.[37-39]

X is most often a sulphur atom but can in some cases be a CH_2 group. The correct selection of the Z and R groups are essential to maximise polymerisation. Z groups determine the rate of addition and fragmentation of the growing polymer chains due to their effect on the stabilisation of the radical (**7**). Trithiocarbonate (where Z = S-R_1) CTAs are more reactive (than dithiocarbonates) as the sulphur atom aids in maintaining the double-bond C=S of the thiocarbonylthio group which is more reactive towards radicals. A balance is necessary between reactivity of the CTA and the stability of the R leaving group. It is important that the R radical is able to reinitiate polymerisation otherwise, termination reactions dominate, and polydispersity will greatly increase. Ultimately, the R group must readily cleave from the CTA and must subsequently provide high levels of re-initiation to maintain control.[39]

Due to the wide range of monomers suitable for polymerisation via RAFT, CTA selection is vital. Monomers can be classified as either 'more-activated' (M-A) or 'less-activated' (L-A) depending on the nature of the C=C bond. Conjugated alkene monomers (i.e. to an aromatic or carbonyl group) are considered to be M-A and show low reactivity towards radicals. L-A monomers contain adjacent saturated carbon, nitrogen or oxygen atoms and more readily react with radicals. M-A monomers require a more activated CTA to encourage radical propagation and, therefore, commonly require trithiocarbonate CTAs. Less activated CTA are suitable for L-A monomers. Ultimately, the monomer selection determines the type of CTA that should be used to achieve optimal polymerisation and, therefore, must be carefully designed for each polymerisation reaction.[39]

2.3.4 Cu(0)-mediated and single-electron transfer LRP

Cu(0)-mediated LRP offers an alternative to RAFT that is widely reported in the literature. The products of this method are often colourless as opposed to yellow

or pink (commonly observed with RAFT). As with RAFT, high levels of conversion are achieved with excellent control of molecular weight distribution. Cu(0)-mediated LRP can also be completed at RT and pressure due to initiation via a catalysed decomposition of a substituted alkyl halide. The resulting alkyl radical is then able to react with an unsaturated alkene to initiate the polymerisation. The precise mechanism of Cu(0)-mediated LRP is still debated; however, it is believed that dormant chains become active through a heterogeneous outer-sphere electron transfer.[40, 41]

Cu(0)-mediated polymerisation of M-A monomers such as acrylates, methacrylates, and acrylamides produces highly functional polymers and often yields high conversion in a few hours. Narrow dispersities of ≈1.1 are possible under ambient conditions and in a range of solvents, including water, alcoholic beverages, and blood serum.[41] Typically, polymerisation of methacrylates is slower than the analogous acrylate monomers due to their reduced activity; however, high conversion can be achieved in DMSO at RT in just 24 hours.[42] Critically, L-A monomers cannot be polymerised through Cu(0)-mediated LRP as they are unable to complex to the Cu centre during polymerisation. High molecular weight control and little bimolecular termination allows the synthesis of highly ordered polymers that are ideal for self-healing architectures.[43]

Compared to RAFT and FRP, the Cu(0)-mediated LRP reaction has a more complex mixture of components. An initiator, monomer, CuX_2 halide, Cu(0) source, ligand, and solvent (although bulk reactions are possible) are required for adequate control of the polymerisation. The initiator is typically an alkyl halide where the halide can be easily abstracted before rapidly and selectively migrating between the growing chain and the Cu-centred complex. Typically, Cl or Br are used however, I has been shown to be effective for some acrylate polymerisations. The C-F bond is too strong to undergo homolytic cleavage and so cannot be used.[44] The ligand (L) is essential for establishing the catalyst structure. Through complexation with the CuX_2 halide and Cu(0)-source, the activated catalyst (X-Cu(I)-L) is produced. This catalyst is able to undergo redox reactions to cleave the halide onto propagating polymer chains (Cu(0)-L) to temporarily lock them in a dormant state before later rebinding with the X atom to reactivate the polymer radical. Without the L, disproportionation of the Cu-X bond

is not possible, and control is lost. A separate Cu(0) source is required to facilitate the homolytic cleavage of the alkyl halide bond to initiate the polymerisation.[41]

The mechanism centres around the Cu and the equilibrium between three oxidation states (Figure 2.6). Cu(0) acts as the activator following complexation with a L. Typically, *tris*[2-(dimethylamino)ethyl]amine (Me$_6$TREN) is used. The resulting complex rapidly activates the initiator molecules to homolytically cleave the halide atom and produce a radical species. The radical initiator then propagates through the double bonds of the monomer species whilst becoming periodically deactivated by the Cu(I) and Cu(II) complexes. The rate of activation and deactivation is significantly faster than the rate of propagation, and therefore, polymer growth is well controlled. This also provides limited opportunity for termination reactions resulting in excellent end group fidelity.[41]
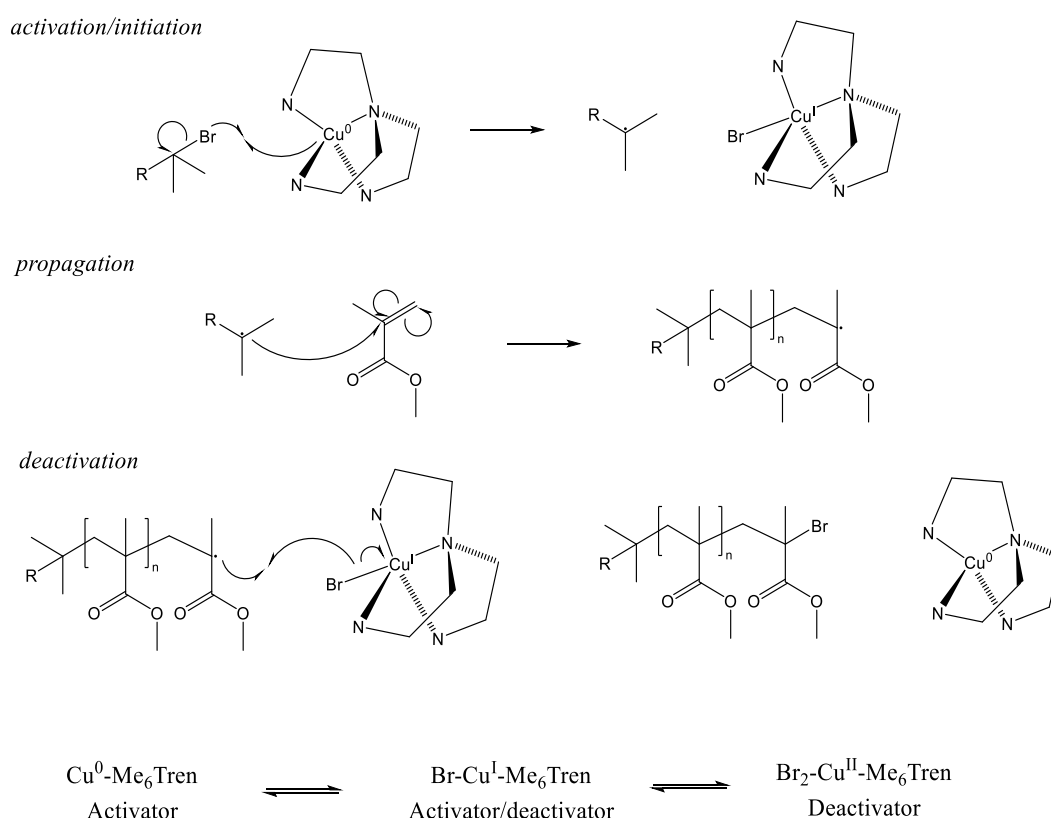
Figure 2.6 – Simplified Cu(0)-mediated LRP mechanism for polymerisation of MMA.

Cu(0)-mediated LRP provides a versatile technique for the production of highly controlled polymer architectures without extensive purification. Polymerisation of methacrylate polymers is widely reported and is found to achieve excellent conversion and dispersity.[42, 45, 46] Through polymerisation at RT, any thermal side-effects instigated by initiation at high temperature are circumvented, and the final thermal stability of the polymer is likely to be improved over RAFT alternatives. Simply, Cu(0)-mediated LRP provides an effective alternative to RAFT for the preparation of self-healing polymers.

2.4 Nacre-mimetic materials

2.4.1 Introduction

Nacre, otherwise known as 'mother-of-pearl,' is an extraordinary material that has attracted significant scientific interest for many decades. Present in the shells of the mollusc family, Nacre is a two-component composite material consisting of 95% by volume calcium carbonate platelets and 5% biopolymer protein. The resulting material displays mechanical properties that far exceed the component parts. This is achieved through the collaborative interactions between the two components enabling multiple stress dissipation mechanisms.[47, 48] Due to the high nanoplatelet content, a highly structured morphology is produced where multiple layers of aragonite (the planar polymorph of $CaCO_3$) are adhered together by the biopolymer. The uni-directional layered morphology is widely referred to as a 'brick and mortar' structure. The aragonite sheets provide a stiff, rigid structure that provides the bulk of the mechanical strength, whilst the biopolymer is much softer and behaves as a shock absorber. In cases of high force stress, sacrificial bonds are broken on the nanoscale. This prevents complete failure of the material by hindering the propagation of high stress throughout the entire material. Ultimately, Nacre is able to absorb remarkably high levels of macroscale stress whilst also providing localised nanoscale sacrificial pathways that extend the lifetime of the material and protect the mollusc within.

2.4.2 Mechanical properties of Nacre

Evolution in the natural world has developed numerous materials with exceptional mechanical properties. As a result, nature is widely used as an inspiration for novel research. Nacre displays similar mechanical properties to a range of other

naturally occurring rigid materials (Figure 2.7 a)), including bone, antler, and enamel, all of which are known for their high strength. Interestingly, when compared to traditional polymer materials, Nacre displays significantly increased tensile strength whilst maintaining similar impact toughness (Figure 2.7 b)). It is, therefore clear that nacre-mimetic materials have the potential to improve the mechanical properties of the polymer coatings currently used in the automotive industry.
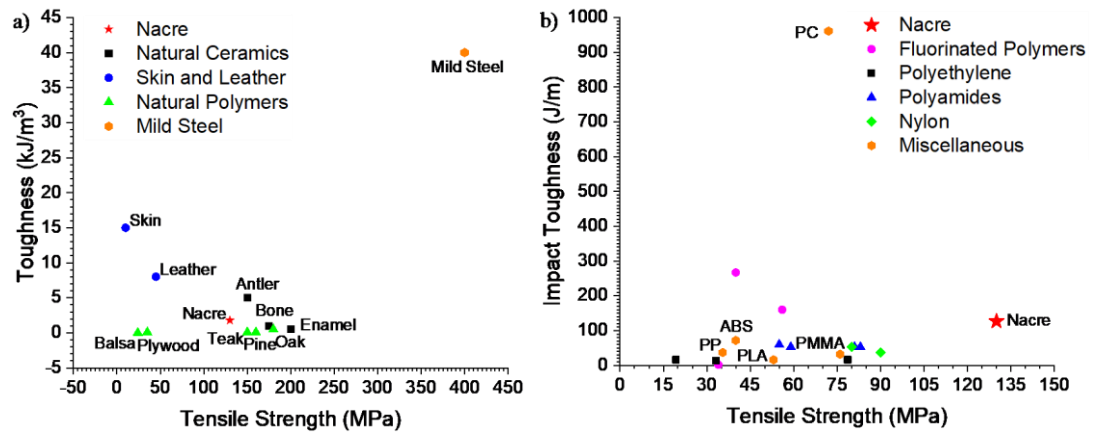
Figure 2.7 – Comparison of the mechanical properties of Nacre[49] with a) natural materials and mild steel (non-nacre properties collated from work by Ashby et al.[50]) and b) example polymers[51] (impact toughness extrapolated from work by Lee et al.[52])

Work by Jackson et al. outlined the widely accepted mechanical properties of natural nacre.[49] A Young's modulus (E) of up to 70 GPa when dry and 60 GPa when wet was recorded. The minimal effect of water was reported to be due to the low water retention capacity of the nacre structure. A tensile strength (σ) of between 130 ± 24 and 167 ± 22 MPa was recorded, a significant increase on previous reports,[53] and toughness was found to vary greatly depending on the experimental conditions. It was also reported that two failure mechanisms were observed under tensile load. In the first case, at a low nanoplatelet aspect ratio, the cross-sectional load within the material can exceed the shear-strength. This results in the nanoplatelet shearing out of the matrix. At a high aspect ratio, the cross-sectional strength is reduced, and so the maximum nanoplatelet load is exceeded, causing platelet fracture. Jackson et al. did,

however, theorise that in natural nacre, the pull-out failure mechanism is preferred due to the nanoplatelet dimensions and the effect of water on properties. This insight suggests aspect ratio is a key variable when discussing the mechanical failure of nacre-mimetic materials. Already, the properties displayed by natural nacre have been dwarfed by anthropogenic analogues, reaching values in excess of 650 MPa,[54] in part due to the availability of high strength nanoplatelets and polymer systems.

2.4.3 Methods for the production of nacre-mimetic materials

Nacre-mimetic films have been produced via multiple methods. Whilst nature utilises a templating process where the protein binder aids in the construction of individual layers of aragonite in a stepwise process,[55] human-derived alternatives often use similar favourable interactions to facilitate self-assembly. Directional stimuli can be used to encourage linear orientation when self-assembly is not possible. Ultimately, construction of the uni-directional layered morphology is a highly delicate process and thus limits the production methods available to researchers. Techniques such as extrusion and injection moulding are unlikely to provide adequate conditions for effective templating of the layered arrangement.

Layer-by-layer (LbL) approaches offer the closest replication of the technique used naturally; however, it is a highly time-consuming process and is unsuitable for large-scale manufacture. Using a systematic process, alternate layers of nanoplatelet and polymer are adhered to a substrate material (Figure 2.8).[56-58] Each step applies a single layer to the growing film, and so high levels of control are possible. There is also a potential for multiple different nanoplatelets or polymers to be used in the same material to produce hybrid structures. Highly precise films are possible; however, manufacturing time limits the potential of this technique.

Vacuum-assisted filtration is a widely used technique producing nacre-mimetic films quickly and efficiently.[60-64] A dispersion of nanoplatelets and polymer binder is produced in a suitable solvent. The dispersion is then passed through a vacuum filtration setup, where the vacuum applies a directional stimulus to encourage an orientated assembly. Following drying, it is common for the nacre-mimetic film to be peeled from the substrate (Figure 2.9). Whilst efficient, this method has little scale-up potential at this time and so is limited to proof of concept works.[65-67]
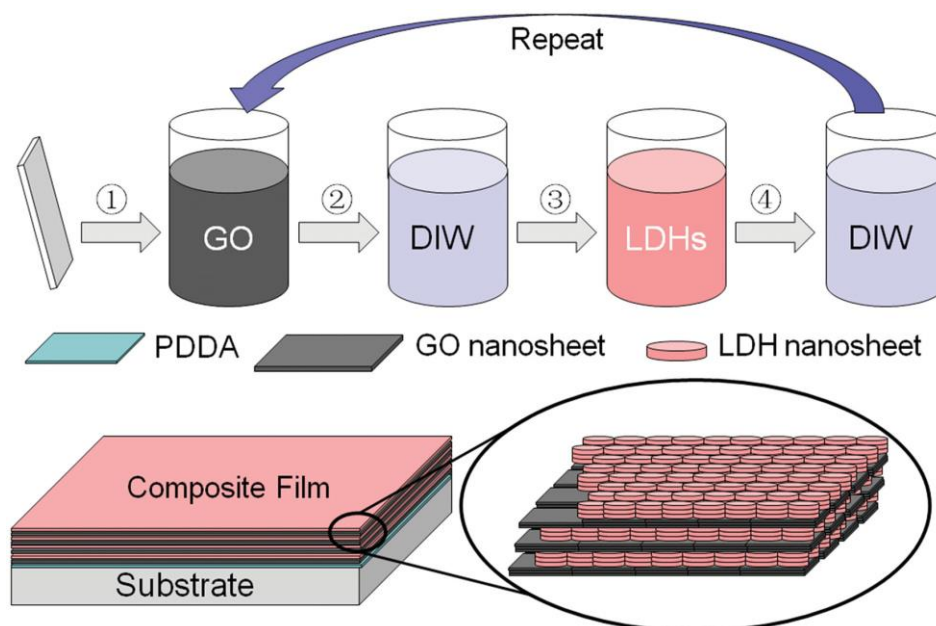
Figure 2.8 – The LbL approach to the production of nacre-mimetic films. Reproduced from work by Yan *et al.*[59] DIW = deionised water, LDH = layered double hydroxide, PDDA = poly(diallyldimethylammonium chloride).
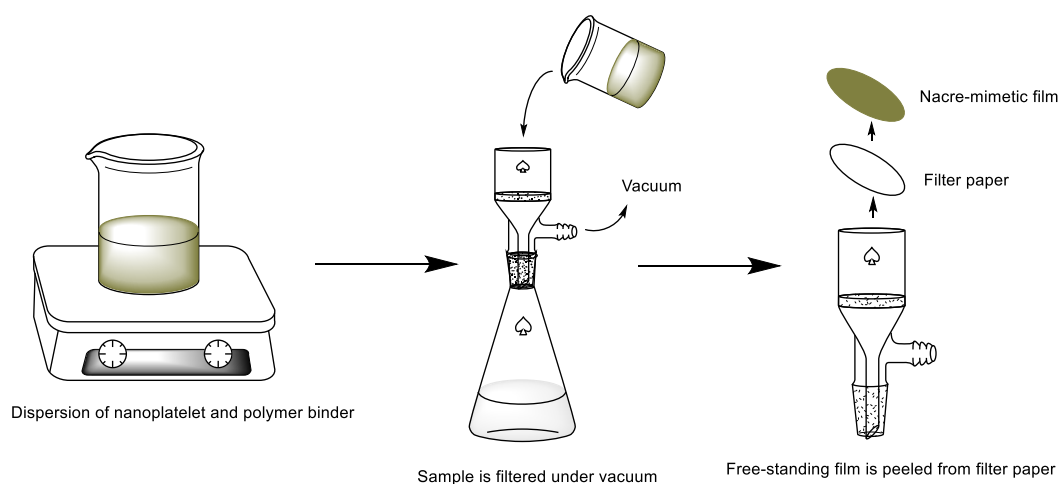
Figure 2.9 – Schematic diagram of the vacuum-assisted filtration approach for the production of nacre-mimetic films.

Solution (or solvent) casting offers an alternative approach with improved scalability.[68-73] A dispersion is produced in a similar fashion to the vacuum-assisted filtration method; however, the dispersion is ultimately cast into a mould and allowed

to dry through solvent evaporation (Figure 2.10). It is essential when using solution casting that the nanoplatelet and polymer have complimentary interactions due to the lack of directional stimuli. The nanoplatelet and polymer are forced to self-assemble[74] as the solvent evaporates, and so poor interactions result in inhomogeneous films with poor properties.
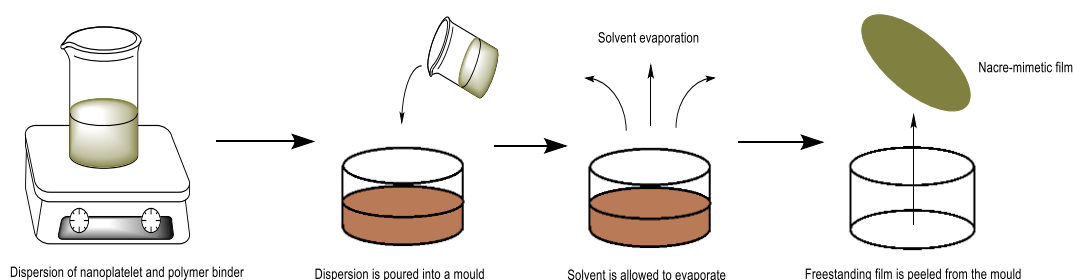
Figure 2.10 – Schematic illustration of the solution casting approach for the production of nacre-mimetic films.

Spray coating is arguably the most industrially scalable technique reported and has been shown to be effective with multiple nanoplatelet types.[4, 65, 75, 76] Despite attracting less interest than other methods, the spray technique enables self-assembly of suitable nanoplatelet-polymer combinations during the evaporation of the solvent micro-droplets (Figure 2.11). With suitable optimisation, this technique can be used to allow large-scale, automated production and thus an application of nacre-mimetic materials (films) to numerous industrial components.

There are also techniques requiring specialised equipment such as doctor blading[3, 78] and bi-directional freeze-drying.[77, 79-81] The bi-directional freezing method has significant potential for the development of highly controlled materials with previously incompatible components. Production of hybrid films is also possible using this technique. Critically, the equipment necessary to produce nacre-mimetic films via this method is typically bespoke (homemade) and not available to the wider research community. For a complete overview of the multitude of production approaches for these materials, see Corni *et al*.[82]

Nanoplatelet and binder dispersed in solvent   Dispersion sprayed onto surface and dried   Brick and mortar structure self-assembles during drying
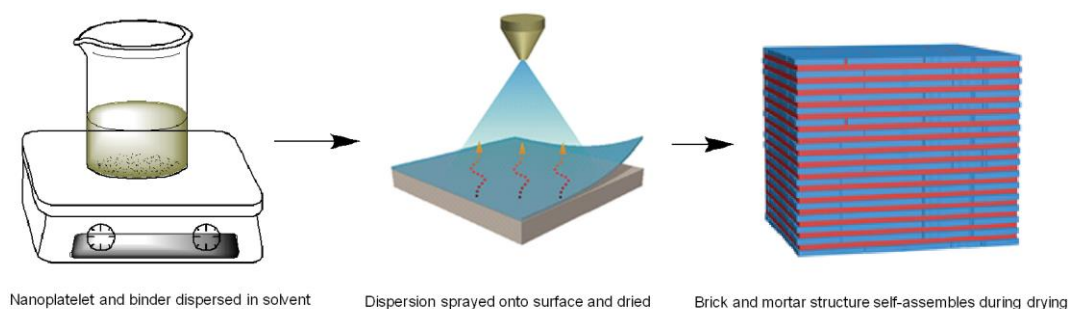
Figure 2.11 – Spray coating process for production of nacre-mimetic films. Images reproduced from works by Pan *et al.*[4] and Bai *et al.*[77]

2.4.4 Mechanical and physical properties of nacre-mimetic materials

Nacre-mimetic materials based on graphene or reduced-graphene oxide (rGO) often record exceptionally high mechanical properties.[61, 63, 83] The highly uniform structure of graphene enables excellent packing that aids the efficient dissipation of energy. Graphene is also an extremely strong material.[84] GO has weaker mechanical properties but has other beneficial properties (e.g., dispersibility in water). There are numerous examples of GO being used as a precursor to rGO to utilise the improved processability of GO with mechanical properties close to pristine graphene.[70, 85, 86] The reduction of GO to rGO in nacre-mimetic films involves submersion in hydroiodic acid, which is a hazardous process with environmentally dangerous by-products. GO is also of great interest as a standalone nanoplatelet due to dispersion in a range of solvents and compatibility with multiple polymers allows freedom for researchers. The surface of GO can also be functionalised to aid the interactions within the film however, this has not been explored in this context.

One of the key considerations when designing nacre-mimetic materials is the intermolecular interactions between the nanoplatelet and polymer components. Cheng *et al.* employed a UV process to covalently cross-link graphene nanosheets with 10,12-pentacosadiyn-1-ol (PCDO) monomers.[87] A vacuum filtration method was used to assemble a neat GO paper before the resulting film was submerged in PCDO and THF. The PCDO infiltrates between the GO layers and undergoes esterification with the carboxylic acid groups on the GO surface. This provides a covalent anchor between the GO and PCDO. UV radiation is then applied, initiating a 1,4-addition

polymerisation between the PCDO anchors, covalently cross-linking the GO sheets. Following the reduction in HI acid, a tensile strength (σ) of 129.6 ± 18.5 MPa and tensile toughness 3.9 ± 0.3 MJm^{-3} was reported. The toughness observed corresponds to double that of natural nacre; however, the authors did not discuss the relative improvement caused by the UV cross-linking reaction. Later work explored covalent cross-linking of dopamine monomers to GO sheets via an alkali initiated self-polymerisation reaction.[69] Following a HI acid treatment, the films had σ = 204.9 ± 17.0 MPa and toughness of 4.0 ± 0.9 MJm^{-3}, confirming an increase over Nacre in both cases. The σ was also observed to increase by a factor of 2 over a neat GO control sample. It was thus proven that covalent cross-linking was a suitable approach to improve interactions between the components and increase mechanical properties.

Non-covalent cross-linking has also been explored through hydrogen bonding. Wang *et al.* functionalised poly(dopamine) (PDA) with the 4-fold hydrogen bonding synthon, 2-ureido-4[1*H*]-pyrimidinone (UPy), as outlined in Figure 2.12.[64] The resulting PDA was assembled with GO through vacuum filtration to produce nacre-mimetic materials with strong hydrogen bonding between the polymer chains. Due to the cooperative templating between the UPy groups, it is likely that there is a negligible increase in hydrogen bonding to the GO. Despite this, σ and toughness reached 325.6 ± 17.8 MPa and 11.1 ± 1.3 MJm^{-3}, representing a 2.7- and 4-fold increase over an un-functionalised GO-PDA film. The improved interactions between the polymer chains in the structure provide a significant increase in the properties observed. Despite the success of this work, there has been no report on direct functionalisation of GO with the same UPy group or a two-component nacre-mimetic material where both the GO and polymer have been functionalised with UPy.

The versatility and control of the LbL approach were emphasised by work from Yang *et al.* who produced a self-healing nacre-mimetic material.[88] In an attempt to mimic the human epidermis, a two-phase film was produced where a nacre-mimetic film was supported on a polymer substrate. The nacre-mimetic layer contained a GO and poly(vinyl alcohol) (PVA) layered structure (*l*-LbL), and the substrate behaved as a polymer pool, containing two different molecular weight PVA polymers and tannic acid (*e*-LbL). The LbL approach allows high control over the thickness and composition of both the phases in this structure. The harder *l*-LbL layer provides the

mechanical strength, whereas the *e*-LbL is able to migrate towards any cracks or delamination within the *l*-LbL to mend the damage and recover properties. The densely packed structure of nacre-mimetic materials makes polymer migration challenging and thus the material required submersion in water to facilitate healing. It was discovered that healing was only possible with films of between 8 and 12 GO-PVA bilayers therefore, confirming the importance of the LbL control in this application. Critically, mechanical properties were not reported, and so the extent of self-healing could not be quantified.
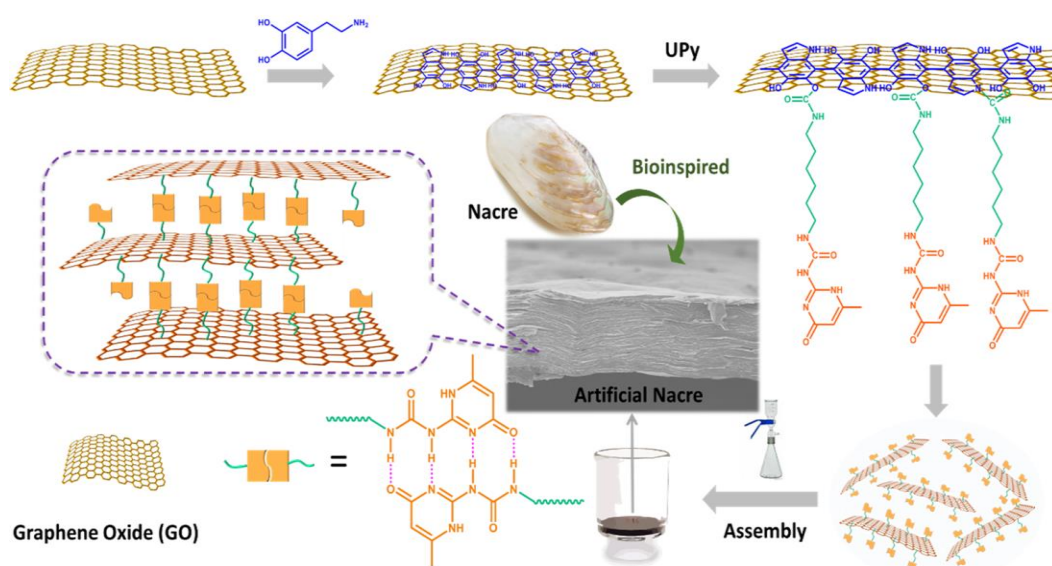
Figure 2.12 – Schematic diagram of production of GO-PDA films containing the 4-fold hydrogen bonding synthon, UPy. Figure reproduced from Wang *et al*.[64]

The combination of GO and PVA is quite common due to the complementary hydrogen bonding between the two components. Initial works by Putz *et al*. highlighted the self-assembly of GO and PVA through a vacuum-assisted filtration approach.[89] Varying polymer content (0, 25, 50, 75, 100 wt%) films were produced, and it was discovered that tensile strength and maximum strain could reach 149.4 MPa and 1.65%, respectively, for neat GO. The addition of PVA resulted in a reduction of both tensile strength and maximum strain; however, Young's modulus increased. Later work by Li *et al*. used solution casting to produce films with PVA content

ranging from 0 to 40 wt% and reported that a 20 wt% PVA content yielded optimal tensile strength (118 MPa).[68] Maximum strain trended downwards with increasing PVA content. Ultimately, the PVA facilitated an optimal increase of 76% in tensile strength and 178% in Young's modulus. Reduction of the GO with hydroiodic acid further improved mechanical properties and electrical conductivity, for reasons described in section 2.6.1.

Since the first development of nacre-mimetic materials, the race to achieve the best mechanical properties has been intense. This has ultimately resulted in extremely strong materials that highlight the significant potential of films of this nature. Xiong *et al.* reported $\sigma = 655 \pm 102$ MPa through a slight deviation from truly biomimetic conditions.[54] By using a 65% by weight of graphene (as opposed to 95%) and 35% modified cellulose nanocrystals (CNCs), films with an elastic modulus comparable to Kevlar were produced. The CNCs arrange into a 'haystack' morphology, orientating randomly between the graphene sheets. Critically, this bridges multiple graphene nanoplatelets to dissipate energy over a large area.

The materials produced by Xiong *et al.* could not be analysed using traditional tensile testing, and so a 'bulge test' was employed. This highlights a concern throughout this field of research where standard testing conditions have not been established. Instead, researchers are able to use conditions that best suit their materials to maximise the properties reported. As a result, a wide range of properties are reported, and direct comparison of the strength of these materials can be difficult. It also challenges new research groups that have not optimised testing conditions to compete with established research methodologies. Ultimately, this can lead to a disparity in the true performance of new films.

Alternative nanoplatelet 'nacre-like' films have been produced with nanoclays,[71, 90, 91] boron nitride nanosheets[62, 92] and alumina[75, 93, 94] to name just three. Whilst reporting, on average, lower mechanical properties than graphene and GO-based nacre-mimetic films, these alternative materials offer a multitude of advantages and functionalities. Transparency,[71, 95] thermochromic transitions,[65] self-healing,[23] and electromagnetic interference shielding[96] have all been described, highlighting the wide potential of nacre-mimetic films as functional materials for a range of applications, including functional coatings.

2.5 Use of α-Zirconium phosphate (α-ZrP) in nanocomposite materials

2.5.1 Introduction

Nanoclay-based nacre-mimetic materials have been widely reported;[71, 90, 95, 97] however, the use of α-ZrP is very limited. Previous α-ZrP based nanocomposites have been shown to display optical transparency and therefore offer certain advantages over GO-based coatings. Zirconium phosphate is an inorganic platelet material that has multiple morphologies, depending on the preparation method employed. Of these, the alpha form (α-ZrP) is most common and can be produced through a simple reflux reaction of zirconium and phosphate salts,[98-101] or through a hydrothermal treatment of the same reagents. The intrinsic bulk modulus of α-ZrP is known to be 15.2 GPa, as reported by Readman *et al*.[102]

2.5.2 Structure and properties of α-ZrP

The α-ZrP morphology is organised in a layered structure whereby the zirconium ions sit out of the *ab* plane in an alternating 'above' and 'below' conformation.[103] An octahedral structure is produced as three of the phosphate-bound oxygen atoms bind to separate Zr ions. The fourth oxygen points perpendicular to the plane, where it forms a hydrogen bond with a single water molecule in the interlayer cavity (Figure 2.13).
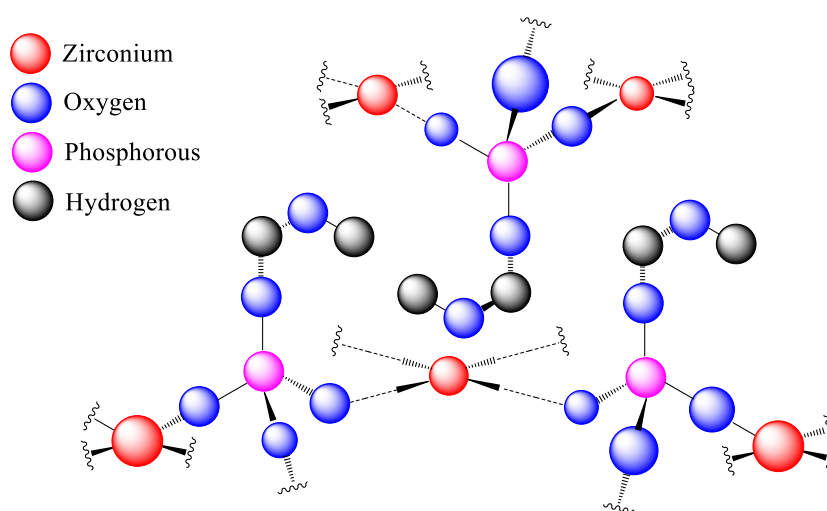
Figure 2.13 – Proposed α-ZrP layered structure, including trapped H_2O in the interlayer space.

Interestingly, significant research has been completed into the intercalation of molecules between the α-ZrP sheets[104, 105] and chemical functionalisation reactions at these sites.[99, 106, 107] The high cationic exchange potential of α-ZrP is known,[108] and this enables penetration of compatible reagents between the α-ZrP layers. Intercalated bi-layers of this nature have applications as biosensors,[109-111] colloid stabilisers,[112, 113] for nanoencapsulation,[114-116] and protein immobilisation,[117-119] to name a few. Intercalation can also be employed to facilitate the exfoliation of α-ZrP in aqueous media. Terminal amine groups of polymers such as poly(ether amine)s (PEAs) undergo cationic exchange with the α-ZrP surface. The long alkyl polymer chain then behaves like a surfactant and repels adjacent α-ZrP sheets creating a well-exfoliated mixture. This effect can be exploited in traditional nanocomposites to aid dispersion but also has great potential for the preparation of nacre-mimetic films by facilitating an improved self-assembly process.

2.5.3 Nanocomposite/nacre-mimetic structures of α-ZrP

The use of α-ZrP has been reported in traditional nanocomposites with several examples, including polymer matrices[120-122] and in mono- or multi-layer films[99, 105, 106, 108, 123] supported on a substrate surface. Despite this understanding, reports on nacre-mimetic materials of this kind are very limited. Work by Waraich *et al.* reports the preparation of nacre-mimetic films using α-ZrP and chitosan.[124] In this work, a LbL method was employed, providing high control over the film thickness and composition. Unfortunately, the films could not be separated from the substrate material (silicon), and so nanoindentation was used for mechanical property analysis. Nanoindentation has not been widely used to study the mechanical properties of nacre-mimetic materials, with conventional tensile testing being far more common. Nevertheless, a reduced Young's modulus (E_r) of 2.6 GPa and hardness (H) of 70 MPa were recorded. With no similar films reported previously, a comparison of these values with other examples is impossible and thus provide an initial benchmark for these types of materials. Han *et al.* have also explored a LbL assembled α-ZrP nacre-mimetic material but only completed studies on the barrier properties of the film towards oxygen and vanadium.[125]

2.6 Functionalisation of graphene oxide (GO)

2.6.1 Introduction

GO is a 2D planar structure of carbon, oxygen and hydrogen that is analogous to graphene. The structure contains graphene-like domains of delocalised six-carbon rings in a honeycomb arrangement. Critically, GO contains oxygenated surface groups[126] that disrupt the ratio of sp^2 to sp^3 hybridisation leading to surface defects that ultimately reduce the mechanical and transport (electrical and thermal conduction) properties of the material. Nonetheless, the surface functionality allows for functionalisation through a number of techniques producing materials with specialised properties. GO can be easily dispersed in water and other polar protic solvents, enabling wider processing conditions than are possible with graphene whilst allowing greater interactions with polymers with complimentary groups (e.g., hydroxyl or ketonic). It is quite common that GO is employed for surface functionalisation before being reduced to graphene to combine the specific properties of the grafted moiety and the high mechanical and electrical properties of the graphene structure. GO has been shown to display an intrinsic Young's modulus of between 290 GPa and 470 GPa, depending on the order and oxygen group coverage.[127] It was also reported that the intrinsic strength of GO ranges from 27.9 GPa to 47.8 GPa and critical failure strain ranges from 10% to 20%.

2.6.2 Functionalisation techniques

Reactions of oxidised graphitic structures have received significant interest from the research community in recent years[128-130] due to their potential to develop interesting new smart materials. As a result, there are a plethora of approaches to functionalise GO towards the desired application. This project focuses on covalent functionalisation methods; however, there is significant research into non-covalent alternatives.[131]

Amination is a widely used method where amine-functionalised groups react through the carboxylic acid groups on the GO surface. A condensation reaction produces an amide, covalently binding the functional group to the surface.[129] Fang *et al.* showed that GO can be aminated with diazonium salts towards Co ion capture whilst Liu *et al*. used organic diamines for adsorption of dye-pollutants.[132] Amination

of GO has been effective at producing materials capable of gas separation,[133] for energy storage,[134] as lipid biosensors,[135] and catalysis.[136]. The versatility of this technique is in part due to the wide range of functional chemicals that can be treated to amine-terminated analogues. Functionalisation with this method often requires the use of harmful solvents and/or elevated temperatures that can reduce the overall sustainability of the reaction.

The reaction of thiols with C=C bonds has been reported as early as 1905 but has received significant interest since the isolation of graphene and GO.[137] These aromatic structures contain an abundance of C=C bonds and as a result, thiol-ene reactions offer a fast and simple method towards functionalisation.[138, 139] Luong *et al*. reported the production of functional rGO for inclusion in an electrically conductive rGO/Pt nanocomposite[140] whilst Yu *et al*. used a similar approach towards UV curable nanocomposite materials.[141] Many other examples have been published exploring optimisation of the thiol-ene route to functionalisation.[142, 143] There is on-going research on thiol-ene click chemistry as a tool to grow polymers onto GO[144, 145] and to further functionalise a pre-treated GO/rGO material.[146, 147] Unfortunately, a radical initiator such as AIBN, non-aqueous solvents and an inert atmosphere are necessary and hence there is debate over whether the reaction is truly 'click' chemistry. Purification steps are also required, drastically hindering the sustainability and overall cost-effectiveness of this approach.

Silane functionalisation has proved a popular technique due to the simplicity of the reaction and relatively mild conditions (typically 70 °C for 24 hours). A trioxysilane (e.g. (3-aminopropyl) trimethoxysilane, widely known as APTES) undergoes reaction with the oxygenated functional groups on the GO surface. This results in covalent functionalisation, where the end group of the silane agent can be used for further treatment or polymerisation. The nature of the pendant group is essential for subsequent reactions, typically targeted towards aiding dispersion of the GO within a polymer matrix. Epoxy-functionalised silanes have been reported that enable direct polymerisation with other epoxy monomers[148, 149] whilst vinylic silanes could be employed in radical polymerisation.[128] Thus far, the applications of this approach are wide including mechanically enhanced epoxy materials,[149, 150] organic photovoltaic cells and LEDs,[148] and corrosion protection.[151]

The reaction between GO and an isocyanate is arguably the most simplistic method to achieve surface functionalisation of GO. Functionalisation can be achieved at RT within 24 hours and in excellent yields. Critically, the isocyanate functional group is highly reactive towards most oxygenated functional groups, as emphasised by the condensation reaction with water. The multitude of functional groups on the GO surface readily react with free isocyanates through the mechanisms outlined in Scheme 2.1. The reaction between a carboxylic acid and an isocyanate has been known for many years[152] and proceeds via a condensation reaction releasing CO_2 as a by-product.[152, 153] Initially, the carboxylate ion attacks the electropositive sp carbon of the isocyanate (Scheme 2.1 a)) producing an anhydride intermediate that undergoes intramolecular rearrangement, expelling CO_2 to produce an amide. Hydroxyl and epoxide groups can also undergo a similar mechanism to yield a carbamate (Scheme 2.1 b)) and oxazolidone[154] (Scheme 2.1 c)) respectively. Typically, the reactivity of isocyanates towards aromatic species is lower than that of aliphatic analogues. Despite this, in the case of GO, the aromatic nature of graphene is disrupted close to the functional groups and so they behave similarly to aliphatic species. The reaction of isocyanate with GO can be followed easily with FTIR.[155]
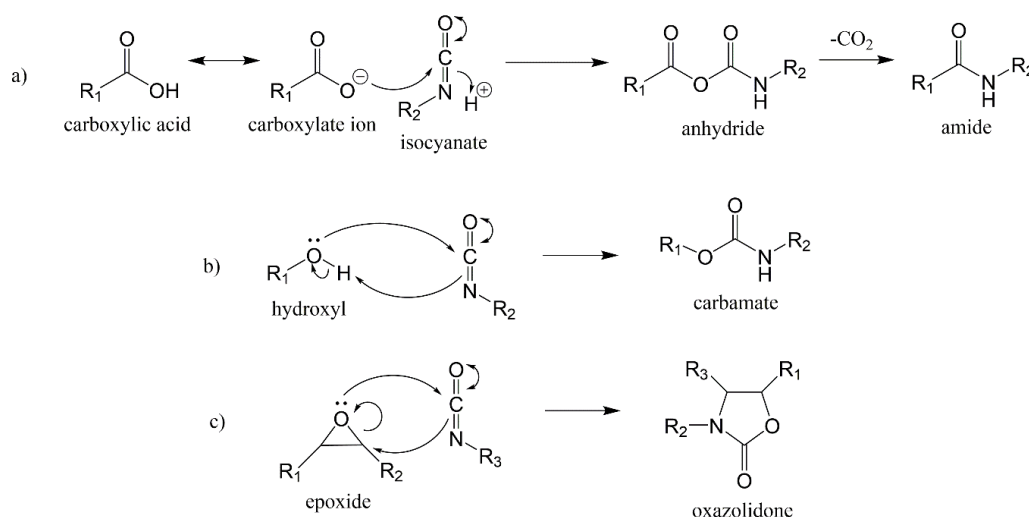
Scheme 2.1 – Isocyanate reactions with surface functional groups of GO where a) reaction of a carboxylic acid with an isocyanate to produce an amide via a condensation reaction, b) reaction between a hydroxyl group and an isocyanate producing a carbamate, and c) reaction between an epoxide and an isocyanate producing an oxazolidone.

2.7 Concluding remarks

In conclusion, two separate approaches have been selected to investigate routes for the production of potentially useful automotive coatings. Self-healing technology offers the potential to heal any micro-scale damage on the surface of coatings; however, an appropriate selection of the healing mechanism is important. Microencapsulation is able to yield high levels of mechanical recovery but is unable to heal on more than one occasion. This, coupled with the increased likelihood of crack formation at pre-healed sites, prevents this technique from being suitable for the target application. Repeated healing, as is observed in both TRDA and with intermolecular forces, is the only way to significantly improve the lifetime of a coating. Despite the RT healing potential of intermolecular forces (e.g., hydrogen bonding), the current applications of this technology are mostly focused on elastomeric materials. Ideally, polymers currently used in similar applications must be functionalised to facilitate self-healing. This combines the recovery properties with those that made the polymers ideal for the application in the first instance. Current automotive polymers (including PMMA) can be readily functionalised with an MFC to enable TRDA reactions. The hypothesis is that this would allow the production of targeted polymers that display the required mechanical properties, whereby they have the ability to mend any damage that may occur during their lifetime. To realise such polymers, controlled polymerisation methods will be necessary to maintain consistency. RAFT and Cu(0)-mediated LRP have both been shown to be highly effective for polymerisation of MMA and in some cases for functionalised MMA monomers towards TRDA functionality.

Alternatively, using nacre-mimetic materials can improve the base mechanical properties of coatings and therefore increase resistance to small-scale damage. GO shows many useful properties for the production of nacre-mimetic materials, most notably, dispersibility in water and reactivity towards surface functionalisation. Direct functionalisation of GO towards use in nacre-mimetic structures is widely unreported, and hence the hypothesis is that functionalisation of GO with a hydrogen bonding isocyanate group will dramatically improve the mechanical properties of the film (coating). It is also believed that functionalisation of PVA with the same group will produce extremely strong interactions between the two components that should increase the mechanical properties of these structures. Finally, the literature on the use

of α-ZrP in nacre-mimetic films is extremely limited. As a result, there is significant potential for novel research and generating nacre-like films with interesting functionality. The use of suitable PEAs will allow high levels of exfoliation of the α-ZrP sheets but the hypothesis is that the PEA will also behave as the polymer component in the final structure, adding to the mechanical properties of the film.

2.8 References

1. A. Patnaik, A. Satapathy, N. Chand, N. M. Barkoula and S. Biswas, *Wear*, 2010, **268**, 249-263.

2. P. A. Sørensen, S. Kiil, K. Dam-Johansen and C. E. Weinell, *Journal of Coatings Technology and Research*, 2009, **6**, 135-176.

3. A. Walther, I. Bjurhager, J. M. Malho, J. Pere, J. Ruokolainen, L. A. Berglund and O. Ikkala, *Nano Letters*, 2010, **10**, 2742-2748.

4. X. F. Pan, H. L. Gao, Y. Lu, C. Y. Wu, Y. D. Wu, X. Y. Wang, Z. Q. Pan, L. Dong, Y. H. Song, H. P. Cong and S. H. Yu, *Nature Communications*, 2018, **9**, 2974-2982.

5. M. L. Mangoni, A. M. McDermott and M. Zasloff, *Experimental Dermatology*, 2016, **25**, 167-173.

6. S. R. White, N. R. Sottos, P. H. Geubelle, J. S. Moore, M. R. Kessler, S. R. Sriram, E. N. Brown and S. Viswanathan, *Nature*, 2001, **409**, 794-797.

7. S. H. Cho, H. M. Andersson, S. R. White, N. R. Sottos and P. V. Braun, *Advanced Materials*, 2006, **18**, 997-1000.

8. M. M. Caruso, B. J. Blaiszik, S. R. White, N. R. Sottos and J. S. Moore, *Advanced Functional Materials*, 2008, **18**, 1898-1904.

9. M. M. Caruso, D. A. Delafuente, V. Ho, N. R. Sottos, J. S. Moore and S. R. White, *Macromolecules*, 2007, **20**, 8830-8832.

10. S. Burattini, H. M. Colquhoun, J. D. Fox, D. Friedmann, B. W. Greenland, P. J. Harris, W. Hayes, M. E. Mackay and S. J. Rowan, *Chemical Communications*, 2009, **44**, 6717-6719.

11. C. Xu, L. Cao, X. Huang, Y. Chen, B. Lin and L. Fu, *ACS Applied Materials & Interfaces*, 2017, **9**, 29363-29373.

12. W. Wang, M. Chen, Y. Niu, Q. Tao, L. Bai, H. Chen and Z. Cheng, *RSC Advances*, 2017, **7**, 47316-47323.

13. S. Bode, R. K. Bose, S. Matthes, M. Ehrhardt, A. Seifert, F. H. Schacher, R. M. Paulus, S. Stumpf, B. Sandmann, J. Vitz, A. Winter, S. Hoeppener, S. J. Garcia, S. Spange, S. van der Zwaag, M. D. Hager and U. S. Schubert, *Polymer Chemistry*, 2013, **4**, 4966-4973.

14. C. Shao, H. Chang, M. Wang, F. Xu and J. Yang, *ACS Applied Materials & Interfaces*, 2017, **9**, 28305-28318.

15. P. Cordier, F. Tournilhac, C. Soulie-Ziakovic and L. Leibler, *Nature*, 2008, **451**, 977-980.

16. P. Baek, N. Aydemir, Y. An, E. W. C. Chan, A. Sokolova, A. Nelson, J. P. Mata, D. McGillivray, D. Barker and J. Travas-Sejdic, *Chemistry of Materials*, 2017, **29**, 8850-8858.

17. A. Feula, A. Pethybridge, I. Giannakopoulos, X. Tang, A. Chippindale, C. R. Siviour, C. P. Buckley, I. W. Hamley and W. Hayes, *Macromolecules*, 2015, **48**, 6132-6141.

18. J. Cao, X. Zhang, C. Lu, Y. Luo and X. Zhang, *Macromolecular Rapid Communications*, 2017, **38**, 1700406-1700412.

19. K. Zhu, Q. Song, H. Chen and P. Hu, *Journal of Applied Polymer Science*, 2018, **135**, 45929-45936.

20. Q. Rong, W. Lei, L. Chen, Y. Yin, J. Zhou and M. Liu, *Angewandte Chemie International Edition England*, 2017, **56**, 14159-14163.

21. J. Wang, F. Liu, F. Tao and Q. Pan, *ACS Applied Materials & Interfaces*, 2017, **9**, 27745-27753.

22. N. Samadi, M. Sabzi and M. Babaahmadi, *International Journal of Biological Macromolecules*, 2018, **107**, 2291-2297.

23. B. Zhu, N. Jasinski, A. Benitez, M. Noack, D. Park, A. S. Goldmann, C. Barner-Kowollik and A. Walther, *Angewandte Chemie International Edition England*, 2015, **54**, 8653-8657.

24. X. Chen, M. A. Dam, K. Ono, A. Mal, H. Shen, S. Nutt, K. Sheran and F. Wudl, *Science*, 2002, **295**, 1698-1702.

25. C. Cai, Y. Zhang, X. Zou, R. Zhang, X. Wang, Q. Wu and P. Sun, *RSC Advances*, 2017, **7**, 46336-46343.

26. A. Gandini, A. J. D. Silvestre and D. Coelho, *Journal of Polymer Science Part A: Polymer Chemistry*, 2010, **48**, 2053-2056.

27.   A. M. Peterson, R. E. Jensen and G. R. Palmese, *ACS Applied Materials & Interfaces*, 2010, **2**, 1141-1149.

28.   Y. Heo and H. A. Sodano, *Composites Science and Technology*, 2015, **118**, 244-250.

29.   J. A. Syrett, G. Mantovani, W. R. S. Barton, D. Price and D. M. Haddleton, *Polymer Chemistry*, 2010, **1**, 102-106.

30.   Y. Heo, M. H. Malakooti and H. A. Sodano, *Journal of Materials Chemistry A*, 2016, **4**, 17403-17411.

31.   E. B. Murphy, E. Bolanos, C. Schaffner-Hamann, F. Wudl, S. Nutt and M. L. Auad, *Macromolecules*, 2008, **41**, 5203-5209.

32.   J. Kötteritzsch, S. Stumpf, S. Hoeppener, J. Vitz, M. D. Hager and U. S. Schubert, *Macromolecular Chemistry and Physics*, 2013, **214**, 1636-1649.

33.   G. Scott, in *Degradable Polymers*, ed. G. Scott, Kluwer Academic Publishers, Dordrecht, 2002, vol. 2, ch. 1, pp. 1-15.

34.   C. Boyer, J. Liu, V. Bulmus and T. P. Davis, *Australian Journal of Chemistry*, 2009, **62**, 830-847.

35.   Y. N. Zhou, Q. Zhang and Z. H. Luo, *Langmuir*, 2014, **30**, 1489-1499.

36.   G. G. Odian, *Principles of Polymerisation*, Wiley, New York, 3rd edn., 1991.

37.   G. Moad, E. Rizzardo and S. H. Thang, *Polymer*, 2008, **49**, 1079-1131.

38.   G. Moad, E. Rizzardo and S. H. Thang, *Australian Journal of Chemistry*, 2009, **62**, 1402-1472.

39.   D. J. Keddie, G. Moad, E. Rizzardo and S. H. Thang, *Macromolecules*, 2012, **45**, 5321-5342.

40.   Q. Zhang, P. Wilson, Z. Li, R. McHale, J. Godfrey, A. Anastasaki, C. Waldron and D. M. Haddleton, *Journal of the American Chemical Society*, 2013, **135**, 7355-7363.

41.   A. Anastasaki, V. Nikolaou and D. M. Haddleton, *Polymer Chemistry*, 2016, **7**, 1002-1026.

42.   G. R. Jones, R. Whitfield, A. Anastasaki, N. Risangud, A. Simula, D. J. Keddie and D. M. Haddleton, *Polymer Chemistry*, 2018, **9**, 2382-2388.

43.   K. Matyjaszewski, *Macromolecules*, 2012, **45**, 4015-4039.

44.   K. Matyjaszewski and J. Xia, *Chemical Reviews*, 2001, **101**, 2921-2990.

45.   S. Fleischmann and V. Percec, *Journal of Polymer Science Part A: Polymer Chemistry*, 2010, **48**, 2236-2242.

46. S. Fleischmann and V. Percec, *Journal of Polymer Science Part A: Polymer Chemistry*, 2010, **48**, 4884-4888.

47. L. Li and C. Ortiz, *Nature Materials*, 2014, **13**, 501-507.

48. B. L. Smith, T. E. Schaffer, M. Viani, J. B. Thompson, N. A. Frederick, J. Kindt, A. Belcher, G. D. Stucky, D. E. Morse and P. K. Hansma, *Nature*, 1999, **399**, 761-763.

49. A. P. Jackson, J. F. Vincent and R. M. Turner, *Proceedings of the Royal Society of London B*, 1988, **234**, 415-440.

50. M. F. Ashby, L. J. Gibson, U. Wegst and R. Olive, *Proceedings of the Royal Society of London A*, 1995, **450**, 123-140.

51. J. Brandrup, E. H. Immergut and E. A. Grulke, *Polymer Handbook*, Wiley, New York, 4th edn., 1999.

52. S. Lee, E. E. Novitskaya, B. Reynante, J. Vasquez, R. Urbaniak, T. Takahashi, E. Woolley, L. Tombolato, P.-Y. Chen and J. McKittrick, *Materials Science and Engineering: C*, 2011, **31**, 730-739.

53. J. D. Currey, in *The Mechanical Properties of Biological Materials*, eds. J. D. Currey and J. F. V. Vincent, Cambridge University Press, Symposia of the Society for Experimental Biology, 1980, vol. 34, pp. 75-97.

54. R. Xiong, K. Hu, A. M. Grant, R. Ma, W. Xu, C. Lu, X. Zhang and V. V. Tsukruk, *Advanced Materials*, 2016, **28**, 1501-1509.

55. S. Weiner and L. Hood, *Science*, 1975, **190**, 987-989.

56. P. Podsiadlo, A. K. Kaushik, B. S. Shim, A. Agarwal, Z. Tang, A. M. Waas, E. M. Arruda and N. A. Kotov, *Journal of Physical Chemistry B*, 2008, **112**, 14359-14363.

57. Y. Shu, P. Yin, B. Liang, H. Wang and L. Guo, *Industrial & Engineering Chemistry Research*, 2015, **54**, 8940-8946.

58. M. Farhadi-Khouzani, C. Schütz, G. M. Durak, J. Fornell, J. Sort, G. Salazar-Alvarez, L. Bergström and D. Gebauer, *Journal of Materials Chemistry A*, 2017, **5**, 16128-16133.

59. Y. X. Yan, H. B. Yao, L. B. Mao, A. M. Asiri, K. A. Alamry, H. M. Marwani and S. H. Yu, *Small*, 2016, **12**, 745-755.

60. H. B. Yao, Z. H. Tan, H. Y. Fang and S. H. Yu, *Angewandte Chemie International Edition England*, 2010, **49**, 10127-10131.

61. S. Wan, J. Peng, Y. Li, H. Hu, L. Jiang and Q. Cheng, *ACS Nano*, 2015, **9**, 9830-9836.

62. X. Zeng, L. Ye, S. Yu, H. Li, R. Sun, J. Xu and C. P. Wong, *Nanoscale*, 2015, **7**, 6774-6781.

63. S. Wan, H. Hu, J. Peng, Y. Li, Y. Fan, L. Jiang and Q. Cheng, *Nanoscale*, 2016, **8**, 5649-5656.

64. Y. Wang, T. Li, P. Ma, S. Zhang, H. Zhang, M. Du, Y. Xie, M. Chen, W. Dong and W. Ming, *ACS Nano*, 2018, **12**, 6228-6235.

65. J. Peng, Y. Cheng, A. P. Tomsia, L. Jiang and Q. Cheng, *ACS Applied Material Interfaces*, 2017, **9**, 24993-24998.

66. Y. Yao, X. Zeng, F. Wang, R. Sun, J.-b. Xu and C.-P. Wong, *Chemistry of Materials*, 2016, **28**, 1049-1057.

67. Y. Gao, L.-Q. Liu, S.-Z. Zu, K. Peng, D. Zhou, B.-H. Han and Z. Zhang, *ACS Nano*, 2011, **5**, 2134-2141.

68. Y. Q. Li, T. Yu, T. Y. Yang, L. X. Zheng and K. Liao, *Advanced Materials*, 2012, **24**, 3426-3431.

69. W. Cui, M. Li, J. Liu, B. Wang, C. Zhang, L. Jiang and Q. Cheng, *ACS Nano*, 2014, **8**, 9511-9517.

70. M. Zhang, L. Huang, J. Chen, C. Li and G. Shi, *Advanced Materials*, 2014, **26**, 7588-7592.

71. S. Ming, G. Chen, J. He, Y. Kuang, Y. Liu, R. Tao, H. Ning, P. Zhu, Y. Liu and Z. Fang, *Langmuir*, 2017, **33**, 8455-8462.

72. K. Shahzadi, I. Mohsin, L. Wu, X. Ge, Y. Jiang, H. Li and X. Mu, *ACS Nano*, 2017, **11**, 325-334.

73. Z. Shen and J. Feng, *ACS Applied Nano Materials*, 2018, **1**, 94-100.

74. S. Sarin, S. Kolesnikova, I. Postnova, C.-S. Ha and Y. Shchipunov, *RSC Advances*, 2016, **6**, 33501-33509.

75. G. Dwivedi, K. Flynn, M. Resnick, S. Sampath and A. Gouldstone, *Advanced Materials*, 2015, **27**, 3073-3078.

76. X. Yan, F. Li, K. D. Hu, J. Xue, X. F. Pan, T. He, L. Dong, X. Y. Wang, Y. D. Wu, Y. H. Song, W. P. Xu and Y. Lu, *Scientific Reports*, 2017, **7**, 13851-13861.

77. H. Bai, F. Walsh, B. Gludovatz, B. Delattre, C. Huang, Y. Chen, A. P. Tomsia and R. O. Ritchie, *Advanced Materials*, 2016, **28**, 50-56.

78. M. Mirkhalaf and F. Barthelat, *Journal of the Mechanical Behaviour of Biomedical Materials*, 2016, **56**, 23-33.

79. H. Bai, Y. Chen, B. Delattre, A. P. Tomsia and O. R. Ritchie, *Science Advances*, 2015, **1**, e1500849.

80. N. Zhao, M. Yang, Q. Zhao, W. Gao, T. Xie and H. Bai, *ACS Nano*, 2017, **11**, 4777-4784.

81. G. Du, A. Mao, J. Yu, J. Hou, N. Zhao, J. Han, Q. Zhao, W. Gao, T. Xie and H. Bai, *Nature Communications*, 2019, **10**, 800-808.

82. I. Corni, T. J. Harvey, J. A. Wharton, K. R. Stokes, F. C. Walsh and R. J. Wood, *Bioinspiration and Biomimetics*, 2012, **7**, 031001.

83. S. Wan, F. Xu, L. Jiang and Q. Cheng, *Advanced Functional Materials*, 2017, **27**, 1605636-1605643.

84. C. Lee, X. Wei, J. W. Kysar and J. Hone, *Science*, 2008, **321**, 385-388.

85. J. Ling, M. Z. Rong and M. Q. Zhang, *Polymer*, 2012, **53**, 2691-2698.

86. C. Huang, J. Peng, Y. Cheng, Q. Zhao, Y. Du, S. Dou, A. P. Tomsia, H. D. Wagner, L. Jiang and Q. Cheng, *Journal of Materials Chemistry A*, 2019, **7**, 2787-2794.

87. Q. Cheng, M. Wu, M. Li, L. Jiang and Z. Tang, *Angewandte Chemie International Edition England*, 2013, **52**, 3750-3755.

88. X. Qi, D. Zhang, Z. Ma, W. Cao, Y. Hou, J. Zhu, Y. Gan and M. Yang, *ACS Nano*, 2018, **12**, 1062-1073.

89. K. W. Putz, O. C. Compton, M. J. Palmeri, S. T. Nguyen and L. C. Brinson, *Advanced Functional Materials*, 2010, **20**, 3322-3329.

90. B. Liang, Y. Shu, P. Wan, H. Zhao, S. Dong, W. Hao and P. Yin, *Composites Science and Technology*, 2019, **182**, 107747-107756.

91. H. Xie, X. Lai, Y. Wang, H. Li and X. Zeng, *Journal of Hazardous Materials*, 2019, **365**, 125-136.

92. J. Han, G. Du, W. Gao and H. Bai, *Advanced Functional Materials*, 2019, **29**, 1900412-1900421.

93. K. Evers, H. Porwal, R. I. Todd and N. Grobert, *Carbon*, 2019, **145**, 586-595.

94. X. Wang and P. Wu, *ACS Applied Materials and Interfaces*, 2019, **11**, 28943-28952.

95. Y. Song, J. Gerringer, S. Qin and J. C. Grunlan, *Industrial & Engineering Chemistry Research*, 2018, **57**, 6904-6909.

96. W. T. Cao, F. F. Chen, Y. J. Zhu, Y. G. Zhang, Y. Y. Jiang, M. G. Ma and F. Chen, *ACS Nano*, 2018, **12**, 4583-4593.

97. L. J. Bonderer, A. R. Studart and L. J. Gauckler, *Science*, 2008, **319**, 1069-1073.

98. G. Alberti, M. Casciola and U. Constantino, *Journal of Colloid and Interface Science*, 1985, **107**, 256-263.

99. D. M. Kaschak, S. A. Johnson, D. E. Hooks, H.-N. Kim, M. D. Ward and T. E. Mallouk, *Journal of the American Chemical Society*, 1998, **120**, 10887-10894.

100. W. Boo, L. Sun, J. Liu, A. Clearfield, H. Sue, M. Mullins and H. Pham, *Composites Science and Technology*, 2007, **67**, 262-269.

101. L. Sun, W. J. Boo, H.-J. Sue and A. Clearfield, *New Journal of Chemistry*, 2007, **31**, 39-43.

102. J. E. Readman, A. Lennie, J. A. Hriljac, *Acta Crystallographica Section B*, 2014, **70**, 510-516.

103. J. M. Troup and A. Clearfield, *Inorganic Chemistry*, 1977, **16**, 3311-3314.

104. B. Ha, K. Char and H. S. Jeon, *Journal of Physical Chemistry B*, 2005, **109**, 24434-24440.

105. T. Takei, Y. Kobayashi, H. Hata, Y. Yonesaki, N. Kumada, N. Kinomura and T. E. Mallouk, *Journal of the American Chemical Society*, 2006, **128**, 16634-16640.

106. T. Takei, Q. Dong, Y. Yonesaki, N. Kumada and N. Kinomura, *Langmuir*, 2011, **27**, 126-131.

107. H. Huang, M. Li, Y. Tian, Y. Xie, X. Sheng, X. Jiang and X. Zhang, *Progress in Organic Coatings*, 2020, **138**, 105390-105400.

108. J. Kerimo, D. M. Adams, P. F. Barbara, D. M. Kaschak and T. E. Mallouk, *Journal of Physical Chemistry B*, 1998, **102**, 9451-9460.

109. L. M. Tender, R. L. Worley, H. Fan and G. P. Lopez, *Langmuir*, 1996, **12**, 5515-5518.

110. Z. Peng, J. Tang, X. Han, E. Wang and S. Dong, *Langmuir*, 2002, **18**, 4834-4839.

111. A. Glidle, T. Yasukawa, C. S. Hadyoon, N. Anicet, T. Matsue, M. Nomura and J. M. Cooper, *Analytical Chemistry*, 2003, **75**, 2559-2570.

112. A. Swami, A. Kumar and M. Sastry, *Langmuir*, 2003, **19**, 1168-1172.

113. H. Fan, K. Yang, D. M. Boye, T. Sigmon, K. J. Malloy, H. Xu, G. P. Lopez and C. J. Brinker, *Science*, 2004, **304**, 567-571.

114. Z. L. Wang, S. A. Harfenist, R. L. Whetten, J. Bentley and N. D. Evans, *Journal of Physical Chemistry B*, 1998, **102**, 3068-3072.

115. E. T. Kisak, B. Coldren and J. A. Zasadzinski, *Langmuir*, 2002, **18**, 284-288.

116. W. Bu, H. Li, W. Li, L. Wu, C. Zhai and Y. Wu, *Journal of Physical Chemistry B*, 2004, **108**, 12776-12782.

117. C. V. Kumar and G. L. McLendon, *Chemistry of Materials*, 1997, **9**, 863-870.

118. C. V. Kumar and A. Chaudhari, *Journal of the American Chemical Society*, 2000, **122**, 830-837.

119. A. Chaudhari, J. Thota and C. V. Kumar, *Microporous and Mesoporous Materials*, 2004, **75**, 281-291.

120. H.-J. Sue, K. T. Gam, N. Bestaoui, N. Spurr and A. Clearfield, *Chemistry of Materials*, 2004, **16**, 242-249.

121. M. Wong, R. Ishige, K. L. White, P. Li, D. Kim, R. Krishnamoorti, R. Gunther, T. Higuchi, H. Jinnai, A. Takahara, R. Nishimura and H. J. Sue, *Nature Communications*, 2014, **5**, 3589-3601.

122. X. Lin, D. Schmelter, S. Imanian and H. Hintze-Bruening, *Scientific Reports*, 2019, **9**, 16389-16404.

123. F. Carosio, J. Alongi and G. Malucelli, *Journal of Materials Chemistry*, 2011, **21**, 10370-10376.

124. S. M. Waraich, B. Hering, Z. Burghard, J. Bill, P. Behrens and H. Menzel, *Journal of Colloid and Interface Science*, 2012, **367**, 74-82.

125. D. Han, Y. Luo, Q. Ju, X. Xiao, M. Xiao, N. Xiao, S. Chen, X. Peng, S. Wang and Y. Meng, *Polymers (Basel)*, 2018, **10**, 1082-1097.

126. F. Kim, L. J. Cote and J. Huang, *Advanced Materials*, 2010, **22**, 1954-1958.

127. L. Liu, J. Zhang, J. Zhao, F. Liu, *Nanoscale*, 2012, **4**, 5910-5917.

128. S. S. Abbas, G. J. Rees, N. L. Kelly, C. E. J. Dancer, J. V. Hanna and T. McNally, *Nanoscale*, 2018, **10**, 16231-16242.

129. Y. Song, Y. Gao, H. Rong, H. Wen, Y. Sha, H. Zhang, H.-J. Liu and Q. Liu, *Sustainable Energy & Fuels*, 2018, **2**, 803-810.

130. J. Wu, G. Huang, H. Li, S. Wu, Y. Liu and J. Zheng, *Polymer*, 2013, **54**, 1930-1937.

131. V. Georgakilas, J. N. Tiwari, K. C. Kemp, J. A. Perman, A. B. Bourlinos, K. S. Kim and R. Zboril, *Chemical Reviews*, 2016, **116**, 5464-5519.

132. Y. Liu, F. Luo, S. Liu, S. Liu, X. Lai, X. Li, Y. Lu, Y. Li, C. Hu, Z. Shi and Z. Zheng, *Small*, 2017, **13**, 1603174-1603181.

133. Y. Zhao, H. Ding and Q. Zhong, *Applied Surface Science*, 2012, **258**, 4301-4307.

134. C.-M. Chen, Q. Zhang, X.-C. Zhao, B. Zhang, Q.-Q. Kong, M.-G. Yang, Q.-H. Yang, M.-Z. Wang, Y.-G. Yang, R. Schlögl and D. S. Su, *Journal of Materials Chemistry*, 2012, **22**, 14076-14084.

135. M. A. Ali, K. Kamil Reza, S. Srivastava, V. V. Agrawal, R. John and B. D. Malhotra, *Langmuir*, 2014, **30**, 4192-4201.

136. H. Chen and K. C. Carroll, *Environmental Pollution*, 2016, **215**, 96-102.

137. C. E. Hoyle and C. N. Bowman, *Angewandte Chemie International Edition England*, 2010, **49**, 1540-1573.

138. P. L. Yap, S. Kabiri, Y. L. Auyoong, D. N. H. Tran and D. Losic, *ACS Omega*, 2019, **4**, 19787-19798.

139. P. L. Yap, S. Kabiri, D. N. H. Tran and D. Losic, *ACS Applied Materials & Interfaces*, 2018, **11**, 6350-6362.

140. N. D. Luong, H. Sinh le, L. S. Johansson, J. Campell and J. Seppala, *Chemistry*, 2015, **21**, 3183-3186.

141. B. Yu, Y. Shi, B. Yuan, L. Liu, H. Yang, Q. Tai, S. Lo, L. Song and Y. Hu, *RSC Advances*, 2015, **5**, 13502-13506.

142. M. Castelaín, G. Martínez, C. Marco, G. Ellis and H. J. Salavagione, *Macromolecules*, 2013, **46**, 8980-8987.

143. Z. Peng, H. Li, Q. Li and Y. Hu, *Colloids and Surfaces A: Physicochemical and Engineering Aspects*, 2017, **533**, 48-54.

144. M. Wang, L. Ma, L. Shi, P. Feng, X. Wang, Y. Zhu, G. Wu and G. Song, *Composites Science and Technology*, 2019, **182**, 107751-107760.

145. K. Zhao, Y. Wang, W. Wang and D. Yu, *Journal of Materials Science*, 2018, **53**, 14262-14273.

146. Y. Oz, A. Barras, R. Sanyal, R. Boukherroub, S. Szunerits and A. Sanyal, *ACS Applied Materials & Interfaces*, 2017, **9**, 34194-34203.

147. J. Yang, X. He, L. Chen and Y. Zhang, *Journal of Chromatography A*, 2017, **1513**, 118-125.

148. C. Y. Lee, Q. V. Le, C. Kim and S. Y. Kim, *Physical Chemistry Chemical Physics*, 2015, **17**, 9369-9374.

149. C. Y. Lee, J.-H. Bae, T.-Y. Kim, S.-H. Chang and S. Y. Kim, *Composites Part A: Applied Science and Manufacturing*, 2015, **75**, 11-17.

150. Y.-J. Wan, L.-X. Gong, L.-C. Tang, L.-B. Wu and J.-X. Jiang, *Composites Part A: Applied Science and Manufacturing*, 2014, **64**, 79-89.

151. S. Pourhashem, A. Rashidi, M. R. Vaezi and M. R. Bagherzadeh, *Surface and Coatings Technology*, 2017, **317**, 1-9.

152. I. S. Blagbrough, N. E. MacKenzie, C. Ortiz and A. I. Scott, *Tetrahedron Letters*, 1986, **27**, 1251-1254.

153. C. Gürtler and K. Danielmeier, *Tetrahedron Letters*, 2004, **45**, 2515-2521.

154. M. T. DeMeuse, J. K. Gillham and F. Parodi, *Journal of Applied Polymer Science*, 1996, **64**, 15-25.

155. S. Stankovich, R. D. Piner, S. T. Nguyen and R. S. Ruoff, *Carbon*, 2006, **44**, 3342-3347.

3. Experimental Details

3.1 Materials

3.1.1 General reagents and solvents

exo-7-Oxabicyclo[2.2.1]hept-5-ene-2,3-dicarboxylic anhydride, ethanolamine, methanol, triethylamine (Et_3N), toluene, anhydrous dichloromethane (DCM), methacryloyl chloride, ammonium chloride (NH_4Cl), sodium chloride, 2,2'-azobisisobutyronitrile (AIBN), DCM, 1-dodecanethiol, carbon disulfide, diethylether, *tert*-butoxide, iodine, sodium sulfate, ethylacetate, hexane, 1-ethylpiperidine hypophosphite (EPHP), basic alumina, sodium hydrogen carbonate, 1,1'-azobis(cyclohexanecarbonitrile) (ACHN), Cu(II) bromide, dimethylsulfoxide (DMSO), hydrochloric acid, chloroform, hexamethylene diisocyanate (HDI), 2-amino-4-hydroxy-6-methylpyrimidine, *n*-pentane, dimethylformamide (DMF), dibutylamine (DBA), bromophenol blue, sodium hydroxide and isopropylalcohol (IPA) were all purchased from Sigma-Aldrich or Fischer Scientific and used as received.

3.1.2 Methyl methacrylate (MMA)

Methyl methacrylate (MMA), density of 0.94 g/cm^3, was purchased from Sigma-Aldrich and passed through an alumina column immediately prior to use to remove any radical inhibitors.

3.1.3 Furfuryl methacrylate (FMA)

Furfuryl methacrylate (FMA), density of 1.078 g/cm^3, was purchased from Sigma-Aldrich and passed through an alumina column immediately prior to use to remove any radical inhibitors.

3.1.4 *Tris*-[2-(dimethylamino)ethyl]amine (Me₆TREN)

Tris-[2-(dimethylamino)ethyl]amine (Me₆TREN) was kindly donated by Dr Paul Wilson (University of Warwick) and used without further purification. The Me₆TREN had been synthesised using a previously reported procedure.[1]

3.1.5 Copper (0) wire

Copper (0) wire was kindly donated by Dr Paul Wilson (University of Warwick) and activated by immersion in conc. HCl immediately prior to use.

3.1.6 Methyl α-bromophenylacetate (MBPA)

The methyl α-bromophenylacetate (MBPA) initiator was kindly donated by Dr Paul Wilson (University of Warwick) and used as received.

3.1.7 Graphene oxide (GO)

Graphene oxide (GO) paste was purchased from Abalonyx, Norway (product no. 1.1). The GO was synthesised using a modified Hummer's method and supplied directly as a paste without further treatment. The paste is reported to consist of 25 – 26 % GO, 73 – 74 % water and 1 – 1.5 % HCl with a bulk density of 1.2 g/cm^3.

GO powder was purchased from Abalonyx, Norway (product no. 1.8). The GO powder is produced using a similar method as the paste (see above) and is freeze-dried prior to delivery. The powder is reported to consist of 97 – 98 % GO, 2 – 3 % water (from ambient moisture) and < 1% HCl and has a bulk density of 1.2 g/cm^3.

Both GO products are chemically similar. The reported (Abalonyx) sheet thickness = 1 nm with lateral dimensions of 2 – 20 µm. The GO flakes are composed 64 – 65 % carbon, 33 – 34 % oxygen and 1 – 2 % sulphur with residual nitrogen and chloride. The ratio of the D and G bands (Raman spectroscopy) is reported to be 1.09 showing a large variance from the values determined in this work.

3.1.8 Water-soluble polyurethane (wsPU)

Water-soluble polyurethane (wsPU) was supplied by Covestro (product code Bayhydrol® UV 2282). The latex dispersion is reported to contain 39% by weight polyurethane and a density of 1.06 g/cm^3. UV2282 is unstable in acidic conditions.

3.1.9 Irgacure 500 (I500)

Irgacure 500 (I500) is a tradename for a 50:50 mix of benzophenone and 1-hydroxycyclohexylphenylketone (1HCPK). Benzophenone was purchased from VWR International and 1HCPK was purchased from Sigma-Aldrich. Equal mass of both

compounds were weighed into a volumetric flask and dissolved into DI water at a known concentration before use in sample preparation.

3.1.10 Poly(vinyl alcohol) (PVA)

Poly(vinyl alcohol) (PVA) with a molecular weight of 89 – 98 k and hydrolysed content of >99% was purchased from Sigma-Aldrich and used as received.

3.1.11 α-Zirconium phosphate (α-ZrP)

Two grades of α-Zirconium phosphate (α-ZrP) were kindly supplied by Sunshine Factory Company Ltd., China and used as received. The reported lateral dimensions of the nanosheets were 1.61 and 1.65 µm. The 1.61 µm sample had a specific surface area of 2.79 m^2/g.

3.1.12 Jeffamine M600 (PEA)

Jeffamine M600 (PEA) was purchased from Sigma-Aldrich, licenced by Huntsman International LLC. The PEA has a molecular weight of 600 Da with a propylene oxide:ethylene oxide molar ratio of 9:1, a pH of 12 and density of 0.979 g/cm^3.

3.1.13 Ancillaries

The poly(tetrafluoroethylene) (PTFE) filter membranes were purchased from Sigma-Aldrich on behalf of Omnipore. The PTFE membranes are hydrophilic and have a pore size of 0.2 µm. Molecular sieves (3 Å) were purchased from Fischer and activated by heating at 350 °C for at least 4 hours prior to use.

3.2 Characterisation methods

3.2.1 Fourier-transform infrared spectroscopy (FTIR)

Fourier-transform infrared spectroscopy (FTIR) measurements were made using a Bruker Tensor 27 spectrometer equipped with an attenuated total reflectance (ATR) crystal. Spectra were processed using OPUS analysis software between 500 and 4000 cm^{-1}. A resolution of 2 cm^{-1} was used with an average of 12 scans used to acquire each spectrum.

3.2.2 Solution-state nuclear magnetic resonance spectroscopy (NMR)

^{1}H and ^{13}C nuclear magnetic resonance (NMR) spectra were recorded on a Bruker DPX-400 spectrometer using a CDCl$_3$ solvent. Chemical shifts are reported in ppm (δ) relative to a tetramethylsilane (Me$_4$Si) zero standard and referenced to the chemical shift of the deuterated solvent. Monomer conversion was determined via comparison of the integral values of monomeric and polymeric signals and are discussed in greater detail in the relevant 'Results and Discussion' chapters.

3.2.3 Solid-state NMR (SSNMR)

All solid-state NMR (SSNMR) measurements were performed at 9.4 T using a Bruker Avance-400 spectrometer operating at ^{1}H and ^{13}C Larmor frequencies (v_o) of 400.13 and 100.59 MHz, respectively. Single pulse ^{13}C (direct detection) experiments facilitating a quantitative analysis of the carbon speciation were performed using a Bruker 4 mm HX probe which enabled a magic-angle-spinning (MAS) frequency of 12 KHz to be implemented. Pulse length calibration was performed using solid alanine from which a $\pi/2$ pulse time of 3 μs was measured. All ^{13}C MAS NMR experiments were implemented using a $\pi/2$ nutation angle and a relaxation delay of 60 s between excitation pulses. For all experiments, 100 kHz of ^{1}H decoupling was applied during the acquisition of all FIDs. All ^{13}C chemical shifts were externally referenced against the IUPAC recommended primary reference of Me$_4$Si (1 % in CDCl$_3$, $\delta = 0.0$ ppm), via the secondary solid alanine reference ($\delta = 20.5$ ppm).[2]

3.2.4 Differential scanning calorimetry (DSC)

Differential scanning calorimetry (DSC) measurements were performed on a Mettler Toledo (DSC1, model 700, 400W) equipped with a FRS5 thermocouple sensor, robotic sample changer and were evaluated using STARe Version 15.01 software. The instrument was calibrated using Indium and Zinc as standards. Scans were performed under a flow of N$_2$ gas. Typically, 6-12 mg of sample were inserted in the instrument in an aluminium pan with a pierced lid. The sample was heated to between 25 °C and 270 °C at 10 K/min to eliminate any thermal history. The sample would then be cool from 270 °C to -40 °C at 10 K/min, held for 5 minutes, heated again to 270 °C at 10 K/min, held for 5 minutes before cooling rapidly to RT. The

thermograms were used to determine the T_g of the samples with onset, mid-point and end point calculated by the software.

3.2.5 Thermo-gravimetric analysis (TGA)

Thermo-gravimetric analysis (TGA) measurements were completed using a Mettler Toledo TGA1-STARe system using a gentle flow of air (40-60 cm^3/min). Samples of 6-10 mg were loaded into 70 µL alumina pans and heated from RT to 800 °C at a constant rate of 10 K/min. Decomposition temperatures were calculated from the onset of weight loss in both the weight loss and derivative curves.

3.2.6 Size-exclusion gel-permeation chromatography (GPC)

Size-exclusion gel-permeation chromatography (GPC) was completed using an Agilent Infinity II MDS instrument equipped with differential refractive index (DRI), viscometry (VS) and dual angle light scattering (LS) detectors. The system was equipped with 2 x PLgel Mixed C columns (300 x 7.5 mm) and a PLgel 5 µm guard column. The eluent was $CHCl_3$ with 2 % Et_3N (triethylamine) additive. Samples were eluted at 1 ml/min at 30 °C. Poly(methyl methacrylate), and polystyrene standards (Agilent EasyVials) were used for calibration. Ethanol was added as a flow rate marker. Analyte samples were filtered through a GVHP membrane with 0.22 μm pore size before injection. Respectively, experimental molar mass ($M_{n,SEC}$) and dispersity values of all synthesized polymers were determined by conventional calibration using Agilent GPC/SEC software.

3.2.7 Raman spectroscopy

Raman spectra were collected on a Renishaw inVia Raman microscope instrument, using a 532 nm laser in the wavenumber range 100 cm^{-1} and 3200 cm^{-1} with a 10-second exposure time. 15 accumulations were collected with the laser power set at 10%. Samples were normally measured in powder or film form however, neat α-ZrP was first compressed to a pellet before analysis.

3.2.8 X-ray photoelectron spectroscopy (XPS)

X-ray photoelectron spectroscopy (XPS) was carried out using a Kratos Axis Ultra DLD Spectrometer at RT and with a base pressure of 2 x 10^{-10} mbar, using a monochromated Al k_α X-ray source. In order to prevent surface charging the data was

collected while the sample was exposed to a flux of low energy electrons from the charge neutralizer built in to the hemispherical analyser entrance, with the binding energy scale retrospectively calibrated to the sp^3 C-C peak at 284.6 eV. The data was analysed with CasaXPS software, using Shirley backgrounds and mixed Gaussian-Lorentzian (Voigt) line shapes and asymmetry parameters where appropriate. For compositional analysis, the analyser transmission function was determined using clean metallic foils to determine the detection efficiency across the full binding energy range.

3.2.9 X-ray diffraction (XRD)

X-ray diffraction (XRD) measurements were performed on a 3rd generation Malvern Panalytical Empyrean instrument equipped with multicore (iCore/dCore) optics and a Pixcel3D detector operating in 1D scanning mode. A Cu tube was utilised giving Cu K$_{\alpha1/2}$ radiation (1.5419 Å) and a beam knife to reduce air scatter at the low angles. Scans were recorded in the range 4° to 30° 2θ with a step size of 0.0263° and a counting time of ~ 130 s/step. Using the measured diffraction angle, 2θ, the interlayer spacing (d) was calculated using Bragg's Law, $n\lambda = 2d\sin\theta$ (where λ = 1.541 Å).

3.2.10 Droplet shape analysis (Contact angle)

Contact angle measurements were performed using a Krüss Droplet Shape Analyser 100. The sessile drop mode was used where a small microlitre droplet (≈10 µL) of DI water was applied to the surface of the material. The contact angle is then determined using a high precision camera and the DSA100 analysis software. A repeat experiment using diiodomethane (CH_2I_2) was used to calculate surface free energy and polar/dispersive component values using the Fowkes model where the dispersive component is calculated using equation (1) and the polar component is calculated using equation (2).[3] Interfacial tension between two phases was calculated using equations outlined by Cao *et al.*[4]

$$\gamma_s^d = \frac{\gamma_l(1 + cos\theta)^2}{4} \tag{1}$$

Equation 3.1 – Calculation of the dispersive component of a measured surface (γ_s^d) where γ_l = surface tension of known liquid (in this case diiodomethane) and θ = measured contact angle.

$$\sqrt{\gamma_l^d \gamma_s^d} + \sqrt{\gamma_l^p \gamma_s^p} = \frac{\gamma_l(1 + cos\theta)}{2} \tag{2}$$

Equation 3.2 – Calculation of the polar component of a measured surface (γ_s^p) where γ_l = surface tension of known liquid (in this case water) and θ = measured contact angle, γ_s^d= the dispersive component of the measured surface (from equation 1), γ_l^d = dispersive component of known liquid and γ_l^p = the polar component of known liquid.

3.2.11 UV-Vis spectroscopy

UV-Vis spectra were recorded using an Agilent Cary 60 UV-Vis spectrometer between wavelengths of 200 – 1000 nm. Samples were dissolved into DI water and measured using a 10 mm x 10 mm Quartz 6030 UV cuvette.

3.2.12 Scanning-electron microscopy (SEM)

Scanning-electron microscopy (SEM) micrographs were obtained using a Zeiss Sigma instrument using an InLens detector at 10kV. Powdered samples were prepared by dispersion in water at low concentration ($\approx$0.01 wt%) before applying a single droplet to carbon adhesive tape on an aluminium SEM stub. Images were collected following drying of the droplet. Cross-sectional images were achieved by cutting film samples that were fractured via tensile testing. The fracture surface was mounted perpendicular to the SEM stub using carbon adhesive tape. All samples were sputter coated using an Au/Pd target before imaging.

3.2.13 Gaseous barrier permeation

The gas (oxygen and carbon dioxide) and water vapour barrier properties of the GOx films and the water vapour barrier properties of the α-ZrP films were assessed using a Totalperm permeability analyzer (Extrasolution Srl, Pieve Fosciana, Italy)

equipped with both an electrochemical sensor (for oxygen) and an infrared sensor (for carbon dioxide and water vapour). Specimens of approximately 2 cm x 2 cm were sandwiched between two aluminium-tape masks, exposing a surface of 2.01 cm² for the permeation of the gas/vapour molecules. The oxygen and carbon dioxide transmission rate ((O$_2$TR and CO$_2$TR) in cm³ m^{-2} 24h^{-1}) were determined according to ASTM FD3985 and ASTM F2476, at 23° C and 0% relative humidity (RH). Water vapour transmission rate (WVTR, expressed in g m^{-2} 24h^{-1}) was determined according to ASTM F1249 at 38° C and 90% RH. All the tests were carried out with a carrier flow (N$_2$) of 10 mL min^{-1} and at 1 atm partial pressure difference (for O$_2$ and CO$_2$) and, 59.04 mbar vapour partial pressure difference (for WVTR) on the two sides of the specimen. To reset any difference in the transmission rate (TR) values possibly arising from different thicknesses, TR values were used to determine a permeability coefficient (*P'O$_2$, P'CO$_2$* and *P'WV*) using the following equation:

$$P'G = PG \times t = \frac{GTR}{\Delta p} \times t \qquad (3)$$

where, *P'G* is the gas (or vapour) permeability coefficient (cm³ mm m^{-2} 24h^{-1} atm^{-1}), *PG*, is the permeance (defined as the ratio of the *GTR* to the difference between the partial pressure of the gas on the two sides of the film, D*p*), and *t* is the total thickness of the material.

3.2.14 Dynamic light scattering (DLS)

Dynamic light scattering (DLS) measurements were performed on a Malvern instrument Zetasizer Nano Series instrument with a detection angle of 173°, where the intensity weighted mean hydrodynamic size (Z-average) and the width of the particle size distribution (PSD) were obtained from analysis of the autocorrelation function. 1 μL of latex was diluted with 1 mL of deionized water previously filtered with 0.20 μm membrane to ensure the minimization of dust and other particulates. At least 5 measurements at 25 °C were made for each sample with an equilibrium time of 10 min before starting each measurement.

3.2.15 Static tensile testing

Tensile testing was completed using an Instron 5800R machine equipped with a 500N load cell and a loading rate controlled at 1 mm/min. Test specimens were cut

into bars of width 10 mm and length 40 mm using a razor blade (thicknesses were determined from cross-sectional SEM analysis and the average taken from 10 measurements). The RT tensile mechanical properties were determined from an average of at least five (5) specimens. The Young's modulus was calculated from the gradient of the linear region of the stress-strain curve and tensile toughness calculated from the area under the stress-strain curves.

3.2.16 Nanoindentation

Nanoindentation measurements were performed using a nanoindentation instrument (Micro Materials Ltd, UK) with a standard Berkovich indenter, which constantly measures force and displacement. Measurements were made for each sample at 25 points to a maximum load of 5 mN. Deformation of less than 15% of the film thickness was recorded for all samples (except α-ZrP-PEA = 95:5), avoiding the substrate influencing the results. Reduced Young's modulus (E_r) and hardness (H) were derived from the loading-unloading curve according to the Oliver and Pharr method.[5] The Oliver-Pharr hardness scale was employed due to the nanoscale indentation (closest simulation of nanoscale impact and abrasion from road dirt). Other hardness scales, including Rockwell, Vickers and Knoop, are only effective on the macro- or micro-scale.[6]

3.2.17 GOx titrations

A 0.1 mol/L DBA solution was prepared by dissolving DBA (6.22 g, 0.05 mol) in toluene (500 cm^3). Bromophenol blue (101.4 mg, 0.15 mmol) was dissolved in MeOH (100 cm^3) before a 0.1 mol/L solution of NaOH in MeOH was added until the mixture became blue. A 0.1 mol/L HCl solution was obtained by diluting 4.15 cm^3 of concentrated HCl (12M) to 500 cm^3 with DI water. DBA blanks were produced by combining the DBA solution (15 cm^3) with IPA (70 cm^3) and stirring for 24 hours. Bromophenol blue indicator solution was then added before titration against the 0.1 mol/L HCl solution. The GOx samples were produced by suspending 50 mg in the DBA solution (15 cm^3) and stirring for 24 hours. Then, IPA was added (70 cm^3) and the mixture filtered under gravity. Bromophenol blue indicator solution was added and the mixture titrated against the 0.1 mol/L HCl solution. The end point of the titration is observed by a colour change from blue to yellow.

3.3 Sample syntheses

3.3.1   2-(2-hydroxyethyl)-3a,4,7,7a-tetrahydro-1H-4,7-epoxyisoindole-1,3(2H)-dione (2)
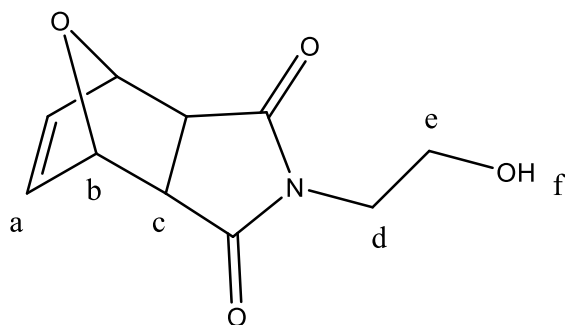
exo-7-Oxabicyclo[2.2.1]hept-5-ene-2,3-dicarboxylic anhydride (29.96 g, 0.180 mol) was dissolved in MeOH (500 cm^3) and purged with Ar gas for 20 mins. Ethanolamine (14.0 cm^3, 0.231 mol) and Et$_3$N (25.2 cm^3, 0.181 mol) were added and the mixture heated under reflux in an inert atmosphere for 19 hours. The mixture was cooled causing formation of white crystals. The crystals were collected via vacuum-assisted filtration and dried in a vacuum oven at 60 °C overnight (32.2 g, 0.154 mol, 86%). ^{1}H NMR (CDCl$_3$, 400 MHz, 298 K), δ (ppm): 2.92 (s, 2H, *c*), 3.41 (s, 4H, *d+e*), 4.78 (t, 1H, *f*), 5.12 (s, 2H, *b*), 6.54 (s, 2H, *a*). ^{13}C NMR (CDCl$_3$, 400 MHz, 298 K), δ (ppm): 41.07, 47.60, 57.73, 80.74, 136.93, 176.95. FTIR (neat) (cm^{-1}) (s = sharp, b = broad): 3473 (s, O-H), 3009, 2974, 2943, 2933, 2895 (s, C-H), 1682 (b, C=O + C=C). This data matches closely with that reported by Fuhrmann *et al.*[7]

3.3.2 (3aR,7R,7aS)-2-(2-hydroxyethyl)-4-(hydroxymethyl)-3a,4,7,7a-tetrahydro-1H-4,7-epoxyisoindole-1,3(2H)-dione (4)
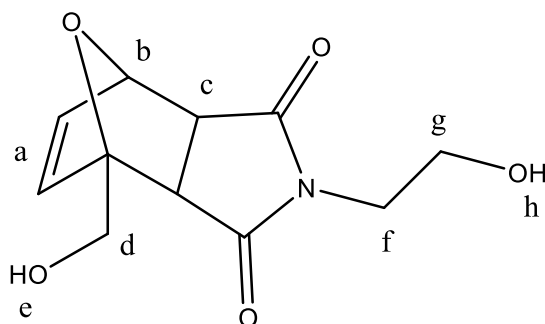
2 (25.3 g, 0.121 mol) was dissolved in toluene (180 cm^3) and heated under reflux for 22 hours. The reaction was quickly quenched in an ice bath at 3 °C. A white, fluffy precipitate formed and the reaction was stored in a freezer overnight to

63

maximise yield. The precipitate was collected via vacuum-assisted filtration and the white powder dried in a vacuum oven at 40 °C overnight (14.8 g, 0.105 mol, 87%). The white powder (9.53 g, 67.6 mmol) was then dissolved in toluene (150 cm^3) before furfuryl alcohol (6.00 cm^3, 69.2 mmol) was added. The reaction was heated at 75 °C overnight yielding a yellow precipitate. The solvent was removed under reduced pressure before the yellow solid was washed with ether and dried in a vacuum oven at 80 °C for 4 days (14.2 g, 59.0 mmol, 87%). ^{1}H NMR (CDCl$_3$, 400 MHz, 298 K), δ (ppm): 2.95 (dd, 2H, c), 3.41 (s, 4H, $f+g$), 3.86 (ddd, 2H, d), 4.72 (m, 1H, h), 4.90 (t, 1H, e), 5.07 (s, 1H, b), 6.52 (s, 2H, a). ^{13}C NMR (CDCl$_3$, 400 MHz, 298 K), δ (ppm): 41.01, 48.21, 57.78, 59.43, 80.66, 92.08, 136.92, 138.52, 175.43, 176.88. FTIR (neat) (cm^{-1}) (s = sharp, b = broad): 3458 (b, O-H), 3023, 2972, 2944, 2888 (s, C-H), 1679 (b, C=O + C=C). This data concurs with that reported by Dobbins *et al.*[8]

3.3.3 ((3a*R*,7*R*,7a*S*)-2-(2-(methacryloyloxy)ethyl)-1,3-dioxo-1,2,3,3a,7,7a-hexahydro-4*H*-4,7-epoxyisoindol-4-yl)methyl methacrylate (5)
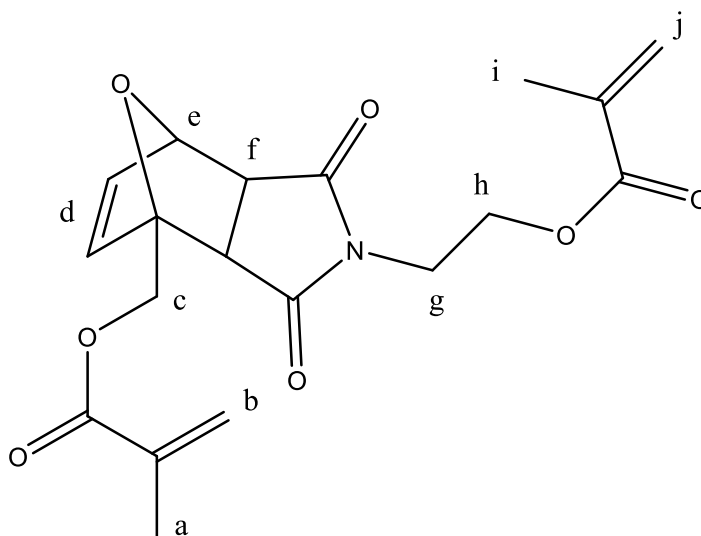
4 (5.08 g, 21.2 mmol), was dissolved in anhydrous DCM (100 cm^3). Et$_3$N (6.10 cm^3, 43.8 mmol) was added and the mixture purged with Ar gas for 1 hour. The mixture was then submerged in a salt ice bath at 0 °C before methacryloyl chloride (4.10 cm^3, 42.0 mmol) was added. The mixture was stirred for 24 hours and allowed to warm to RT, yielding a burgundy coloured liquid. Additional DCM (100 cm^3) was added before the mixture was washed with aqueous NH$_4$Cl (5% w/v, 4 x 250 cm^3), H$_2$O (2 x 250 cm^3) and brine (4 x 250 cm^3). The organic layer was then dried with Na$_2$SO$_4$ and gravity filtered. The solvent was removed under reduced pressure yielding

a brown oil. The crude product was purified by column chromatography through silica using a 1:3 EtOAc:petroleum ether eluent (2.91 g, 7.76 mmol, 37%). ^{1}H NMR (CDCl$_3$, 400 MHz, 298 K), δ (ppm): 1.80 (s, 3H, *a*), 1.86 (s, 3H, *i*), 3.08 (dd, 2H, *f*), 3.67 (t, 2H, *h*), 4.19 (t, 2H, *g*), 4.34 – 4.83 (m, 2H, *c*), 5.12 (s, 1H, *e*), 5.65 (d, 2H, *b*), 5.98 (d, 2H, *j*), 6.54 (dd, 2H, *d*). FTIR (neat) (cm^{-1}) (s = sharp, b = broad): 2959 (b, C-H), 1695 (s, C=O), 1639 (s, C=C). This data is in good agreement with that reported by Dobbins *et al.*[8]

3.3.4   2-(1,3-dioxo-1,3,3a,4,7,7a-hexahydro-2H-4,7-epoxyisoindol-2-yl)ethyl methacrylate (MiMA)
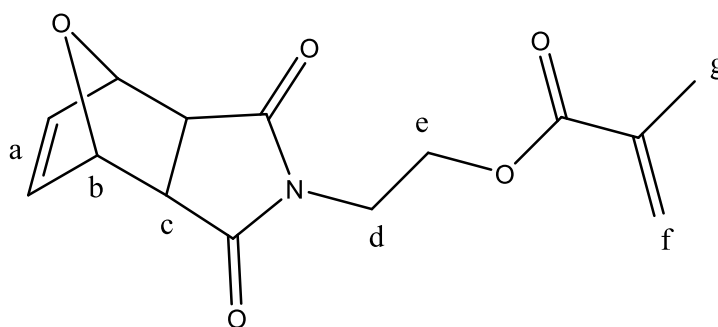
2 (7.60 g, 36.3 mmol) was dissolved in anhydrous DCM (250 cm^3). Et$_3$N (6.10 cm^3, 43.8 mmol) was added and the mixture flushed with N$_2$ gas for 30 minutes. The reaction mixture was submerged in a salt ice bath at 0 °C before methacryloyl chloride (3.60 cm^3, 32.2 mmol) was added. The reaction was then left for 4.5 hours whilst warming to RT before washing with aqueous NaHCO$_3$ (5% w/v, 2 x 150 cm^3) and H$_2$O (2 x 150 cm^3). The resulting pink solution was dried with Na$_2$SO$_4$ and gravity filtered. Solvent was removed under reduced pressure yielding a pink oil. The crude product was purified by column chromatography through silica using a 4:5 EtOAc/DCM eluent yielding a colourless oil that later solidified (4.20 g, 15.1 mmol, 47%). ^{1}H NMR (CDCl$_3$, 400 MHz, 298 K), δ (ppm): 1.86 (s, 3H, *g*), 2.83 (s, 2H, *c*), 3.77 (t, 2H, *d*), 4.24 (t, 2H, *e*), 5.21 (s, 2H, *b*), 5.52, 6.03 (s, 2H, *f*), 6.48 (s, 2H, *a*). FTIR (neat) (cm^{-1}) (s = sharp, b = broad): 3103, 2962, 2961, 2927 (s, C-H), 1697 (s, C=O), 1634 (s, C=C). This data concurs with that reported by Fuhrmann *et al.*[7]

3.3.5 2-cyano-2-propyl dodecyl trithiocarbonate (CTA)
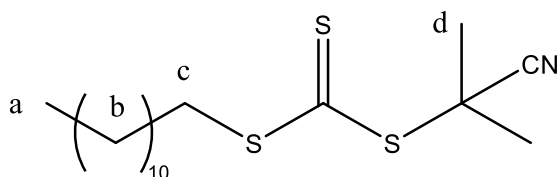
Diethylether (150 cm^3) was flushed with Ar gas for 30 minutes. ^{t}BuOK (9.41 g, 77.0 mmol) was added, forming a suspension. 1-dodecanethiol (15.6 g, 77.2 mmol) was added dropwise over a 10 minute period producing a thick white suspension. CS$_2$ (5.10 cm^3, 83.7 mmol) was added and a yellow, mousse-like mixture was produced. The product was vacuum filtered and collected before diethylether (100 cm^3) was added. Iodine was then added portion-wise until the mixture became dark red. The mixture was then stirred for 1 hour before being washed with aqueous sodium thiosulfate (10% w/v, 5 x 100 cm^3) and H$_2$O (4 x 100 cm^3). The solvent was removed under vacuum yielding a red/orange oil that was dried overnight. EtOAc (250 cm^3) was added and the mixture brought to reflux for 1 hour. AIBN (8.31 g, 50.6 mmol, 2 eq.) was added portion-wise over a 10 minute period. The reaction was then refluxed for 24 hours. Solvent was removed under reduced pressure and the crude product was purified by column chromatography in silica using a 1:9 EtOAc/n-hexane eluent. Recrystalisation in hot n-hexane yielded an orange liquid that solidified in the fridge (8.13 g, 24.4 mmol, 32%). ^{1}H NMR (CDCl$_3$, 400 MHz, 298 K), δ (ppm): 0.89 (s, 3H, a), 1.27 (m, 20H, b), 1.88 (s, 6H, d), 3.34 (t, 2H, c). FTIR (neat) (cm^{-1}) (s = sharp, b = broad): 2922, 2852 (s, C-H), 1461, 1384, 1366, 1071 (S-(C=S)-S). This data concurs with that reported by Wang $et\ al.$[9]

3.3.6 2-Ureido-4[1H]-pyrimidinone (UPy)
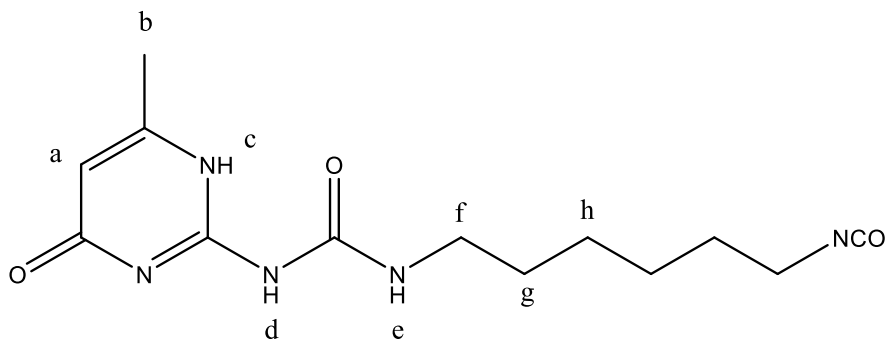
2-amino-4-hydroxy-6-methylpyrimidine (4.38 g, 35.0 mmol) was combined with an excess of HDI (38.0 cm^3, 237 mmol), and heated at 100 °C for 24 hours. A

white precipitate formed and was filtered under vacuum. The resulting solid was washed multiple times with *n*-pentane achieving a white powder in excellent yield (10.17 g, 34.7 mmol, 99%). ^{1}H NMR (CDCl$_3$, 400 MHz, 298 K), δ (ppm): 1.41 (m, 4H, *h*), 1.63 (quint, 4H, *g*), 2.23 (s, 3H, *b*), 3.27 (m, 4H, *f*), 5.82 (s, 1H, *a*), 10.19 (s, 1H, *e*), 11.87 (s, 1H, *d*), 13.11 (s, 1H, *c*). FTIR (neat) (cm^{-1}) (s = sharp, b = broad): 3213, 3144, 3028 (s, N-H), 2934, 2857 (s, C-H), 2284 (s, C=N), 1699, 1663, 1570 (s, C=O). This data concurs with that reported by Folmer *et al.*[10]

3.3.7 UPy-functionalised GO (GOx)

Functionalisation of GO with UPy was achieved using the method outlined by Stankovich *et al.*[11] Typically GO ($\approx$1.5 g) was combined in solid form with UPy at a weight ratio of GO:UPy = 1:1, 1:0.1 and 1:0.01 and are referred to as GO50, GO10 and GO1, respectively (unmodified GO will be referred to as GO0 in this context). Anhydrous DMF (75 cm^3) was added and the mixture degassed with N$_2$ for 1 hour, then stirred for 24 hours. The resultant dispersion was coagulated in DCM ($\approx$200 cm^3), filtered under vacuum, and washed with DCM. The resulting brown powder was dried overnight at 40 °C under vacuum. ^{1}H-^{13}C MAS NMR (^{1}H = 400 MHz, ^{13}C = 100 MHz, 9.4 K), δ (ppm): 19.1 (*d*), 30.0 (*l*-amide), 31.8 (*h, k*), 35.5 (*g*), 37.5-39.1 (*i, j*), 44.6 (*l*-

carbamate), 60.9 (*C-O-C*), 71.0 (*C-OH*), 118.9-129.5 (*sp² GO, c, e*), 132.0 (*sp² GO*), 150.5 (*b*), 156.4 (*f*), 165.4-166.1 (*COOH*), 174.7 (*a*) (assignments relative to Figure 3.1). FTIR (neat) (cm⁻¹) (s = sharp, b = broad): 3176 (b, N-H), 2937, 2861 (s, C-H), 1699, 1646 (C=O).
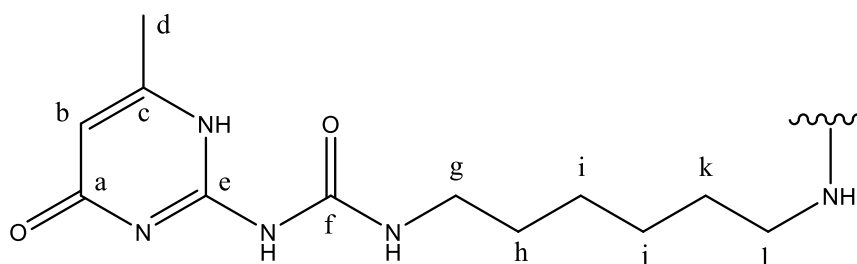
Figure 3.1 – UPy pendant group of GOx product.

3.3.8 UPy-functionalised PVA (PVAy)
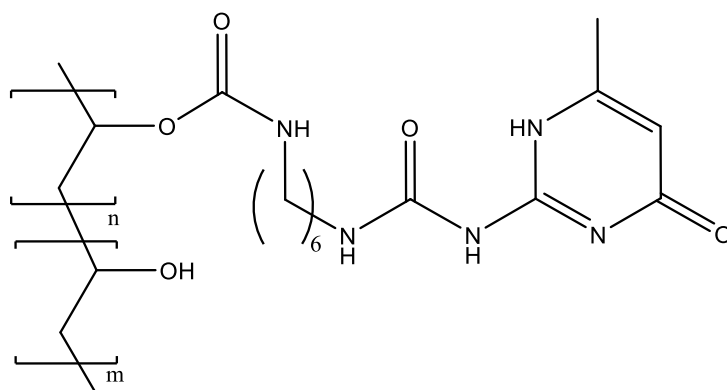
PVA (9.96 g) was dissolved in DMSO (100 cm³) by heating at 60 °C until full dissolution was observed. The resulting mixture was then stored over activated molecular sieves (3 Å) for 24 hours to ensure anhydrous conditions. The dried PVA solution (10 cm³) was combined with UPy of suitable mass (see Table 3.1) before degassing under a flow of Ar gas for 15 minutes. The mixture was then heated at 80 °C (whereby the UPy would dissolve) for 16 hours. 'Gel-like' products were produced so DMSO (10 cm³) was added and the mixture agitated to aid dissolution of the polymer product. Precipitation was achieved in IPA (200 cm³) yielding a 'cotton-like'

product. UPy content of 20 wt% and above could not be re-solubilised following the reaction so could not be isolated. Unmodified PVA is denoted as PVA0.

Table 3.1 – Mixing ratios of 10 wt% DMSO/PVA solution and UPy to produce targeted UPy content in functionalised product.

Nomenclature	Target wt% UPy	DMSO/PVA (cm^3)	UPy (mg)	Product (g)
PVA0	0	N/A	0	N/A
PVA1	1	10	11.2	1.00
PVA5	5	10	50.9	1.00
PVA10	10	10	107.9	1.09

3.4 Polymerisation reactions

3.4.1 Free-radical polymerisation protocol

MMA (9.60 cm^3, 90.1 mmol) and **5** (3.79 g, 10.0 mmol) were weighed out and AIBN (0.10 g, 0.61 mmol) added to the mixture which was degassed for 1 hour under a flow of N_2 gas. The mixture was then heated to 70 °C causing rapid polymerisation and gas evolution after 7 minutes. The reaction was removed from the heat after 8 minutes. DCM was added to remove the product from the flask and was precipitated into MeOH (400 cm^3). A sand coloured powder was obtained (8.80 g).

3.4.2 Typical RAFT polymerisation protocol

The CTA (0.44 g, 1.32 mmol, 1 eq), MMA and functionalised methacrylate (MA) monomers (totalling 52.8 mmol, 40 eq) were added to a Schlenk tube. AIBN (43 mg, 0.26 mmol, 0.2 eq) and toluene ($\approx$ 3.5 cm^3) were added and the mixture degassed through 3 freeze-pump-thaw cycles. The reaction was then heated at 70 °C for up to 24 hours. The resulting polymer was then diluted with toluene and precipitated into cold diethylether yielding 4-5 g of product. The resulting polymer samples were collected and analysed by ^{1}H NMR and FTIR spectroscopy, GPC and TGA. The samples for ^{1}H NMR and GPC were diluted in $CDCl_3$ and $CHCl_3$ respectively.

3.4.3 CTA end-group removal

ACHN (4 mg, 0.02 mmol), the CTA-terminated polymer (225-300 mg, 1 eq), EPHP (50 mg, 0.28 mmol, 5 eq) was added to a Schlenk tube with toluene (1 cm^3). The mixture was degassed with 3 freeze-pump-thaw cycles and heated at 100 °C for 2 hours. During this time, the solution turned from yellow to colourless. The product was precipitated in MeOH (200 cm^3) yielding a white powder at low yield.

3.4.4 Typical Cu(0)-mediated LRP protocol

Cu(0)-mediated LRP was achieved using a similar method to that reported by Jones *et al.*[12] Cu^{II}Br$_2$ (4.2 mg, 0.02 mmol, 0.05 eq.), Me$_6$TREN (18 µL, 0.61 mmol, 0.18 eq.), MBPA (59 µL, 0.38 mmol, 1 eq.), DMSO (2 cm^3) and MMA and functionalised MA monomers (totalling 18.75 mmol, 50 eq.) were added to a vial. The mixture was then degassed for 15 minutes under a flow of Ar. Meanwhile, the Cu(0) wire was activated with concentrated HCl before being washed with water and acetone and dried. The Cu(0) wire was then added under an Ar blanket and the mixture reacted at 25 °C for 24 hours. The product was then diluted with DMSO and samples taken for ^{1}H NMR spectroscopy and GPC. The remaining sample was passed through an Al$_2$O$_3$ column and precipitated into MeOH (200 cm^3). Samples of the purified polymer were collected for analysis by ^{1}H NMR and FTIR spectroscopy, GPC, TGA and DSC. The samples for ^{1}H NMR and GPC were diluted in CDCl$_3$ and CHCl$_3$, respectively.

3.5 Sample preparation

3.5.1 Hot pressing of poly((((3a*R*,7*R*,7a*S*)-2-(2-(methacryloyloxy)ethyl)-1,3-dioxo-1,2,3,3a,7,7a-hexahydro-4*H*-4,7-epoxyisoindol-4-yl)methyl methacrylate-*co*-methyl methacrylate) P(5-*co*-MMA)

The P(**5**-*co*-MMA) powder was added to disc shaped moulds made of steel and sandwiched between two steel plates. The samples were then hot pressed using a Collin P200 P/M automated hot press using a range of conditions as outlined in the table below (Table 3.2).

Table 3.2 – Hot pressing conditions for P(**5**-*co*-MMA). # = number of cycles.

Method	Heat (°C)	Pressure (bar)	Hold (s)	Degas (# x s)	Degas (bar)	Heat (°C)	Pressure (bar)	Hold (s)
1	170	5	15	5 x 5	5	170	180	180
2	180	5	15	10 x 5	5	180	180	300
3	200	5	15	5 x 5	5	200	180	30
(cont.)	210	180	30	-	-	75	180	600
4	170	5	600	5 x 5	5	170	180	600
(cont.)	140	180	300	-	-	75	180	300

3.5.2 UV-cured wsPU films

Neat wsPU films were produced by first weighing out I500 (0.30 g, benzophenone = 0.150 g, 1HCPK = 0.153 g) before adding the water-borne wsPU latex (30 cm^3, 12.4 g solid content). The resulting mixture was stirred for 3 hours before 1 cm^3 aliquots were added to plastic moulds with a diameter of 15 mm. The samples were dried at RT in the dark for 72 hours. The resulting solid materials were cut from the moulds and cured at 5 minute time intervals using an Omnicure Series 2000 UV lamp fitted with a 320-390 nm filter and at 50% laser intensity.

3.5.3 GO film substrate testing

Typically, stock GO solutions of 1 mg/cm^3 were produced by dispersing GO paste in DI water and stirring for 1 hour. In some cases, a sonicator probe was employed for 30 minutes. Et$_3$N was then added to adjust the pH >7 before the wsPU latex was added at the required volume to achieve 5 wt% of GO. In some cases, I500 was also added at this point to the equivalent of 2 wt% of GO. The resulting dispersion was stirred for an extra 30 minutes to adequately mix the wsPU before being cast onto the substrate. The aliquot size, drying conditions and I500 content for the different substrates are listed in Table 3.3.

Table 3.3 – Aliquot size and drying conditions of GO-wsPU films on different substrates.

Substrate	I500 (Y/N)	Aliquot size (cm^3)	Drying time (hours)	Temperature (°C)
Glass slide	N	2.5	24	60
PS petri-dish	N	2.5	120	25
PTFE boat	Y	10	48	25
PTFE petri-dish	Y	3	72	25
Substrate removal (PS)	Y	2.5-7.5	24	40
PET	Y	30	24	40

3.5.4 Solution casting of GO-wsPU films

Typically, a GO stock solution of 1 mg/cm^3 was produced by dispersing 20 g of GO paste, or 5 g of GO powder, in 500 cm^3 of DI water and stirring for 1 hour. This stock solution was then treated with Et$_3$N or NaOH to adjust the pH >7. wsPU was then added at a suitable volume to achieve the desired weight ratio with GO before I500 solution was added to achieve 2 wt% of the GO content. Aliquots of 30 cm^3 were then dried in a poly(styrene) (PS) petri-dish fitted with a poly(ethyleneterephthalate) (PET) disc and at 40 °C for 24 hours. The films were then peeled from the substrate.

3.5.5 Solution casting of GOx

GOx powder (≈300 mg) was suspended in water (30 cm^3) and stirred for 24 hours. The samples were then sonicated using a sonicator probe for 30 minutes. The mixture was cast into a PS petri-dish fitted with a PET disc and dried at 40 °C for 24 hours at which point the film could be peeled from the substrate.

3.5.6 Vacuum-assisted filtration of GOx films

Due to the poor stability of GOx in water, DMSO was used as an alternative solvent. GOx (≈500 mg) was suspended in DMSO (50 cm^3) and stirred for 2 hours. The resulting dispersion was then filtered through a hydrophilic PTFE membrane positioned on top of a traditional filter paper of equivalent size. The GOx film and

PTFE membrane were peeled from the filter paper and dried in a fan-assisted oven at 40 °C for 24 hours. The GOx film was then peeled from the PTFE membrane.

3.5.7 Vacuum-assisted filtration of GOx/PVAy films

PVAy solutions of 1 wt% were produced by dissolving PVAy (150 mg) in DMSO (15 cm^3) at 80 °C until complete dissolution was observed. GOx powders (≈500 mg) were suspended in DMSO (50 cm^3) and stirred for 2 hours. The PVAy solution (≈2.5 g) was then added dropwise under stirring. The mixture was stirred for 1 hour before being filtered through a hydrophilic PTFE membrane positioned on top of a traditional filter paper of equivalent size. The GOx/PVAy film and PTFE membrane were peeled from the filter paper and dried in a fan-assisted oven at 40 °C for 24 hours. The film could then be peeled from the PTFE membrane. The nomenclature of the GOx/PVAy films can be seen in Table 3.4 and will be used from hereon.

3.5.8 Solution casting of α-ZrP-PEA films

A PEA stock solution was produced by diluting PEA (1.02 g) with DI water (9.11 g) achieving a 10 wt% solution. The α-ZrP powder (400 mg) was suspended in DI water (40 cm^3) before addition of the PEA solution. The mixture was then stirred for 2 hours before casting into a PS petri-dish fitted with a PET disc. The resultant samples were dried in a fan assisted oven for 24 hours before peeling the film from the substrate. The specific volumes of α-ZrP and PEA for each weight ratio are listed in Table 3.5.

Table 3.4 – Nomenclature and composition of GOx/PVAy films used in this study.

Nomenclature	UPy content on GO (wt%)	UPy content on PVA (wt%)
GO0	0	N/A
GO0/PVA0	0	0
GO0/PVA1	0	1
GO0/PVA5	0	5
GO0/PVA10	0	10
GO1	1	N/A
GO1/PVA0	1	0
GO1/PVA1	1	1
GO1/PVA5	1	5
GO1/PVA10	1	10
GO10	10	N/A
GO10/PVA0	10	0
GO10/PVA1	10	1
GO10/PVA5	10	5
GO10/PVA10	10	10
GO50	50	N/A
GO50/PVA0	50	0
GO50/PVA1	50	1
GO50/PVA5	50	5
GO50/PVA10	50	10

Table 3.5 – Specific mass ratios of α-ZrP and PEA used when producing films.

Target PEA content (wt%)	α-ZrP (mg)	PEA sol^n (g)	PEA (mg)	True PEA content (wt%)
1	404	0.057	5.7	1.4
5	408	0.218	21.8	5.1
9	400	0.407	40.7	9.2
17	408	0.798	79.8	16.4
23	402	1.225	122.5	23.4
29	399	1.609	160.9	28.7
33	404	2.011	201.1	33.2

3.6 References

1.   M. Ciampolini and N. Nardi, *Inorganic Chemistry*, 1966, **5**, 41-44.

2.   R. K. Harris, E. D. Becker, S. M. Cabral de Menezes, R. Goodfellow and P. Granger, *Solid State Nuclear Magnetic Resonance*, 2002, **22**, 458-483.

3.   F. M. Fowkes, *Industrial & Engineering Chemistry*, 1964, **12**, 40-52.

4.   L. Cao, S. Deng and Z. Lin, *Polymers (Basel)*, 2016, **8**, 50-62.

5.   W. C. Oliver and G. M. Pharr, *Journal of Materials Research*, 1992, **7**, 1564-1583.

6.   E. Broitman, *Tribology Letters*, 2017, **65**, 23.

7.   A. Fuhrmann, R. Gostl, R. Wendt, J. Kotteritzsch, M. D. Hager, U. S. Schubert, K. Brademann-Jock, A. F. Thunemann, U. Nochel, M. Behl and S. Hecht, *Nature Communications*, 2016, **7**, 13623-13630.

8.   D. J. Dobbins, G. M. Scheutz, H. Sun, C. A. Crouse and B. S. Sumerlin, *Journal of Polymer Science*, 2019, **58**, 193-203.

9.   S. Wang, M. Li, H. Zhang, X. Yang, X. Zhang, Y. Tao and X. Wang, *Journal of Polymer Science Part A: Polymer Chemistry*, 2016, **54**, 1633-1638.

10.   B. J. B. Folmer, R. P. Sijbesma, R. M. Versteegen, J. A. J. van der Rijt and E. W. Meijer, *Advanced Materials*, 2000, **12**, 874-878.

11.   S. Stankovich, R. D. Piner, S. T. Nguyen and R. S. Ruoff, *Carbon*, 2006, **44**, 3342-3347.

12.   G. R. Jones, R. Whitfield, A. Anastasaki, N. Risangud, A. Simula, D. J. Keddie and D. M. Haddleton, *Polymer Chemistry*, 2018, **9**, 2382-2388.

4. Synthesis of Maleimide- and Furfuryl-functionalised Methacrylate Monomers for Self-healing Polymers

4.1 Introduction

By incorporating self-healing properties to existing polymers used in industry, it is thought that the lifetime of the material could be extended. Target polymers included the poly(methyl methacrylate) (PMMA) coating used on the 'halo' components of the B, C, and D pillars in Jaguar-Land Rover (JLR) vehicles. These components are linear, impact modified structures that are prone to micro-scratches during handling, manufacture, and everyday use, and thus, a protective film is required throughout the car production. The film is only removed once the entire car is fully constructed.

Over the previous two decades, materials with the ability to mend or repair damage have been developed using a multitude of different chemical approaches.[1-6] Of the methods reported to date, thermally-reversible Diels Alder (TRDA), microcapsules and intermolecular forces (IF) have shown the most promise. In this work, microcapsule technology was disregarded due to the inability of this approach to allow for multiple healing events. IF techniques, although often effective at healing damage at RT, do not provide the same mechanical properties as a fully covalent network. TRDA allows for reversible self-healing whilst also maintaining a covalently cross-linked network. It is hypothesised that the covalent cross-linking of the PMMA using a TRDA structure could negate the requirement of the impact modifier currently employed by JLR to achieve a strong thermoset-like coating that can be converted to a thermoplastic during healing. It is critical that the reversible Diels-Alder (DA) activation temperature is above the upper limit experienced by the target component. It must also be low enough that heating the material to the healing temperature is not too costly, laborious or hazardous. As reported by JLR, the maximum temperature expected for bodywork components is 100 °C, higher than reported in much of the previous literature.[7] The maleimide-furan coupling (MFC) is widely explored with the retro-Diels Alder (rDA) reaction occurring at ≈120 °C.

PMMA is synthesised from polymerisation of methyl methacrylate (MMA) using radical processes. In recent decades, techniques have been developed that allow

for control of the molecular weight of the polymer through living radical polymerisation (LRP) techniques.[8-11] LRP is achieved through multiple approaches including reversible addition-fragmentation chain-transfer (RAFT),[9, 10] single-electron transfer LRP (SET-LRP)[11] and Cu(0)-mediated LRP.[8] These are referred to as reversible deactivation radical polymerisation (RDRP) techniques. In this work, free-radical polymerisation (FRP) was initially employed as a 'proof of concept' before LRP methods were used. Different LRP methods were investigated to determine the most suitable approach for production of stable polymers which could both have the required self-healing functionality and be processed using conventional techniques.

TRDA polymers with self-healing properties are produced using a number of approaches.[12-14] Firstly, a cross-linking moiety can be employed in collaboration with pendant functional groups on the polymer backbone.[15] The cross-linker has multiple functional groups that couple with the diene/dienophile on the polymer backbone through a DA reaction. Due to the small molecular volume of the cross-linker (in comparison to another polymer chain), it has high mobility, leading to improved recombination upon healing and increased recovery of properties. Alternatively, a polymer can be produced containing both the diene and dienophile.[16] The polymer is heated to break the DA bond and when cooled, the groups recombine. There is, to the best of my knowledge, no examples in the literature of a zip-like approach to healing as explored in this work. In two separate reactions, a 'male' and 'female' polymer are produced. Following polymerisation, the two polymers are combined and heated. The heating process expels the protecting group present on the dienophile, and cooling then allows a DA reaction to proceed.

It is proposed that this approach could be useful in a number of ways. Firstly, the ratio of a diene to dienophile in the two polymer systems can be manipulated such that the DA coupling partners become more numerous. A simple 1:1 ratio of diene to dienophile leads to a number of functional groups remaining trapped in a 'frozen' polymer system. If a polymer were to have, for example, five diene groups for every dienophile, the likelihood of a dienophile coupling to a diene is significantly improved. Secondly, it is thought this approach could be utilised to homogenise two different polymer types. For example, functionalisation of a PMMA polymer with a diene and

a poly(propylene) (PP) with a dienophile could result in the coupling of the two polymer systems to yield the beneficial properties of both.

MMA has a range of sister compounds that can allow reactions to produce functionalised methacrylate (MA) monomers (Figure 4.1). One example of this is methacryloyl chloride, which reacts readily with hydroxyl groups to produce ester linkages.[17, 18] This reactivity can be exploited to produce functionalised MA monomers and MA terminated cross-linkable monomers. The polymerisation of these monomers with MMA was investigated.
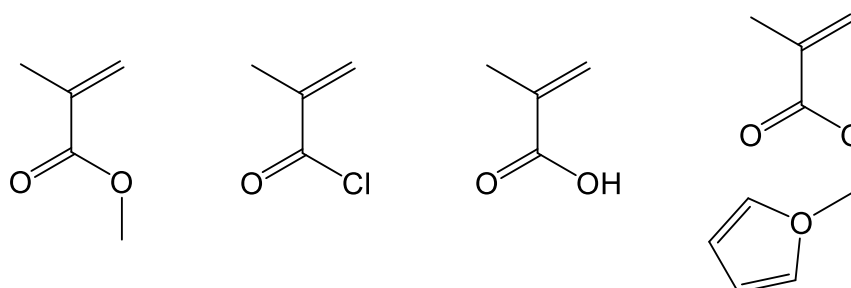
Figure 4.1 – Methyl methacrylate and relevant sister compounds. From left to right: methyl methacrylate, methacryloyl chloride, methacrylic acid and furfuryl methacrylate.

4.2 Synthesis, polymerisation and processing of a maleimide-based cross-linker

A maleimide-based cross-linker was synthesised using a modified version of the route reported by Syrett *et al.*[1] The approach described was easily manipulated to achieve the desired maleimide functionalised MA cross-linker.

4.2.1 Synthesis of ((3a*R*,7*R*,7a*S*)-2-(2-(methacryloyloxy)ethyl)-1,3-dioxo-1,2,3,3a,7,7a-hexahydro-4*H*-4,7-epoxyisoindol-4-yl)methyl methacrylate (5)

The cross-linking moiety is synthesised in a three-step process as shown in Scheme 4.1. Firstly, the cyclic anhydride (**1**) undergoes two nucleophilic substitution reactions to yield a 'maleimide-like' product. This is achieved through a two-step, ring opening-ring closing mechanism releasing water as a by-product.[19, 20] The inclusion

of base encourages the substitution reaction to proceed and the intramolecular nature of the ring closing step results in high conversion to the cyclic maleimide product (as opposed to a di-functionalised amide-like product).
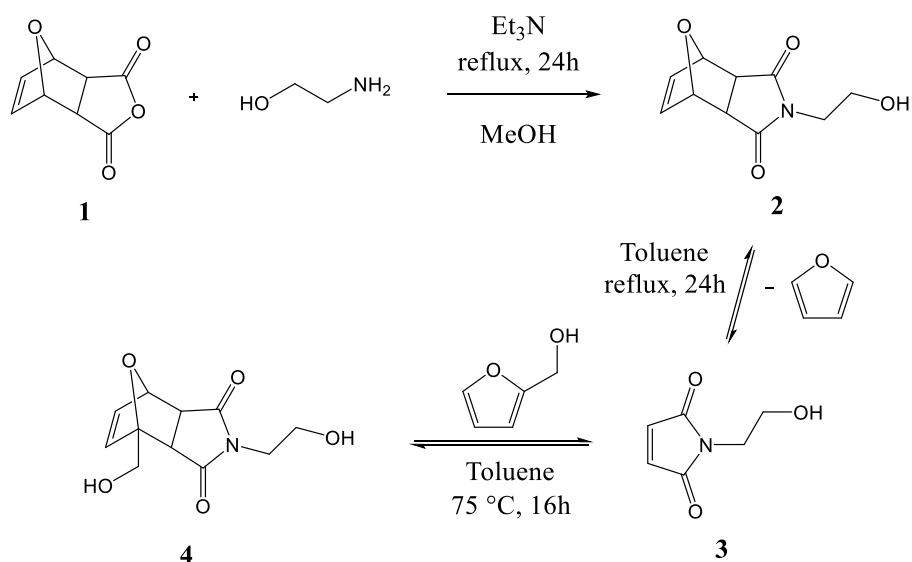
Scheme 4.1 – Reaction scheme for the synthesis of the hydroxyl-terminated maleimide-based cross-linker.

Next, furan is removed by refluxing a solution of the 'maleimide-like' product (**2**) in toluene. This facilitates the rDA reaction, cleaving the furan group from the maleimide (**3**). Critically, the mixture is quenched in an ice bath after reflux to rapidly precipitate **3** whilst the furan remains in solution. It was found that other methods did not adequately separate the furan, resulting in recombination.

Finally, **3** is heated with furfuryl alcohol to allow the DA reaction to proceed. An elevated temperature (75 °C) is employed to improve the rate of the reaction but also allows isomeric control.[21] The kinetically favoured *endo* conformation is produced but undergoes a dissociation-recombination process to isomerise to the thermodynamically favoured *exo* isomer. The use of furfuryl alcohol provides the cross-linking product (**4**) with hydroxyl functional groups at the termini of the compound allowing further functionalisation.

Figure 4.2 shows the ^{1}H NMR spectrum of the product with assignments reported in Table 4.1. Minor solvent impurities can be assigned at 1.05, 2.50 and 3.47 ppm.[22] Splitting of the peaks centring at 2.95 and 3.87 ppm arises due to the coupling between two 'non-equivalent' protons.[23] The 'roofing' between the two peaks confirms proton 5a is able to couple to a proton of almost equivalent environment, 5b, and vice versa. Similarly, the protons at position 3 display roofing. It would be expected these protons could rotate freely due to their aliphatic environment however, it is likely they are locked in position through hydrogen bonding of the terminal hydroxyl group to the carbonyl present on the maleimide ring (Figure 4.3). This prevents rotation and thus forces the protons into separate, non-equivalent environments.
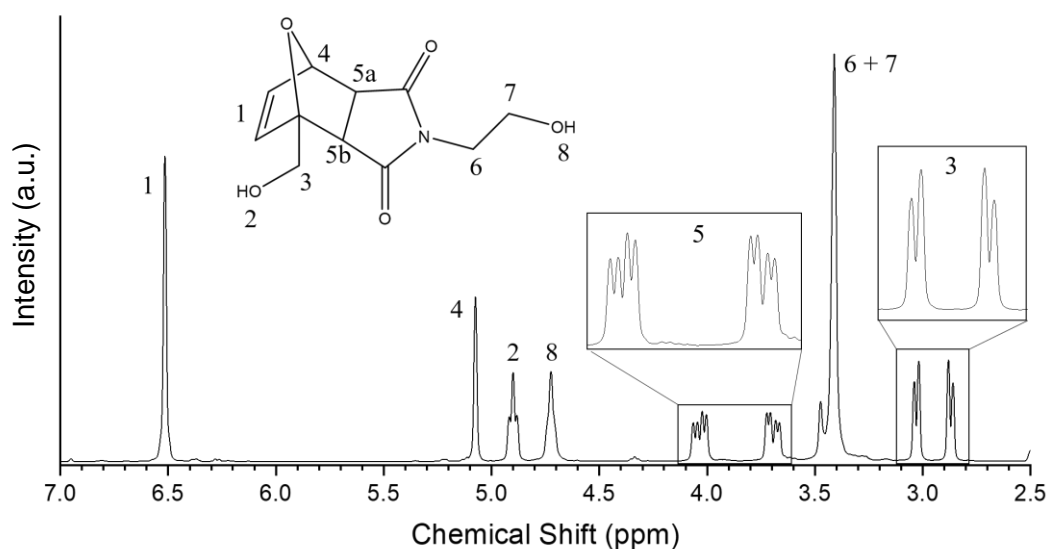
Figure 4.2 – ^{1}H NMR spectrum of compound **4**.

Table 4.1 – Chemical shifts, integration, splitting and assignments for the ^{1}H NMR of **4**.

Chemical Shift (ppm)	Integration (H)	Splitting	Assignment	J splitting (Hz)
2.95	2	d-d	3	48, 6
3.41	4	s	6+7	-
3.87	2	d-d-d	5a+b	102, 12, 6
4.72	1	t	8	6
4.90	1	t	2	6
5.07	1	s	4	-
6.52	2	s	1	-
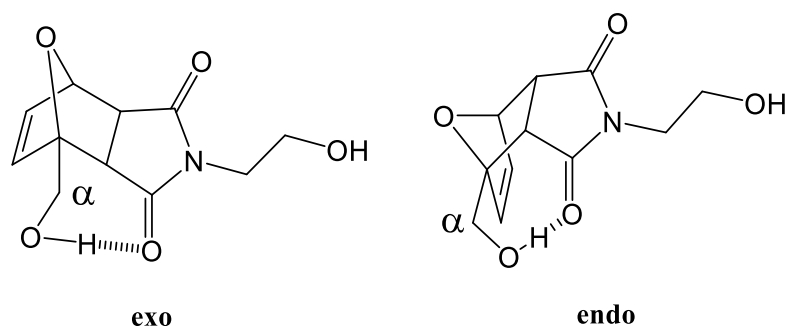
Figure 4.3 – *exo* and *endo* isomers of the maleimide compound. Hydrogen bond trapping of protons in the α position is shown through interactions between terminal hydroxyl and carbonyl groups.

Protons at positions 6 and 7 have similar shifts and so cannot be resolved. Proton 2 is assigned to the peak at 4.90 ppm due to the more defined splitting of the peak. Coupling to two non-equivalent hydrogen atoms results in strong splitting. The splitting of the peak at 4.72 ppm results in a triplet where the two outer peaks appear as shoulders. Conformational tumbling of the hydrogens at position 7 causes a broadening of the signal, and thus the triplet is not fully resolved.[24]

The FTIR spectrum of compound **4** was recorded, see Figure 4.4. Distinctive peaks for hydroxyl, alkane, and amide-carbonyl stretches can be observed at 3457 cm^{-1}, 3022-2892 cm[-1,] and 1682 cm^{-1}, respectively. Interestingly, a peak is present at 1762 cm^{-1} that is likely due to incomplete ring-closure during synthesis. During the initial

reaction of ethanolamine with the oxonorbornene anhydride, it is possible the open-ring conformation is trapped as a minor by-product (Scheme 4.2).

For polymerisation reactions, the hydroxyl groups are converted to MA groups. This is achieved using methacryloyl chloride in an anhydrous dichloromethane (DCM) solution (Scheme 4.3). It is critical that this reaction is completed in anhydrous conditions due to the reactivity of methacryloyl chloride towards water.[25] It was also noted that compound **4** must first be milled to a powder and dissolved at RT before the reaction setup is cooled to 0 °C. It appears that **4** is weakly soluble in DCM and so care must be taken to ensure it is fully dissolved prior to the addition of methacryloyl chloride.
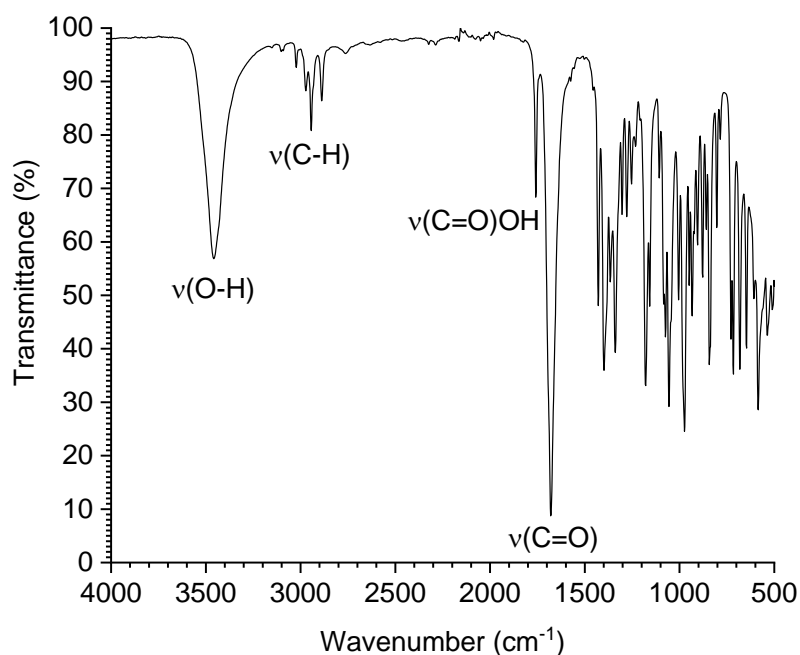
Figure 4.4 – FTIR spectrum of compound **4**.
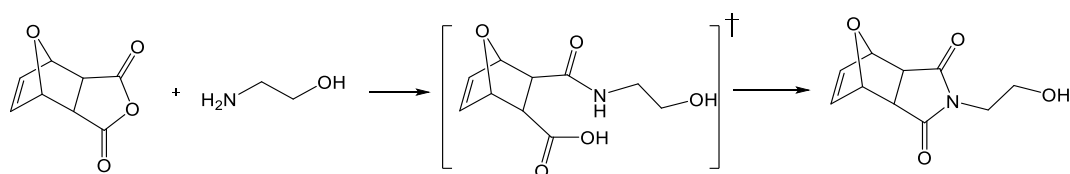
Scheme 4.2 – Reaction pathway from the oxonorbornene anhydride to the maleimide via an intermediate. The intermediate contains a carboxylic acid group not otherwise present in the other compounds.
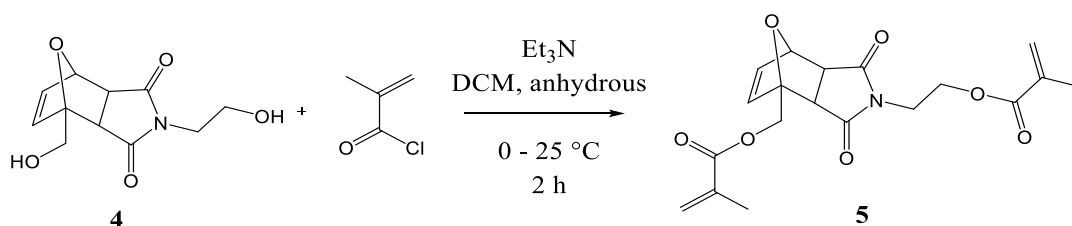
Scheme 4.3 – Synthetic route towards the methacrylate functionalised maleimide species, **5**.

Following addition of methacryloyl chloride, the reaction is stirred for two hours whilst the mixture is warmed to RT. The resulting solution is exposed to air before undergoing multiple washes with sodium hydrogen carbonate, water and brine. The product is then purified through column chromatography achieving a white solid (**5**) with a yield of 77%.
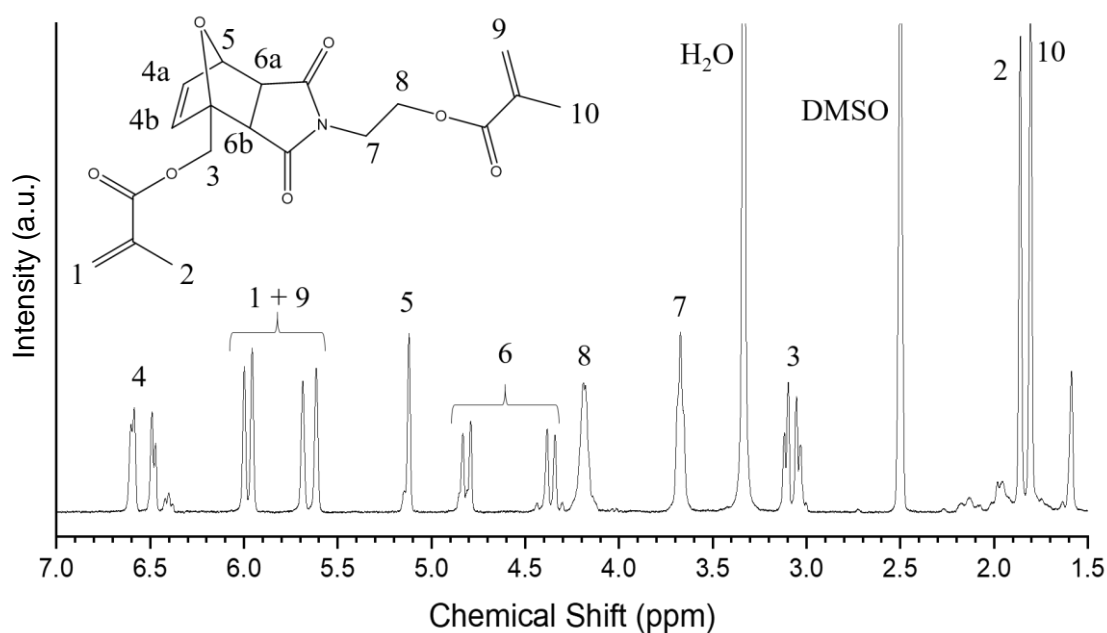
Figure 4.5 – ^{1}H NMR spectrum and assignments for compound **5**.

Table 4.2 – Chemical shifts, integration, splitting and assignments for the ^{1}H NMR of **5**.

Chemical Shift (ppm)	Integration (H)	Splitting	Assignment	J splitting (Hz)
1.80/1.86	6	s	2+10	-
3.08	2	d, d	3	21, 6
3.67	2	s	7	-
4.19	2	s	8	-
4.59	2	d, d	6	135, 12
5.12	1	s	5	-
5.61-6.00	4	s	1+9	-
6.54	2	d, d	4a+b	33, 6

The ^{1}H NMR spectrum is displayed, see Figure 4.5 and the associated assignments outlined in Table 4.2. Petroleum ether (column chromatography co-solvent) impurities are detected in the alkyl proton region below 1.5 ppm. The formation of two new peaks at 1.80 ppm and 1.86 ppm are assigned to the methyl group of the methacrylate end groups. The protons at position 3 display roofing as is present in the starting material however the splitting between the two peaks is much

smaller. This suggests the protons are still non-equivalent but have much more similar environments. Hydrogen bonding is not possible in this structure however, it is likely the steric interference of the methacrylate end group and the carbonyl species of the maleimide ring lock the protons in position. Protons in positions 7 and 8 are seen to separate to different shifts. The de-shielding influence of the methacrylate group is much stronger on proton 8 due to relative proximity and thus causes a shift of 0.78 ppm downfield. The alkene protons at position 1 and 9 are detected between 5.61 ppm and 6.00 ppm and consist of four separate environments. As the double bond is unable to rotate, the two protons are fixed in position and thus can be treated as two separate environments.[26] Critically, the two peaks associated with the hydroxyl protons of the starting materials are absent confirming a successful reaction.
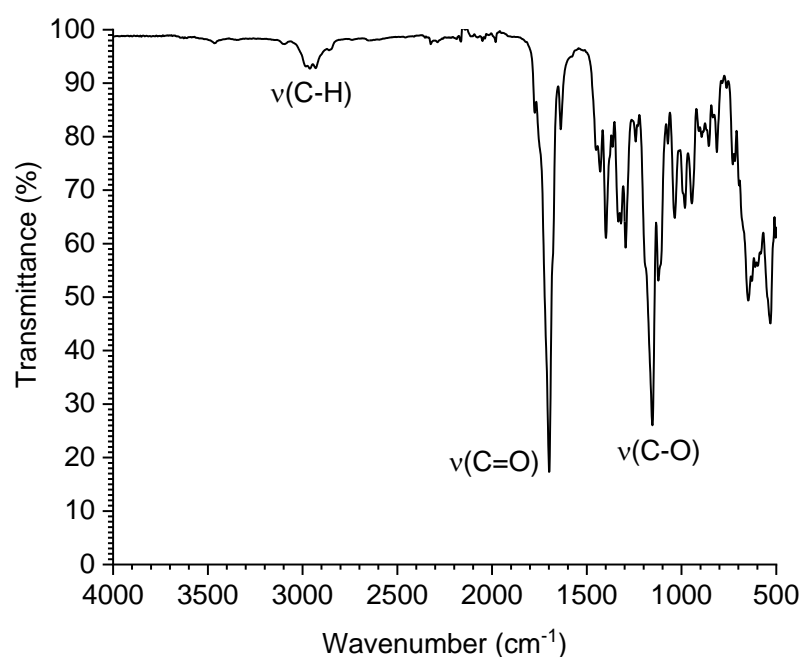
Figure 4.6 – FTIR spectrum of compound **5**.

The FTIR spectrum of compound **5** (Figure 4.6) shows peaks for the C-H, C=O, and C-O (ester) stretches as would be expected for the desired product. It is important to note the absence of an O-H stretching mode further reinforces the

evidence that the hydroxyl functionalities have been converted to methacrylate end groups.

4.2.2 FRP of the maleimide-based cross-linker (5) with MMA

Following the successful synthesis of compound **5**, polymerisation with MMA was attempted (Scheme 4.4). FRP was used as a 'proof-of-concept' as it was not deemed essential to achieve low polydispersity. After mixing the reagents and undergoing a degas cycle, the reaction mixture was heated to 70 °C in an oil bath. The polymerisation occurred rapidly, with a solid material produced in 6 minutes and a large evolution of gas occurring after 7 minutes. The reaction was removed from the heat after 8 minutes to prevent any further gas evolution. The resulting material was firmly adhered to the surface of the glassware and so was freed using DCM. Further addition of DCM and precipitation into methanol (MeOH) yielded a sand coloured powder. It was noted that the maleimide-based cross-linker can be collected as an orange/brown oil and so is responsible for the colour observed.
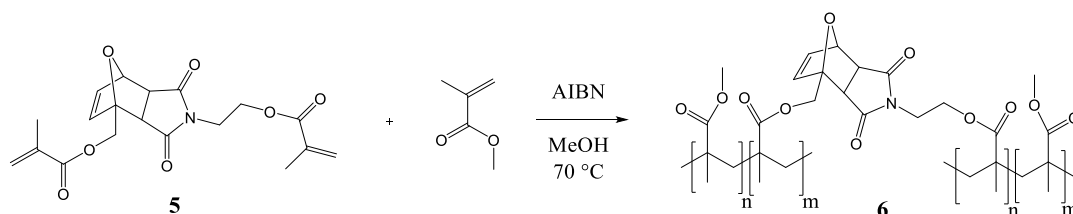
Scheme 4.4 – Polymerisation reaction of MMA with the maleimide-based cross-linker (**5**) to produce polymer **6**.

Due to the highly cross-linked nature of the polymer, it proved difficult to characterise through traditional solution-based techniques. For this reason, solution NMR and GPC could not be completed. Nonetheless, TGA (Figure 4.7) and DSC (Figure 4.8) were completed to establish the thermal properties of the polymer.
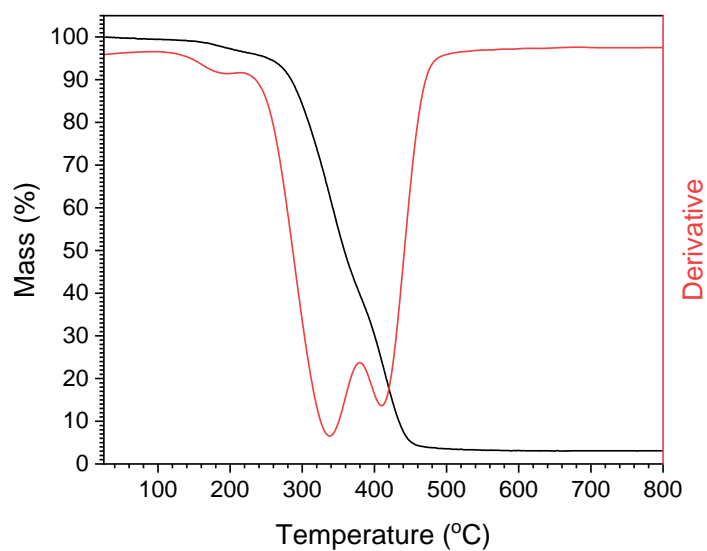
Figure 4.7 – TGA curve of the cross-linked PMMA/maleimide polymer. Mass percentage loss is shown as a function of temperature and the derivative of the mass loss is shown.
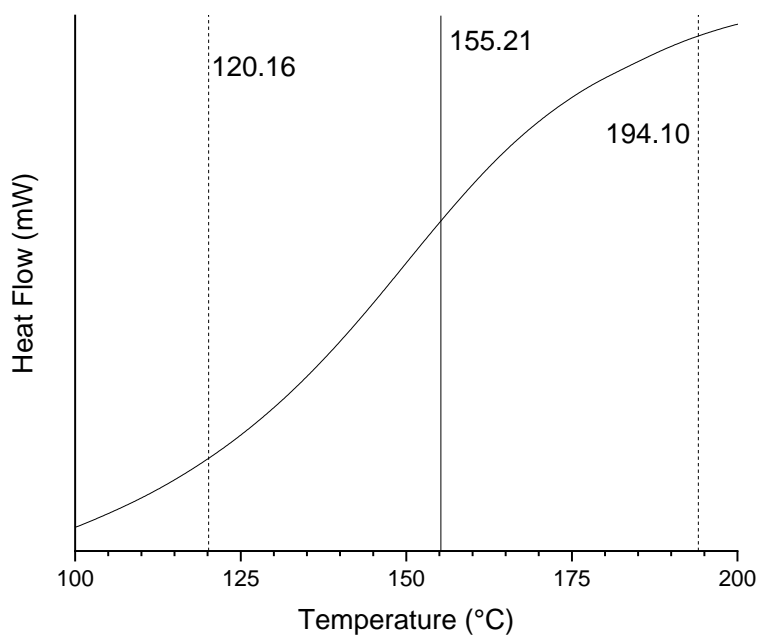
Figure 4.8 – DSC trace of the cross-linked PMMA/maleimide polymer. Onset, endset, and midpoint temperatures are highlighted.

It can be seen from the differentiated TGA trace that the polymer displays degradation phases centred at 192 °C, 340 °C, and 415 °C as is consistent with neat PMMA.[27] The DSC trace displays a T_g at 155 °C, which far exceeds the value of 108 °C expected for pure PMMA.[28] It is interesting to note that there is no endothermic artefact between 100 °C and 140 °C that would be consistent with a rDA reaction.[29, 30] There is however literature that has shown that other thermal effects (including T_g) can mask the rDA reaction.[29, 31] It is reported that the polarity of neighbouring groups has an effect on the rDA temperature with lower polarity groups increasing the onset temperature of the rDA reaction.[16] Kavitha and Singha reported an acrylate polymer cross-linked via maleimide structures with a broad rDA endotherm between 120 and 190 °C.[32]

Hot pressing of the polymer powder was attempted yielding inhomogeneous and discoloured materials (Figure 4.9). Temperatures between 170 °C and 200 °C were explored to ensure the polymer was above the T_g of 155 °C. By way of comparison, hot pressing of PMMA at similar temperatures has been reported for many years.[33, 34] Despite this, later research confirmed that amorphous polymers should be processed at ≈100 °C+ above T_g. The granular texture of the resulting discs suggested an incomplete transition and so longer heating and cooling cycles were employed in an attempt to encourage the formation of a homogenous morphology. These steps failed to improve the quality of the samples produced. It was therefore proposed that a reduction in polydispersity would improve the consistency of the thermal properties of the polymer chains, facilitating the production of more homogeneous samples. Such

a strategy was shown to be flawed. Instead it confirmed the maleimide-based cross-linker was undergoing irreversible branching during polymerisation.

Figure 4.9 – Digital photographs of hot-pressed samples produced from the cross-linked polymer (structure **6**).

4.2.3 Synthesis of chain-transfer agent (CTA), 2-cyano-2-propyl dodecyl trithiocarbonate

RAFT is known to be more compatible with a wider range of monomers and solvent systems than other LRP methods and, considering the relative unknown compatibility of the maleimide cross-linker monomers with other LRP reagents, RAFT was investigated first.[35-37] Reaction optimisation is also much simpler for RAFT polymerisation than for other competing LRP techniques.[35] Wise selection of the chain-transfer agent (CTA) is essential to achieve effective polymerisation.[38] Both the Z and R group (Figure 4.10) can be controlled so as to minimise polydispersity and improve the rate of reaction. In the case of MMA polymerisation, it has been shown previously that a tertiary cyano group provides a high partition coefficient when employed in the R position.[39] Functionality in the Z position should be selected to avoid side reactions which are more common with electron withdrawing groups. As a result, the dodecyl group yields a high transfer constant whilst preventing side reactions.[40]
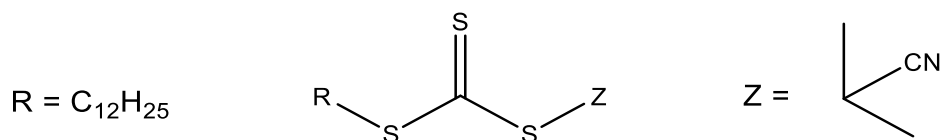
Figure 4.10 – Typical trithiocarbonate CTA structure labelled with ideal R and Z groups for MMA polymerisation.

2-cyano-2-propyl dodecyl trithiocarbonate was synthesised by a previously reported method.[41] The method was modified to include the non-nucleophilic base potassium *tert*-butoxide (*t*-BuOK) in the place of sodium hydride (NaH). This has been shown to simplify work up and reduces undesired side reactions.[42] The ^{1}H NMR for the CTA product can be seen in Figure 4.11. The assignments are in agreement with previous literature.[41]
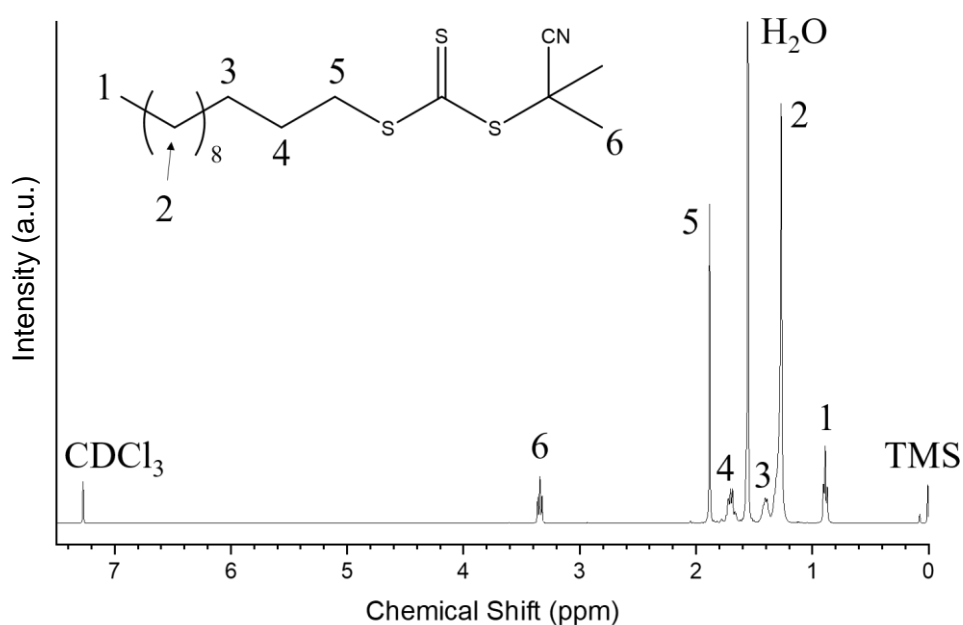
Figure 4.11 – ^{1}H NMR spectrum of the 2-cyano-2-propyl dodecyl trithiocarbonate CTA.

4.2.4 RAFT polymerisation of the maleimide-based cross-linker (5) with MMA

Initially, MMA was polymerised via RAFT as a control. It has been previously reported that polymers synthesised via RAFT can display relatively poor thermal stability, often undergoing degradation at a similar temperature to that of the pure CTA.[42] The widely accepted mechanism for the degradation of RAFT-PMMA species is via a homolysis disproportionation process in which the trithocarbonate CTA cleaves from the PMMA chain before breaking down into carbon disulfide and a sulfide radical.[43] Meanwhile, the PMMA unzips in a reverse of the polymerisation process yielding a mixture of MMA monomers and oligomers (Scheme 4.5). Consequently, the thermal stability of both the CTA and the RAFT-PMMA were analysed by TGA (Figure 4.12). The CTA shows major degradation peaks at 240 °C and 297 °C however, does show minor weight loss from approximately 100 °C. This becomes more prominent with PMMA as a distinct peak is observed at 125 °C. This suggests the PMMA is destabilised by the CTA resulting in a reduction in thermal stability. Due to the proximity of this degradation to the targeted self-healing temperature of 120 °C, it is essential to remove the CTA from the polymer before processing.

Removal of the CTA can be achieved in a number of ways. When using a dithiocarbonate, thermolysis can often cleanly remove the end group without initiating the same unzipping that is observed with a trithiocarbonate.[43] Alternatively, Perrier *et al.* have shown that by using an excess of radical initiator such as AIBN, the CTA can be overwhelmed as the AIBN terminates the polymer chains irreversibly.[44] Unfortunately, this approach requires strict parameters and a 20-times excess of AIBN. A radical-induced reduction has been reported by Chong *et al.* in which 1-ethylpiperidine hypophosphite (EPHP) is used as a hydrogen donor to convert the trithiocarbonate-terminated PMMA to an analogous hydride-terminated species (Scheme 4.6).[41] The by-products of this reaction are soluble in water and so can be removed with a simple wash.

Scheme 4.5 – Reaction mechanism for the degradation of RAFT-PMMA where a) homolysis, b) unzipping and c) disproportionation.

Figure 4.12 – TGA curves for a) CTA, (**9**) b) PMMA produced via RAFT polymerisation.

Scheme 4.6 – Reaction of a CTA-terminated PMMA with EPHP to yield a hydride-terminated PMMA species.
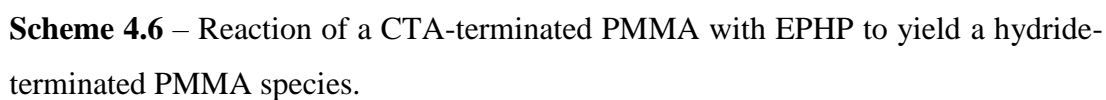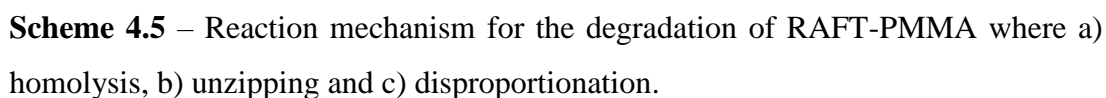
Removal of the CTA from the RAFT-PMMA polymer control was completed using the radical-induced reduction method. Simply, the polymer, EPHP and AIBN

were combined in toluene before the mixture was degassed and heated at 70 °C for 18 hours to ensure complete removal. A 5-fold excess of EPHP was used. The ^{1}H NMR of the starting material and product can be seen in Figure 4.13. Critically, the CTA peak at 3.25 ppm is not present following the reaction and thus proves the treatment was a success.

RAFT polymerisation of the maleimide cross-linker (**5**) with MMA was attempted in toluene. Despite multiple attempts, polymerisation could not be achieved. It can be seen from the ^{1}H NMR (Figure 4.14) that the product collected was neat PMMA.[45] It was observed during experiments that the cross-linker **5** would not fully dissolve into the reaction medium and therefore, it is likely that **5** is not polymerised due to the heterogeneous nature of the mixture. Solubility was not improved, despite increased temperature, use of alternative solvents (EtOAc, acetonitrile, dioxane or DMF) or a larger solvent content.
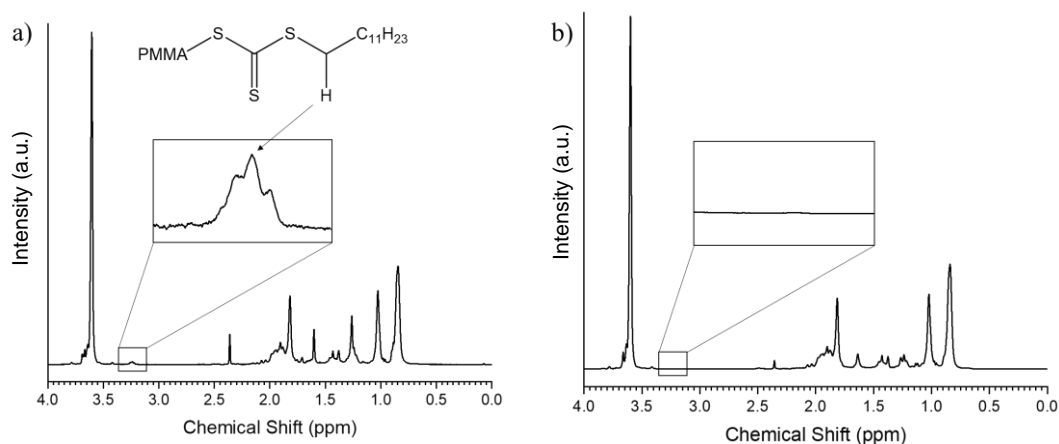
Figure 4.13 – ^{1}H NMR spectra of a) RAFT-PMMA and b) RAFT-PMMA following CTA end group removal via radical-induced reduction with EPHP.
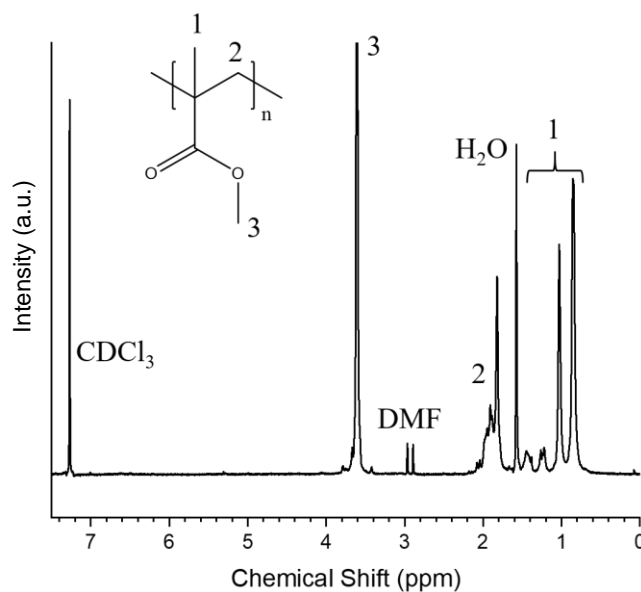
Figure 4.14 – ^{1}H NMR spectrum for the polymer product following RAFT polymerisation of MMA and **5**, showing signals for PMMA only.

4.3 RAFT polymerisation of furfuryl methacrylate and maleimide methacrylate towards zip-like polymers

An alternative approach was developed in which the two components of the maleimide-based cross-linker were synthesised and polymerised separately before being combined at a later stage. The two polymers 'zip' together to produce a similar cross-linked network as was targeted in the previous section (Scheme 4.7). As described in the introduction, this approach offers a number of advantages over the previous process. Furfuryl methacrylate (FMA) is commercially available and so requires no treatment before polymerisation. Maleimide methacrylate (MiMA) requires synthesis however, the process has been reported previously.[17]
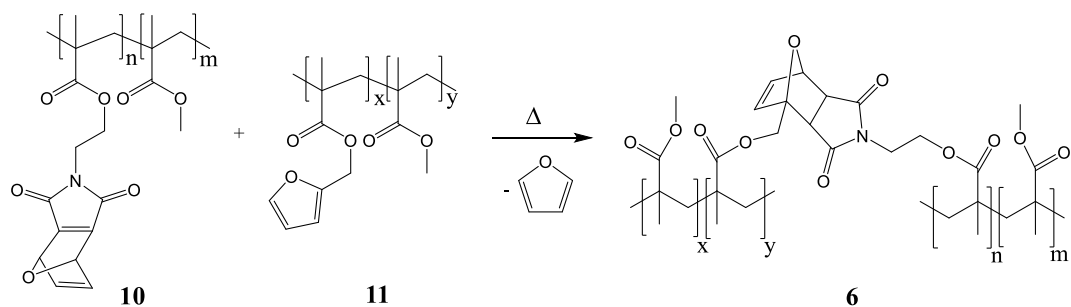
Scheme 4.7 – 'Zip' like approach to cross-linking PMMA polymer utilising FMA- and MiMA-functionalised polymers.

4.3.1 RAFT polymerisation of FMA

The polymerisation of FMA has been widely reported[46-49] however, it has been shown that FRP of FMA results in the formation of a gel-like product due to cross-linking through the C-5 position of the furan ring.[49-51] As a result, controlled LRP techniques are necessary to minimise FMA cross-linking. Initially, equimolar volumes of MMA and FMA were polymerised using a monomer:RAFT:AIBN ratio of 40:1:0.12. This was found to produce a gel-like polymer because of cross-linking through the furan ring. By increasing the AIBN content to 0.2 equivalents, a polymer powder was obtained following two precipitation steps. From the integration of the peaks at 3.58 ppm and 6.36-6.40 ppm in the ^{1}H NMR (Figure 4.15), the final ratio of FMA:MMA in the polymer can be determined. A MMA:FMA ratio of 1.02:1 is calculated suggesting a similar rate of polymerisation for both MMA and FMA. The RAFT diagnostic CTA signal at 3.25 ppm is observed and thus proves the polymerisation has been efficiently controlled under RAFT conditions. ^{1}H NMR also confirms successful polymerisation due to the loss of acrylate signals between 5.50 ppm and 6.25 ppm. Assignments are in good agreement with the literature.[49]
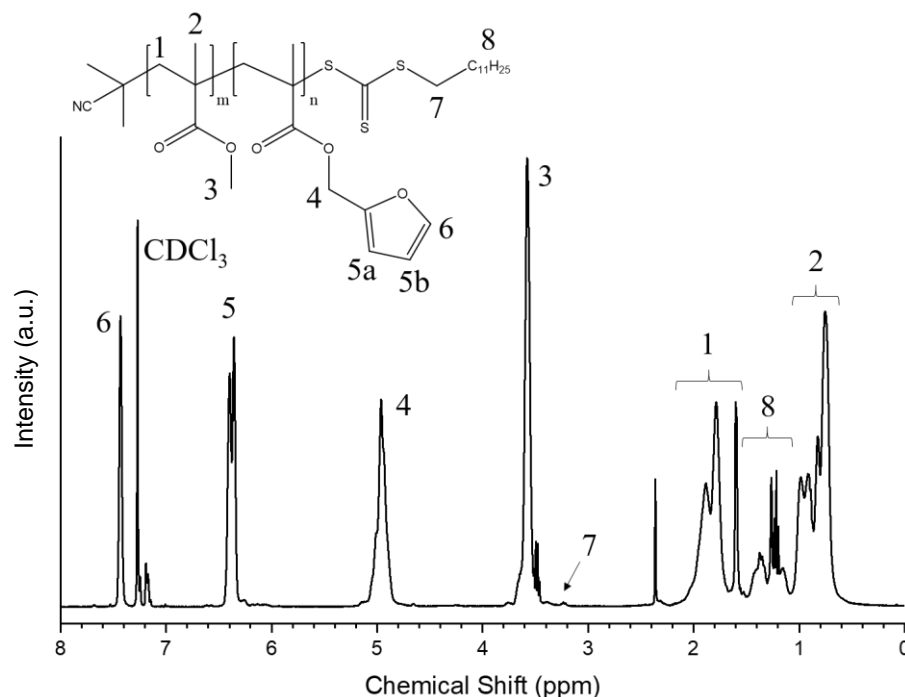
Figure 4.15 – ^{1}H NMR for the P(MMA-*co*-FMA) polymer where MMA:FMA = 1:1.

Kinetics were followed via ^{1}H NMR and GPC (Figure 4.16). Conversion of both MMA and FMA is followed by ^{1}H NMR. The ratio of the integration of diagnostic peaks allows the conversion at each time point to be calculated as a percentage. Figure 4.16 a)-c) shows the conversion of both MMA and FMA for polymers with a FMA content of 15, 10 and 5 molar%, respectively. Conversion is consistent with all mixtures recording >93% conversion within 9 hours. GPC is used to follow the evolution of the number average molecular weight (M_n) (Figure 4.16 d)). A plateau is seen after 7 hours for all three polymers. Interestingly, between 9 and 24 hours, the M_n increases. Critically, the reaction mixture is still active during this time and the CTA still transfers between polymer chains. As a result, there is potential for polymerisation to proceed through the C-5 position of the furan ring, as is observed during FRP. It is interesting to note that the largest increase in M_n is seen in the sample with the highest FMA content, trending downwards with FMA content. This strongly suggests that polymerisation occurs at the C-5 position but at a much slower rate than the acrylate groups. It is likely there is polymerisation at this position throughout the reaction. Ultimately, it can be confirmed through these kinetic studies that the optimal

reaction time for this polymerisation is 7 hours due to high conversion and minimal cross-linking.
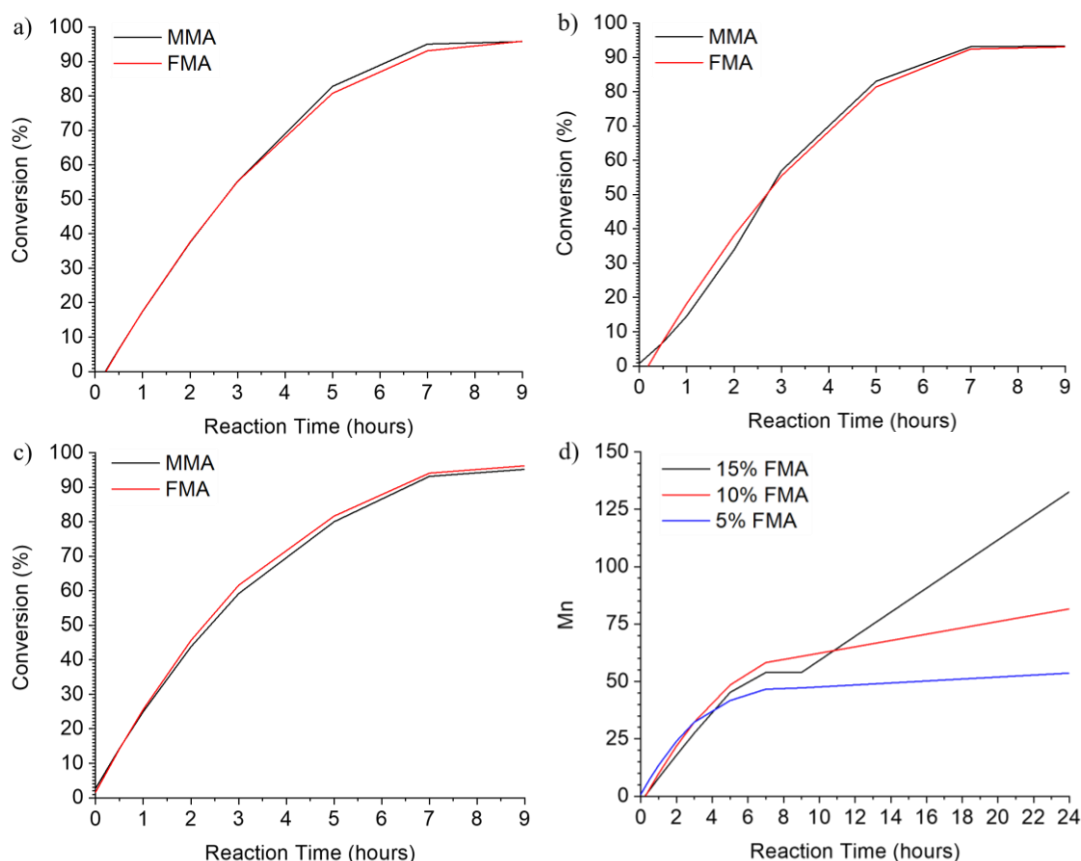
Figure 4.16 – Kinetics plots of MMA-FMA polymerisation via RAFT. Plots a)-c) are determined from the ^{1}H NMR and show the conversion of MMA and FMA over time for a) 15, b) 10 and c) 5 molar% FMA contents. Plot d) is calculated from GPC analysis showing the number average molecular weight (M_n) evolution over time.

TGA was also completed on the polymers to determine their thermal stability, see Figure 4.17. In all cases, residual solvent is vaporised up to 100 °C. The degradation of the CTA is observed at ≈220 °C as seen for the neat CTA in Figure 4.12, section 4.2.3. This degradation is then seen to transition into a significant mass loss between ≈350 °C and ≈450 °C, much like that observed for the RAFT-PMMA polymers.
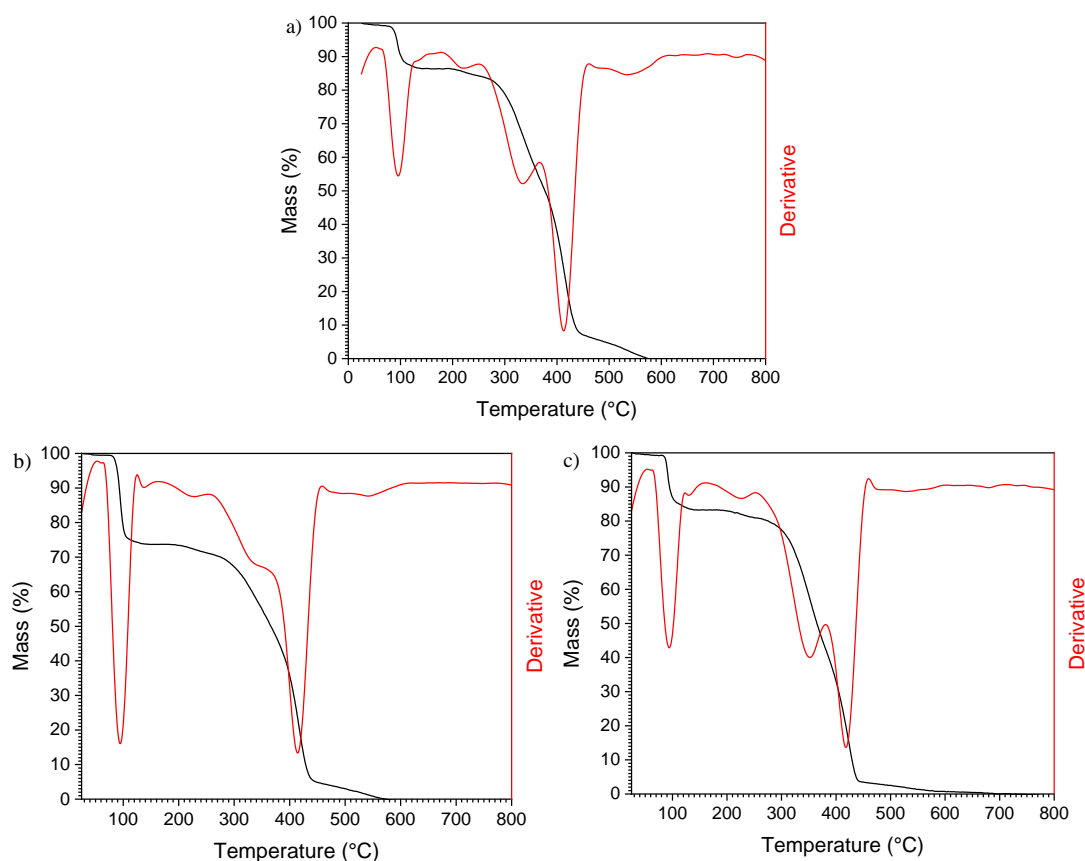
Figure 4.17 – TGA curves of P(MMA-*co*-FMA) polymers produced by RAFT where a) 15, b) 10 and c) 5 molar% FMA content.

The CTA agent was removed using the radical-induced reduction approach with EPHP. In this case, 1,1'-azobis(cyclohexanecarbonitrile) (ACHN) was used as the initiator over AIBN as per previous literature.[41] It was observed that the reaction mixture undergoes a colour change from yellow to white. The ^{1}H NMR also confirmed efficient removal of the CTA (Figure 4.18).
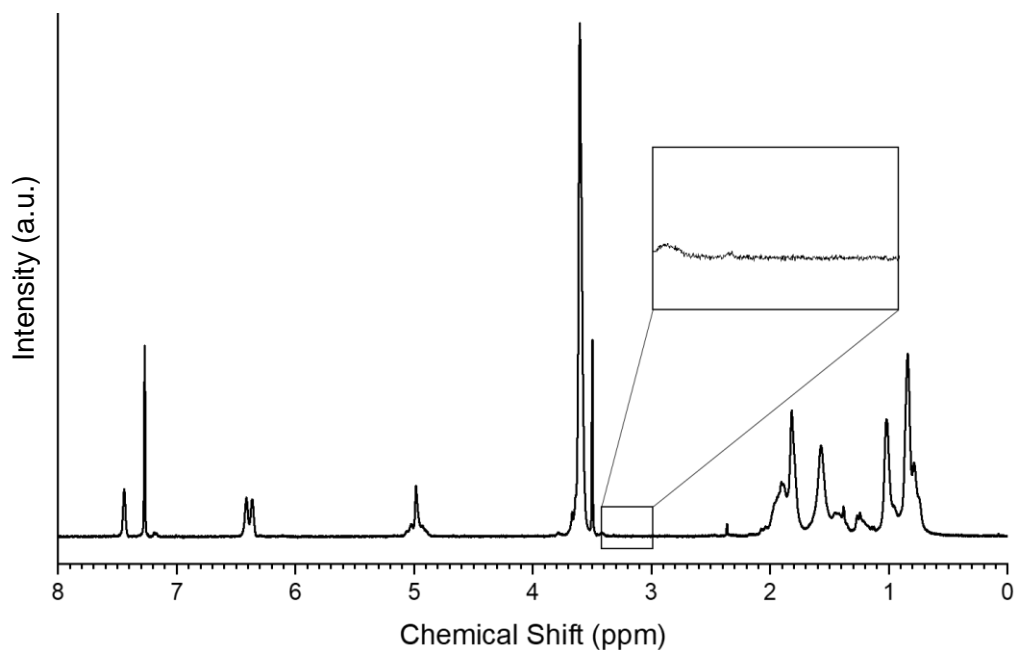
Figure 4.18 – Example ^{1}H NMR for the removal of the CTA from the P(MMA-*co*-FMA) polymer with EPHP. This spectrum was collected for the 15 molar% FMA polymer.

4.3.2 Synthesis of MiMA

Synthesis of a maleimide methacrylate (MiMA) was achieved following the method outlined by Furhmann *et al.*[17] It was found that a number of impurities were present and so column chromatography was used to purify the product before use in polymerisation reactions. The ^{1}H NMR of MiMA can be seen in Figure 4.19. Ethyl acetate (EtOAc) was used as a co-solvent in the column chromatography and is still present in the ^{1}H NMR spectrum. The peaks for the MiMA structure are observed and in agreement with the literature.[17] The stability of MiMA is unknown towards auto-polymerisation so heating the product under vacuum to remove EtOAc was considered an unnecessary risk.
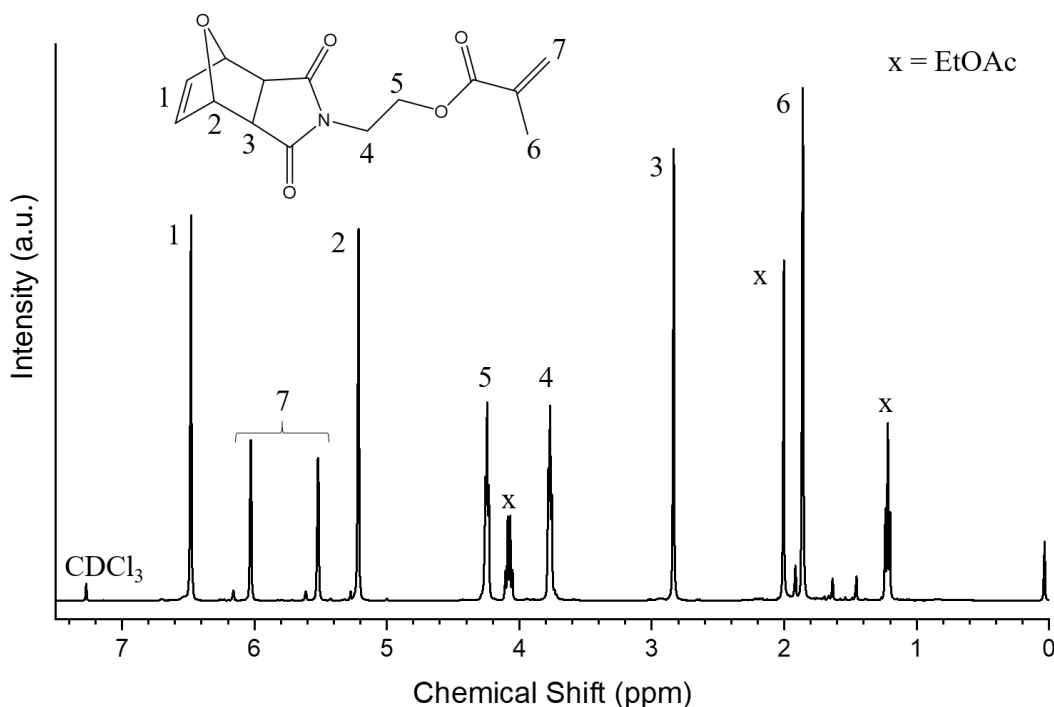
Figure 4.19 – ¹H NMR spectrum of MiMA following column chromatography.

4.3.3 RAFT polymerisation of MiMA

A constant ratio of monomer:RAFT:AIBN of 40:1:0.12 was used throughout to target similar molecular weight polymers to those previously reported in this chapter. The ratio of MMA to MiMA was altered to produce different levels of functionalisation of the PMMA product. Initial experiments at a 1:1 MMA:MiMA ratio showed incomplete polymerisation due to poor solubility of MiMA in toluene. Despite this, it was found that at lower MiMA content, complete polymerisation could be achieved. MiMA content of 15, 10 and 5 molar% were tested and polymerisation confirmed via ¹H NMR. An example ¹H NMR spectrum is shown in Figure 4.20 corresponding to the 15 molar% MiMA content. Through comparison of the integration of the peaks for the methyl group of MMA (position 3, Figure 4.20) and the vinyl protons of the MiMA group (position 8, Figure 4.20), the overall MiMA content in the polymer can be determined. The true percentage molar content of MiMA in the final polymers are equal to 13.4%, 7.7% and 4.1% for 15, 10 and 5 molar%, respectively.
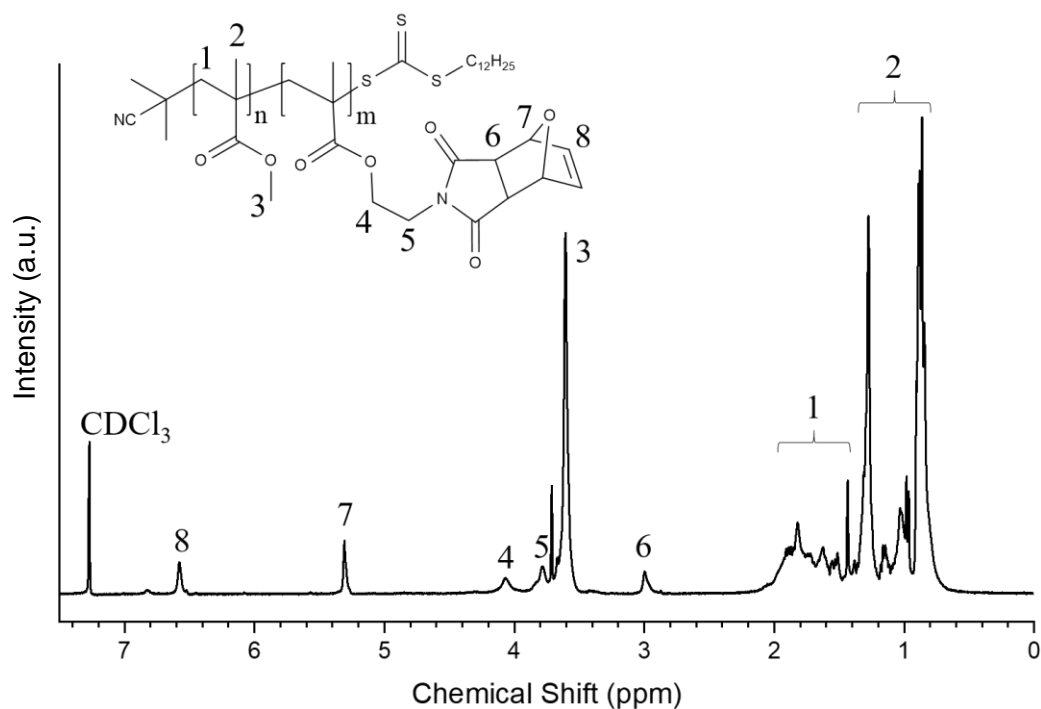
Figure 4.20 – ^{1}H NMR spectrum of the P(MiMA-*co*-MMA) precipitate with a 15 molar% MiMA.

GPC was used to follow the evolution of M_n for the 15 molar% MiMA polymer (Figure 4.21). As expected, the polymer peak develops over time towards high M_n whilst the monomer peak (retention time = 18.5 mins) reduces in intensity. A shoulder can be seen at slightly higher retention time compared to the main polymer signal. This effect is more prominent at lower reaction times. Figure 4.21 c) shows the de-convoluted plot with two distinct peaks present. Critically, the polydispersity of the polymer is 3.43, which is significantly higher than for RAFT polymers reported in the literature.[45]

It has been widely reported that the de-protected maleimide can undergo radical polymerisation however, this is commonly observed at high temperature.[52-55] The de-protected maleimide produces stable radicals due to the carbonyl species within the five-membered ring (Scheme 4.8). As a result, the polymerisation will occur through both the desired methacrylate group but also through the maleimide ring. Ultimately, this produces a branched polymer that explains the shoulder in the GPC and the high polydispersity observed. Alternative methods include the use of a lower

temperature thermal initiator, photo-induced initiation or different LRP techniques. Similarly it would also be necessary to remove the CTA using EPHP.
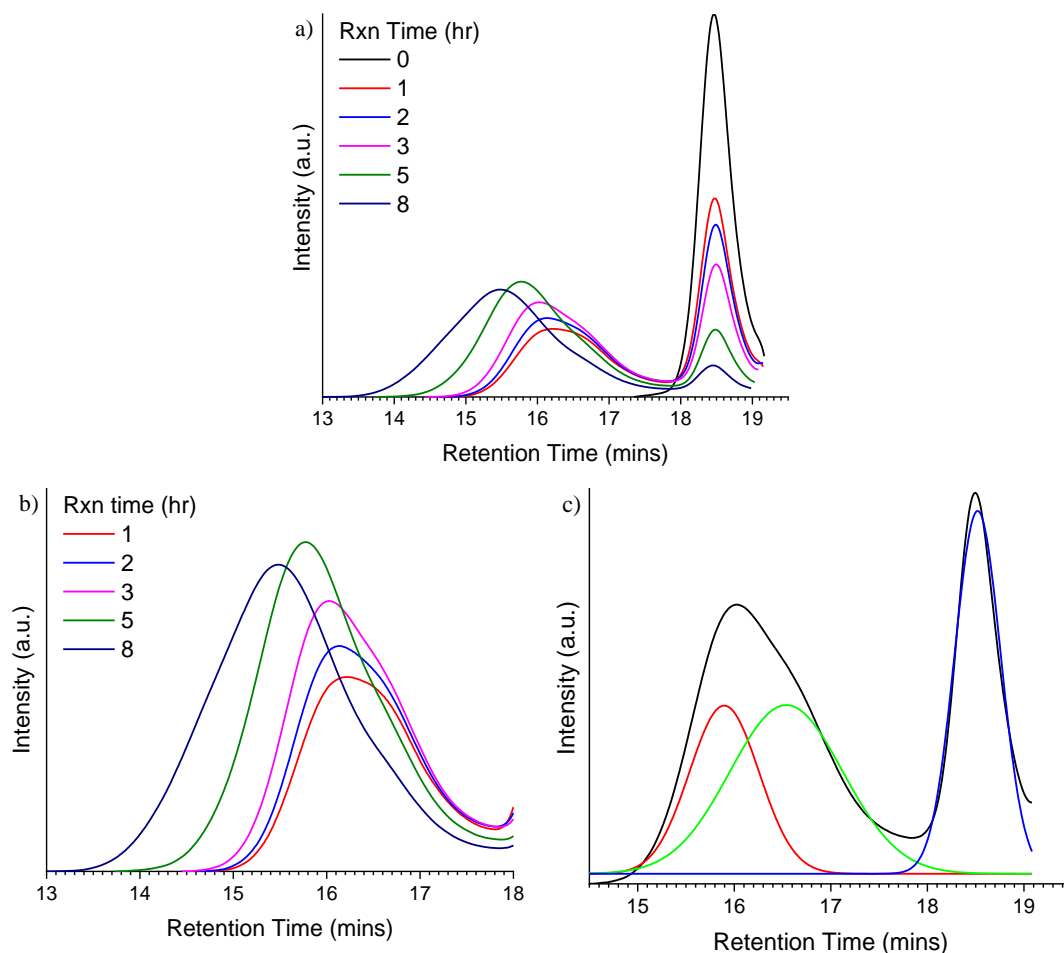
Figure 4.21 – Kinetic GPC plots of the RAFT polymerisation of MMA and MiMA at a 15 molar% MiMA content. a) Complete plot for each time point showing evolution of polymer and reduction of monomer signals, b) expanded view of the polymer signal at each time point and c) de-convoluted plot of the 3 hour time point showing the evolution of two peaks.

The thermal stability of each polymer was analysed using TGA, see Figure 4.22. As was observed with the P(MMA-*co*-FMA) polymers, residual solvent was trapped within the dried polymer samples and so was vaporised at ≈100 °C. A second degradation step is detected at 155 °C. This corresponds to the evaporation of furan

following cleavage due to the rDA reaction. The remaining polymer shows gradual degradation above 300 °C.
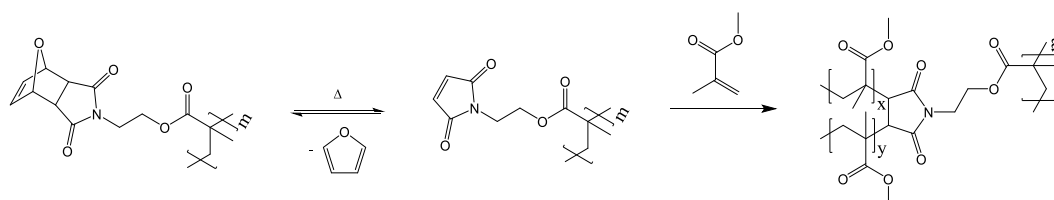
Scheme 4.8 – Branching mechanism observed from radical polymerisation of poly(maleimide methacrylate) at elevated temperature.
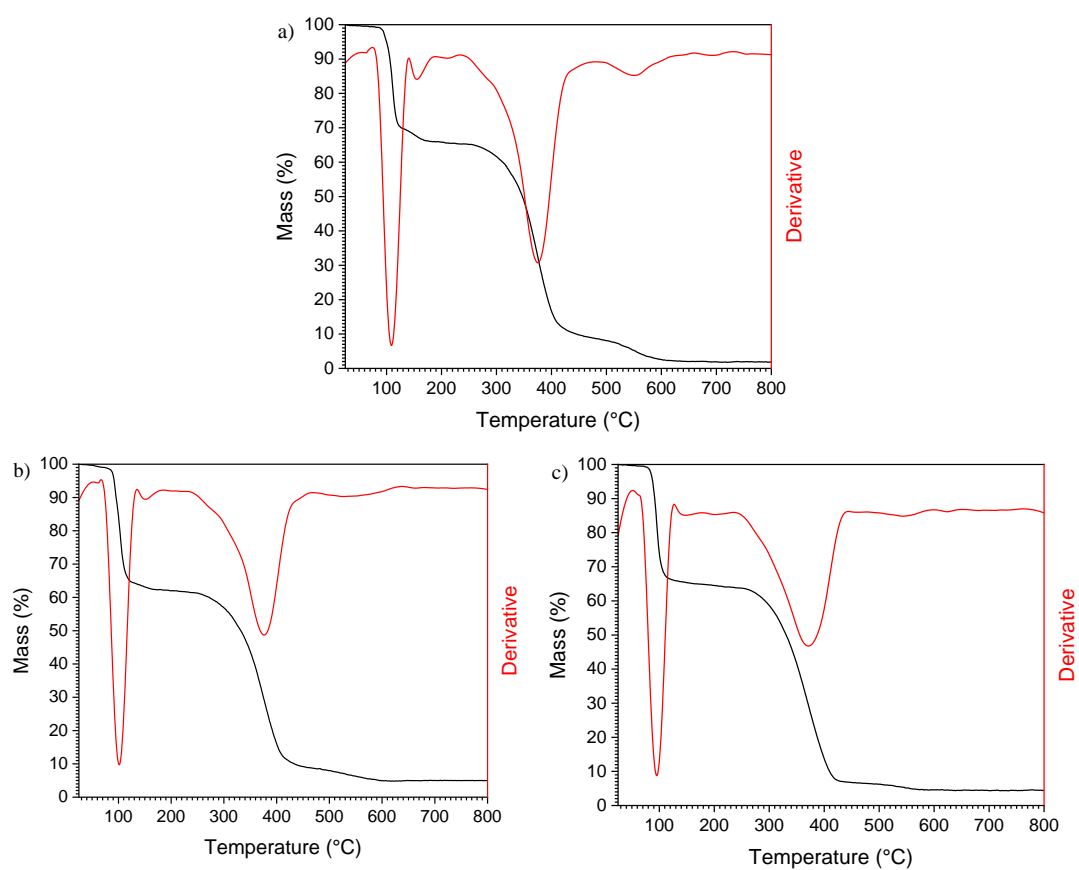
Figure 4.22 – TGA curves of P(MMA-*co*-MiMA) polymers produced by RAFT where a) 15, b) 10 and c) 5 molar% MiMA content.

In summary, the use of RAFT has facilitated production of P(MMA-*co*-FMA) polymers with good control and consistent kinetics. The use of a high temperature initiator resulted in branching of MiMA through the maleimide ring, removing potential DA cross-linking with FMA polymers. As a result, an alternative method is required whereby the MiMA can remain protected throughout polymerisation. This can be achieved using RAFT however, the polymerisation will need to be completed at close to RT. This would require photo-initiation and optimisation of the reaction as the rate of polymerisation would be different between RT and 70 °C. Ultimately, it was decided that Cu(0)-mediated LRP offered a simpler route towards polymerisation of MiMA at RT.

4.4 Cu(0)-mediated LRP of FMA and MiMA.

SET-LRP and Cu(0)-mediated LRP proceed by chemical initiation and as a result do not require stimuli such as heat or light. It has previously been reported that MMA can be polymerised at RT using dimethylsulfoxide (DMSO) as solvent.[11] In this work, a similar method was used to produce P(MMA-*co*-FMA) and P(MMA-*co*-MiMA). The Cu(0)-mediated process uses a ligand that complexes with Cu during polymerisation. In this work, *tris*[2-(dimethylamino)ethyl]amine (Me$_6$TREN) was used. The complexation of Me$_6$TREN to Cu allows for homolytic halide transfer from the initiator to produce an initiator radical that can then instigate polymerisation. Me$_6$TREN was kindly supplied by the Warwick chemistry department and was used as received. Traditionally, ethyl α-bromoisobutyrate (EBiB) or ethyl 2-bromopropionate (EBP) are used as initiators for acrylate monomers however, both have been shown to result in poor conversion and molecular weight control when employed in MMA polymerisation. Methyl α-bromophenylacetate (MBPA) is reported to yield good polydispersity of 1.10, even at high conversion (90%) for PMMA synthesis. For these reasons, MBPA was used in this work.

PMMA was synthesised as a control and the ^{1}H NMR spectra can be seen in (Figure 4.23). Comparison of the integrations for the peaks at 3.61 ppm and 3.76 ppm allows conversion to be calculated at 80.7%. Following precipitation, the remaining monomer peaks are lost and thus proves isolation of the pure PMMA polymer. GPC was used to confirm M_n = 9506 Da and dispersity = 1.13 (Figure 4.24 a)) representing excellent molecular weight control. TGA analysis also shows good thermal stability

of the final product showing an improvement over the RAFT technique (Figure 4.24 b)).
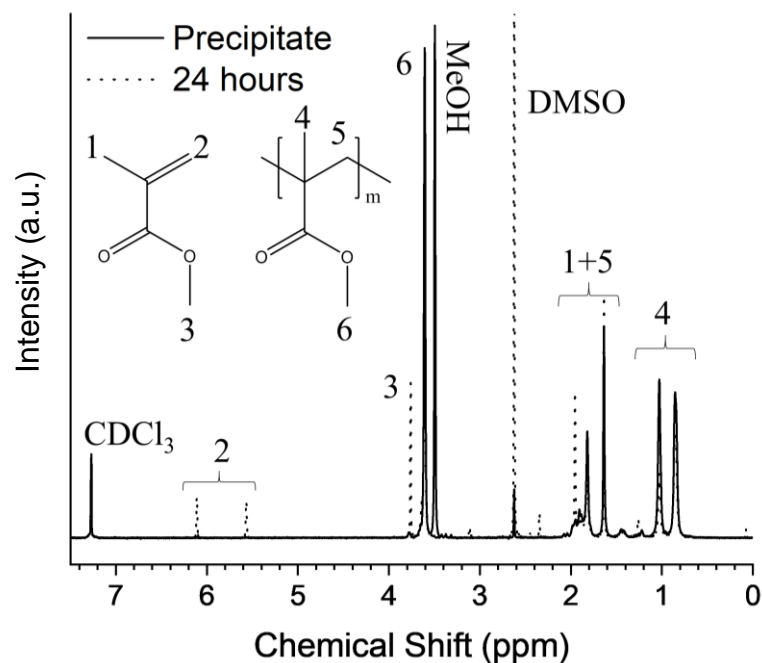
Figure 4.23 – ¹H NMR spectra of the polymerisation of MMA via Cu(0)-mediated LRP after 24 hours (dotted line) and following precipitation (solid line).
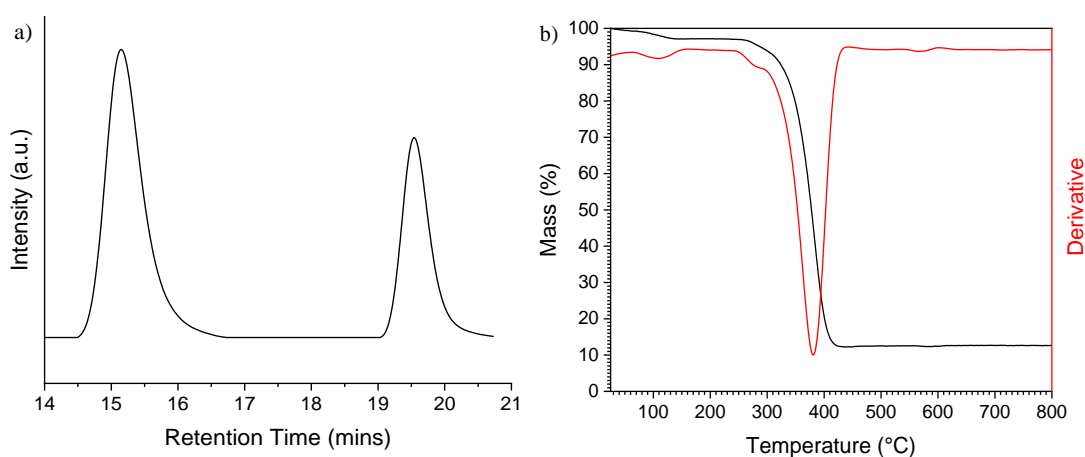
Figure 4.24 – a) GPC chromatogram of PMMA after 24 hours showing both the polymer (left) and monomer (right) peaks and b) TGA curve showing good thermal stability of PMMA.

4.4.1 Cu(0)-mediated LRP of FMA

Atom transfer radical polymerisation (ATRP) of FMA has been reported previously in the literature[56] and also for use in self-healing materials.[49] In this work, a slightly altered method was used to allow polymerisation at RT and FMA content of 10, 5 and 2 molar% were explored. Figure 4.25 shows the ^{1}H NMR for the polymer with 10 molar% FMA content showing conversion of MMA and FMA to be 89.1% and 63.3%, respectively. The peaks annotated were used for conversion calculations. In the case of 5 molar% and 2 molar% FMA, monomer peaks at 5.69 and 6.21 ppm were used due to the annotated peaks being low intensity. The conversion and final FMA content of all the polymers produced in this section can be seen in Table 4.3. Conversion of MMA is good in all cases however, conversion of FMA is low. This is most likely a result of the reaction conditions reducing the rate of polymerisation. Final ratios of FMA to MMA are close to the targeted contents.
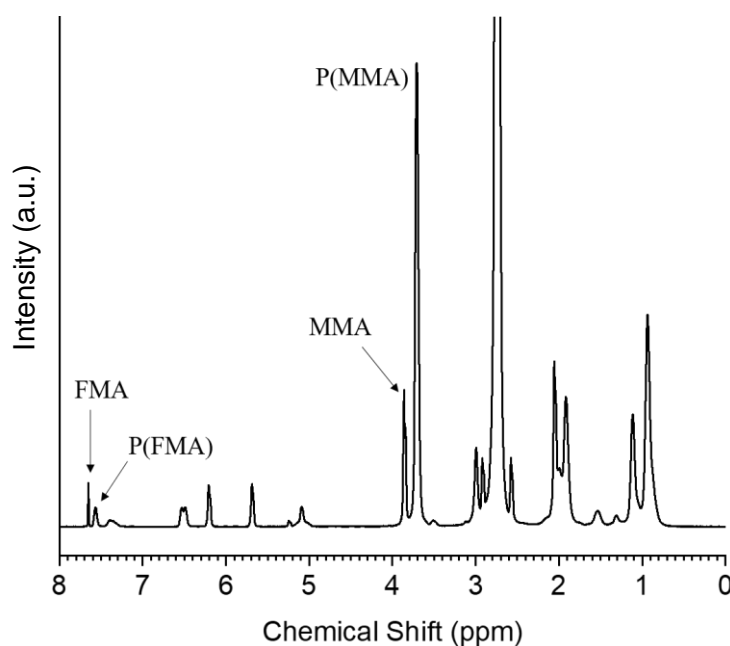
Figure 4.25 – ^{1}H NMR of the MMA-*co*-FMA polymerisation after 24 hours.

GPC analysis was used to confirm the M_n and dispersity of the polymers (Figure 4.26). It can be seen that the three polymers are of similar molecular weight

and a lower molecular weight than the PMMA control. This is likely due to the low conversion of FMA. Dispersity was determined to be 1.2-1.4 for all the polymers showing good control that is comparable to other ATRP examples of PMMA in the literature.[49]

Table 4.3 – MMA and FMA conversion and final FMA content calculated by ^{1}H NMR.

Polymer	MMA Conversion (%)	FMA Conversion (%)	FMA content (molar%)
10 molar% FMA	89.1	63.3	10.8
5 molar% FMA	85.3	62.9	3.8
2 molar% FMA	88.3	48.8	1.5
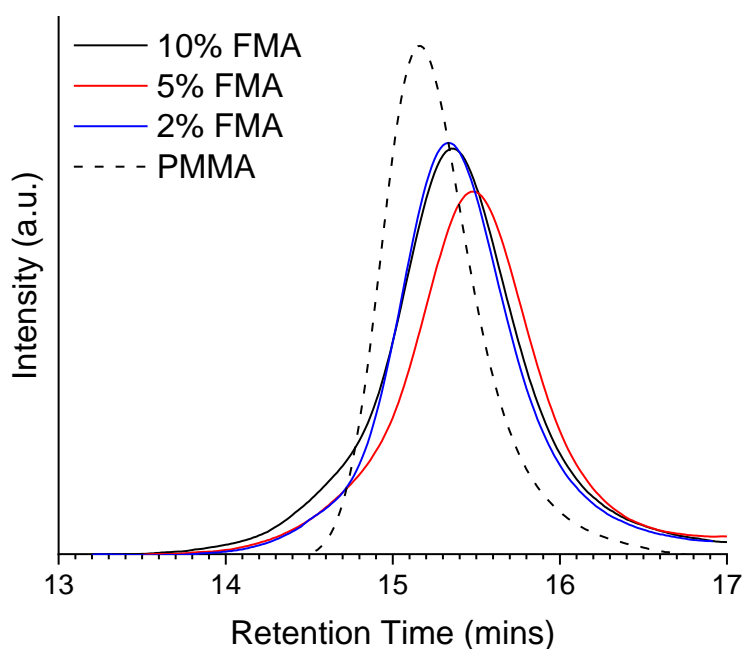
Figure 4.26 – GPC chromatogram for the P(MMA-*co*-FMA) polymers compared to neat PMMA.

4.4.2 Cu(0)-mediated LRP of MiMA

It was essential to confirm that Cu(0)-mediated LRP was successful in preventing MiMA branching. By keeping the reaction temperature low, the rDA reaction is significantly reduced to the point where the effect is negligible. The ^{1}H NMR of the polymer produced with 10 molar% MiMA is shown in Figure 4.27. The presence of broad MiMA peaks confirms polymerisation, and conversion is calculated using the peaks at 6.46 ppm and the contribution to the peak at 5.42 ppm. The percentage conversion of MMA, MiMA and the ratio of MMA to MiMA in the polymer are listed in Table 4.4, showing good conversion in all cases. The final MiMA content in the polymers are also close to the targeted values.
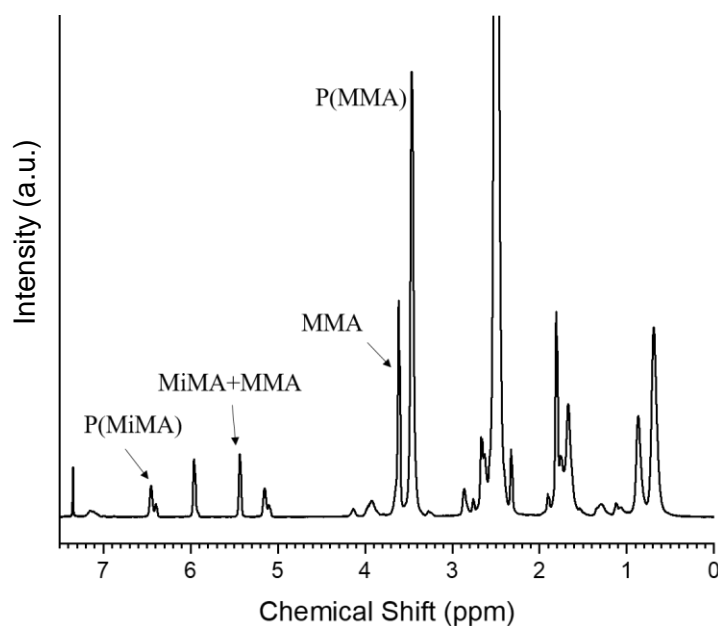
Figure 4.27 – ^{1}H NMR spectrum of P(MMA-*co*-MiMA) with 10 molar% MiMA content. The diagnostic peaks used for conversion calculations are annotated.

GPC analysis was used to confirm a reduction in branching (Figure 4.28). There is no clear shoulder-peak, suggesting branching was prevented. The polydispersity of 1.25-1.5 is vastly improved over the RAFT polymers produced in section 4.3.3. With reduced branching, it is expected the polydispersity would be reduced.

Table 4.4 – MMA and MiMA conversion and final MiMA content calculated by ^{1}H NMR.

Polymer	MMA Conversion (%)	MiMA Conversion (%)	MiMA Content (molar%)
10 molar% MiMA	82.6	81.6	9.3
5 molar% MiMA	91.9	88.7	5.8
2 molar% MiMA	90.4	96.6	1.8
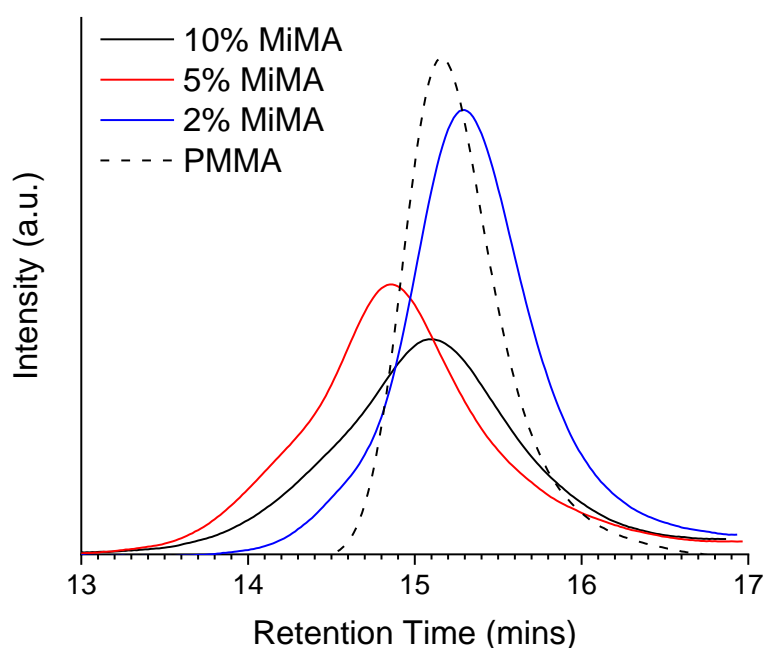
Figure 4.28 – GPC chromatograms for P(MMA-*co*-MiMA) compared to neat PMMA.

4.4.3 Thermal properties of P(MMA-*co*-FMA) and P(MMA-*co*-MiMA) polymers synthesised by Cu(0)-mediated LRP

Understanding the thermal properties of the polymers is essential so they can be processed effectively. Figure 4.29 shows the TGA curves for the P(MMA-*co*-FMA) and P(MMA-*co*-MiMA) polymers. For P(MMA-*co*-FMA), initial evaporation of residual methanol is observed below 100 °C. There is no further degradation detected until ≈300 °C. A similar curve is recorded for the P(MMA-*co*-MiMA) polymers but furan evaporation is observed at around 165 °C following a rDA reaction. A single

degradation peak is detected that centres at ≈350 °C. Finally, a degradation process is observed at ≈525 °C that is proportional to MiMA content. This transition is most likely due to the degradation of the free maleimide group.
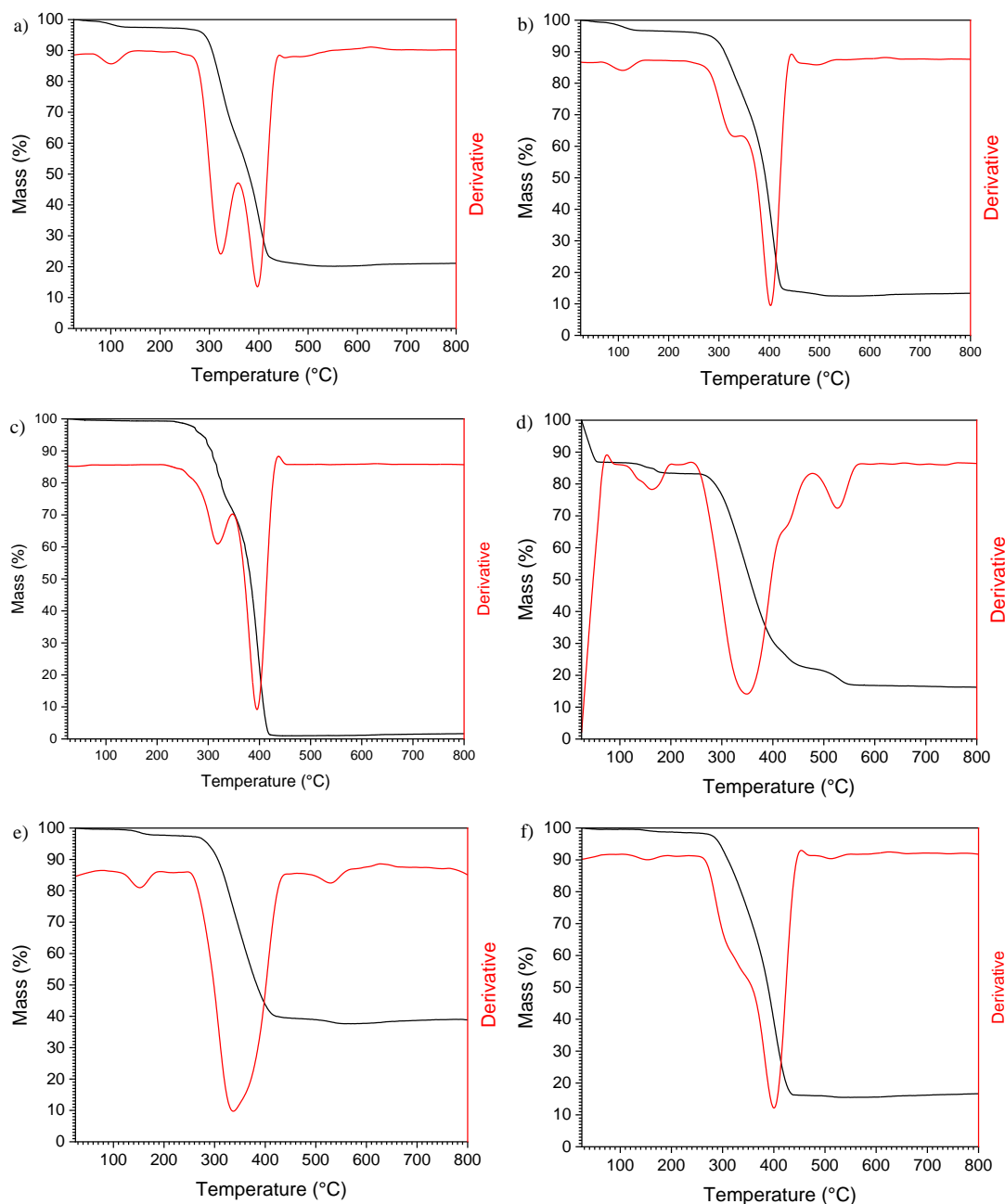
Figure 4.29 – TGA curves for P(MMA-*co*-FMA) produced via Cu(0)-mediated LRP where a) 10, b) 5 and c) 2 molar% FMA and P(MMA-*co*-MiMA) TGA curves where d) 10, e) 5 and f) 2 molar% MiMA.
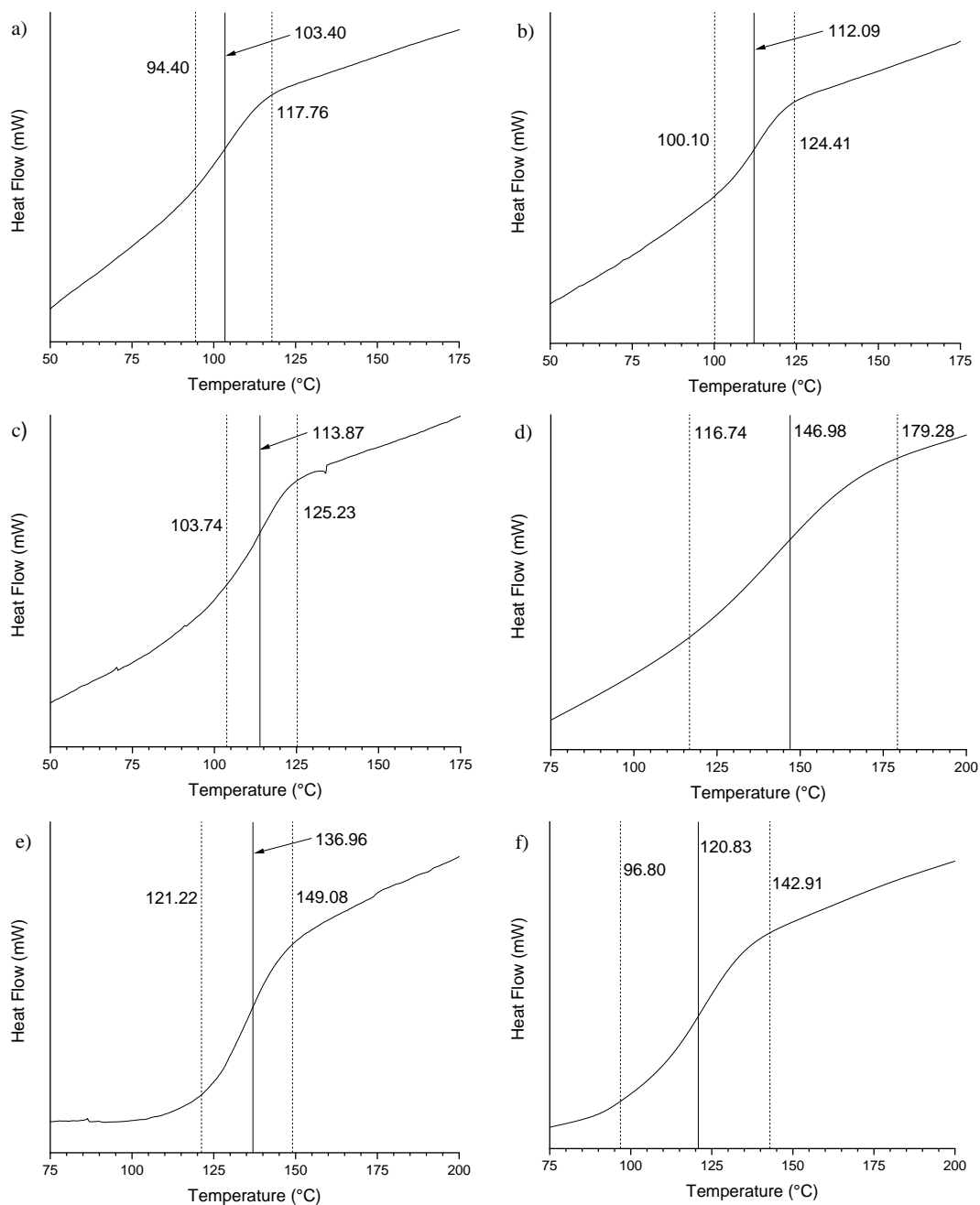
Figure 4.30 – DSC traces for the P(MMA-*co*-FMA) polymers produced by Cu(0)-mediated LRP where a) 10, b) 5 and c) 2 molar% FMA content and P(MMA-*co*-MiMA) polymers where d) 10, e) 5 and f) 2 molar% MiMA content. Onset, endset and midpoint temperatures are highlighted.

DSC was completed to observe the thermal transitions within the polymers, see Figure 4.30. No melting transitions (T_m) are observed, as expected for a PMMA based polymer. Instead, glass-transitions (T_g) are observed. In the P(MMA-*co*-FMA)

polymers, the T_g was found to centre at 103-114 °C. In the P(MMA-*co*-MiMA) polymers, the T_g is detected at 147, 137 and 121 °C for the 10 , 5 and 2 molar% MiMA content polymers, respectively. These values are higher than those for polymers containing FMA and the increase between MiMA content suggests it has a proportional effect on T_g.

4.5 Concluding remarks

In this chapter, significant progress was made towards producing self-healing PMMA-based polymers using MFC through multiple approaches. Initially, a pre-coupled cross-linking monomer was synthesised before polymerisation using FRP and RAFT techniques. It was found through initial hot-pressing tests that the melting properties of the polymer were inconsistent and was initially attributed to the poor polydispersity of the polymer. As a result, RAFT polymerisation was utilised to control the molecular weight. Polymerisation of the maleimide-based cross-linker proved unsuccessful due to poor solubility of the cross-linker. Individual polymers, each containing either the furfuryl or maleimide components of the cross-linker were designed and synthesised by RAFT. Polymerisation of the furfuryl polymer proved successful and follow-up reactions to cleave the CTA also proved effective. Despite this, the maleimide polymers produced branched networks due to the high temperature employed during the reaction.

Cu(0)-mediated LRP was employed as an alternative that facilitated RT polymerisation. This technique prevented the branching observed when using RAFT and yielded polymers of both furfuryl and maleimide functionality with good thermal stability. Conversion was found to be good after 24 hours and the MMA:FMA/MiMA ratio was found to be close to the target.

Despite the successes of the Cu(0)-mediated LRP reactions, the synthetic process was complex. As a result, numerous steps were employed to first synthesise and then polymerise MiMA. Critically, this reduces yield. In this case, the optimum yield from starting materials to monomer was approximately 54%. Equally, atom economy is very low with numerous protecting groups, RDRP reagents and solvents being used and then disposed of. Multiple toxic reagents are used throughout, greatly reducing the environmental friendliness of the process. To be used industrially, the use

of green solvents, reagents and methods are increasingly essential. With a focus towards industrial manufacture, it was decided that more efficient and green chemistries were necessary in further work.

4.6 References

1.   J. A. Syrett, G. Mantovani, W. R. S. Barton, D. Price and D. M. Haddleton, *Polymer Chemistry*, 2010, **1**, 102-106.

2.   S. R. White, N. R. Sottos, P. H. Geubelle, J. S. Moore, M. R. Kessler, S. R. Sriram, E. N. Brown and S. Viswanathan, *Nature*, 2001, **409**, 794-797.

3.   A. Feula, A. Pethybridge, I. Giannakopoulos, X. Tang, A. Chippindale, C. R. Siviour, C. P. Buckley, I. W. Hamley and W. Hayes, *Macromolecules*, 2015, **48**, 6132-6141.

4.   J. F. Patrick, N. R. Sottos and S. R. White, *Polymer*, 2012, **53**, 4231-4240.

5.   P. M. Lopez-Perez, R. M. P. da Silva, I. Strehin, P. H. J. Kouwer, S. C. G. Leeuwenburgh and P. B. Messersmith, *Macromolecules*, 2017, **50**, 8698-8706.

6.   J. Ling, M. Z. Rong and M. Q. Zhang, *Polymer*, 2012, **53**, 2691-2698.

7.   P. Hu, X. Han, W. D. Li, L. Li and Q. Shao, *International Journal of Adhesion and Adhesives*, 2013, **41**, 119-126.

8.   L. Xue, U. S. Agarwal and P. J. Lemstra, *Macromolecules*, 2002, **35**, 8650-8652.

9.   C. Li, J. Han, C. Y. Ryu and B. C. Benicewicz, *Macromolecules*, 2006, **39**, 3175-3183.

10.   J. Rosselgong, E. G. L. Williams, T. P. Le, F. Grusche, T. M. Hinton, M. Tizard, P. Gunatillake and S. H. Thang, *Macromolecules*, 2013, **46**, 9181-9188.

11.   G. R. Jones, R. Whitfield, A. Anastasaki, N. Risangud, A. Simula, D. J. Keddie and D. M. Haddleton, *Polymer Chemistry*, 2018, **9**, 2382-2388.

12.   M. J. Barthel, T. Rudolph, S. Crotty, F. H. Schacher and U. S. Schubert, *Journal of Polymer Science Part A: Polymer Chemistry*, 2012, **50**, 4958-4965.

13.   S. Chen, F. Wang, Y. Peng, T. Chen, Q. Wu and P. Sun, *Macromolecular Rapid Communications*, 2015, **36**, 1687-1692.

14.   A. Gandini, A. J. D. Silvestre and D. Coelho, *Journal of Polymer Science Part A: Polymer Chemistry*, 2010, **48**, 2053-2056.

15. X. Chen, F. Wudl, A. Mal, H. Shen and S. Nutt, *Macromolecules*, 2003, **36**, 1802-1807.

16. J. Kötteritzsch, S. Stumpf, S. Hoeppener, J. Vitz, M. D. Hager and U. S. Schubert, *Macromolecular Chemistry and Physics*, 2013, **214**, 1636-1649.

17. A. Fuhrmann, R. Gostl, R. Wendt, J. Kotteritzsch, M. D. Hager, U. S. Schubert, K. Brademann-Jock, A. F. Thunemann, U. Nochel, M. Behl and S. Hecht, *Nature Communications*, 2016, **7**, 13623-13630.

18. F. Gao, S. R. Schricker, Y. Tong and B. M. Culbertson, *Journal of Macromolecular Science, Part A*, 2002, **39**, 267-286.

19. L. E. Coleman, J. F. Bork and H. Dunn, *Journal of Organic Chemistry*, 1959, **24**, 135-136.

20. U. Schmidt, S. Zschoche and C. Werner, *Journal of Applied Polymer Science*, 2003, **87**, 1255-1266.

21. Y. Arai, M. Matsui, T. Koizumi and M. Shiro, *Journal of Organic Chemistry*, 1991, **56**, 1983-1985.

22. N. R. Babij, E. O. McCusker, G. T. Whiteker, B. Canturk, N. Choy, L. C. Creemer, C. V. D. Amicis, N. M. Hewlett, P. L. Johnson, J. A. Knobelsdorf, F. Li, B. A. Lorsbach, B. M. Nugent, S. J. Ryan, M. R. Smith and Q. Yang, *Organic Process Research & Development*, 2016, **20**, 661-667.

23. A. C. Dona, M. Kyriakides, F. Scott, E. A. Shephard, D. Varshavi, K. Veselkov and J. R. Everett, *Computational and Structural Biotechnology Journal*, 2016, **14**, 135-153.

24. K. Pervushin, *Journal of Biomolecular NMR*, 2001, **20**, 275-285.

25. J. Warneke, Z. Wang, M. Zeller, D. Leibfritz, M. Plaumann and V. A. Azov, *Tetrahedron*, 2014, **70**, 6515-6521.

26. F. H. A. Rummens, J. S. Lomas, B. Tiffon, C. Coupry and N. Lumbroso-Bader, *Organic Magnetic Resonance*, 1982, **19**, 35-38.

27. P. Gałka, J. Kowalonek and H. Kaczmarek, *Journal of Thermal Analysis and Calorimetry*, 2013, **115**, 1387-1394.

28. C. E. Porter and F. D. Blum, *Macromolecules*, 2000, **33**, 7016-7020.

29. C. Cai, Y. Zhang, X. Zou, R. Zhang, X. Wang, Q. Wu and P. Sun, *RSC Advances*, 2017, **7**, 46336-46343.

30. J. Zhao, R. Xu, G. Luo, J. Wu and H. Xia, *Journal of Materials Chemistry B*, 2016, **4**, 982-989.

31. N. Bai, G. P. Simon and K. Saito, *New Journal of Chemistry*, 2015, **39**, 3497-3506.

32. A. A. Kavitha and N. K. Singha, *Macromolecules*, 2010, **43**, 3193-3205.

33. H. Inoue, A. Matsumoto, K. Matsukawa, A. Ueda and S. Nagai, *Journal of Applied Polymer Science*, 1990, **41**, 1815-1829.

34. J.-H. Wang, T.-H. Young, D.-J. Lin, M.-K. Sun, H.-S. Huag and L.-P. Cheng, *Macromolecular Materials and Engineering*, 2006, **291**, 661-669.

35. D. J. Keddie, *Chemical Society Reviews*, 2014, **43**, 496-505.

36. A. B. Lowe and C. L. McCormick, *Progress in Polymer Science*, 2007, **32**, 283-351.

37. P. B. Zetterlund, Y. Kagawa and M. Okubo, *Chemical Reviews*, 2008, **108**, 3747-3794.

38. D. J. Keddie, G. Moad, E. Rizzardo and S. H. Thang, *Macromolecules*, 2012, **45**, 5321-5342.

39. Y. K. Chong, J. Kristina, T. P. T. Le, G. Moad, A. Postma, E. Rizzardo and S. H. Thang, *Macromolecules*, 2003, **36**, 2256-2272.

40. E. Bicciocchi, Y. K. Chong, L. Giorgini, G. Moad, E. Rizzardo and S. H. Thang, *Macromolecular Chemistry and Physics*, 2010, **211**, 529-538.

41. Y. K. Chong, G. Moad, E. Rizzardo and S. H. Thang, *Macromolecules*, 2007, **40**, 4446-4455.

42. J. Gupta, D. J. Keddie, C. Wan, D. M. Haddleton and T. McNally, *Polymer Chemistry*, 2016, **7**, 3884-3896.

43. B. Chong, G. Moad, E. Rizzardo, M. A. Skidmore and S. H. Thang, *Australian Journal of Chemistry*, 2006, **59**, 755-762.

44. S. Perrier, P. Takolpuckdee and C. A. Mars, *Macromolecules*, 2005, **38**, 2033-2036.

45. Y. K. Chong, G. Moad, E. Rizzardo, M. A. Skidmore and S. H. Thang, *Macromolecules*, 2007, **40**, 9262-9271.

46. N. B. Pramanik, G. B. Nando and N. K. Singha, *Polymer*, 2015, **69**, 349-356.

47. N. B. Pramanik and N. K. Singha, *RSC Advances*, 2015, **5**, 94321-94327.

48. C. M. Q. Le, H. H. P. Thi, X. T. Cao, G.-D. Kim, C.-W. Oh and K. T. Lim, *Journal of Polymer Science Part A: Polymer Chemistry*, 2016, **54**, 3741-3750.

49. A. A. Kavitha and N. K. Singha, *Macromolecular Chemistry and Physics*, 2007, **208**, 2569-2577.

50. J. Lange, J. Rieumont, N. Davidenko and R. Sastre, *Polymer*, 1998, **39**, 2537-2542.

51. E. Goiti, M. B. Huglin and J. M. Rego, *Polymer*, 2001, **42**, 10187-10193.

52. R. C. P. Cubbon, *Polymer*, 1965, **6**, 419-426.

53. G. D. Lyle, J. S. Senger, D. H. Chen, S. Kilic, S. D. Wu, D. K. Mohanty and J. E. McGrath, *Polymer*, 1989, **30**, 978-985.

54. C. D. Vlad and C. Hulubei, *High Performance Polymers*, 2002, **14**, 31-40.

55. T. H. Kim, *Journal of Applied Polymer Science*, 2004, **94**, 2117-2122.

56. A. A. Kavitha, A. Choudhury and N. K. Singha, *Macromolecular Symposia*, 2006, **240**, 232-237.

5. Nacre-like Water-soluble Polyurethane/GO Nanocomposite Films Prepared by Solution Casting

5.1 Introduction

Nacre-mimetic materials have been shown to display remarkable mechanical properties (see Chapter 2) and thus it was proposed that through development of suitable similar materials of this nature, the improvement in mechanical properties would aid in preventing scratch formation and propagation.

Nacre-mimetic materials have shown high potential for application across a number of industries. It was important that the processes employed in the manufacture of these nacre-mimetic materials be kept as 'green' and sustainable as possible. Production of materials on large-scale are under greater scrutiny to meet increasingly strict ethical and environmental standards. Therefore, the intention with this aspect of the project was to utilise environmentally friendly and benign reagents and solvents, where possible. GO is well dispersed in water and provides excellent mechanical properties for use in nacre-mimetic materials.[1, 2] Polyurethanes (PU) are typically insoluble in water but can be functionalised with ionic groups to encourage solubility in aqueous media.[3] Alternatively, micellar dispersions of PU can be produced.[4] The environmental impact of PUs is very low, with most examples being non-toxic, non-flammable and they do not pollute air or water.[5]

The ultimate strength of nacre-mimetic materials originates from the intrinsic mechanical properties of the nanoplatelet component and the interfacial interactions between the two components. Localised stresses are dissipated throughout the entire material and different failure mechanisms can be observed. GO has both sp^3 and sp^2 carbon domains and thus has a multitude of vinylic carbon bonds. These can react through radical processes, much like the polymerisations described in Chapter 4. By introducing a covalently cross-linked network, the interfacial interactions will be much stronger than non-covalent interactions alone. Water-soluble (or waterborne) PUs (wsPUs) were investigated in this work and were chosen due to their UV activity. Acrylate pendant groups undergo cross-linking via the use of a UV initiator and a radical polymerisation. When incorporated into a nacre-mimetic material with GO, it

was anticipated that the same cross-linking was possible, through the sp^2 carbon bonds of GO to create a covalent network throughout the entire material.

Initially, solution casting was employed to provide 'proof-of-concept' through comparison of GO-wsPU freestanding films with those reported in the literature. Previous reports of solution cast samples are wide however, the precise methodology for sample preparation is often omitted[6-8] leaving researchers new to the field the challenge of developing an effective method. This chapter also discusses this process.

In this chapter, the characterisation of GO using techniques including FTIR, Raman, XPS, TGA and SEM is given. The wsPU (UV2282) is then characterised to determine the chemical structure and particle size, as it is latex based. Development of a suitable solvent casting method is discussed including the utilisation of a number of substrate materials. The production of nacre-like films using GO and wsPU is outlined and their mechanical properties determined from tensile testing. The introduction of a sonication step, and then the selection of base are assessed and the role both play, if any, on the mechanical properties observed.

5.2 Characterisation of GO

GO was purchased in a paste form and contains 25 wt% GO, 75 wt% water and residual HCl from the GO synthesis. The GO was characterised through TGA whilst still in paste form and freeze-dried before characterisation through FTIR, Raman, XPS and SEM.

The FTIR and Raman spectra of the GO paste are shown in Figure 5.1. The FTIR spectrum reveals the peaks expected for an oxygenated graphitic structure.[9] A hydroxyl stretch is observed at 3360 cm^{-1}, with other oxygenated vibrations observed at 2652 cm^{-1}, 1717 cm^{-1} and 1341-1045 cm^{-1}. These are assigned to an O-H carboxylic stretch, C=O stretches and epoxy C-O stretches, respectively. The graphitic nature of the structure is confirmed by a peak at 1617 cm^{-1} that corresponds to skeletal aromatic vibrations of the C=C bond. Finally, a band associated with C-H stretching is observed at 2800 cm^{-1}.

The Raman spectra of GO displays two main peaks at approximately 1355 cm^{-1} (D band), and close to 1600 cm^{-1} (G band). The D band corresponds to an in-plane

vibration of sp^2 carbons in close proximity to a sp^3 region. The G band is a primary in-plane vibration assigned to pristine sp^2 domains.[10] In this case, the D band is detected at 1358 cm^{-1} and the G band at 1600 cm^{-1}. Comparison of the intensity of these peaks (I_D/I_G) provides information on the volume of defects on the GO surface and I_D/I_G = 0.848 for this GO material. Two further peaks are observed at 2684 cm^{-1} and 2930 cm^{-1} that are assigned to second order Raman features known as the 2D or G′ and D+D′ bands, respectively.[11]
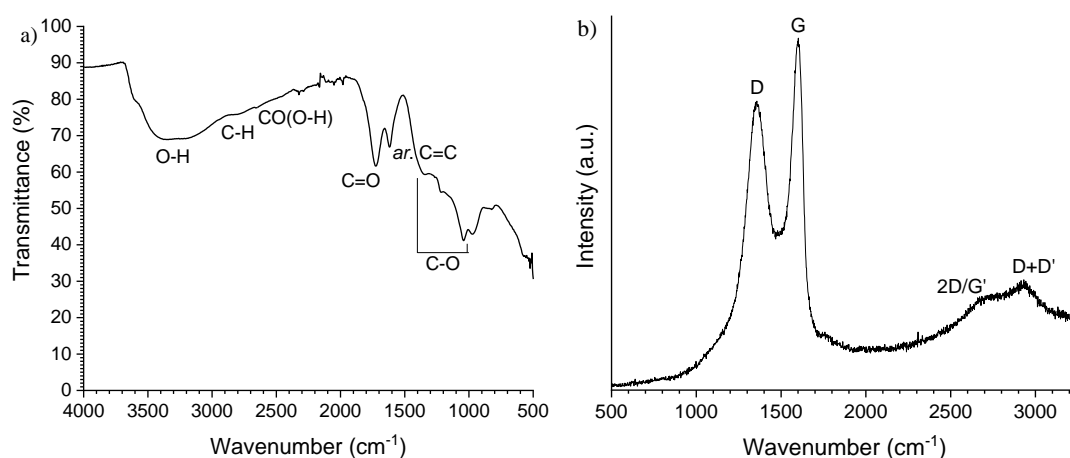
Figure 5.1 – Vibrational spectra, a) FTIR and b) Raman of GO.

XPS was used to analyse the elemental composition of the GO and the bonding environments within the structure. Table 5.1 confirms the bulk content of the GO is carbon and oxygen as would be expected. Residual heteroatoms are also detected and are most likely present due to the method of GO synthesis used by the supplier. The survey and de-convoluted peak data (Figure 5.2) show intense C_{1s} and O_{1s} peaks with multiple carbon and oxygen environments. The C_{1s} peak confirms the graphene-like structure with the presence of graphene and π-π* shake-up signals. Oxygenated surface groups are also detected further confirming the highly oxidised graphene structure.

Table 5.1 – Elemental composition of freeze-dried GO paste determined by XPS.

Element	C	O	N	S	Si	Cl
% Content	63.32	34.28	0.42	0.88	0.77	0.33
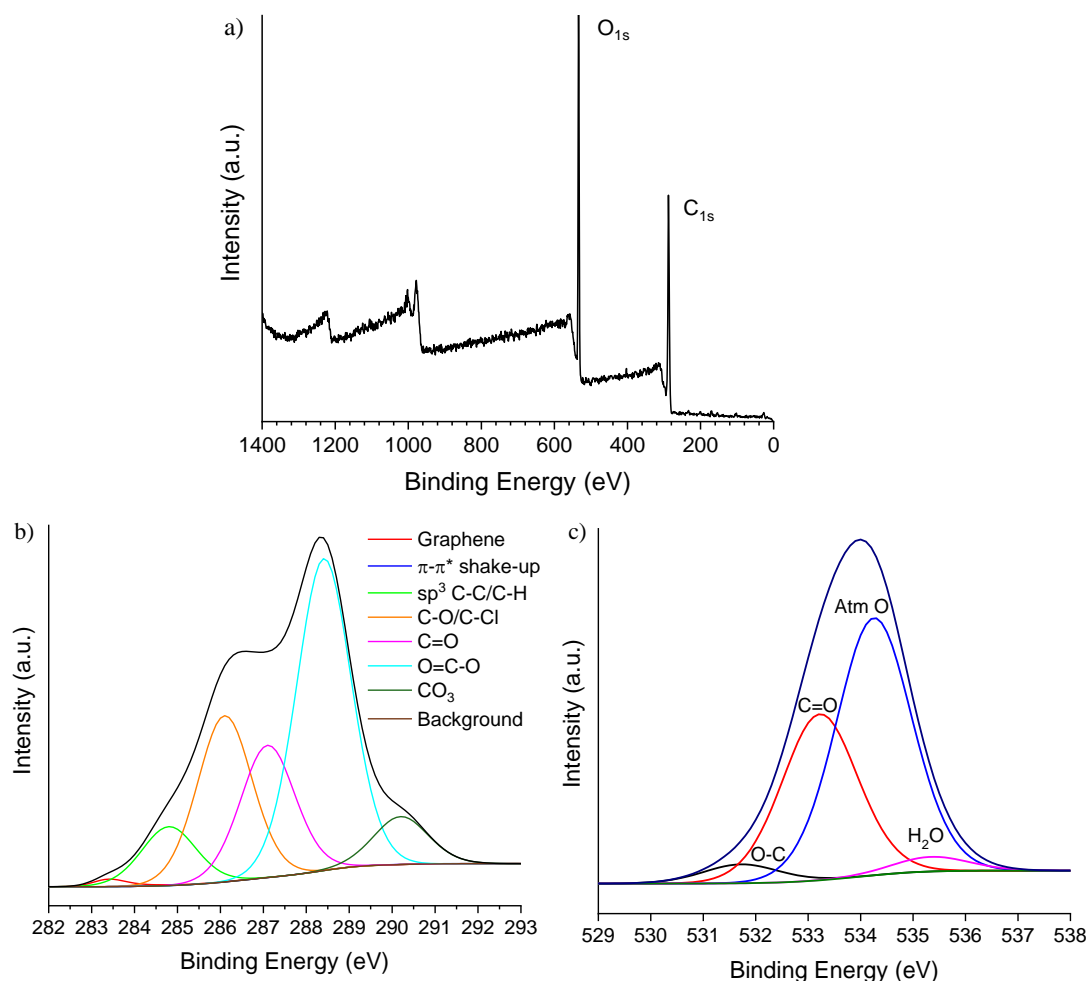
Figure 5.2 – XPS spectra for freeze-dried GO paste where a) XPS survey, b) de-convoluted C_{1s} peak and c) de-convoluted O_{1s} peak.

The thermal properties of the GO were analysed by TGA (Figure 5.3). A significant mass loss is observed below 100 °C that is assigned to the loss of water through evaporation. The loss of 63% aligns somewhat closely with the water content in the GO paste, as reported in the supplier data sheet. A further mass loss is detected at 207 °C that is symptomatic of thermal degradation of the oxygenated surface

groups, ultimately reducing the GO to a 'graphene-like' structure.[12] The remaining material is thermally stable to 800 °C and thus shows no further degradation.
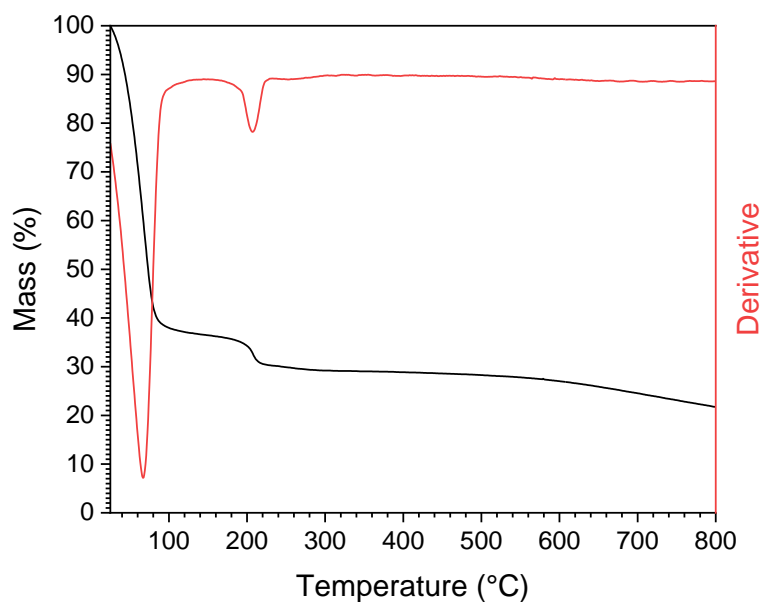
Figure 5.3 – TGA curves for the GO paste showing percentage mass loss as a function of temperature and the derivative of the mass loss curve.
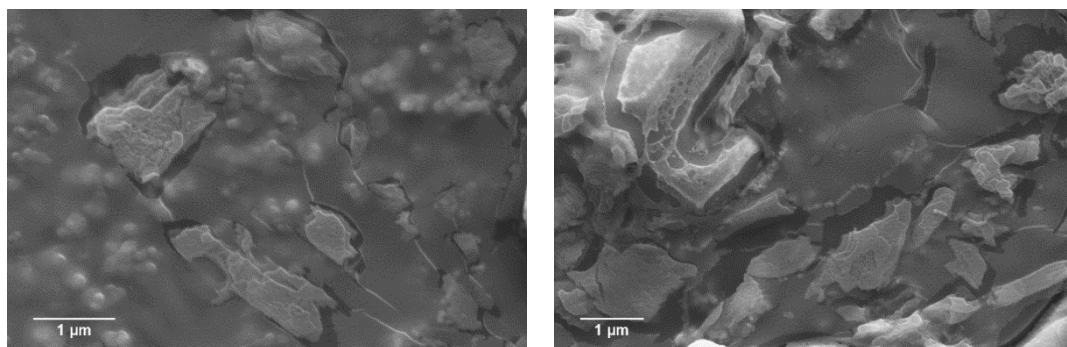
Figure 5.4 – SEM images of freeze-dried GO diluted to 0.001 wt% in water and allowed to dry at RT.

GO platelet size has been shown to have an impact on the properties displayed by nacre-mimetic materials.[6] The lateral dimensions of the GO platelets were

characterised by SEM and images of the GO are shown in Figure 5.4. Isolated sheets were measured and the average lateral dimension was found to be 1.32 ± 0.41 µm, from measurements of 10 platelets.

5.3 Characterisation of wsPU

The wsPU polymer was freeze-dried before analysis using FTIR, ^{1}H NMR, ^{13}C NMR and [1]H-^{1}H Correlated Spectroscopy (COSY) NMR. Thermal properties were analysed with TGA and DSC and nanoindentation measurements completed to follow the effect of UV curing on mechanical properties. Finally, the water-based emulsion was analysed using dynamic light scattering (DLS) to determine the particle size of the wsPU micelles.

5.3.1 Chemical characterisation of wsPU

Assignments of peaks in the FTIR spectrum are given in Table 5.2 and Figure 5.5. Notably, there is no peak centring at 3500 cm^{-1} confirming there are no hydroxyl groups present in the structure. Bands at 3356 cm^{-1} and 1634 cm^{-1} correspond to N-H bonding of the repeat unit structure with the C-N bond observed at 1238 cm^{-1}. Both alkane and alkene C-H stretching signals are detected in the range 2869-2935 cm^{-1}. A carbonyl stretch is detected at 1721 cm^{-1} and C-O bonding observed at 1183 cm^{-1}, present in both acrylate groups and the PU repeat unit. An ether group is also observed at 1107 cm^{-1} that, in collaboration with other characterisation techniques, was confirmed to be part of a poly(ethylene glycol) (PEG) chain.

Table 5.2 – FTIR peak assignments for wsPU.

Peak	Wavenumber (cm^{-1})	Assignment	Mode
1	3356	N-H	stretch
2	2935	Alkene C-H	stretch
3	2869	Alkane C-H	stretch
4	1721	C=O	stretch
5	1634	N-H	bend
6	1238	Amine C-N	stretch
7	1183	Ester C-O	stretch
8	1107	Ether C-O	stretch
9	806	C-H	bend
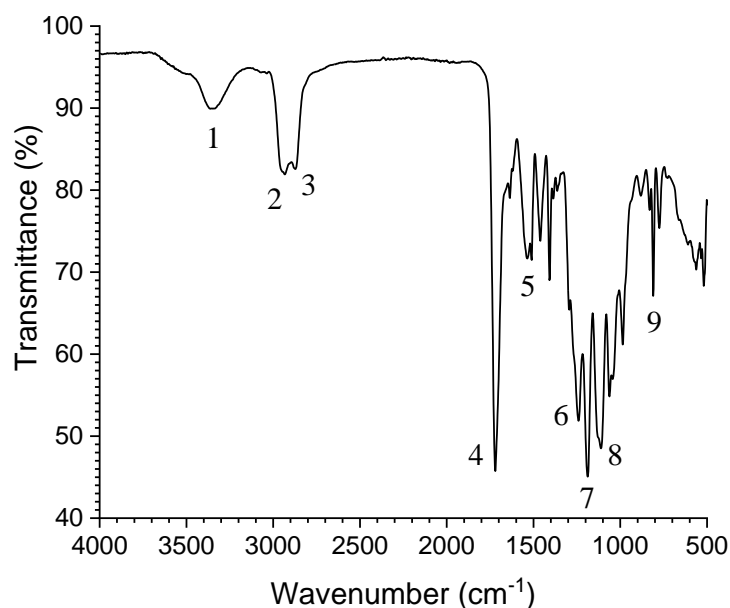
Figure 5.5 – FTIR spectrum of wsPU. Key peaks are numbered and assigned in Table 5.2.

^{1}H NMR enabled the number of acrylate groups per repeat unit to be calculated. The wsPU spectrum is shown in Figure 5.6. Protons '***b***', '***c***' and '***d***' can be assigned to the acrylate and are considered 'non-equivalent' due to the double bond locking them in position. As a result, each proton is in an individual environment and have different chemical shifts. Proton '***a***' is assigned to the PU linkage due to the strong de-shielding effect of the carbonyl group at the β-position and hydrogen bonding, which is known to cause downfield shifting.[13] It is believed these peaks are formed as two separate environments due to the presence of different functional groups at the R_1 position. Critically, the integration of these peaks allows the ratio of acrylate:PU to be calculated. When integration of proton '***a***' = 1, the combined integration of protons '***b***', '***c***' and '***d***' = 3.35. As there are 3 protons in each acrylate group, the PU:acrylate ratio can be calculated as 1:1.12. wsPU is end-capped with acrylate groups, so it can be assumed that the terminal acrylate groups contribute 0.12 to the total integration. The remaining contribution is due to acrylate side groups within the polymer repeat unit and therefore, the ratio of PU:acrylate is found to be 1:1.
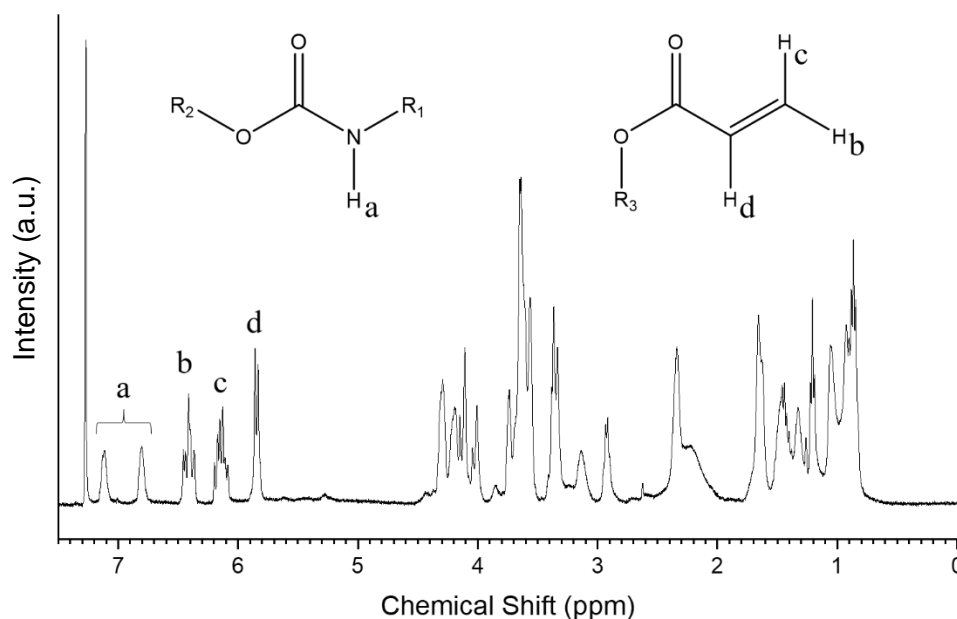
Figure 5.6 – ^{1}H NMR of wsPU with key peaks assigned for determination of acrylate:PU ratio.

The ^{13}C NMR spectrum confirms the presence of a number of functional groups (Figure 5.7). Supported by the 2D COSY experiments, the precise structure of the wsPU can be established. An attached proton test (APT) pulse sequence was used to separate quarternary (C) and methylene (CH_2) signals from the methine (CH) and methyl (CH_3) signals. The *d*-chloroform solvent contains a quarternary carbon and therefore is commonly observed as a negative peak.[14] In this work, a different pulse sequence was employed causing peak inversion. The C=O environment has not been detected, possibly due to the polarising sequence removing this peak as is observed in distortionless enhancement by polarization transfer (DEPT) experiments. Peaks at 131 ppm and 128 ppm are assigned to the vinylic carbons of the acrylate groups and the peaks between 71 ppm and 69 ppm are assigned to the CH_2 of the PEG chain. A range of chemical shifts are detected because of the varying proximity to ether and PU linkages producing numerous different environments. At 63 ppm, a linking carbon between the pendant acrylate group and the PEG chain is detected. The peak at 45 ppm is assigned to the carbon of the PEG chain that is bonded to the acrylate linking carbon. Due to the positive signal, this environment is quaternary and therefore must be bonded to the ethyl group detected via the peaks at 24 ppm and 8-9 ppm. Finally,

the peak at 34 ppm is assigned to the CH_2 immediately adjacent to the nitrogen of the PU linkage due to the slight de-shielding effect of the nitrogen atom.
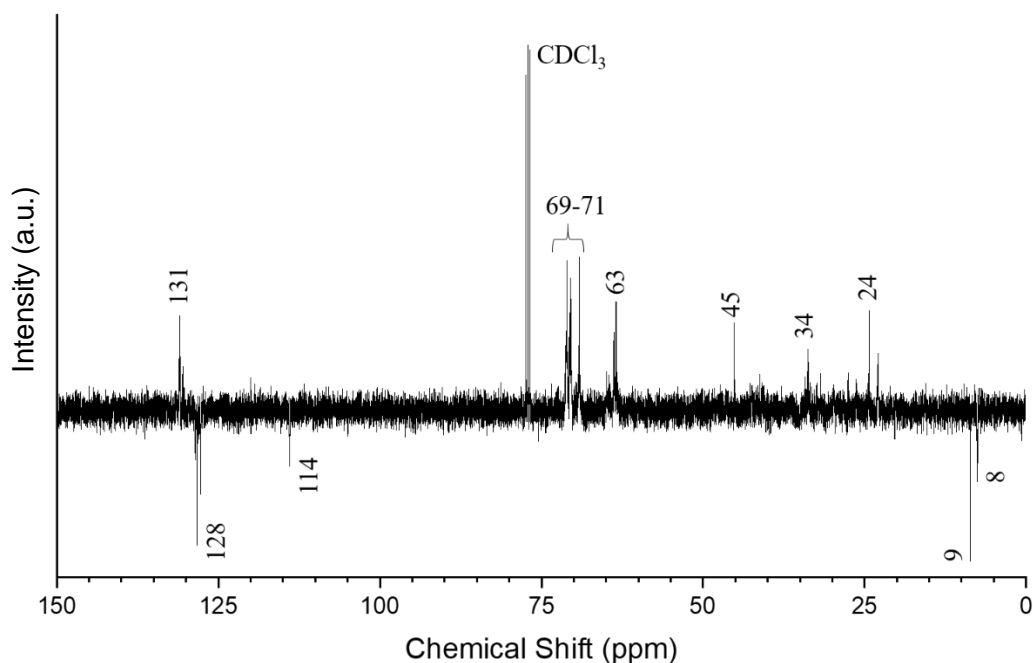
Figure 5.7 – APT ^{13}C NMR of wsPU. All annotated values are in ppm.

From the 2D ^{1}H-^{1}H COSY experiments (Figure 5.8), the complete PU structure can be deduced to a high degree of certainty. COSY analysis provides information on protons in proximity by detecting coupling through space.[15, 16] The pendant ethyl group is detected at 0.9 ppm and 1.4 ppm and coupling is observed between these two peaks. A distinctive cluster of coupling peaks is observed between 5.8 ppm and 6.4 ppm. These are assigned to the acrylate protons and can be assigned individually due to the coupling intensities. Protons in fixed environments around a double-bonded carbon couple more favourably to protons in certain proximity. Protons on the same carbon couple strongly to each other whilst coupling to the proton on the β-carbon is stronger when in a *trans* arrangement. As a result, the three environments can be assigned where 5.8 ppm = '*d*', 6.2 ppm = '*c*' and 6.4 ppm = '*b*' (using assignments from Figure 5.6).

PEG protons are detected at around 3.7 ppm with the ethylene glycol unit immediately adjacent to an acrylate group appearing at 4.2-4.3 ppm.[17] Critically, the protons in the β-position relative to the nitrogen of a PU linkage are also expected at ≈4.1 ppm. The high number of PEG environments explains the complex coupling patterns observed in this region. A series of couplings between the PEG protons and those in the alkyl region (below 1.5 ppm) are also detected. These correspond to the multiple PEG environments coupling to the pendant ethyl group. The N-H group of the PU linkage is seen to couple to itself due to H-bond dimerization.
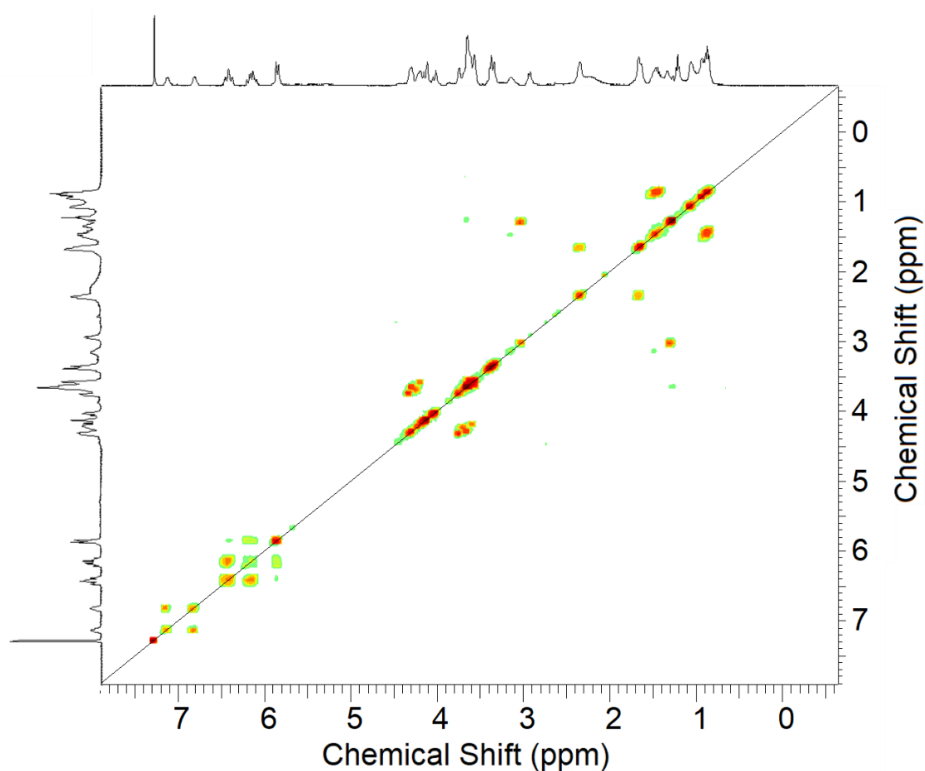
Figure 5.8 – ^{1}H-^{1}H 2D COSY NMR of wsPU sample. Transition of intensity from low to medium to high = green to yellow to red.

The predicted chemical structure of the wsPU is given in Figure 5.9. The presence of acrylate groups, a PEG chain, PU linkages and pendant ethyl groups can be confirmed. The presence of the quarternary carbon centre was detected through ^{13}C NMR and multiple PEG environments detected through 2D COSY. Due to the

complex nature of the PEG signals in ^{1}H-based NMR studies, it is likely the acrylate and ethyl groups are present at interchangeable locations within the PEG backbone. Critically, from the integration values in the ^{1}H NMR spectrum there is an average of one acrylate-ethyl carbon centre for each repeat unit.

Figure 5.9 – Predicted structure of the wsPU. The pendant acrylate group and ethyl group can be present at any location marked with '*' however, averaging once per repeat unit.

Dynamic light scattering (DLS) was completed to determine the particle size of the polymer micelles, see Figure 5.10. The particles show a number average particle size of 121.4 ± 0.2 nm. Micellar assembly in bulk films is widely used however, the incorporation of such polymers into nacre-mimetic structures is broadly unexplored and technically challenging. It is currently unknown whether micelles diffuse into layers of adequate thickness for production of bi-layers (i.e. one layer of GO and one layer of wsPU). The wsPU must deform to less than 1% of the micelle diameter to produce highly ordered bi-layers.

Figure 5.10 – DLS trace of wsPU showing an average particle size of 121.4 ± 0.2 nm.

5.3.2 Nanoindentation measurements of wsPU

The extent of UV curing of wsPU was correlated with the evolution of mechanical properties as determined from nanoindentation studies. Aliquots of 1 mL of the wsPU solution were dried in moulds approximately 15 mm in diameter before being cured in time intervals of 5 minutes, up to 25 minutes. The dried wsPU samples were a gel before curing however, were sufficiently stiff for nanoindentation measurements. A UV active initiator (Irgacure 500, I500) was included at 2.5 wt% during preparation. I500 is a 1:1 mixture of benzophenone (BPO) and 1-hydroxycyclohexylphenylketone (1HCPK)[18, 19] and is reported to be water soluble. Initial testing suggested that both BPO and 1HCPK are stable in water for a period but eventually settle out of solution, indicating the I500 behaves more like a 'pseudo-stable' dispersion. UV radiation was filtered to 320 nm - 390 nm to initiate the curing reaction and after 5 minutes, the samples became more rigid and were no longer gel-like. Both reduced Young's modulus (E_r) and hardness (H) of the resultant films were determined from nanoindentation measurements, see Figure 5.11. E_r and H increase with cure time, peaking at 20 minutes, before then showing a reduction at 25 minutes. The mechanical properties show a significant increase following even a short curing reaction, confirming the curing reaction is successful and that the ideal cure time for

the wsPU is 20 minutes. When incorporated into a nacre-mimetic film, the GO sheets absorb a portion of the UV radiation and thus the rate of initiation of the cure reaction will be reduced. Critically, optimisation under these conditions is still necessary.
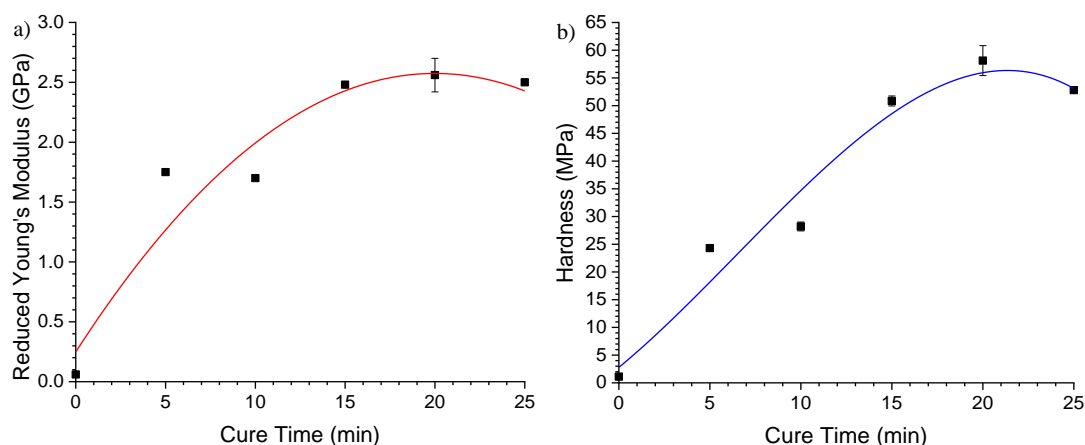
Figure 5.11 – a) reduced Young's modulus (E_r) and b) Hardness (H) of wsPU at differing cure times as determined by nanoindentation measurements.

5.4 Preparation of GO-wsPU films via a solvent-casting method

A preparation method for the production of freestanding nacre-mimetic materials had to be established. The published literature has reported a number of approaches including vacuum filtration,[2] solvent casting,[1] layer-by-layer (LbL)[20] assembly and spray coating.[21] It was important that the method allowed self-assembly of the component parts during production. Because an aqueous medium was employed, solution casting was most promising. The most important variable to consider when designing a mould is the substrate material. The interactions between the substrate and sample need to be repulsive to allow separation following drying. It is also important that they are compatible to prevent any degradation or dissolution of the mould. This could result in strong adhesion of the film to the substrate or contamination of the sample.

5.4.1 Use of a glass substrate

Initially, a glass substrate was used, similar to that described in previous literature.[1] Microscope slides were used due to their low cost and convenient shape. GO-wsPU dispersions were produced in water before a syringe was used to apply a specific volume onto the slides. The resulting sample was then dried at RT or at 60 °C. Figure 5.12 a) and b) show digital photographs of the resulting films. The films are not homogeneous with thicker regions on the edge and the centre of the sample. The drying of solvent can be a complex process and it has been shown that a 'coffee stain' effect occurs.[22, 23] The evaporation around the edge of the droplet causes capillary flow from the more central reservoir of solvent. This carries the solid dispersant to the edges and as the effect compounds, the resulting concentration of GO and wsPU at the edges becomes greater. After a critical point, the outer contact line cannot be replenished further and the solvent begins to evaporate towards the centre of the sample. During this process, the GO and wsPU have higher affinity to the solvent phase so are carried within the solvent until full saturation where the GO and wsPU crash out, causing the formation of a highly concentrated region at the centre of the substrate. Use of a mould with sidewalls prevents inward drying and the 'coffee stain' effect.
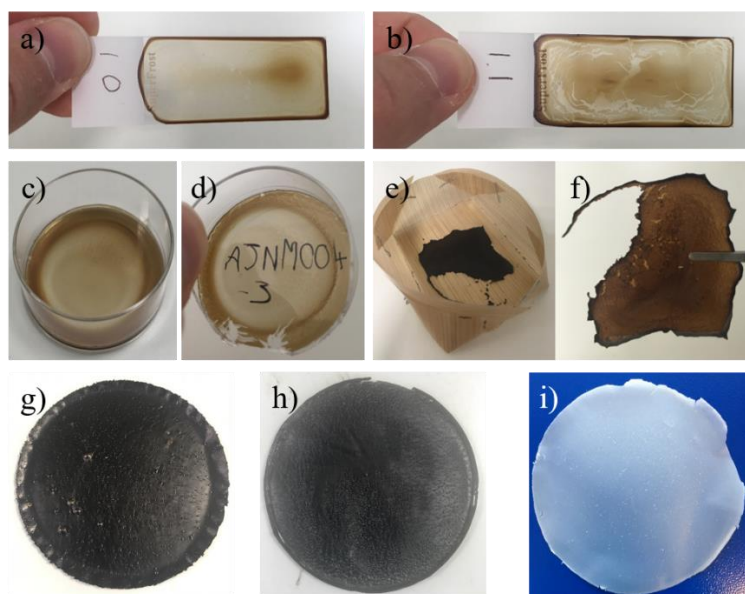
Figure 5.12 – Digital photographs of films produced on different substrates: a-b) glass, c-d) polystyrene, e-f) PTFE and g-i) PET

5.4.2 Use of a polystyrene (PS) substrate

Polystyrene (PS) petri-dishes are widely available and inexpensive. Due to the vertical sidewalls of the petri-dish, evaporation of the solvent occurs perpendicular to the substrate. Critically, this facilitates homogeneous drying over the sample and prevents the 'coffee stain' effect. 2.5 mL of a 1 wt% dispersion of GO, containing 0.05 wt% wsPU was added to the petri-dish and allowed to dry at RT. As can be seen from Figure 5.12 c) and d), the films produced remain inhomogeneous. There is still a high concentration of GO on the outermost regions of the dish but the dense region at the centre is reduced. This suggests the outer regions are recessed or the capillary effect is still occurring. Attempts were made to peel the film from the surface but it was well adhered to the PS. It is likely that the phenyl rings of the substrate are bonding through π-π stacking to the graphene-like regions of GO, resulting in strong adhesion. Due to the thickness of these films, the total strength is very low and it is likely the intermolecular interactions between the film and substrate are dominating. It is for this reason the majority of extremely thin films are produced onto substrates.[24-28]

5.4.3 Use of a poly(tetrafluoroethylene) (PTFE) substrate

It was proposed that films of similar thickness could be produced and successfully peeled from a poly(tetrafluoroethylene) (PTFE) substrate. PTFE is widely used in a range of applications because of low adhesion and chemical inertness in most environments.[29-31] Initially, a woven PTFE film was folded into a 'boat' shape before the GO-wsPU dispersion was added. Figure 5.12 f) shows the film when peeled from the substrate. The 'coffee stain' effect is observed due to the imperfect shape of the mould. The sidewalls are not vertical and the base is not rigid enough to maintain a completely flat surface. As a result, substrate coverage is not homogeneous causing evaporation like that observed in section 5.4.1. Despite this, the film was easily peeled-off suggesting PTFE is a suitable substrate for production of freestanding films.

Follow up attempts were made using a PTFE disk placed in a PS petri-dish. This also proved unsuccessful due to penetration of the dispersion round the edges of the PTFE disc. Ultimately, the dispersion dried onto the petri-dish and could not be peeled-off as was the case in section 5.4.2.

Consequently, a PTFE petri-dish was used to allow peeling of the film whilst maintaining a rigid base and sidewalls. Figure 5.13 a) shows the film immediately after drying without homogeneous coverage of the base of the mould. This suggests the surface is not smooth and the high density of GO around the outer rim implies these areas are recessed. The film could be peeled from the surface however, proved challenging due to the height of the sidewalls. The resulting film was analysed using SEM (Figure 5.13 b) and c)), displaying the ridged surface of the PTFE mould. Cross-sectional SEM provides some confirmation that the nacre-mimetic structure is being successfully formed during self-assembly.
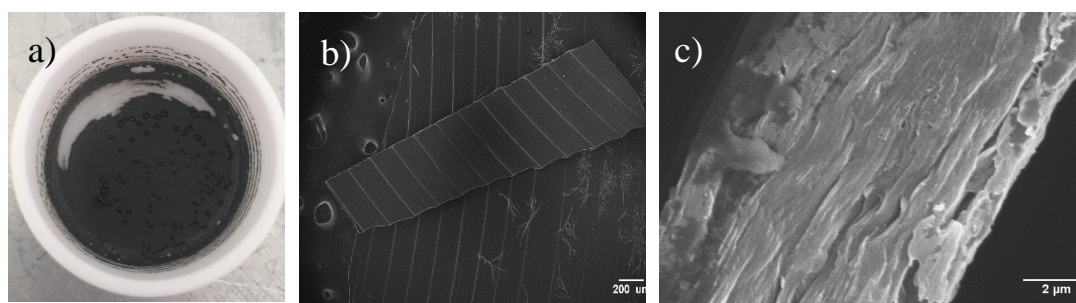
Figure 5.13 – Digital photographs and SEM images of the GO-wsPU films produced by casting into a PTFE petri-dish: a) digital photograph of the film immediately after drying, b) surface SEM of the film displaying the ridged surface of the PTFE mould and c) cross-sectional SEM showing the layered nacre-mimetic structure.

5.4.4 Removing the substrate

There are previous literature examples where films are produced on a substrate before the substrate is either dissolved[32] or treated to cleave the sample from the surface.[1, 33] This concept was employed to remove the PS petri-dish following casting. Multiple volumes of 2.5, 5 and 7.5 mL were cast and it was found that ethyl acetate (EtOAc) was effective at dissolving the PS. Due to the densely packed morphology of the nacre-mimetic films, it was expected that EtOAc would have a negligible effect on the film structure. Following casting, the petri-dishes were submerged in an EtOAc bath and the EtOAc replaced regularly to remove the solubilised PS. Figure 5.14 a)-e) show the samples via this process. All samples display a level of surface deformation

following treatment with EtOAc due to the contraction of the sample. The effect is more prominent on a larger scale (Figure 5.14 f)). Attempts were made to prepare tensile specimens from this film but it was extremely fragile and tore before analysis could be completed.
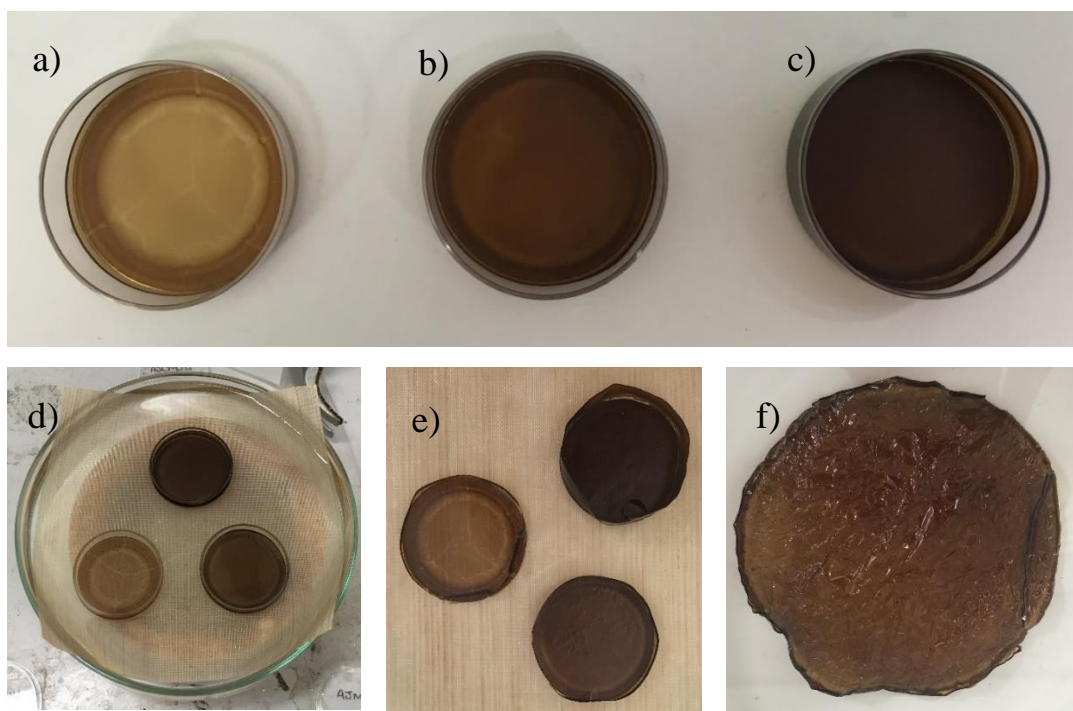
Figure 5.14 – Digital photographs of the GO-wsPU films cast into PS petri-dishes before the PS was dissolved in EtOAc where a) 2.5, b) 5 and c) 7.5 mL casting, d) samples submerged in an EtOAc bath, e) samples following drying at RT and f) large sample (100 mm diameter) following drying at RT.

5.4.5 Use of a poly(ethylene terephthalate) (PET) substrate

Poly(ethylene terephthalate) (PET) has previously been employed as a substrate however, films are rarely removed from the PET following drying.[34-36] Initially, PET was avoided due to the benzene ring present in the repeating unit as it was expected that this would promote strong adhesion to the GO structure in a similar way to PS. Despite this, test samples were produced where a PET disc was inserted onto the base of a PS petri-dish. Following drying, the PET could be peeled away from

133

the petri-dish and the sample film. This method proved to be very effective and was employed for all future solvent casting experiments. Figure 5.12 g), h) and i) show images of representative films produced via this method. The materials are more homogeneous and can be produced at a large enough scale for tensile bars to be produced.

5.4.6 Contact angle measurements

To understand the adhesion between GO-based films and the substrates, contact angle measurements were completed. The polar and dispersive components of the tested surfaces were calculated using the Fowkes model and the resulting data is plotted in Table 5.3.[37]

Table 5.3 – Contact angles detected through droplet shape analysis and the resulting surface free energy (γ_s), dispersive component (γ_s^d) and polar component (γ_s^p) of different substrates.

Substrate	Contact angle (θ)		(mN/m)		
	H_2O	CH_2I_2	γ_s	γ_s^d	γ_s^p
Glass slide	31.80	52.17	65.20	33.06	32.15
PET	77.45	32.85	46.68	43.00	3.68
PS petri-dish	69.70	34.07	49.24	42.45	4.79
PTFE (woven)	119.22	89.84	28.82	28.09	0.73
Neat GO paper	47.23	46.28	57.65	36.32	21.33
GO+UV2282 (no cure)	56.30	43.47	53.07	37.82	15.25

Using the calculations outlined by Cao *et al.* (Equation 5.1), interfacial tension, polar component and surface free energy between both neat-GO and GO-wsPU films with substrate materials were calculated (Figure 5.15).[38] The total surface free energy is determined by comparing the contact angle of two liquids of known surface energy (in this case water and 1,2-diiodomethane). The comparison of these two liquids produces a regression line that is used to determine interfacial tension and the polar

component. Surface free energy is the sum of the polar and dispersive energies of the material.

$$\gamma_{12} = \gamma_1 + \gamma_2 - 2(\sqrt{\gamma_1^d \gamma_2^d} + \sqrt{\gamma_1^p \gamma_2^p}) \qquad (1)$$

Equation 5.1 – Calculation to determine interfacial tension (γ_{12}) where γ_i = total surface free energy, and γ_i^d and γ_i^p = the dispersive and polar contributions of the material, i, respectively.

It is observed that the introduction of the wsPU causes a decrease to the polar component when compared to GO, most likely due to the less polar wsPU coating the surface of the GO. The interfacial tension between the neat GO (Figure 5.15 c)) and GO-wsPU (Figure 5.15 d)) samples with the substrates was analysed. In both cases, the PTFE shows the highest interfacial tension suggesting highest adhesion. PET is the next highest with the PS and glass substrates showing low tension. This contradicts the practical experimentation discussed previously. It should be noted that the surface roughness of the substrate materials can have an impact on the contact angles detected. It is likely that in the cases of PET and particularly PTFE (the woven structure is very rough), the surface topography results in unrepresentative contact angles and thus calculated interfacial tensions are inaccurate. Follow-up experiments were completed where a greater volume of solution was cast onto a glass substrate and freestanding films were produced. Ultimately, the flexibility of the PTFE and PET substrates are critical to the removal of freestanding films from the substrate. When peeling the film from a rigid substrate, the film experiences localised stress that can result in fracture. With a flexible substrate, the substrate can be peeled from the film, preventing flexural or tensile tension and reducing stresses in the sample.
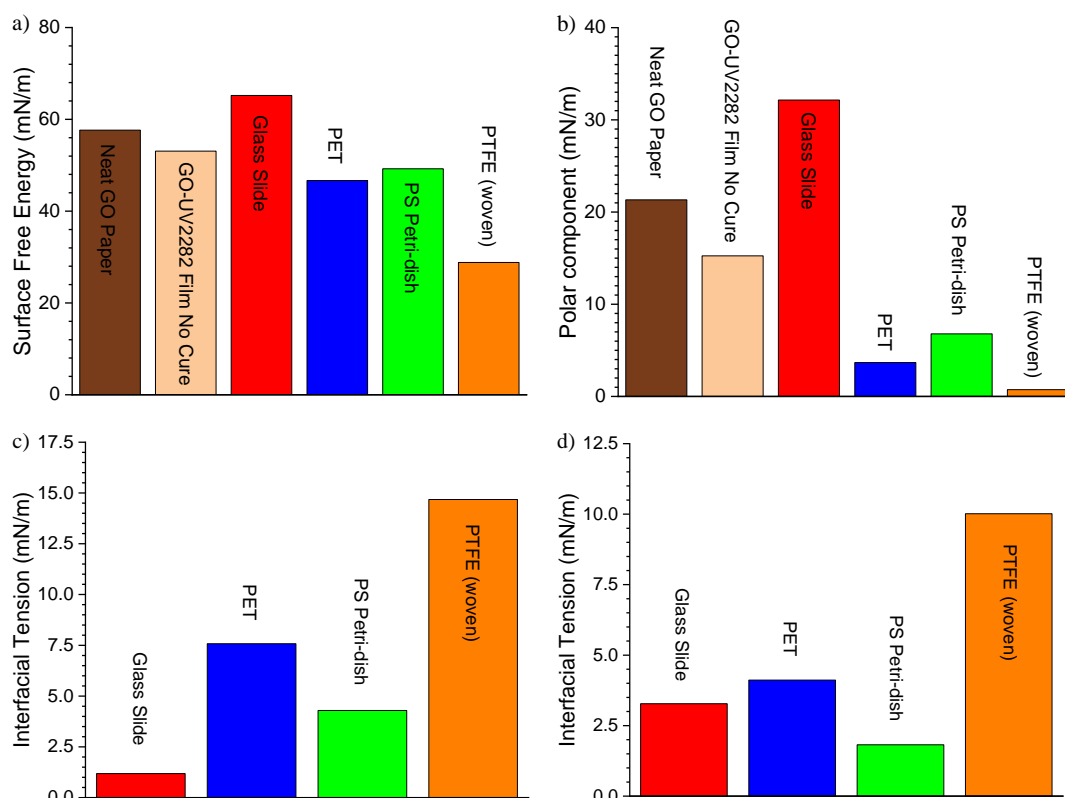
Figure 5.15 – Values calculated for a) surface free energy and b) polar component for all materials tested, c) interfacial tension between neat GO paper and substrate materials and d) interfacial tension between GO-wsPU film and substrate materials.

5.5 Production and characterisation of nacre-like films with GO and wsPU

The production of films using wsPU was achieved by first dispersing GO in de-ionized water at 1 wt%, assisted with stirring and sonication. Following this, a base was added to adjust the pH to >7 due to the instability of the wsPU in acidic conditions. Finally, the wsPU and I500 were added and the mixture stirred before being cast onto the PET substrate. wsPU and I500 were included at 5 wt% and 2.5 wt% of the GO, respectively, unless otherwise stated. In some cases, UV curing was also employed to evaluate the effect of cross-linking on Young's modulus (E), tensile strength (σ), maximum strain (ε) and tensile toughness (U_T).

GO-wsPU films were prepared and UV cured for times ranging between 0 and 20 minutes. The films are mostly homogeneous with some defects visible on the surface (Figure 5.12 g)). SEM imaging confirmed the presence of defects in the

layered structure. Through cross-sectional SEM imaging, the nacre-mimetic layers are seen (Figure 5.16) showing the successful self-assembly of the GO sheets into a layered conformation. Defects are visible, due in part to poor dispersion of the wsPU within the GO prior to drying. Equally, the wsPU is in micelle form when dispersed in water. During the drying process, the micelle must deform from a sphere with a diameter of 121.4 ± 0.2 nm (as confirmed by DLS) to a planar morphology. The interlayer distance between the GO layers is very small, approximately 1 nm (as confirmed by XRD in Chapters 6.4.3 and 6.6.2), and thus the micelle must reduce thickness to <1% of the original diameter, see Figure 5.17. During the drying process, diffusion of the wsPU between the GO layers is restricted by neighbouring GO nanoplatelets that trap the wsPU as an elongated sphere and ultimately, prevents formation of a uniform layer of wsPU. This also prevents homogeneous assembly of the GO and thus causes 'pile-up'. As a result, poor penetration of the wsPU creates defects that are much larger than the wsPU micelle. The SEM images in Figure 5.16 represent the fractured surface following tensile failure. Due to the large number of defects at the fracture surface, it is likely that these imperfections create localised stress points that ultimately lead to premature failure.
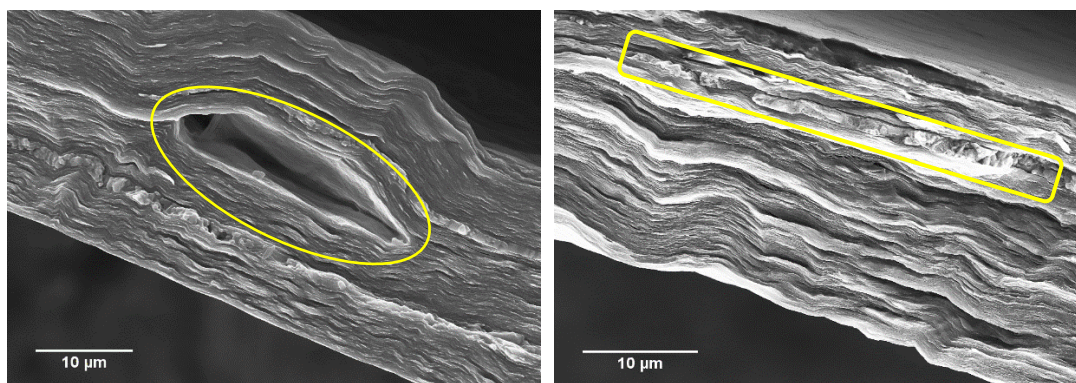
Figure 5.16 – Cross-sectional SEM images of GO-wsPU films clearly displaying the layered nanoplatelet arrangement and the presence of structural defects (highlighted in yellow).
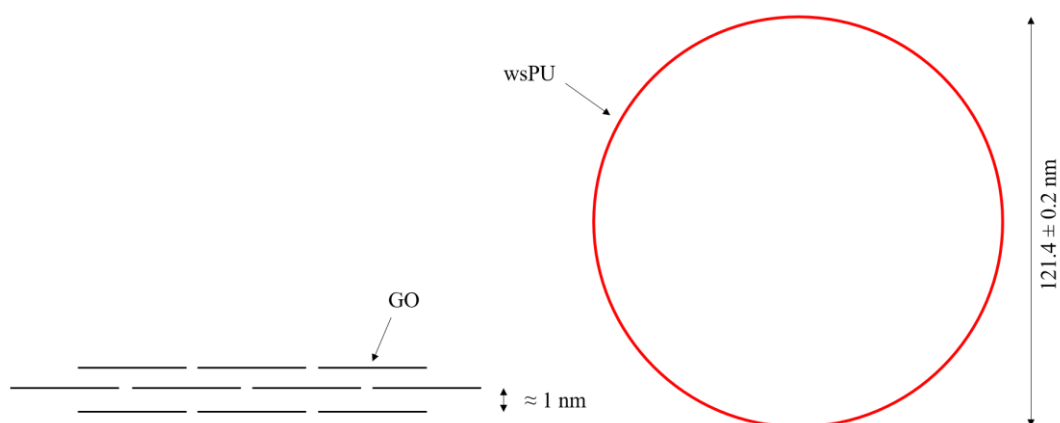
Figure 5.17 – Schematic representation of the difference in size of the wsPU micelle and interlayer distance of the GO layers (not to scale). Adequate distortion is necessary for penetration of wsPU between the GO layers.

5.5.1 Mechanical properties of GO-wsPU nacre-like films

Tensile testing is widely used to compare the performance of nacre-mimetic materials.[1, 2, 39] In this work, the films were cut into bars of 10 mm x 40 mm with thickness ranging from 15-35 µm. Typically, a single film would yield six specimens. Some test specimens broke before analysis or yielded anomalous results and are excluded from the data. Representative stress-strain curves for both neat GO and GO-wsPU films are shown in Figure 5.18. It should be noted that during testing some test specimens were not mounted fully taught. As a result, some of the test specimens display elongation whilst the film is brought under tension. This is most obvious in the sample cured for 5 minutes (Figure 5.18 c)) where in two cases the strain extends to 0.5% before the test specimen reaches tension. Further development of the methodology greatly reduced this requirement. From the stress-strain curves, E, σ, ε and U_T were calculated. E is calculated from the gradient of the linear region of the curve at the steepest point. U_T is determined by calculating the area under the curve.

A comparison of the mechanical properties is shown in Figure 5.19. Due to the introduction of a polymer component, an increase in σ and U_T is expected,[1, 2, 39] whilst typically, polymer stiffening is reported to cause an increase to E.[40] Due to the highly packed structure of the layers, mobility of the polymer is constrained by neighbouring nanoplatelets, thus preventing thermal motion. This causes stiffening of the polymer

chains and ultimately yields an increase in E. To undergo stiffening, the polymer chains must be homogeneously distributed between the nanoplatelet layers. In this work, inclusion of wsPU to GO results in a reduction in E, from 23.88 ± 5.07 GPa for GO to 10.86 ± 1.11 GPa for GO-wsPU without curing, in contrast to previous literature. This suggests the defects in the film structure (seen in the SEM images) prevent uniform stiffening throughout the film. UV curing of the films for 5, 10, 15 and 20 minutes further decreases E to 4.89 ± 0.38 GPa, 4.86 ± 0.38 GPa, 6.10 ± 1.17 GPa and 7.96 ± 0.56 GPa, respectively. This confirms the UV reaction is successful but has a detrimental effect on E. It has been described previously that UV curing causes volume shrinkage of a polymer.[41] The UV reaction replaces non-covalent interactions (in this case hydrogen bonding) with covalent bonds, which are shorter. As a result, the distance between polymer chains is reduced and the overall volume of the polymer decreases. It is likely that the reduction in E is due to the shrinkage of the wsPU within the defects. This shrinkage separates the wsPU from the GO and creates voids in the structure, weakening interfacial interactions and reducing the collaborative stiffening of the film.

GO has σ = 50.15 ± 9.23 MPa. This is reduced following addition of wsPU where σ = 41.24 ± 4.59 MPa for GO-wsPU without UV curing. The imperfections in the films, observed from SEM imaging, disrupt the mechanisms for energy dissipation and cause localised stress points. Critically, this reduces the strength of the interfacial interactions and reduces σ. UV curing further reduces σ to 19.54 ± 3.38 MPa, 24.93 ± 3.14 MPa, 25.42 ± 3.44 MPa and 26.74 ± 4.30 MPa for 5, 10, 15 and 20 minute cure times, respectively. The reduction in the steric volume of the wsPU from UV curing creates voids in the GO-wsPU layered structure. This reduces the interfacial interactions between adjacent layers and ultimately, prevents cooperative dissipation of energy.
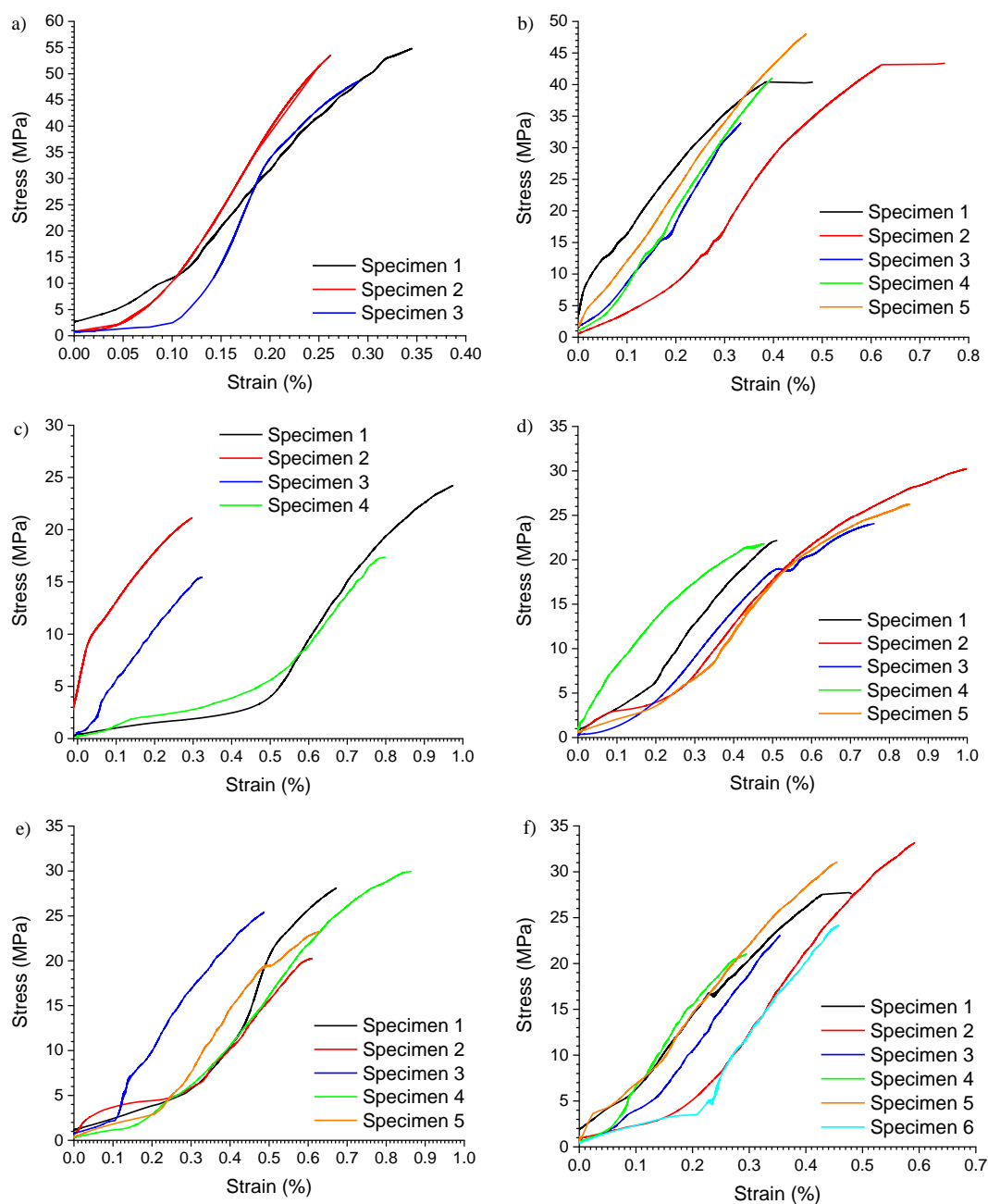
Figure 5.18 – Representative stress-strain curves for GO and GO-wsPU films where a) neat GO, b) GO-wsPU with no UV cure and GO-wsPU with c) 5, d) 10, e) 15 and f) 20 minute cure.
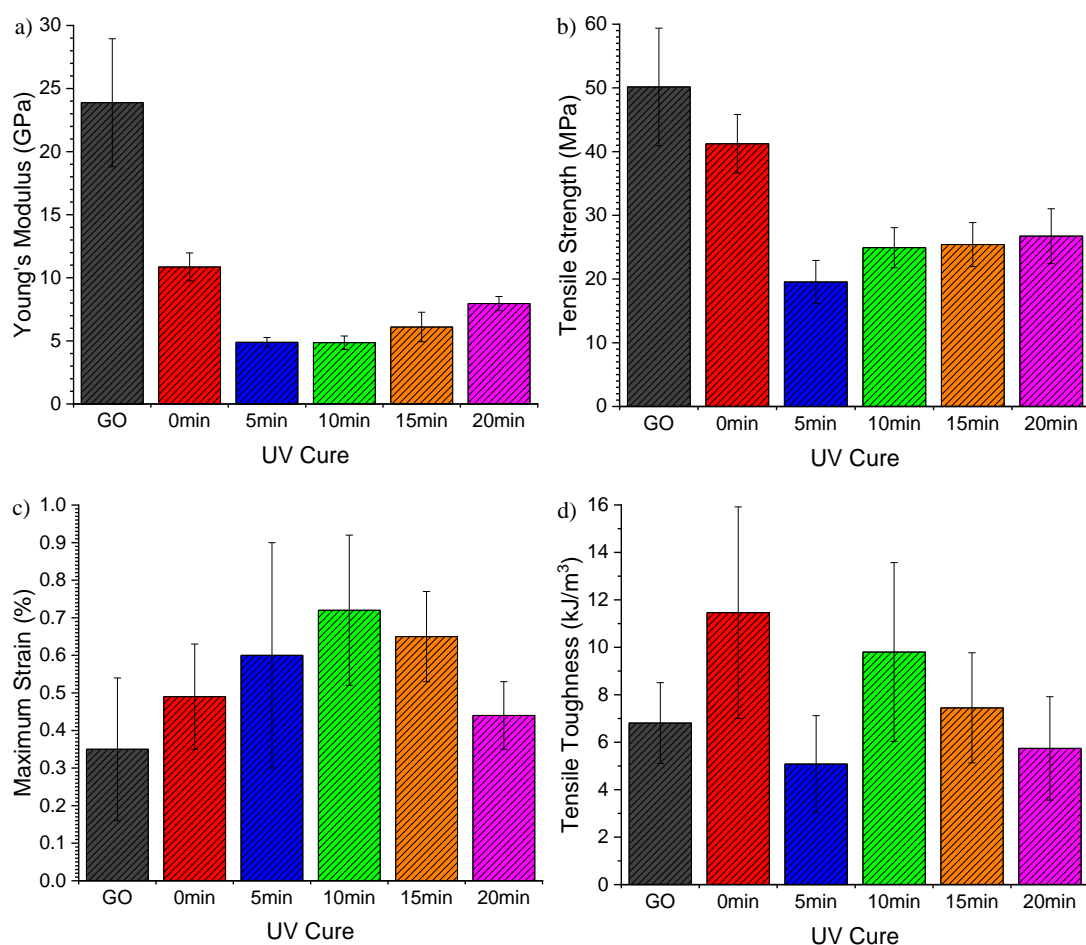
Figure 5.19 – Mechanical properties of GO and GO-wsPU films as a function of cure time as determined from static tensile testing where, a) Young's modulus, b) tensile strength, c) maximum strain and d) tensile toughness.

Interestingly, ε increases following addition of wsPU to the GO structure. For GO, $\varepsilon = 0.35 \pm 0.19\%$ whilst for uncured GO-wsPU, $\varepsilon = 0.49 \pm 0.14\%$. The wsPU component that is well dispersed is able to fill voids within the rigid GO structure. As tensile load is applied, the flexible wsPU chains are able to extend and facilitate greater sliding of the GO platelets prior to failure. UV curing further increases ε with 5 minute curing recording $\varepsilon = 0.60 \pm 0.30\%$ and 10 minute curing yielding $0.72 \pm 0.20\%$. It should be noted that the error in the sample with 5 minute curing is large, in part due to the procedural issues outlined previously. As a result, it is inconclusive what impact UV curing for 5 minutes has on ε. Despite this, the cross-linking reaction initiated by the UV radiation theoretically creates covalent bonds between the GO and wsPU. This covalent bonding allows the wsPU chains to extend further prior to cleavage of the

141

bonds to the GO platelet surface. Covalent cross-linking is observed in the 10 minute cure film due to the increase in ε when compared to the uncured GO-wsPU film. At >10 minute cure, ε decreases (15 minute = 0.65 ± 0.12% and 20 minute = 0.44 ± 0.09%) due to the increasing stiffness of the wsPU, a consequence of UV cross-linking, preventing elongation of the polymer chains.

U_T is dependant on E, σ and ε and so is a good indicator of the overall performance of the film. Initially, the addition of wsPU to GO results in U_T increasing from 6.81 ± 1.70 kJ/m^3 (neat GO) to 11.46 ± 4.46 kJ/m^3 for the uncured GO-wsPU film. This is due to the increase in ε dominating the reduction in both E and σ. The increased elongation at break of the GO-wsPU film enables absorption of more energy than the more rigid GO film. Interestingly, UV curing for 5 minutes reduces U_T to 5.08 ± 2.04 kJ/m^3. The UV curing reduces the steric volume of the wsPU, which yields low E and σ when compared to the other films. Critically, this creates poor interfacial interactions between the components and ultimately hinders dissipation of energy. GO-wsPU cured for 10 minutes shows an increase in U_T (9.80 ± 3.77 kJ/m^3) compared to the sample cured for 5 minutes but a reduction relative to the uncured GO-wsPU film. At 10 minute cure, the optimal ε is recorded (0.72 ± 0.20%), confirming that energy can be dissipated through extension of the film. Despite this, the E and σ are lower than that for the uncured GO-wsPU film. Ultimately, this limits energy dissipation to one mechanism (i.e. extension) and so U_T is reduced. Despite minimal increases in E and σ, the GO-wsPU films, when cured for 15 and 20 minutes, show a reduction in ε compared to the GO-wsPU film cured for 10 minutes. As a result, U_T shows a downward trend with increased UV cure time (7.45 ± 2.32 kJ/m^3 and 5.74 ± 2.18 kJ/m^3 for 15 and 20 minute cures, respectively). This suggests that the reduction in extension is more dominant than the improved interfacial interactions between the GO and wsPU. It should be noted that the E, σ, and ε achieved for these films are much lower than the theoretical maxima for GO (E = 290-470 GPa, σ = 27.9-47.8 GPa, ε = 10-20%)[42] however, without further analysis of the precise GO structure, it is impossible to conclusively state the relative performance of the GO-wsPU against pure GO properties.

Nanoindentation experiments were completed to determine the indentation properties of the films. The mode of deformation is different from static tensile testing,

as is visualised in Figure 5.20 a). As a result, different properties can be analysed. Figure 5.20 b) shows representative depth versus load curves for the GO-wsPU films. Figure 5.20 c) and d) compare E_r and H for neat GO and GO-wsPU films. E_r is significantly reduced from 10.33 ± 0.65 GPa for GO to 2.87 ± 0.23 GPa for uncured GO-wsPU. The UV curing reaction has no further impact on E_r, recording 2.64 ± 0.23 GPa, 2.88 ± 0.78 GPa, 2.51 ± 0.14 GPa and 2.49 ± 0.18 GPa for 5, 10, 15 and 20 minute cure times, respectively. The same trend is observed for H. GO had a $H = 230 \pm 20$ MPa and GO-wsPU films recorded $H = 95.3 \pm 11.1$ MPa, 114.9 ± 12.3 MPa, 85.0 ± 18.7 MPa, 98.4 ± 9.3 MPa and 96.7 ± 7.8 MPa for no cure, 5, 10, 15 and 20 minute cure times, respectively. The reduction in both E_r and H is due to the imperfections that are present in the uni-directional layered structure (as shown in Figure 5.16). In the GO sample, the GO nanoplatelets are densely packed and so under load, the indenter tip is forced to indent the more mechanically strong GO. The addition of wsPU enables indentation of the softer wsPU component that coats the top surface of the film. The UV curing has no impact because the wsPU has an optimal E_r and H of ≈ 2.6 GPa and 70 MPa, respectively. Both these values are equal to or less than those detected for the GO-wsPU films, confirming that the properties observed contain a significant contribution of the GO nanoplatelets. As the wsPU is cured, the contribution of the GO is reduced due to the increased stiffness of the wsPU surface coating, ultimately resulting in little change throughout the UV curing timeframe.

Ultimately, these experiments prove the production of layered, unidirectional films has been successful however, homogeneity of the films is poor. The formation of imperfections, observed by SEM, disrupt the efficacy of the different energy dissipation mechanisms and degradation of a range of mechanical properties. Despite this, both ε and U_T increased on addition of wsPU to GO when the film was uncured. Consequently, it appeared that improvements in dispersion of the GO and wsPU would result in a reduction in the number and size of the imperfections, thus improving the mechanical properties of the films.
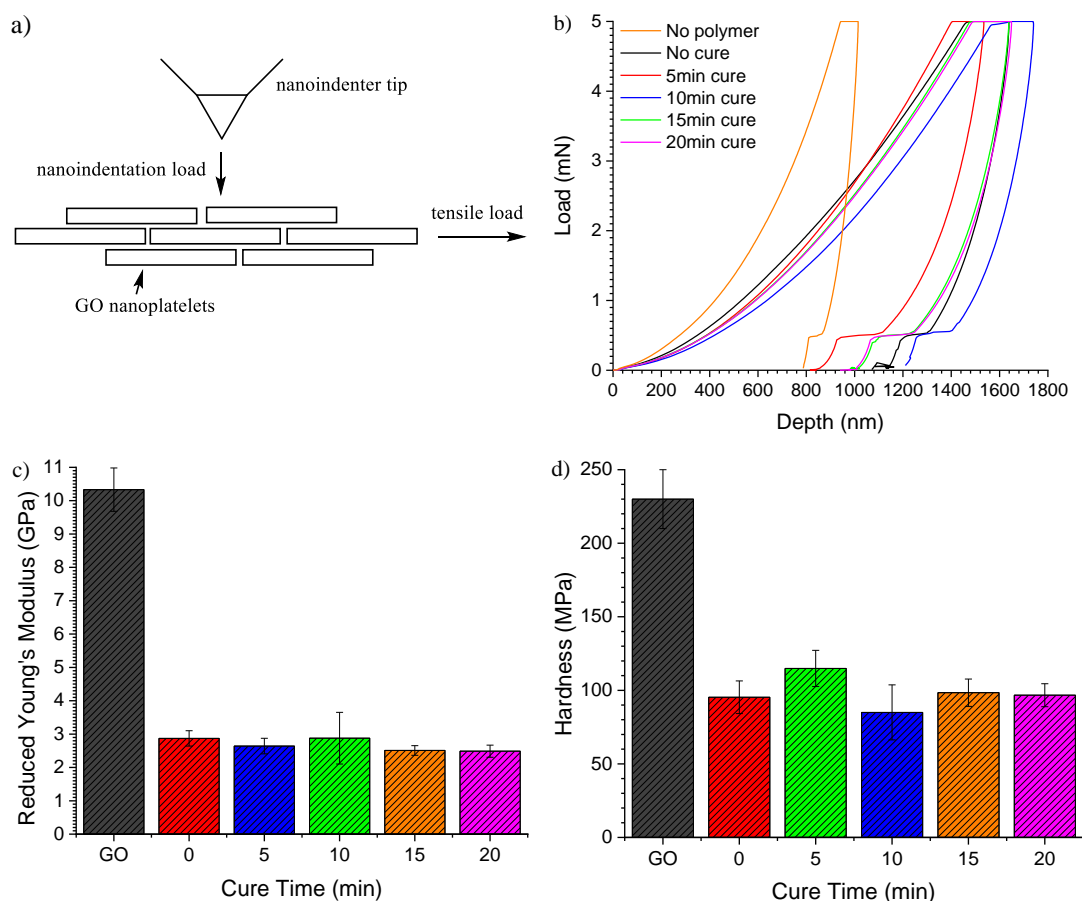
Figure 5.20 – a) schematic representation of the different mode of deformation during nanoindentation and static tensile testing, b) representative depth versus load curves, c) reduced Young's modulus (E_r) and d) Hardness (H) of GO and GO-wsPU of different films as a function of UV cure time.

5.5.2 Methods to improve the dispersion of wsPU within the GO matrix and impact on mechanical properties

Sonication is widely used for aiding the dispersion of GO in water, so a 15 minute sonication step (following addition of the wsPU) was added to evaluate whether the homogeneity of the films could be improved. The resulting films were UV cured and imaged by SEM (Figure 5.21). Imperfections in the layered structure were observed in all samples. Interestingly, the majority of the defects were detected close to the film surface. This suggests the imperfections form early in the assembly process or during the final stages of water evaporation.
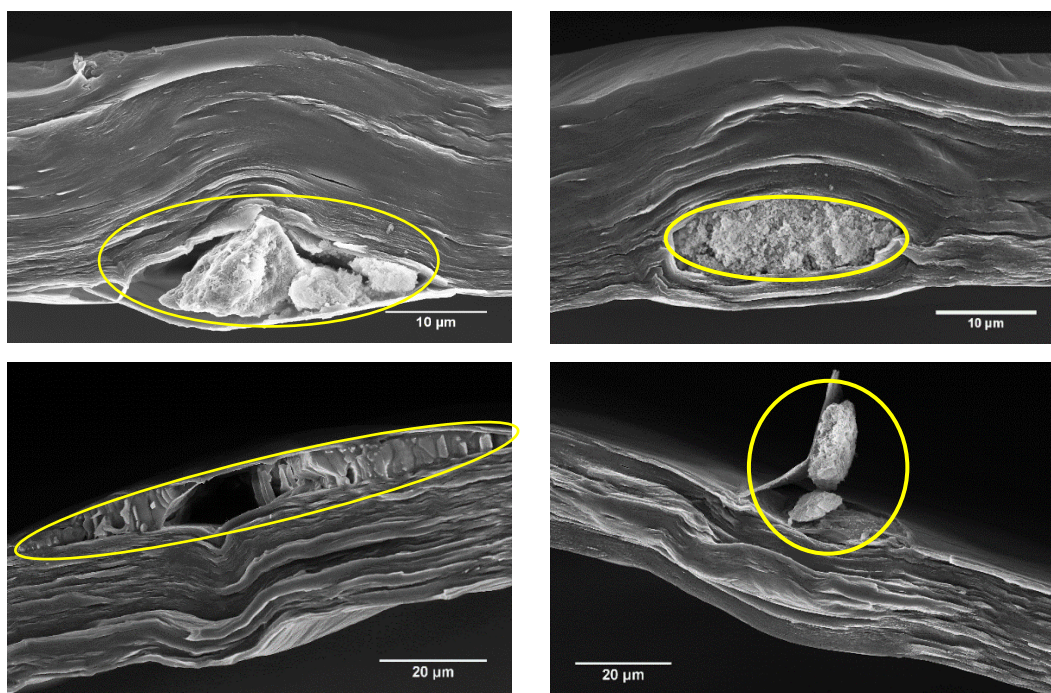
Figure 5.21 – Representative SEM images of the GO-wsPU films showing structural imperfections (highlighted in yellow).

Tensile testing of films produced with the assistance of sonication was completed and the data compared with the films reported in the previous section, see Figure 5.22. As was observed previously, the addition of wsPU has a negative impact on E from 23.88 ± 5.07 GPa for GO to 12.80 ± 2.29 GPa for the uncured GO-wsPU film, although the decrease is less than when compared to the un-sonicated GO-wsPU films with $E = 10.86 \pm 1.11$ GPa. Similarly, as before, UV curing has a negative effect on E, as after 5, 10 and 15 minute curing, E was 10.38 ± 2.53 GPa, 7.96 ± 0.93 GPa and 8.97 ± 1.07 GPa, respectively. Again, the reduction in E is smaller than is observed for the un-sonicated GO-wsPU equivalents. Interestingly, for a 20 minute cure time, $E = 17.87 \pm 2.73$ GPa, much greater than the other GO-wsPU films. This could be due to the UV induced cross-linking between the wsPU and GO however, it is more likely due to improved dispersion and diffusion of wsPU within the structure and the minimisation of defects. To confirm this, a further film was produced and cured for 25 minutes which had $E = 7.44 \pm 1.25$ GPa, suggesting that UV cross-linking was not responsible for the increase in E.
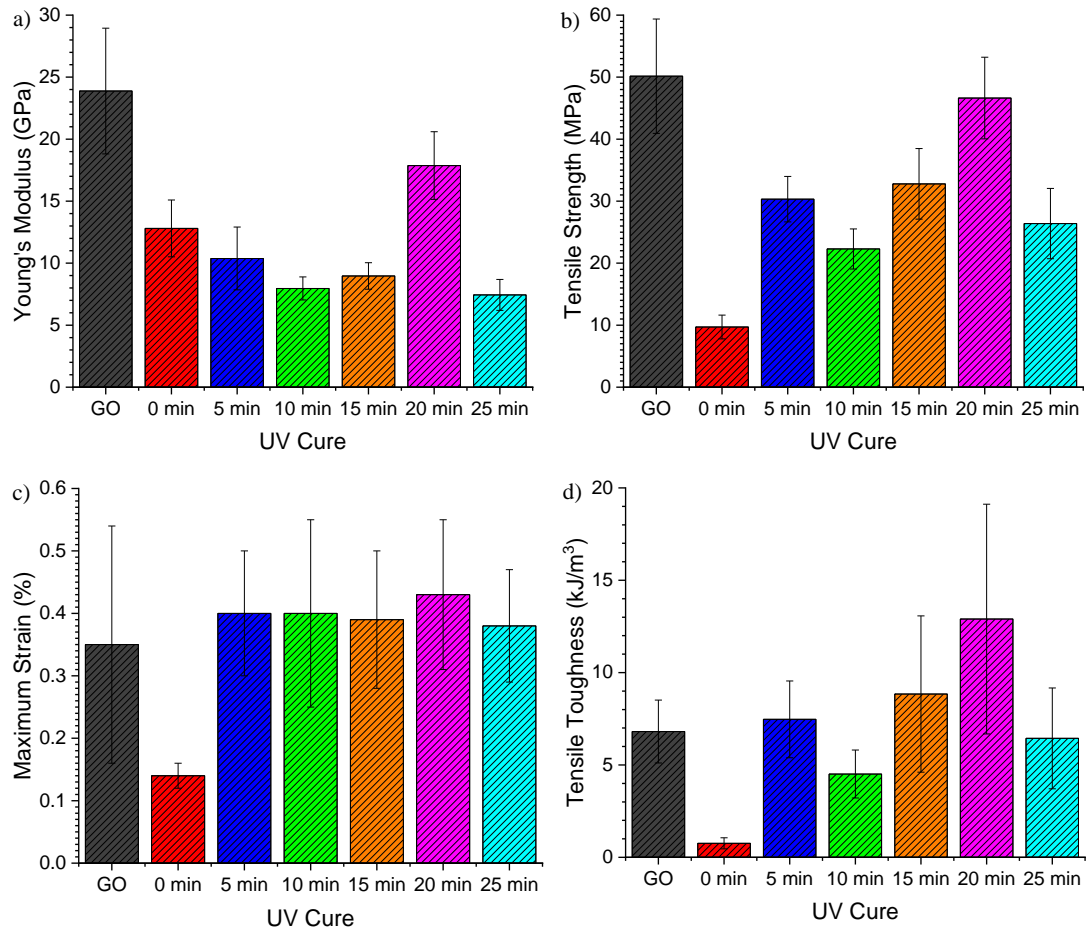
Figure 5.22 – Mechanical properties of GO film and GO-wsPU films produced with sonication prior to casting, a) Young's modulus, b) tensile strength, c) maximum strain and d) tensile toughness as a function of cure time.

A significant reduction in σ was observed on addition of wsPU to GO. For GO $\sigma = 50.15 \pm 9.23$ MPa however, for uncured GO-wsPU $\sigma = 9.70 \pm 1.92$ MPa. UV curing resulted in an increase in σ, where $\sigma = 30.32 \pm 3.66$ MPa, 22.29 ± 3.23 MPa, 32.79 ± 5.70 MPa and 46.63 ± 6.58 MPa for a 5, 10, 15 and 20 minute cure time, respectively. Similarly, ε is reduced from $0.35 \pm 0.19\%$ for GO to $0.14 \pm 0.02\%$ for GO-wsPU before increasing to close to 0.4% following UV curing ($0.40 \pm 0.10\%$, $0.40 \pm 0.15\%$, $0.39 \pm 0.11\%$ and $0.43 \pm 0.12\%$ for 5, 10, 15 and 20 minute cure times, respectively). It is likely that the uncured GO-wsPU film contains a disproportionate quantity of defects, caused by poor mixing or pH control resulting in premature precipitation of the wsPU. As a result, stress is unable to dissipate effectively.

As expected, the U_T of the uncured GO-wsPU film is low (0.76 ± 0.30 kJ/m^3) when compared to the neat GO film (6.81 ± 1.70 kJ/m^3). An increase to U_T is observed following UV curing to 7.47 ± 2.08 kJ/m^3 for 5 minute, 4.51 ± 1.30 kJ/m^3 for 10 minute, 8.84 ± 4.23 kJ/m^3 for 15 minute and 12.90 ± 6.22 kJ/m^3 for 20 minute cure times. In the cases of 5, 10 and 20 minute cure times, an increase in U_T is observed relative to neat GO. Ultimately, sonication has shown minimal increases to E and σ, and an inconsistent impact on ε and U_T compared to the un-sonicated GO-wsPU equivalents. It has been previously reported that sonication reduces micelle aggregates however, the effect on the micelle particle size is minimal.[43] DLS confirmed a very narrow particle size distribution (121.4 ± 0.2 nm) suggesting that micelle aggregation is negligible. Despite this, the minor increase in E and σ are likely correlated to a reduction in micelle diameter that enables an improvement in diffusion and penetration of the wsPU between the GO layers. Critically, the necessary reduction in micelle thickness (to ≈ 1 nm) remains impossible under these conditions and so E and σ remain low and ε and U_T are comparable to neat GO.

5.5.3 Selection of base in determining film morphology and properties

For all compositions to this point, triethylamine (Et$_3$N) was used to adjust the dispersion pH to >7. Et$_3$N has been shown to be readily vaporized at 50 °C[44] and evaporate when solubilised in water at RT.[45] The samples prepared in this work were dried at 40 °C and so evaporation of Et$_3$N is inevitable. It may be that evaporation was beneficial to the formation of a homogeneous film. Provided the Et$_3$N stabilised the wsPU during drying, a change in pH following assembly would have no effect on the film structure. It is more likely the evaporation of Et$_3$N shifts the pH prior to, or during assembly, and therefore causes premature precipitation of the wsPU. This would result in regions of high wsPU content distributed throughout the film. Therefore, an alternative base was used in an attempt to improve the stability of the wsPU. Sodium hydroxide (NaOH) has been previously described in the literature to adjust pH of similar dispersions for production of nacre-mimetic materials,[46] is stable against evaporation, and is easily solubilised in water. Therefore, NaOH was selected as a suitable replacement for Et$_3$N for the following experiments.

UV cured samples were not produced, as previous studies had confirmed that UV curing did not show consistent increases to E, σ, ε and U_T. Instead, a second

GO:wsPU ratio = 90:10 was produced to evaluate the effect of increased wsPU content. These films had less surface defects, see insets in Figure 5.23. In the case of the 95:5 ratio, the film appears very smooth with only a few minor defects. At 90:10 ratio, defects appear much smaller than those observed when using Et_3N.
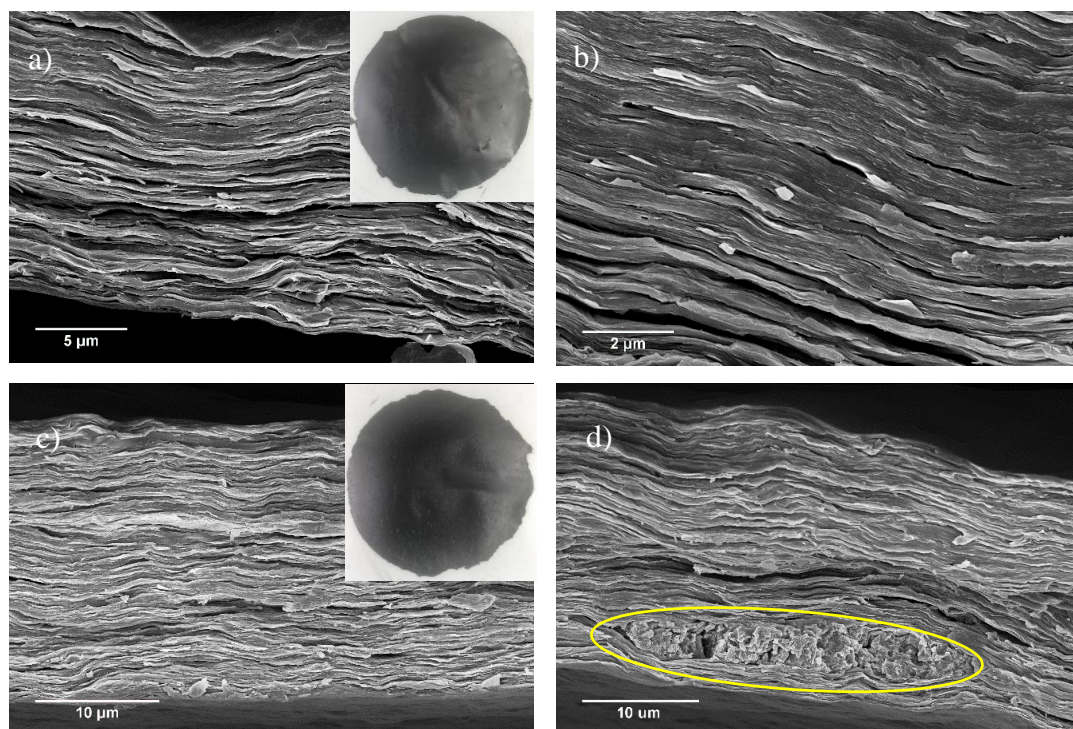
Figure 5.23 – SEM images of GO-wsPU films prepared using NaOH as base for a) and b) 95:5 and c) and d) 90:10 ratios of GO:wsPU at different magnifications (defects are highlighted in yellow). Digital photographs of the films are inset in the SEM images.

SEM imaging provides some interesting details (Figure 5.23). Images a) and b) show a consistent and homogeneous layered morphology without obvious defects. It should also be noted that small granular artefacts are present throughout the material (most clearly shown in Figure 5.23 b)). These are NaOH crystals and confirm evaporation of the base has been limited. For the 90:10 ratio (Figure 5.23 c) and d)), some defects are still observed. As has been previously discussed, it is likely the

micellar nature of the wsPU is still unable to diffuse and penetrate between the GO layers.

Figure 5.24 shows the mechanical properties recorded for neat GO, GO-wsPU using Et$_3$N and the two GO-wsPU films using NaOH. For GO:wsPU 95:5 ratio using NaOH, E = 23.37 ± 7.12 GPa, comparable to that of neat GO (23.88 ± 5.07 GPa). σ = 54.53 ± 6.25 MPa was also comparable to neat GO (50.15 ± 9.23 MPa). An increase in ε is observed from 0.35 ± 0.19% for neat GO to 0.44 ± 0.13% for GO-wsPU 95:5 ratio and NaOH. Consequently, U_T = 12.60 ± 4.54 kJ/m^3 for the GO-wsPU 95:5 ratio prepared with NaOH, a significant increase of 185% over that of GO (6.81 ± 1.70 kJ/m^3). Critically, as E and σ were comparable to GO, this suggests the morphology of the GO-wsPU structure is more homogeneous and the number of defects reduced. Despite this, addition of a polymer component typically results in an increase to E, σ, ε and U_T. In this work, E, σ, and ε do not show significant change and so there must be imperfections still present within the layered structures.

For the GO-wsPU 90:10 ratio, E decreased to 14.94 ± 1.62 GPa when compared to GO (23.88 ± 5.07 GPa) and GO-wsPU 95:5 with NaOH (23.37 ± 7.12 GPa). A stiffening effect is expected when the wsPU forms a layer between the GO platelets however, should the wsPU assemble into thicker layers, stiffening is reduced due to thermal motion within the polymer layer, evident from a decrease in E. It is clear that using NaOH enables the wsPU to disperse and diffuse into a more homogeneous structure. Despite this, complete diffusion (i.e. single layers of GO and planar wsPU) is not achieved.
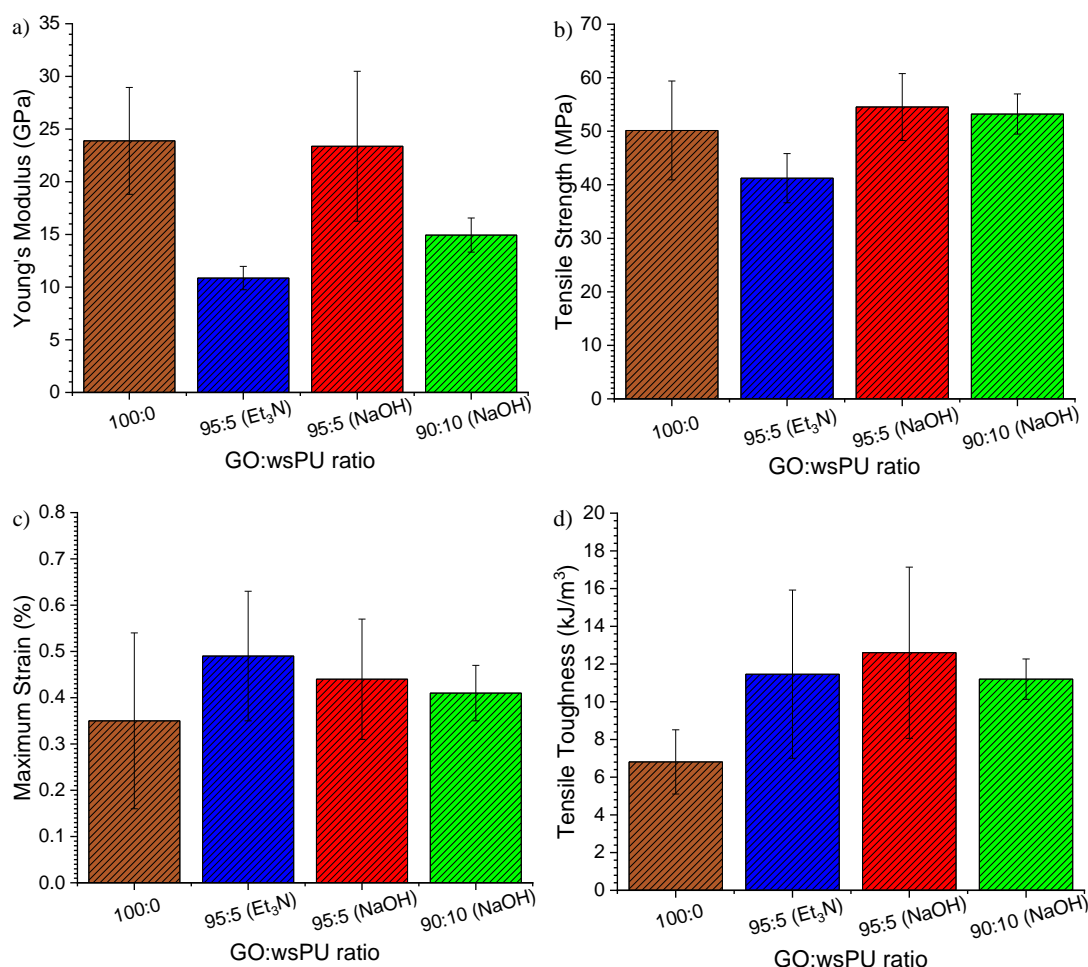
Figure 5.24 – Comparison of mechanical properties of neat GO and GO-wsPU films produced using either Et₃N or NaOH (specified in brackets) where a) Young's modulus, b) tensile strength, c) maximum strain and d) tensile toughness.

5.6 Concluding remarks

It has been shown that production of homogeneous uni-directional layered nacre-like films is challenging when using a micellar wsPU. It was discovered that freestanding films could be produced using a solvent casting approach on a PET substrate. GO-wsPU films showed a reduction in E and σ when compared to neat GO. This was due to imperfections (confirmed by SEM imaging), caused by the micellar wsPU being unable to diffuse and penetrate between the GO layers during drying. UV curing further reduced E and σ, but increased ε. Nanoindentation measurements confirmed that uncured GO-wsPU yielded reductions to E_r (72%), and H (58%) when compared with neat GO. UV curing did not increase E_r or H. Sonication was employed

to encourage dispersion of the wsPU to enable more effective penetration between the GO layers however, only minimal increases to E and σ were recorded when compared to un-sonicated GO-wsPU equivalents. Finally, Et$_3$N was substituted with NaOH to stabilise the pH of the dispersion throughout drying. This produced GO-wsPU films with E, σ and U_T that were comparable to neat GO however, still yielded structural imperfections.

5.7 References

1. W. Cui, M. Li, J. Liu, B. Wang, C. Zhang, L. Jiang and Q. Cheng, *ACS Nano*, 2014, **8**, 9511-9517.

2. S. Wan, J. Peng, Y. Li, H. Hu, L. Jiang and Q. Cheng, *ACS Nano*, 2015, **9**, 9830-9836.

3. S.-W. Wang, W. Liu and R. H. Colby, *Chemistry of Materials*, 2011, **23**, 1862-1873.

4. B. L. Caba, Q. Zhang, M. R. Carroll, R. C. Woodward, T. G. St Pierre, E. P. Gilbert, J. S. Riffle and R. M. Davis, *Journal of Colloid and Interface Science*, 2010, **344**, 81-89.

5. H. Honarkar, *Journal of Dispersion Science and Technology*, 2017, **39**, 507-516.

6. P. Das, J. M. Malho, K. Rahimi, F. H. Schacher, B. Wang, D. E. Demco and A. Walther, *Nature Communications*, 2015, **6**, 5967-5981.

7. K. Shahzadi, I. Mohsin, L. Wu, X. Ge, Y. Jiang, H. Li and X. Mu, *ACS Nano*, 2017, **11**, 325-334.

8. B. Liang, Y. Shu, P. Wan, H. Zhao, S. Dong, W. Hao and P. Yin, *Composites Science and Technology*, 2019, **182**, 107747-107756.

9. S. Y. Toh, K. S. Loh, S. K. Kamarudin and W. R. W. Daud, *Chemical Engineering Journal*, 2014, **251**, 422-434.

10. I. Childres, L. A. Jauregui, W. Park, H. Cao and Y. P. Chen, in *New Developments in Photon and Materials Research*, ed. J. I. Jang, Nova Science Publishers, New York, 2013, pp. 403-418.

11. L. M. Malard, M. A. Pimenta, G. Dresselhaus and M. S. Dresselhaus, *Physics Reports*, 2009, **473**, 51-87.

12. S. S. Abbas, G. J. Rees, N. L. Kelly, C. E. J. Dancer, J. V. Hanna and T. McNally, *Nanoscale*, 2018, **10**, 16231-16242.

13. H. Günther, *NMR Spectroscopy: Basic Principles, Concepts and Applications in Chemistry*, Wiley, 3 edn., 2013.

14. Ö. Alver and G. Dikmen, *Journal of Molecular Structure*, 2016, **1108**, 103-111.

15. S. Wołowiec, *Polyhedron*, 1998, **17**, 1295-1301.

16. H. Masui and H. Hong, *Journal of Chemical Information and Modelling*, 2006, **46**, 775-787.

17. S. Lin-Gibson, S. Bencherif, J. A. Cooper, S. J. Wetzel, J. M. Antonucci, B. M. Vogel, F. Horkay and N. R. Washburn, *Biomacromolecules*, 2004, **5**, 1280-1287.

18. F. Bauer, R. Flyunt, K. Czihal, H. Langguth, R. Mehnert, R. Schubert and M. R. Buchmeiser, *Progress in Organic Coatings*, 2007, **60**, 121-126.

19. R. Schwalm, L. Häußling, W. Reich, E. Beck, P. Enenkel and K. Menzel, *Progress in Organic Coatings*, 1997, **32**, 191-196.

20. W. Xie, S. Tadepalli, S. H. Park, A. Kazemi-Moridani, Q. Jiang, S. Singamaneni and J. H. Lee, *Nano Letters*, 2018, **18**, 987-993.

21. X. Yan, F. Li, K. D. Hu, J. Xue, X. F. Pan, T. He, L. Dong, X. Y. Wang, Y. D. Wu, Y. H. Song, W. P. Xu and Y. Lu, *Scientific Reports*, 2017, **7**, 13851-13861.

22. R. D. Deegan, O. Bakajin, T. F. Dupont, G. Huber, S. R. Nagel and T. A. Witten, *Nature*, 1997, **389**, 827-829.

23. H. Hu and R. G. Larson, *The Journal of Physical Chemistry B Letters*, 2006, **110**, 7090-7094.

24. I. K. Moon, J. I. Kim, H. Lee, K. Hur, W. C. Kim and H. Lee, *Scientific Reports*, 2013, **3**, 1112-1119.

25. A. Aliprandi, T. Moreira, C. Anichini, M. A. Stoeckel, M. Eredia, U. Sassi, M. Bruna, C. Pinheiro, C. A. T. Laia, S. Bonacchi and P. Samori, *Advanced Materials*, 2017, **29**, 1703225-1703231.

26. Z. Liu, Y. Xie, J. Zhao, S. Wu, Z. Zhou, M. Wen, Y.-B. Cheng and J. Zhong, *Thin Solid Films*, 2018, **657**, 24-31.

27. S. Nemala, S. Prathapani, P. Kartikay, P. Bhargava, S. Mallick and S. Bohm, *IEEE Journal of Photovoltaics*, 2018, **8**, 1252-1258.

28. D. W. Shin, M. D. Barnes, K. Walsh, D. Dimov, P. Tian, A. I. S. Neves, C. D. Wright, S. M. Yu, J. B. Yoo, S. Russo and M. F. Craciun, *Advanced Materials*, 2018, **30**, e1802953.

29. S. W. Lee, J. W. Hong, M. Y. Wye, J. H. Kim, H. J. Kang and Y. S. Lee, *Nuclear Instruments and Methods in Physics Research Section B: Beam Interactions with Materials and Atoms*, 2004, **219-220**, 963-967.

30. S. Beckford and M. Zou, *Applied Surface Science*, 2014, **292**, 350-356.

31. Y. Fang, J. Yong, F. Chen, J. Huo, Q. Yang, H. Bian, G. Du and X. Hou, *Applied Physics A*, 2016, **122**, 826-833.

32. R. Xiong, K. Hu, A. M. Grant, R. Ma, W. Xu, C. Lu, X. Zhang and V. V. Tsukruk, *Advanced Materials*, 2016, **28**, 1501-1509.

33. P. Podsiadlo, A. K. Kaushik, B. S. Shim, A. Agarwal, Z. Tang, A. M. Waas, E. M. Arruda and N. A. Kotov, *Journal of Physical Chemistry B*, 2008, **112**, 14359-14363.

34. Y. Q. Li, T. Yu, T. Y. Yang, L. X. Zheng and K. Liao, *Advanced Materials*, 2012, **24**, 3426-3431.

35. Y. Song, J. Gerringer, S. Qin and J. C. Grunlan, *Industrial & Engineering Chemistry Research*, 2018, **57**, 6904-6909.

36. H. Xie, X. Lai, Y. Wang, H. Li and X. Zeng, *Journal of Hazardous Materials*, 2019, **365**, 125-136.

37. F. M. Fowkes, *Industrial & Engineering Chemistry*, 1964, **12**, 40-52

38. L. Cao, S. Deng and Z. Lin, *Polymers (Basel)*, 2016, **8**, 50-62.

39. Q. Cheng, M. Wu, M. Li, L. Jiang and Z. Tang, *Angewandte Chemie International Edition England*, 2013, **52**, 3750-3755.

40. P. Podsiadlo, A. K. Kaushik, E. M. Arruda, A. M. Waas, B. S. Shim, J. Xu, H. Nadivada, B. G. Pumplin, J. Lahann, A. Ramamoorthy and N. A. Kotov, *Science*, 2007, **318**, 80-83.

41. H. Min, N. Zheng, Z. Fan, Y. Jiang and X. Cheng, *Microelectronic Engineering*, 2019, **205**, 32-36.

42. L. Liu, J. Zhang, J. Zhao, F. Liu, *Nanoscale*, 2012, **4**, 5910-5917.

43. M. Yokoyama, A. Satoh, Y. Sakurai, T. Okano, Y. Matsumura, T. Kakizoe and K. Kazunori, *Journal of Controlled Release*, 1998, **55**, 219-229.

44. N. S. Nhlapo, W. W. Focke and E. Vuorinen, *Thermochimica Acta*, 2012, **546**, 113-119.

45. Y. Xie, J. Du, R. Zhao, H. Wang and H. Yao, *Journal of Environmental Chemical Engineering*, 2013, **1**, 1380-1384.

46. K. Hu, L. S. Tolentino, D. D. Kulkarni, C. Ye, S. Kumar and V. V. Tsukruk, *Angewandte Chemie International Edition England*, 2013, **52**, 13784-13788.

6. Nacre-like Freestanding Films Prepared by Self-assembly of Isocyanate-functionalised GO

6.1 Introduction

The strength of nacre-mimetic materials are governed by the intermolecular interactions between the layers that facilitate the dissipation of energy by different mechanisms.[1, 2] Through strong interactions between the nanoplatelet and polymer components, a cooperative effect yields stronger materials. The GO surface is abundant with oxygenated functional groups that enable hydrogen bonding between individual sheets and to suitable polymers (e.g. PVA). As a result, interfacial interactions are commonly strong in GO based nacre-mimetic materials however, with further functionalisation, these interactions can be greatly improved. Previous literature has explored the cross-linking of GO via covalent[3, 4] and non-covalent[5, 6] approaches. Covalent methods require treatment of the nacre-like film post-manufacture that can cause structural deformation, as reported in Chapter 5.4.4. Alternatively, non-covalent approaches can produce stable GO dispersions that can therefore proceed and allow self-assembly of platelets. For this reason, non-covalently functionalised GO was selected.

The 4-fold hydrogen-bonding synthon, 2-ureido-4-[1H]-pyrimidinone (UPy), was chosen so as to maximise the intermolecular forces between the GO sheets. The structure of the terminal ring facilitates an accepter-acceptor-donor-donor arrangement of hydrogen bonding, allowing dimerization between two complimentary UPy groups (Scheme 6.1). As a result, functionalisation of GO with UPy enables a significant increase in hydrogen bonding between adjacent sheets. This ultimately causes strong interfacial interactions that theoretically increase the mechanical properties of the nacre-like films. UPy can be easily produced in a one-step reaction from commercially available and inexpensive reagents.
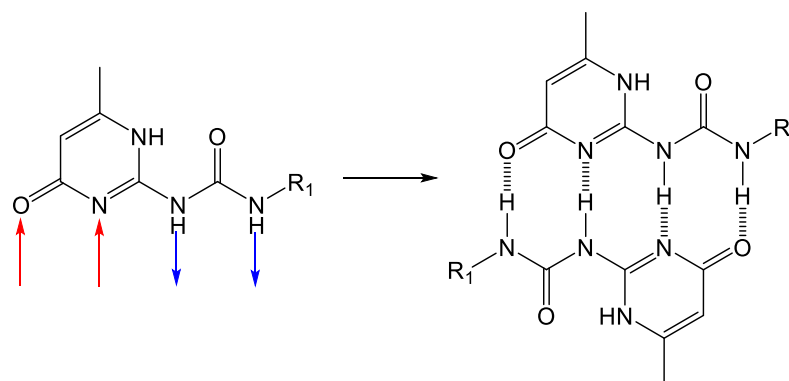
Scheme 6.1 – Hydrogen bonding dimerization of the UPy synthon. The hydrogen bonding sites are displayed as arrows on the UPy structure where red = acceptor and blue = donor sites.

Functionalisation of GO can be achieved using numerous methods.[7-9] Isocyanate-GO reactions allow RT functionalisation within 24 hours and at excellent yields.[10, 11] Despite this, reactions between GO and isocyanates are little explored, most likely due to the hazardous nature of isocyanate compounds. Carboxylic acid, hydroxyl and epoxide groups on the GO surface are able to react with isocyanate species through the mechanisms outlined in Scheme 6.2.[12, 13] The products of these reactions are all relatively benign, significantly reducing the hazard of the functionalised GO (GOx) product.

In this chapter, the hypothesis that functionalisation of GO with the 4-fold hydrogen bonding synthon, UPy, is an effective route for the production of nacre-like films with tailored mechanical properties will be tested. Characterisation of the GO powder is first reported followed by the synthesis of UPy and the associated reactivity towards GO. This reaction was followed using several techniques including FTIR, Raman, X-ray diffraction (XRD), X-ray photoelectron spectroscopy (XPS) and solid-state NMR (SSNMR). Nacre-like films were produced and studied using SEM, XRD and tensile testing.
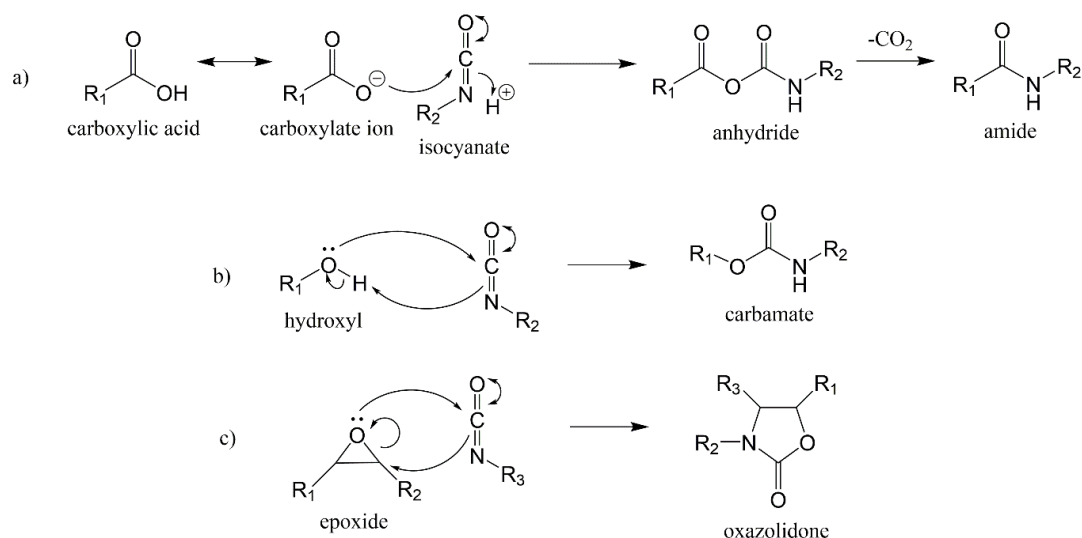
Scheme 6.2 - a) Reaction between a carboxylic acid group and isocyanate to produce an amide via a condensation reaction, b) reaction between a hydroxyl group and an isocyanate to produce a carbamate and c) reaction between an epoxide and an isocyanate to produce an oxazolidone

6.2 Comparison of GO powder and GO paste

Isocyanates readily react with water to produce amines and CO_2.[14] As a result, the GO paste used in the work described in Chapter 5 is unsuitable in this work. GO in powder form was used whereby the paste was freeze-dried. FTIR, Raman and TGA analysis were completed to ascertain if the freeze-dried powder was similar in composition to the paste used previously.

The FTIR spectrum is shown in Figure 6.1 a) and similar peaks are detected to those observed for the GO paste. The intensity of the O-H peak at $\approx$3500 cm^{-1} is higher in the powder, which could be due to an increased abundance of surface hydroxyl groups or a higher volume of atmospheric water. The presence of atmospheric water would prove detrimental to the reaction with isocyanates. Raman spectroscopy (Figure 6.1 b)) revealed the expected peaks for an oxygenated graphitic structure. The I_D/I_G ratio in this case was found to be 0.844 which is comparable to the GO paste (I_D/I_G = 0.848) suggesting a similar ratio of pristine to defect rich regions within/on the GO structure.

157
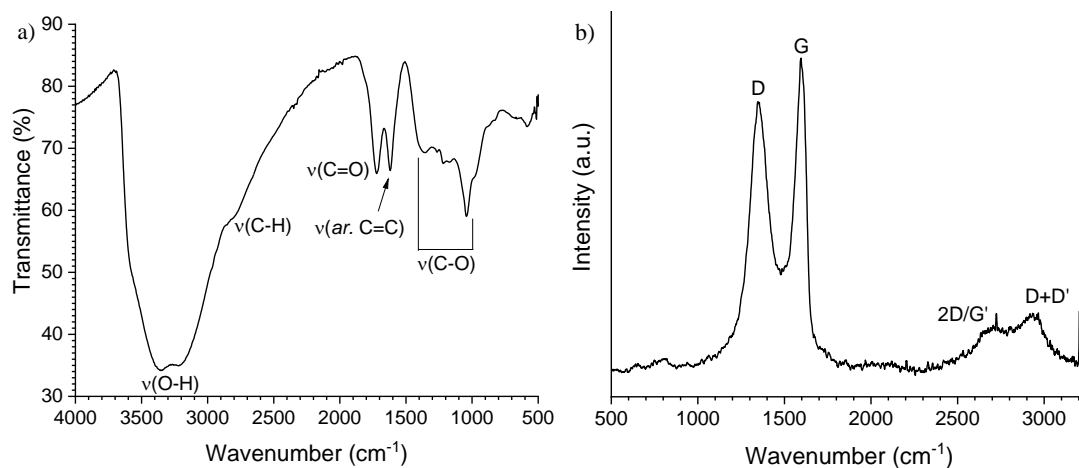
Figure 6.1 – a) FTIR and b) Raman spectra of the GO powder.
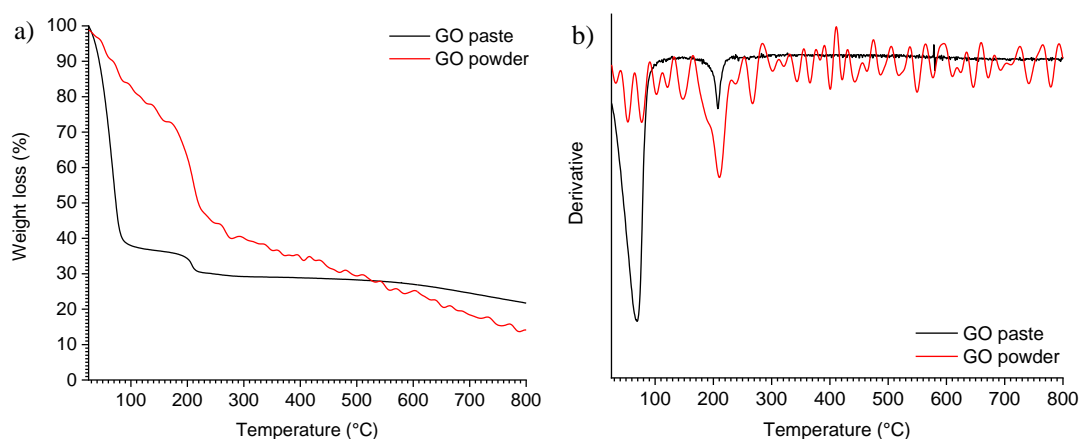
Figure 6.2 – TGA curve and differentiated TGA curve for the GO paste and powder where a) weight loss as a function of temperature and b) the derivative of the weight loss curve.

The TGA curve shows a main degradation peak at 210 °C (Figure 6.2) for the GO powder. An equivalent degradation profile is detected for the paste at 207 °C confirming the thermal properties of both GO samples are similar.

6.3 Functionalisation of GO with UPy

6.3.1 Synthesis of UPy

Synthesis of the UPy was achieved following the method outlined by Folmer *et al.*[15] Simply, 2-amino-4-hydroxy-6-methylpyrimidine (AHMP) is heated at 100 °C in an excess of hexamethylene diisocyanate (HDI) for 16 hours (Scheme 6.3) achieving an excellent yield of 99%. During the reaction, the UPy product precipitates as a white solid and so can be easily removed by filtration before washing with pentane. HDI behaves as a pseudo-solvent and thus no further chemicals are required. This results in some unreacted HDI however, on an industrial scale this could be recycled to improve the greenness of the process.
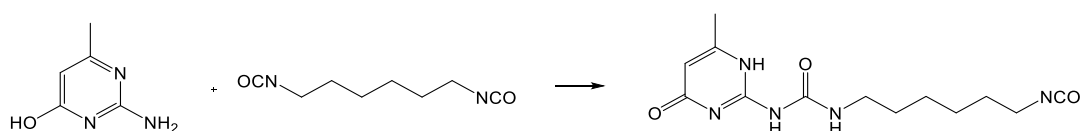
Scheme 6.3 – Reaction between 2-amino-4-hydroxy-6-methylpyrimidine and HDI to produce UPy.

Successful synthesis of UPy was confirmed by FTIR and ^{1}H NMR. The FTIR spectra of both UPy and the starting material, AHMP, are displayed in Figure 6.3. The key difference is seen at 2280 cm^{-1} where the formation of an N=C=O stretch appears in the UPy product. There is also the loss of the peak at 3315 cm^{-1} that corresponds to the hydroxyl group in the starting material. Following reaction with HDI, the cyclic structure undergoes an isomerisation to produce a ketonic group to enable stronger hydrogen bonding and dimerization. The dimerization then traps the structure in this isomeric form.

The ^{1}H NMR of the product can be seen in Figure 6.4. The N-H protons in multiple environments are detected at high chemical shift. In the case of position 3, this is due to the deshielding effect of the double bonds present in β-positions. The two urea protons at positions 4 and 5 experience deshielding from the carbonyl group

whilst proton 4 also experiences deshielding from the double-bonded carbon at the β-position. Assignments are in excellent agreement with previous literature.[15]
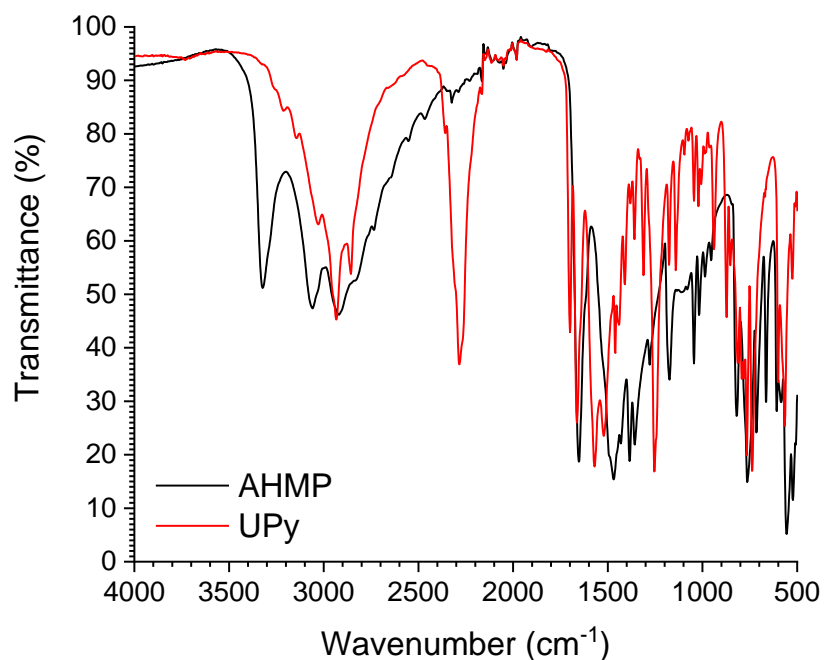
Figure 6.3 – FTIR spectrum of the starting material AHMP and the UPy product.
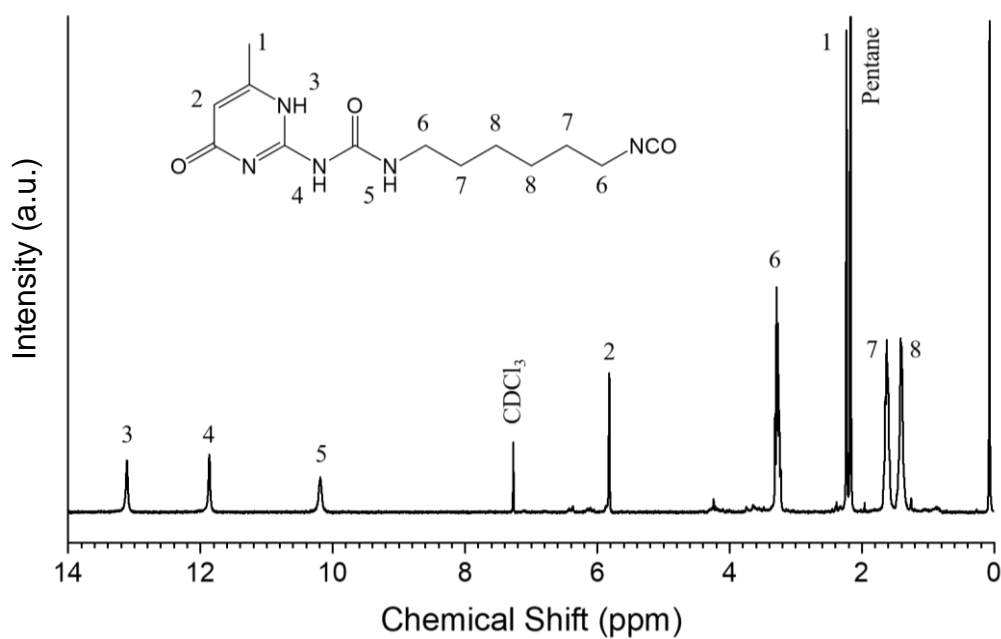
Figure 6.4 – ^{1}H NMR spectrum of UPy with relevant assignments.

6.3.2 Reaction of UPy with GO (GOx)

The reaction between UPy and GO followed the method outlined by Stankovich *et al.*[10] Both GO and UPy were added in powder form to a reaction vial at suitable mass to achieve GO:UPy weight ratios of 99:1, 90:10, and 50:50. These samples are coded as GO1, GO10 and GO50, respectively. GO0 denotes GO that has not been functionalised with UPy. Anhydrous DMF was added before the mixture is degassed and stirred for 24 hours. Brown powders were obtained in each case.

A successful reaction can be detected from FTIR spectroscopy (Figure 6.5 a)). Between 2000 cm^{-1} and 1000 cm^{-1}, GO0 has an O-H bend vibration for trapped water at 1618 cm^{-1}. The C=O stretching of carboxylic acid and ketonic groups is also detected at 1722 cm^{-1}.[16] New peaks are observed following the reaction with UPy at 1643 and 1560 cm^{-1}. The peak at 1643 cm^{-1} is assigned to an amide-carbonyl stretching vibration, otherwise known as the Amide-I vibrational stretch. At 1560 cm^{-1}, a coupling of the C-N stretch and CNH deformation vibration of an amide (known as the Amide-II vibration) is detected. This vibration can also be observed in carbamate species.[10] From the Raman spectra, a change in intensity of the D and G bands of the GO following reaction with UPy (Figure 6.5 b)) is observed. Table 6.1 outlines the quantitative trends and shows an increase in I_D/I_G upon addition of UPy, symptomatic of an increase in the sp^3 domain within the GO. The change to the I_D/I_G ratio is relatively small and therefore suggests the functionalisation has a minimal effect, as would be expected with reaction at already defect-rich domains. The position of the D band is seen to shift by one wavenumber with each progressive increase in UPy content. The G band is also seen to shift following reaction with UPy however, remains constant for all the GOx samples.

Table 6.1 – I_D/I_G ratios for GOx materials

Sample	GO0	GO1	GO10	GO50
D band ($cm^{-1)}$)	1355	1354	1353	1352
G band (cm^{-1})	1600	1597	1597	1597
I_D/I_G ratio	0.848	0.874	0.871	0.919
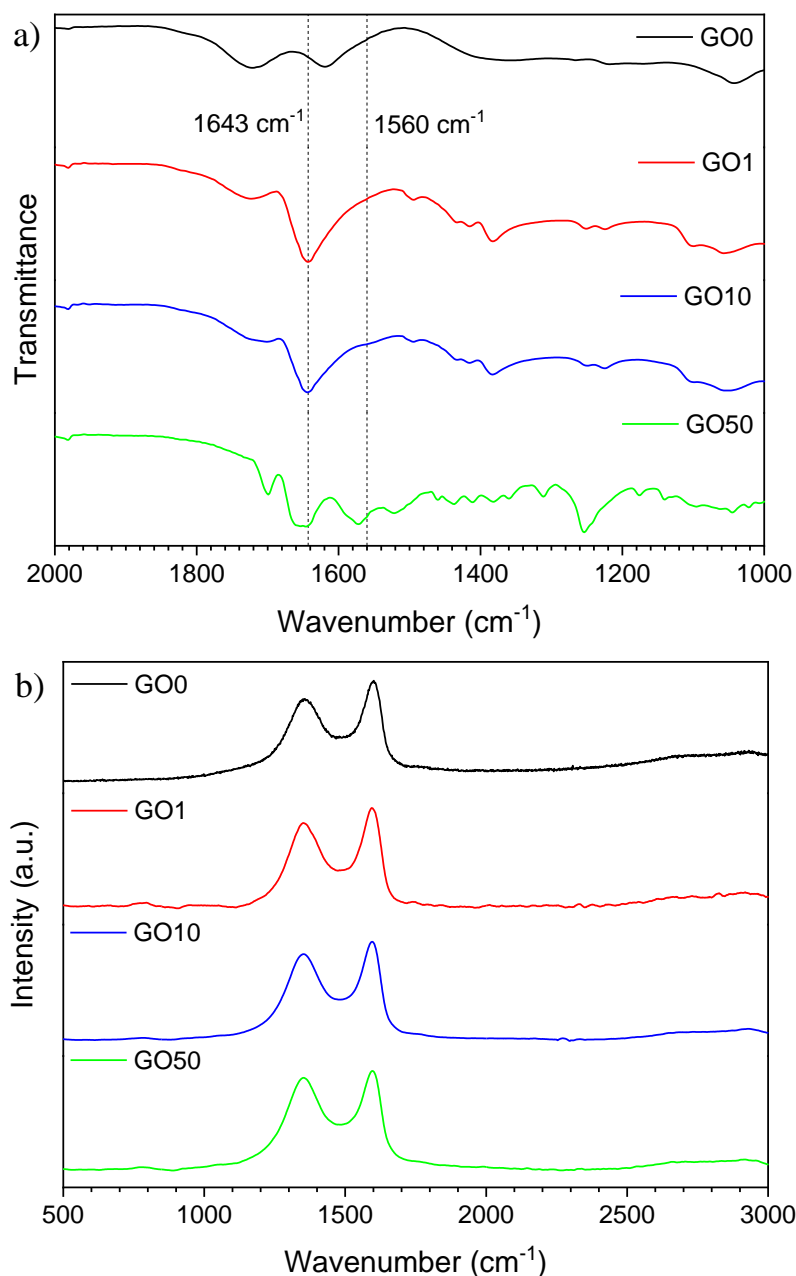
Figure 6.5 – a) FTIR and b) Raman spectra for GOx materials.

XRD can be used to determine interlayer distances of both the GO powder and nacre-like films. Using the measured diffraction angle, 2θ, the interlayer spacing (d) of crystalline material can be calculated using Bragg's Law, $n\lambda = 2d\sin\theta$ (where $\lambda = 1.541$ Å). XRD detects changes in 2θ and thus interlayer distance following reaction of GO with UPy (Figure 6.6). The most dominant peak in the GO0 spectrum is detected at $2\theta = 10.84°$ corresponding to a d spacing of 0.816 nm. This peak is seen to shift toward lower 2θ (i.e. larger d spacing) following the reaction with UPy with

162

greater shifts observed at higher UPy content. In the case of GO50, the *d* spacing increases to 1.144 nm. This trend supports the successful grafting of UPy to the GO surface.
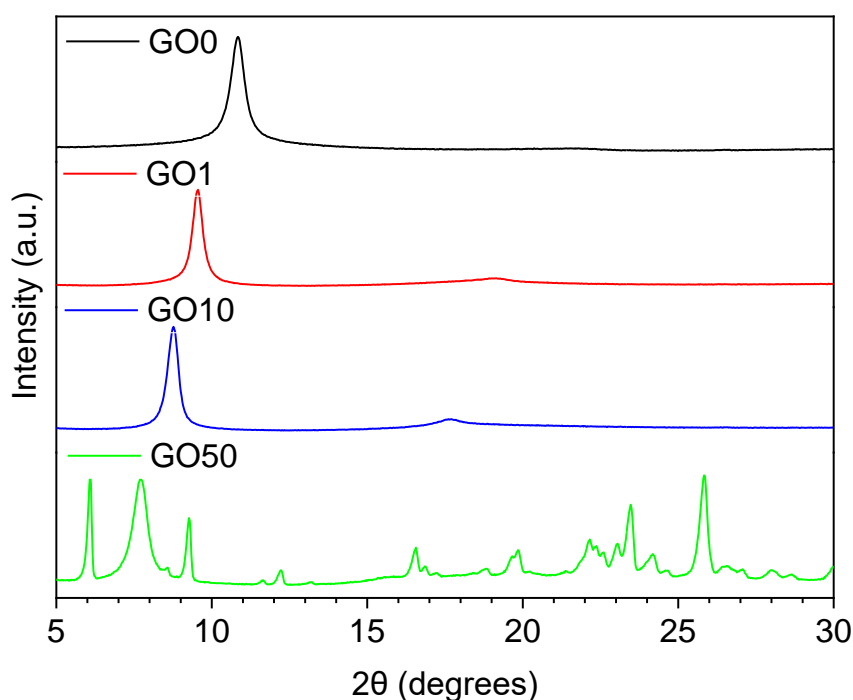
Figure 6.6 – XRD diffractograms of GOx samples in powder form.

Single-pulse ^{13}C magic-angle spinning (MAS) NMR measurements further support successful functionalisation of the GO. The spectrum acquired for GO0 displays characteristic resonances for surface terminated oxygen functional groups including epoxide (δ_{iso} = 61.8 ppm), hydroxyl (δ_{iso} = 70.2 ppm) and carbonyl groups (δ_{iso} = 166.1 ppm) with the sp^2 graphitic region of the GO surface detected as a broad peak at δ_{iso} = 121.4 ppm (Figure 6.7 a)). These assignments are in agreement with previous literature.[17, 18] Functionalisation with UPy produces new resonances at δ_{iso} = 31.8 ppm and δ_{iso} = 37.5 - 39.1 ppm (Figure 6.7 b)-d)). These peaks are assigned to the carbon environments in the six-membered ring of the UPy group. The spectra for GO50 shows a further seven peaks not detected in the other GOx samples. It is possible the UPy in other samples is not at a high enough content to be resolved by the SSNMR

however, is more likely due to unreacted UPy adsorbed to the GO50 surface, as is supported by XPS.
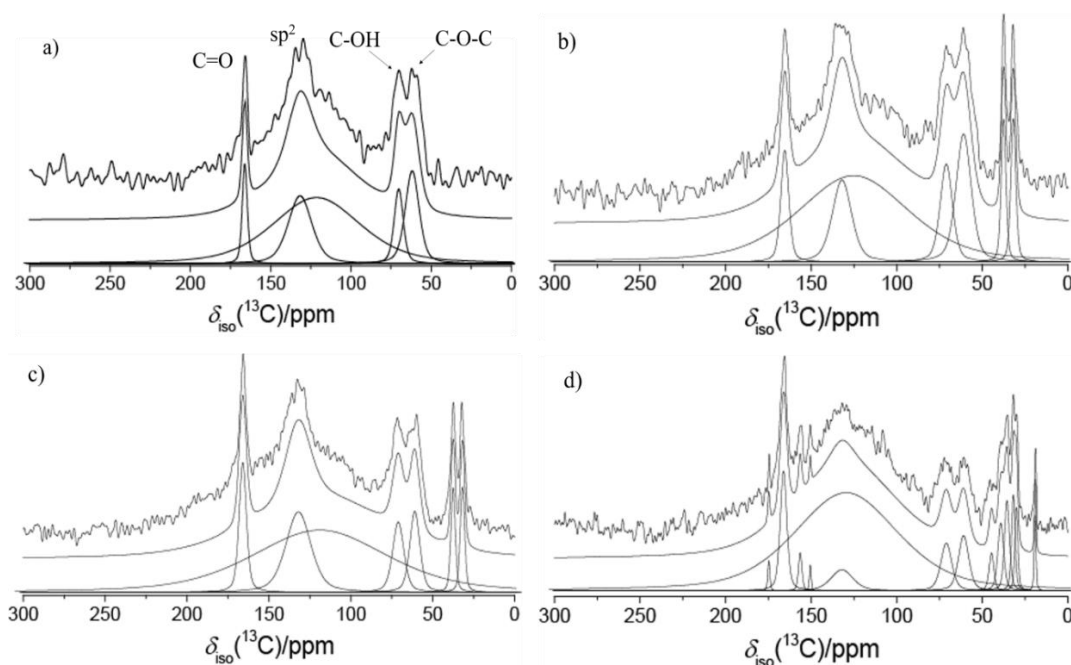
Figure 6.7 – Solid-state ^{13}C MAS spectra acquired for a) GO0, b) GO1, c) GO10, and d) GO50.

The intensity of GO hydroxyl and epoxide resonances decrease with functionalisation with UPy. The epoxide resonance at $\delta_{iso} = 60.9$ - 61.8 ppm decreases in intensity monotonically from 13.4%, 12.0%, 6.1% and 4.1% with increased UPy content. The trend for hydroxyl groups ($\delta_{iso} = 70.2 - 71.0$ ppm) shows an initial increase between GO0 and GO1 however, reduces in intensity with higher UPy content from 7.4% to 5.9% to 3.4%. This confirms the UPy isocyanate group reacts with both epoxide and hydroxyl groups on the GO surface. The resonance for the carbonyl group of the carboxylic acid groups at $\delta_{iso} = 131.7 - 132.0$ ppm shows no trend. This suggests the UPy group does not react at these sites, favouring the hydroxyl and epoxide groups. This corroborates the reaction mechanism outlined in Scheme 6.2 where the carboxylic acid group must be deprotonated before reaction with the isocyanate species. Due to the acidic nature of the GO dispersions, the carboxylic acid

group will remain protonated during the UPy treatment and hence is blocked from reacting.

XPS confirms nitrogen content for the GO0 is 0%. Following reaction with UPy, nitrogen increases proportionally with increasing UPy content (Table 6.2). The evolution of the N_{1s} peak ($\approx$400 eV) is also observed in the XPS survey plot (Figure 6.8 a)) supporting successful UPy grafting.

Table 6.2 – Elemental composition and carbon-nitrogen bonding content for GO and GOx samples from XPS analysis.

Sample	Elemental Composition			N_{1s} region (carbon-nitrogen bonding)		
	C (%)	O (%)	N (%)	C=N (%)	C-N (%)	C-N corrected (%)
GO0	65.84	32.76	0	0	0	0
GO1	67.09	30.55	0.61	0	28.24	28.24
GO10	67.90	28.54	1.68	0	46.04	46.04
GO50	66.78	23.73	7.68	15.15	57.92	68.26

The de-convoluted C_{1s} spectrum of GO50 (Figure 6.8 c)) shows the development of multiple nitrogen-based bonding environments when compared to the C_{1s} of GO0. GO0 displays four peaks attributed to the binding energies of C-C (284.5 eV), C-O (286.4 eV), C=O (287.2 eV) and O=C-O (288.5 eV). Following reaction with UPy, three new peaks are detected that correspond to C-N (285.6 eV), O=C-N (288.1 eV), N-(C=O)-N (290.1 eV). This provides a further indication of successful UPy grafting. The C-C peak also splits into separate sp^2 (284.1 eV) and sp^3 (284.8 eV) signals.

The de-convoluted N_{1s} peak of GO1 (Figure 6.8 d)) and GO10 (Figure 6.8 e)) both detect the presence of two bonding environments; N-C (399.8 and 400.2 eV) and N-H (401.3 and 401.7 eV).[19] The GO50 spectra (Figure 6.8 f)) displays a third environment assigned to N=C (399.0 eV). This is most likely due to unreacted UPy

adsorbing on the GO surface through hydrogen bonding. Assuming the contribution of N=C is from unreacted UPy, the C-N percentage can be corrected to more accurately display the degree of functionalisation of the GO50 sample (Table 6.2). It is expected that the intensity of the N-C and N-H signals would increase proportionally. Despite this, the N-C signal is seen to increase in intensity when compared to N-H at higher UPy content. This is because the UPy dimers form more readily at high content due to increased availability of hydrogen bonding partners. XRD confirmed the increase in interlayer distance at high UPy content and so it is likely the dimers migrate between the layers. As a surface technique, XPS is not able to detect the dimers between the layers however, is able to detect the N-C linking group between the GO and UPy groups. SSNMR confirmed the reaction proceeds via the hydroxyl and epoxide groups that are concentrated on the edges of the GO nanosheets and therefore the N-C link is permanently located in a detectable position.

Previously published literature has outlined titration methods for the determination of isocyanate content in different media.[20, 21] Essentially, these methods utilise the reaction between free isocyanates and dibutylamine (DBA) to observe a change in pH of a controlled solution. A simple acid-base titration is used and the endpoint observed with the colour change of bromophenol blue from blue to a pale yellow. The reaction between the isocyanate and DBA produces a urea (Scheme 6.4). Titration against an acid of known molarity allows accurate calculation of the isocyanate concentration through the following equation:[20]

$$\%\text{NCO} = \frac{C_{HCl} \times (V_{mean\,blank} - V_{sample}) \times M_{NCO}}{W_{sample}} \times 100 \tag{1}$$

where, C_{HCl} = the concentration of HCl in mol/L, V = volume of acid titrated for either blank or test samples, M_{NCO} = molecular weight of an isocyanate group (42 g/mol) and W_{sample} = the mass of isocyanate sample tested.
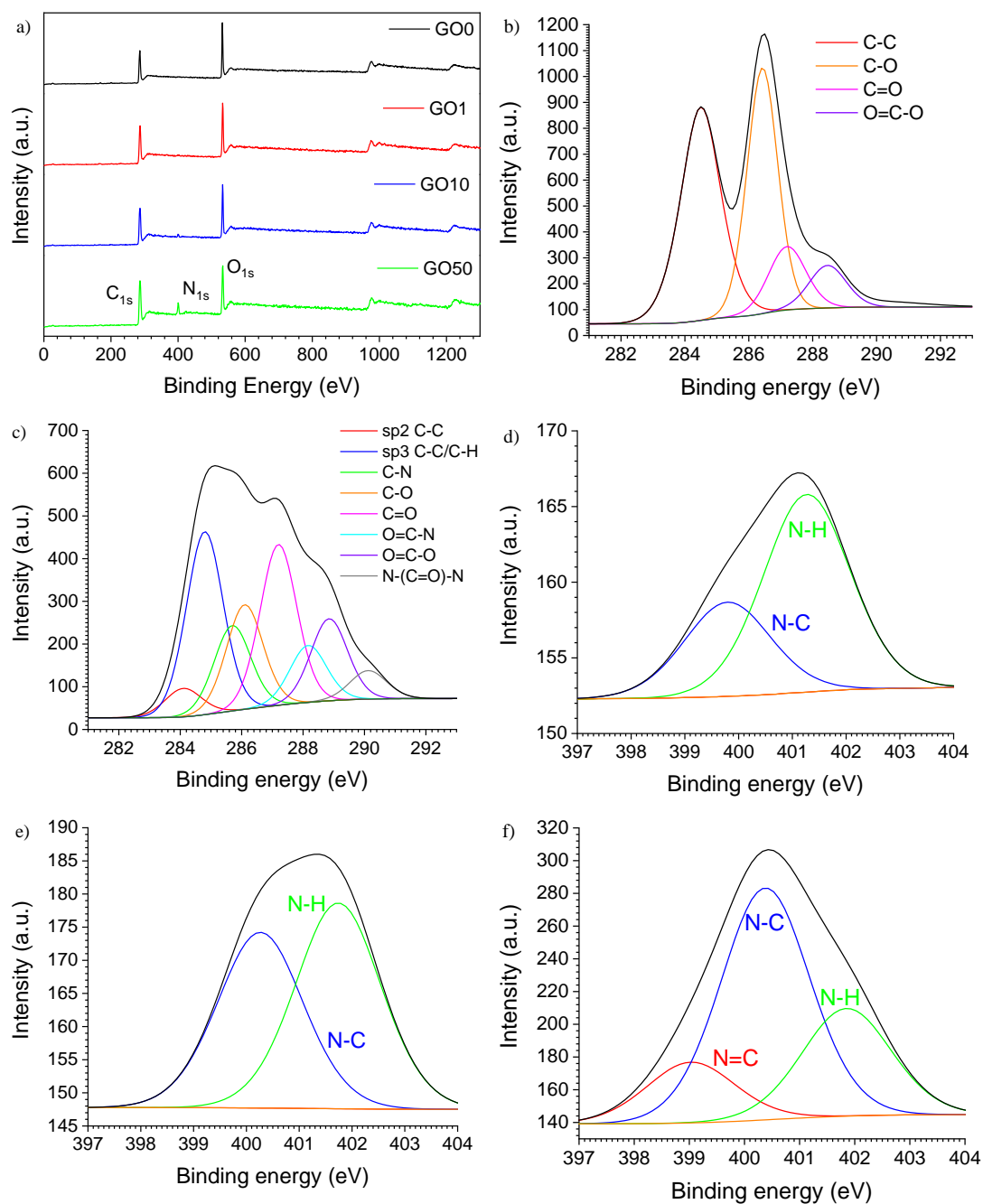
Figure 6.8 – XPS spectra where a) survey spectra, deconvoluted C_{1s} spectra for b) GO0 and c) GO50, and deconvoluted N_{1s} spectra for d) GO1, e) GO10 and f) GO50.
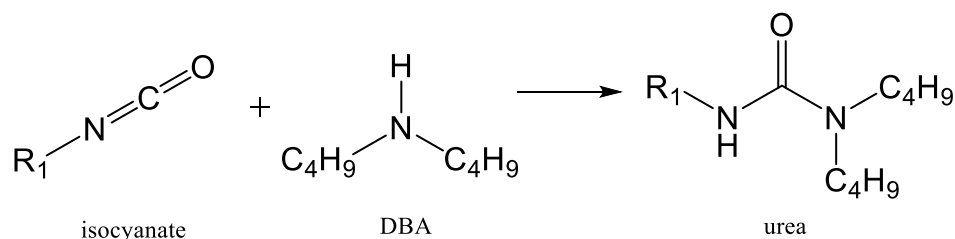
Scheme 6.4 – Reaction of an isocyanate with DBA to produce a urea.

Titrations of the GOx products were completed using a slightly modified method.[20] In each case, ≈50 mg and 5 replicates of each weight ratio were stirred for 24 hours in DBA, gravity filtered and titrated. It is expected that the titre would decrease with increased isocyanate content. On the contrary, the titre volumes for GO1, GO10 and GO50 show an increase when compared to the GO0 blank (i.e. the GO without functionalisation), see Figure 6.9. It is to be expected that the GO0 blank would have a significant impact on the titre volume when compared to DBA due to the highly acidic nature of the GO surface. The GO0 is surface functionalised with carboxylic acid groups that provide the acidic properties observed. Due to the increase in titre volume following functionalisation, it is likely these carboxylic acid groups react with the isocyanate and convert them to a less acidic amide. This is supported by FTIR data however contradicts the SSNMR studies. When inputting the GOx titre volumes into equation (1), negative values are calculated confirming it is not suitable for use in this scenario. To confirm the trends observed, GO was functionalised with a second isocyanate (HDI) using the same methods. It can be seen that a similar trend is observed in this case confirming the validity of the UPy titrations. With further testing, it is believed titrations could be used to effectively follow and quantify isocyanate functionalisation of GO.
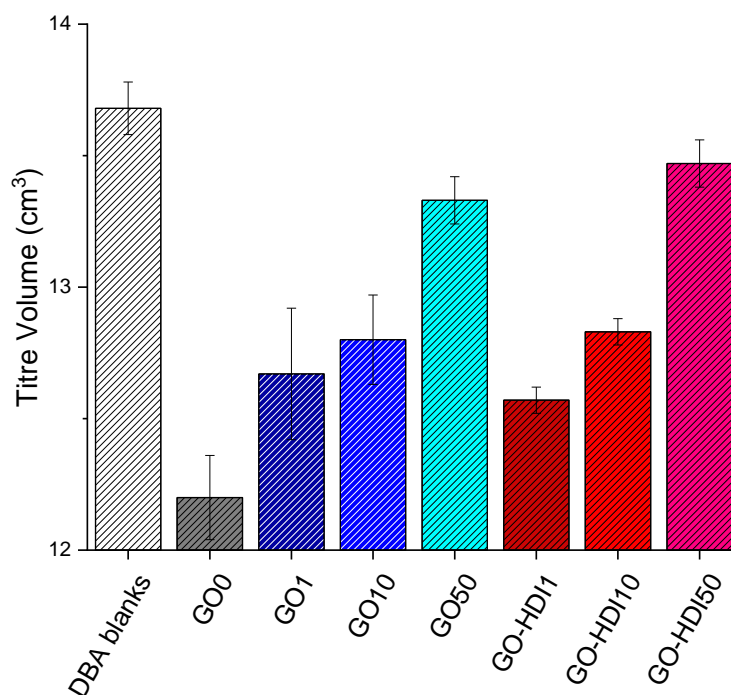
Figure 6.9 – Titre volumes for DBA, GOx and GO-HDI samples.

6.4 Preparation of GOx nacre-mimetic films

6.4.1 Stability of GOx dispersion in suitable solvents

Because of the chemical modification of the GO surface, the aqueous dispersions of GO1, GO10 and GO50 were unstable. This is due to the hydrogen bonding UPy dimers binding the GOx platelets and preventing effective exfoliation. The dispersions were observed to lighten in colour between 0 and 24 hours, symptomatic of solid-phase settling. Production of films via casting of water-based dispersions yielded bi-phasic films (Figure 6.10). The nacre-mimetic layers observed in the top section are produced via self-assembly and the more inhomogeneous orientation in the bottom section results from settling. Due to the morphology observed from this SEM, it is proposed that due to the low content of UPy (1 wt% of GO), not all the GO sheets are functionalised with the UPy group. As a result, the GO1 settles out from the water-phase whilst the un-functionalised GO0 remains stable and self-assembles.
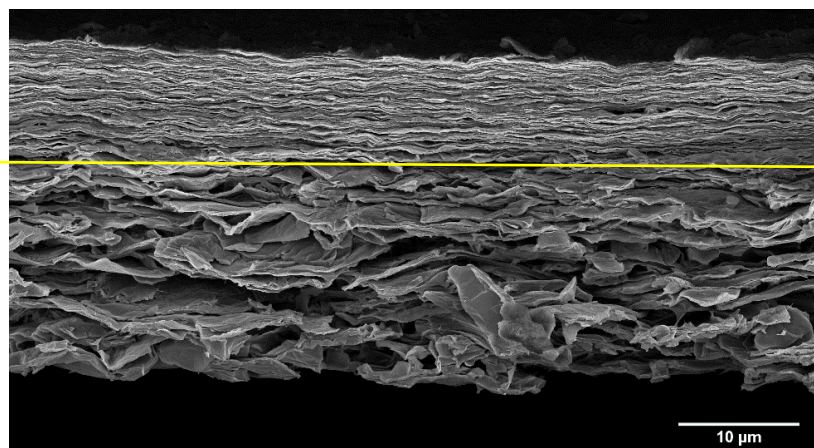
Figure 6.10 – Cross-sectional SEM image of the GO1 sample produced via casting in water. The yellow line shows the boundary between the two morphological sections.

The stress-strain curves and mechanical properties of the GO1 film are shown in Figure 6.11. When compared to GO0, produced by the same method, the Young's modulus (E) and maximum tensile strength (σ) decrease. The maximum strain (ε) and tensile toughness (U_T) increase following functionalisation. The heterogeneous morphology of the lower section, as observed in the SEM above, provides no mechanical strength to the material. As a result, the contribution to E and σ are solely from the nacre-like upper section, greatly reducing the extent of the cooperative energy dissipation mechanisms. The ε increases due to the long carbon chain of the UPy group enabling greater elongation before reaching tension. Ultimately, E and σ for this film are poor due to the heterogeneous structure.

The SEM imaging and tensile testing confirmed that water was not suitable for solution casting. As a result, studies were completed to assess the stability of the GOx dispersions in a range of alternative solvents. These dispersions were photographed immediately following one hour stirring and then subsequently after one hour with no further agitation. Those samples that did not settle were then re-examined after 24 hours, and subsequently 96 hours. The images taken are shown in Table 6.3. Only dispersions in DMF, DMSO and water were stable for 1 hour. The dispersions in DMF became more transparent, symptomatic of settling and, after 24 hours had fully settled.

DMSO was the only solvent that produced a stable dispersion throughout the 96 hour test window and, thus was selected for film preparation.
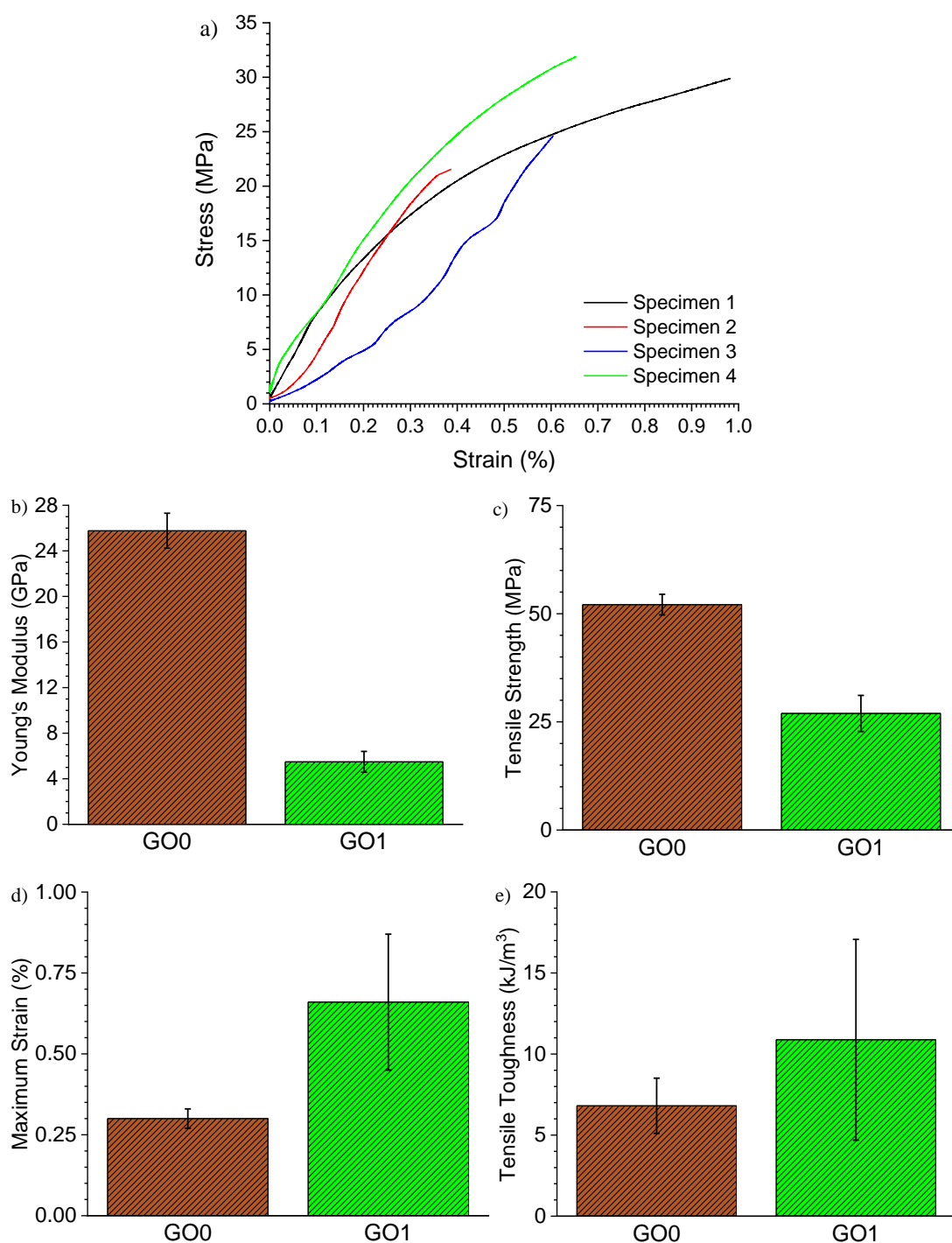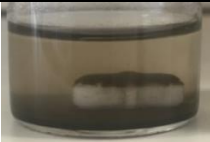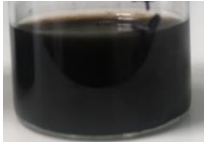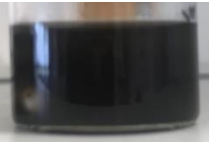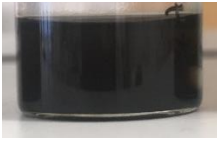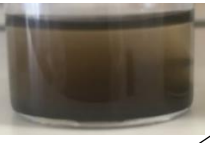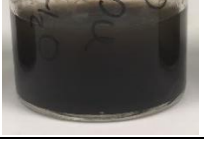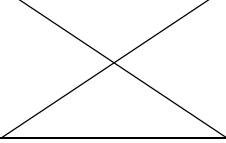
Figure 6.11 – Tensile data for GO1 produced via solution casting in water where a) representative stress-strain curves and b) Young's modulus, c) tensile strength, d) maximum strain, and e) tensile toughness when compared to GO0 films.

Table 6.3 – Dispersions of GO1 in a range of solvent systems to test stability for a period of up to 96 hours.

Time (h)	0	1	24	96
Acetone				
EtOAc				
IPA				
DMF				
DSMO				
DCM				
THF				
Water				

DMSO is a non-hazardous solvent but has a very high boiling point (189 °C) and is not volatile under ambient conditions. For these reasons, solvent casting would only be possible with extremely long drying times or the use of high temperature (which may compromise the stability of the GO structure). From initial tests it was observed that the DMSO was able to solubilise the PET substrate resulting in strong adhesion between the film and the substrate. Ultimately, an alternative sample

172

preparation method was required and vacuum filtration offered the simplest route to achieving similar freestanding films.

6.4.2 Vacuum filtration of GOx dispersions

A simple and widely used method was employed to produce nacre-like films of the GOx samples via vacuum filtration.[5, 22-25] Dispersions of the GOx powders in DMSO were filtered through a PTFE membrane and dried overnight at 40 °C. Once dry, the nacre-like film can be peeled from the membrane to achieve freestanding films.
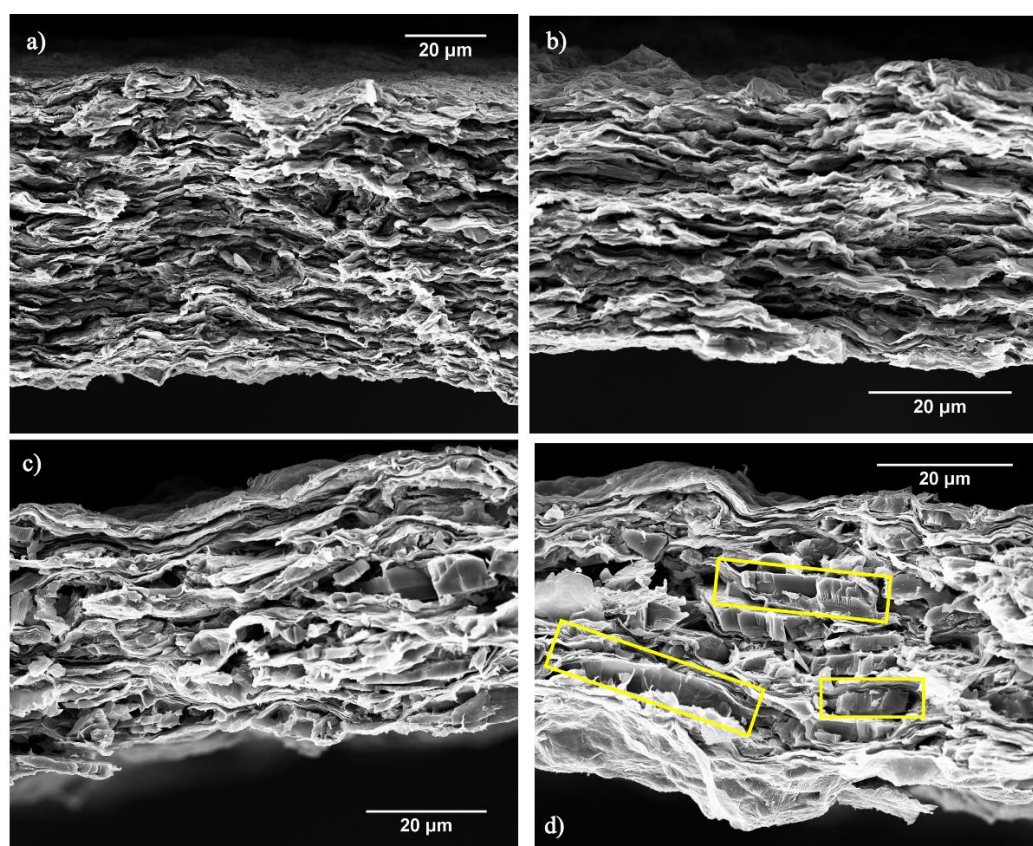
Figure 6.12 – Cross-sectional SEM images of a) GO1, b) GO10, c) GO50 and d) GO50 with highlighted 'brick-like' structure in yellow.

Cross-sectional SEM confirms the production of the uni-directional layered arrangement of GOx, therefore proving the method is suitable for the production of

nacre-mimetic films (Figure 6.12). Morphological defects were confirmed by the presence of 'brick-like' structures throughout the GO50 samples (Figure 6.12 d)). It is possible that these structures are produced from densely packed GO50 creating strongly bound sheets through multiple hydrogen bonding dimers. These structures are in a parallel orientation to the rest of the layers due to the favourable interactions between the surface groups and the bulk GO50 sheets. This phenomenon is not observed for GO1 and GO10 and therefore is directly associated with high UPy functionalisation.

6.4.3 Chemical and mechanical properties of GOx nacre-like films

XRD of the GOx films shows a change in interlayer distance (Figure 6.13). For GO0, the peak at $2\theta = 9.48°$ corresponds to a d-spacing of 0.934 nm. This is larger than that of the GO in powder form (0.816 nm) confirming the powder is more densely packed. Following the reaction with UPy at 1 wt% (GO1), the d-spacing is seen to decrease to 0.921 nm ($2\theta = 9.63°$) and is most likely due to improved packing from stronger intermolecular interactions, facilitated by the increased hydrogen bonding of UPy. Interestingly, further increases of UPy content result in an increase in interlayer distance to 0.943 nm ($2\theta = 9.37°$) and subsequently 0.959 nm ($2\theta = 9.29°$) for GO10 and GO50, respectively. Critically, the increased UPy content creates greater steric effects as the UPy dimers force the GOx sheets apart. At low UPy content (GO1), the increased interactions facilitate dense packing however at UPy >10 wt%, the size of the UPy group dominates and a larger d-spacing is observed.

As is the case with other techniques, GO50 displays additional peaks not detected in the other samples. A lower $2\theta = 6.13°$ peak is detected corresponding to a d-spacing of 1.44 nm and corresponds to highly exfoliated GO50 sheets. Despite this, the d-spacing of the nacre-like films is lower for both GO50 and GO10 than the powder equivalents. This suggests the hydrogen bonding potential of UPy promotes packing when at high content and self-assembled into a uni-directional layered morphology. At low content, platelet packing is improved in a random orientation and is likely a result of the steric effects of the UPy preventing effective alignment of the GOx sheets. The uni-directional layered morphology is aided by the improved self-assembly (facilitated by the UPy group) and so promotes tighter platelet packing at high UPy content.
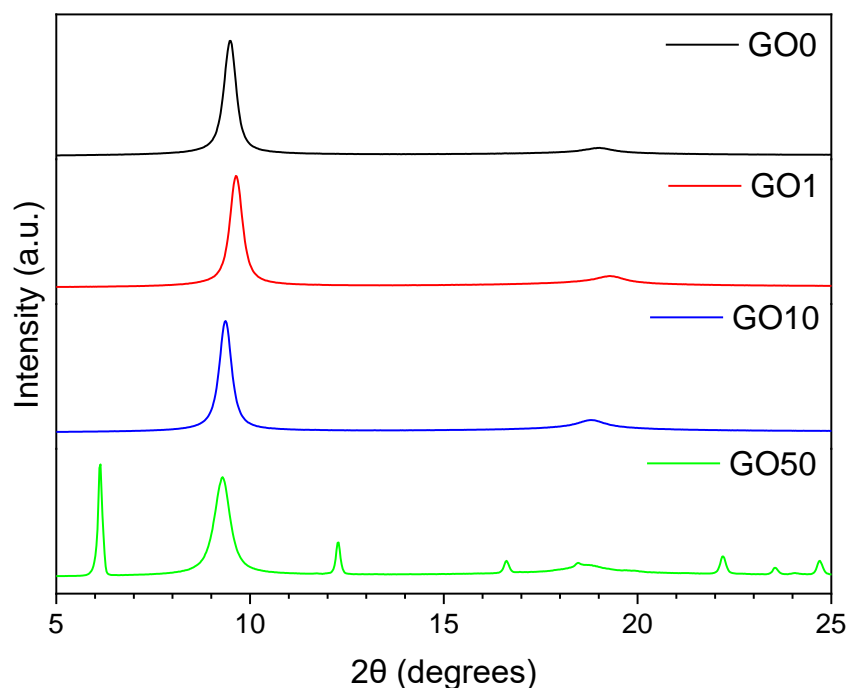
Figure 6.13 – XRD diffractograms for GOx nacre-like films.

The tensile properties of the films were tested with the results displayed in Figure 6.14 and the resulting mechanical properties tabulated, see Table 6.4. The reaction of UPy with GO results in increased E, σ, ε and U_T for all films tested, confirming the hypothesis that the improved hydrogen bonding interactions increase the mechanical properties of the films. Traditionally, nacre-mimetic materials fail through mechanisms including platelet fracture or yielding of the soft interface (i.e. the polymer).[26] The GOx films have no 'soft' component and therefore fail through platelet fracture or yielding of the interface between the GOx layers. By improving the interactions between the GOx sheets, the energy necessary to reach failure increases. This is most clearly observed in σ where an increase of 470% is observed between GO0 and GO50. An increase in σ is observed as the UPy content is increased.
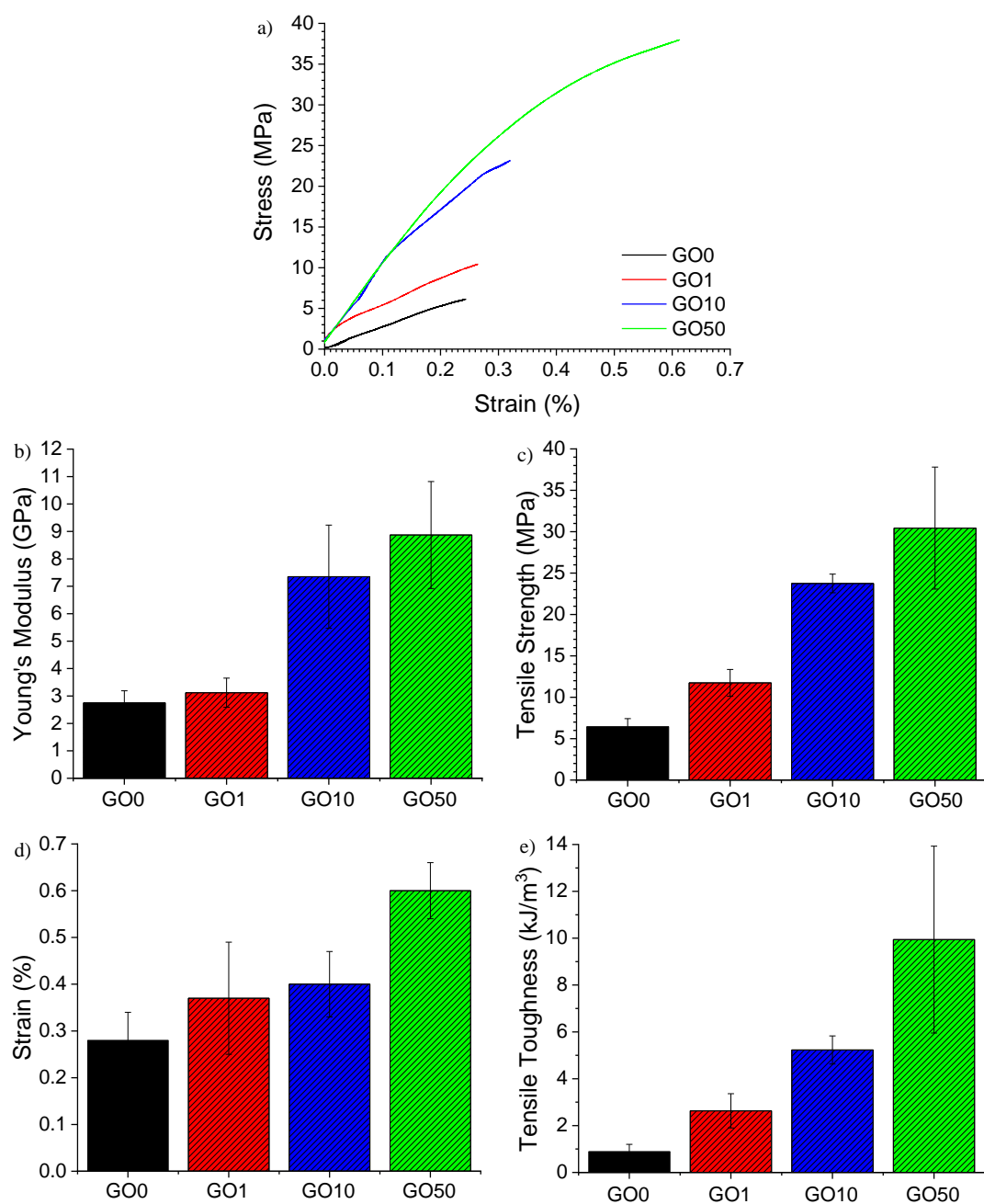
Figure 6.14 – Tensile testing data acquired for GOx films where a) representative stress-strain curves for each composition, b) Young's modulus, c) tensile strength, d) maximum strain and e) tensile toughness.

Table 6.4 – Average values (±standard deviation) for mechanical properties calculated from tensile testing of GOx nacre-like films.

	Young's Modulus (GPa)	Tensile Strength (MPa)	Maximum Strain (%)	Tensile Toughness (kJ/m^3)
GO0	2.75 ± 0.44	6.45 ± 0.97	0.28 ± 0.06	0.89 ± 0.31
GO1	3.12 ± 0.53	11.74 ± 1.62	0.37 ± 0.12	2.63 ± 0.73
GO10	7.35 ± 1.88	23.75 ± 1.13	0.40 ± 0.07	5.23 ± 0.60
GO50	8.87 ± 1.95	30.43 ± 7.37	0.60 ± 0.06	9.94 ± 3.99

A similar trend is observed for ε where a maximum increase of a factor of ≈2 is recorded. This is due to the six-carbon chain of the UPy group unfolding during tension and therefore allowing greater extension before failure. This effect is illustrated schematically in Figure 6.15. As UPy content increases, there are a greater number of six-carbon chains and so elongation will further increase.
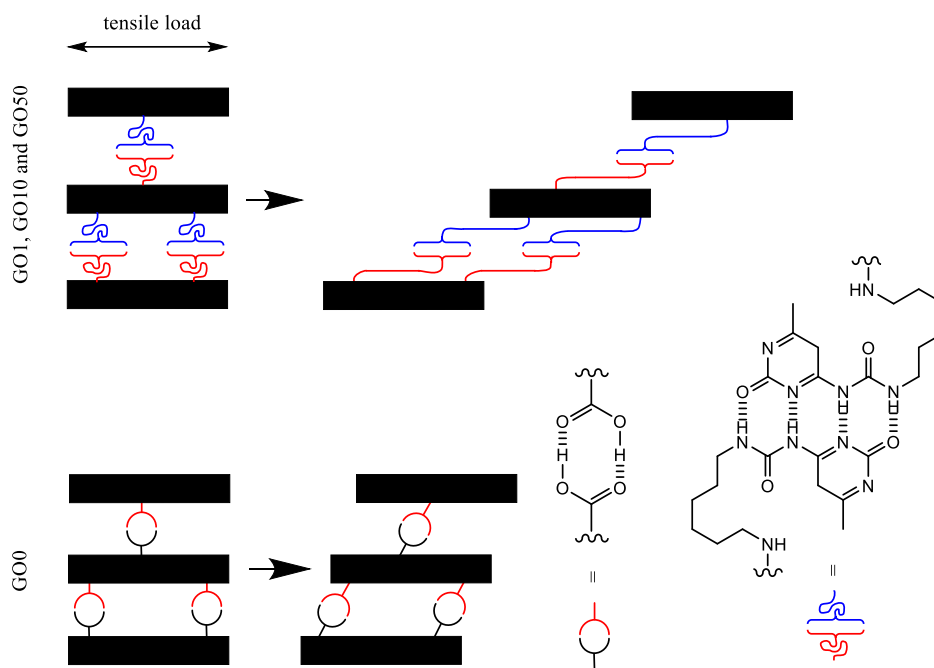
Figure 6.15 – Schematic representation of the change in molecular conformation observed for GO1, GO10 and GO50 films compared to GO0.

E increases with UPy content and is proportional to the ability of the 'matrix' to transfer load and provide reinforcement and dissipate shear stresses during loading. Typically, the matrix consists of the GO and polymer components however, in this structure, UPy behaves as a 'pseudo-polymer'. At high UPy content (i.e. GO10 and GO50), effective load transfer is large and results in a significant increase in *E* however in the case of GO1 and GO0, the 'matrix' effect is minimal due to the low concentration of the 'pseudo-polymer' (i.e. UPy groups). This ultimately results in low *E* and explains the significant increase in *E* between GO1 and GO10. U_T of GO50 shows a maximum increase of 1100%, relative to GO0 thus confirming the significant improvement in interfacial interactions possible through UPy functionalisation of GO. It should be noted that the *E* is decreased when compared to the GO-wsPU films in the previous chapter. This is likely a result of the differing film production method and dispersion solvent (i.e. water and DMSO) impacting on how the films self-assemble and dry.

Nacre-mimetic materials have been shown to enhance gas barrier properties[6, 27, 28] however, these reports typically discuss materials supported on a polymer substrate. Exploration and data on the barrier properties of freestanding nacre-mimetic films is much more limited. The GOx films were tested for oxygen (O_2TR), carbon dioxide (CO_2TR) and water vapour (WVTR) transmission rates, see Figure 6.16. The data shows that functionalisation with 1 wt% UPy increases the gas barrier properties when compared to GO0 however, higher UPy content has a negative impact on barrier performance. XRD confirmed an increase in interlayer distance with addition of higher UPy content and this increased distance between layers reduces the tortuosity and resistance to gas diffusion. Gas barrier properties depend strongly on the tortuosity of the pathway through the film.[29]

The WVTR of the GO50 film is lower than that of GO10. The hydrogen bonding synthon in UPy is able to bind with the water molecules, preventing permeation. UPy dimers have been previously shown to dissociate and exchange with water molecules.[30] The GO0 film has reduced hydrogen bonding potential but has smaller interlayer distances. The tortuous path is dominant in this case and so better barrier properties are observed. The GO1 films have the smallest interlayer distance and minimal potential for water capture and thus record the best barrier properties of

the compositions tested. Both GO10 and GO50 have larger interlayer distances however, GO50 has the greater potential for water capture. The larger interlayer distance results in relatively poor barrier properties but the increased hydrogen bonding potential for GO50 yields an increase over GO10.
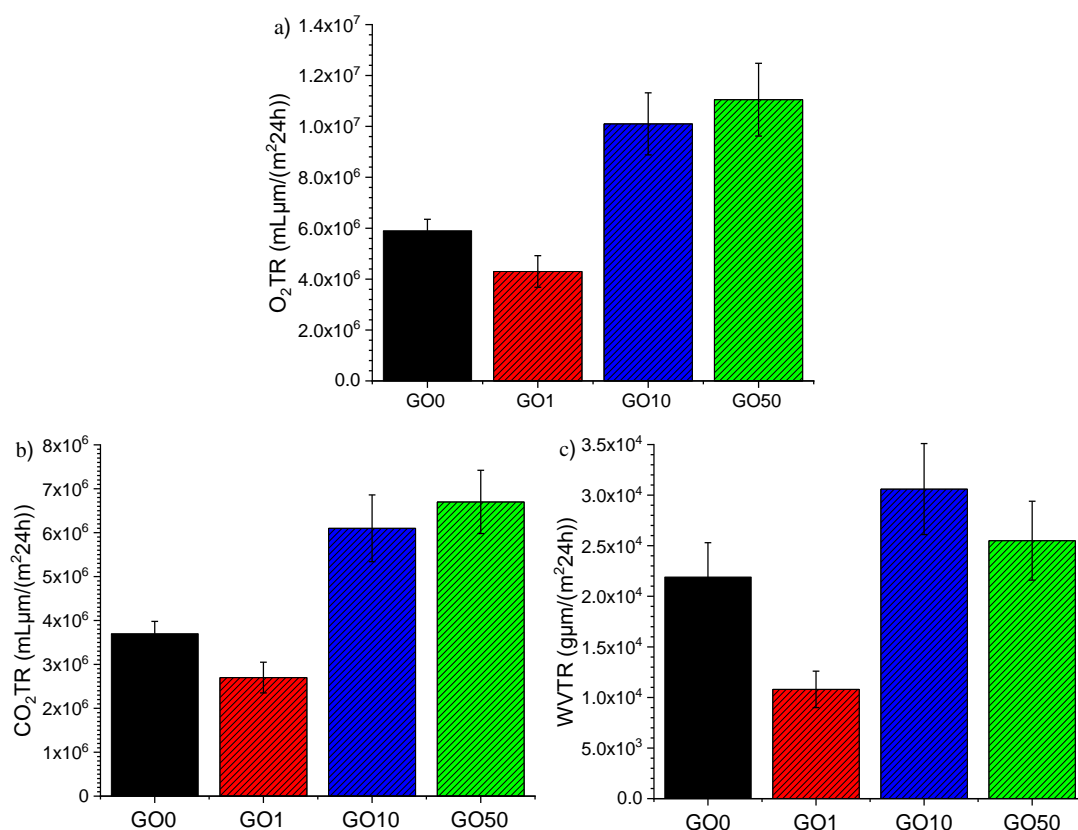
Figure 6.16 – Gas barrier properties for GOx films where a) oxygen transmission rate, b) carbon dioxide transmission rate and c) water vapour transmission rate.

The O_2TR, CO_2TR and WVTR detected for these films are lower than GO based nacre-mimetic materials previously reported[27, 31, 32] however, in each case these films contained a polymer component. The relatively poor barrier observed may be due to increased porosity as outlined by Medina *et al.*[33] for other 2D nanomaterials. The authors were able to determine that a 100 wt% nanoclay material (i.e. no polymer) was significantly more porous than the same nanoclay containing 20 wt% or more polymer. Imperfect nanoplatelet stacking causes 'pile-up' which ultimately produces

voids within the film structure. When a polymer is used, these voids are filled with the polymer material. As a result, it is likely the same phenomenon is occurring in the GOx films in this case. The absence of a polymer component increases porosity of the film and dramatically reduces the 'brick-wall effect'. This allows gases to more easily penetrate and permeate through the film.

6.5 Functionalisation of PVA with UPy (PVAy)

It is likely that the inclusion of a polymer component would greatly improve the mechanical properties of the GOx films through the introduction of further mechanisms to dissipate stress. Through functionalisation of the polymer with the UPy synthon, strong interfacial interactions are possible between the GO and polymer components. Poly (vinyl alcohol) (PVA) was selected as it is abundant with hydroxyl groups that facilitate hydrogen bonding and have therefore been widely used in nacre-mimetic materials.[34-36] The hydroxyl groups provide a good anchor to the GO sheets and also provide reactivity towards the UPy isocyanate. The combination of GO, UPy and PVA is highly novel.
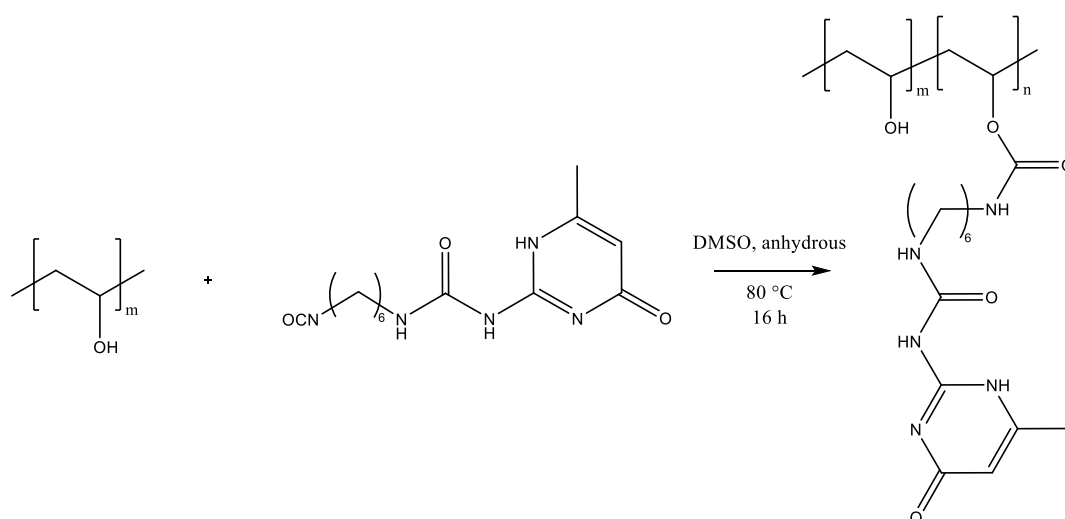
Scheme 6.5 – Synthetic procedure to synthesise PVAy product.

The PVA was functionalised using a simple method, see Scheme 6.5. UPy was first added to a vial followed by a 10 wt% solution of PVA in anhydrous DMSO. The

resulting mixture was degassed for 15 minutes to remove any residual water vapour in the headspace before heating at 80 °C for 16 hours. Mixtures containing >10 wt% UPy gelled, as would be expected for a highly cross-linked polymer system. To free the functionalised PVA (PVAy), excess DMSO was added and the mixture agitated until a homogenous liquid was achieved. The polymer was then precipitated into excess isopropanol (IPA) and dried under vacuum. UPy content between 1 wt% and 50 wt% were produced however those with >10 wt% remained as a gel following addition of DMSO and so could not be precipitated. Powder samples of PVAy, where UPy content = 1, 5 and 10 wt% were synthesised, and will be referred to as PVA1, PVA5 and PVA10, respectively. PVA0 denotes PVA that has not been functionalised with UPy.
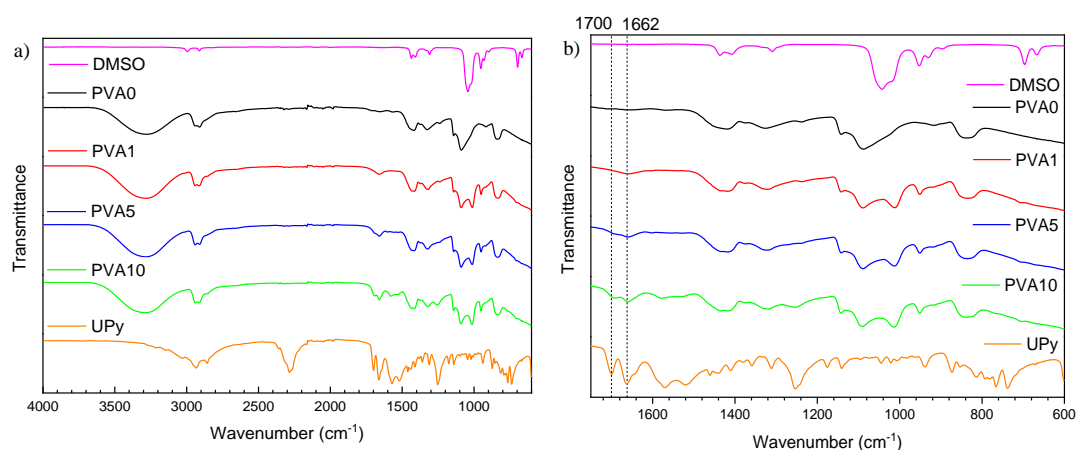
Figure 6.17 – FTIR spectra of DMSO, PVA0 and PVAy samples where a) full spectrum from 4000 to 600 cm^{-1} and b) enlarged region between 1750 and 600 cm^{-1}. Diagnostic peaks are highlighted with a dashed line and labelled with the corresponding wavenumber.

The gelation of the PVAy-DMSO mixtures is an indicator of a successful reaction however, FTIR was employed to confirm functionalisation (Figure 6.17). The DMSO spectrum was included to disregard any peaks that may arise from residual solvent. Despite this, it appears that DMSO is adequately removed as the two peaks below 700 cm^{-1} (C-H bending modes of the methyl groups) are not present in any of the PVA spectra (Figure 6.17 b)). The peak at 1041 cm^{-1} (the S=O stretching vibration)

is not observed, further suggesting the effective removal of DMSO. Following the reaction with UPy, new peaks are detected at 950 cm^{-1} and 1012 cm^{-1} that can be assigned to a C=C-H bend and a C-N bend, respectively. However, peaks at similar shift are observed in the DMSO spectrum. As a result, these peaks cannot conclusively confirm a successful reaction. That the intensity of these peaks is constant further suggests these are derived from DMSO. The peaks at 1662 cm^{-1} and 1700 cm^{-1} increase in intensity at higher UPy content and are not present in the DMSO spectrum. These signals are assigned to a C=O stretch of the urea group and the ketonic C=O stretch from the six-membered ring respectively and are also observed in the UPy spectrum. The evolution of intensity suggests different levels of functionalisation have been achieved and the PVA-UPy reaction can be controlled. It is important to note there is no isocyanate stretch observed at 2286 cm^{-1}, as is detected in the UPy spectrum. This confirms the UPy has grafted to the PVA and is not present as an unreacted side-product.

6.6 Preparation of GOx/PVAy nacre-mimetic films

6.6.1 Sample preparation and SEM

GOx/PVAy films were produced using vacuum filtration as was outlined in section 6.4. For GOx, x denotes the UPy content on the functionalised GO (i.e. GO10 = 90:10 ratio by weight of GO:UPy), whilst for PVAy, y denotes the UPy content on the functionalised PVA (i.e. PVA10 = 90:10 ratio by weight PVA:UPy). All the samples in this section were produced using a GO:PVA weight ratio of 95:5. The GOx was stirred for 2 hours in DMSO to allow adequate dispersion before a 1 wt% PVAy in DMSO solution was added and the mixture stirred for 1 hour. The dispersion was then filtered through a PTFE membrane and dried overnight at 40 °C. Representative digital photographs of the films are displayed in Figure 6.18.
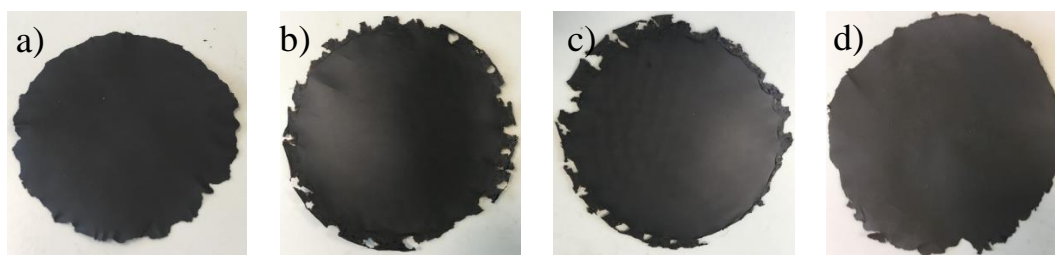
Figure 6.18 – Digital images of representative GOx/PVAy films where a) GO0/PVA10, b) GO1/PVA10, c) GO10/PVA10 and d) GO50/PVA10.

Cross-sectional SEM imaging was completed on the GOx/PVAy films, see Figure 6.19. Variations in the layered structure can be seen for different GOx films. An increased uniformity in the layered structure suggests improved packing between GO0/PVA5 (Figure 6.19 a)) and GO1/PVA5 (Figure 6.19 b)). Despite this, minimal changes are observed in d-spacing (0.965 nm for GO/PVA5 and 0.963 nm for GO1/PVA5). As a result, it is more likely that the variation in cross-sectional morphology is an artefact of the tensile failure used during preparation. The GOx layers in GO10/PVA5 are highly linear (Figure 6.19 c)) when compared to GO0/PVA5 and GO1/PVA5. In this case, it appears that packing is improved (d-spacing is reduced to 0.955 nm) and a highly ordered structure is produced. The layered structure in GO50/PVA5 is disrupted by the presence of the polymer component (Figure 6.19 d)), causing imperfections and voids.

Despite the unidirectional-layered morphology, imperfections were observed in a number of samples. Interestingly, defects were not observed in the GO0/PVAy films (i.e. GO0/PVA0, GO0/PVA1, GO0/PVA5 and GO0/PVA10), most likely due to the weaker hydrogen bonding of the GO0 hydroxyl, carboxylic acid and ketonic groups (compared with UPy) aiding exfoliation. Films containing GO1 and GO10 display some defects (Figure 6.20) that are similar to those reported in Chapter 5 when using wsPU. These imperfections are caused by incomplete exfoliation of the GOx component preventing adequate penetration of the PVAy between the GOx layers. Exfoliation is more challenging with the GO1, GO10 and GO50 (when compared to GO0) due to the greater interactions between the GOx sheets, facilitated by the UPy group.
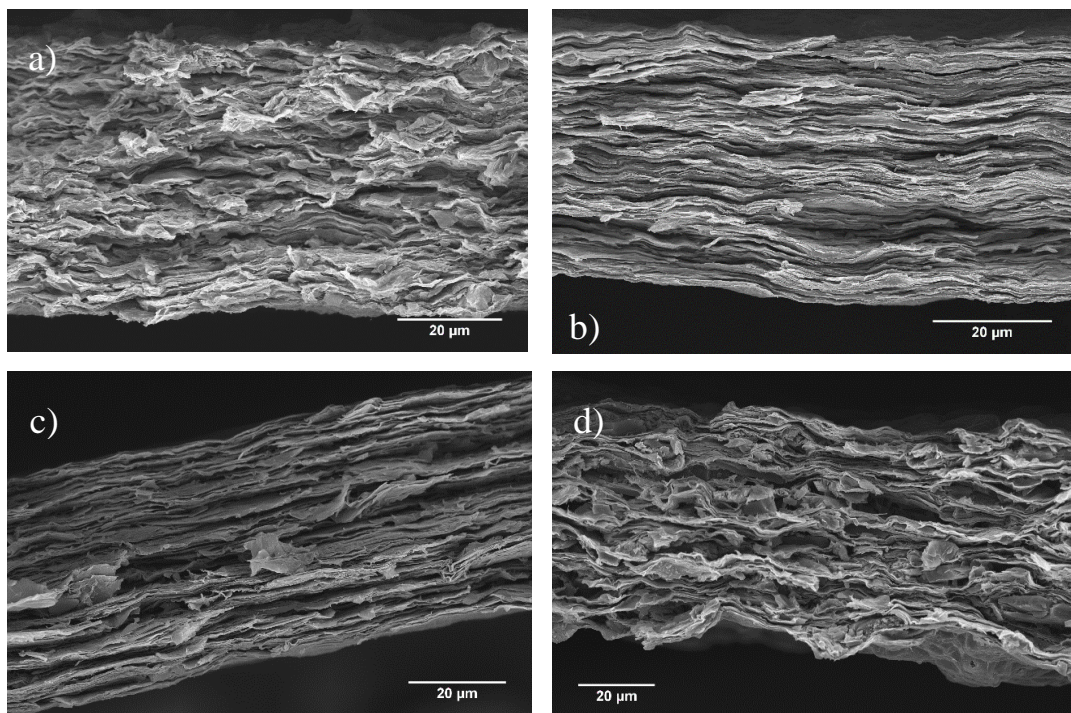
Figure 6.19 – SEM images of GOx/PVAy films displaying variations in layered morphologies where a) GO0/PVA5, b) GO1/PVA5, c) GO10/PVA5 and d) GO50/PVA5.
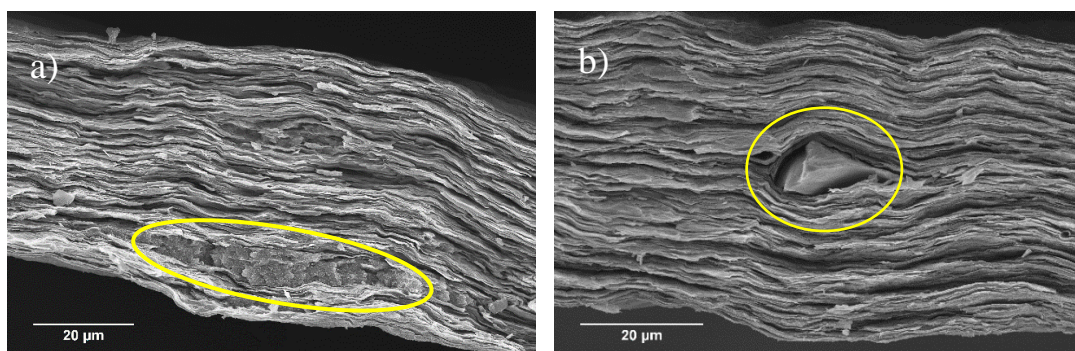
Figure 6.20 – SEM images showing imperfections (highlighted in yellow) in layer packing for the GOx/PVAy films where a) GO1/PVA5, and b) GO10/PVA5.

6.6.2 Chemical and mechanical properties of GOx/PVAy films

XRD measurements were completed (Figure 6.21) to determine the d-spacing between the GO platelets of the films (Figure 6.22). The inclusion of PVA0 increases

the interlayer distance between platelets of the GO0 films from 0.934 nm ($2\theta = 9.48°$) for GO0, to 0.974 nm ($2\theta = 9.08°$) for the GO0/PVA0 film. The PVA0 penetrates between the GO0 sheets, thus separating the GO0 layers. Interestingly, the interlayer distance decreases with increasing UPy (y) content on PVAy from 0.974 nm, to 0.968 nm, 0.965 nm and 0.963 nm for GO0/PVA0, GO0/PVA1, GO0/PVA5 and GO0/PVA10, respectively. This suggests the improved hydrogen bonding of the UPy group aids the packing of the GO0 nanoplatelets. The GO1 and GO10 samples also show an increase in d-spacing following addition of PVA0 from 0.921 nm for GO1 to 0.957 nm for GO1/PVA0 and from 0.943 nm for GO10 to 0.949 nm for GO10/PVA0. Critically, there is no obvious trend in d-spacing when increasing the y content of PVAy in both GO1 and GO10 films. It should be noted that for GO50, the inclusion of PVAy reduces the interlayer distance (0.959 nm for GO50 and 0.941 nm, 0.949 nm, 0.957 nm and 0.944 nm for GO50/PVA, GO50/PVA1, GO50/PVA5 and GO50/PVA10, respectively). This suggests PVAy has no influence on packing of the GOx nanoplatelets when the UPy content on the GOx exceeds 1 wt%. The significance of the interlayer distances (calculated from XRD) are now discussed in more detail in relation to the static tensile testing.

Static tensile testing was completed to determine the mechanical properties of the films. Representative stress-strain curves are shown in Figure 6.23. It is interesting to note that the GO1/PVAy films have the highest $\sigma = 62.85 \pm 7.27$ MPa, whilst GO10/PVAy films have the highest ε of up to $2.39 \pm 0.43\%$. This highlights the complexity of the competing energy dissipation mechanisms occurring within the films.
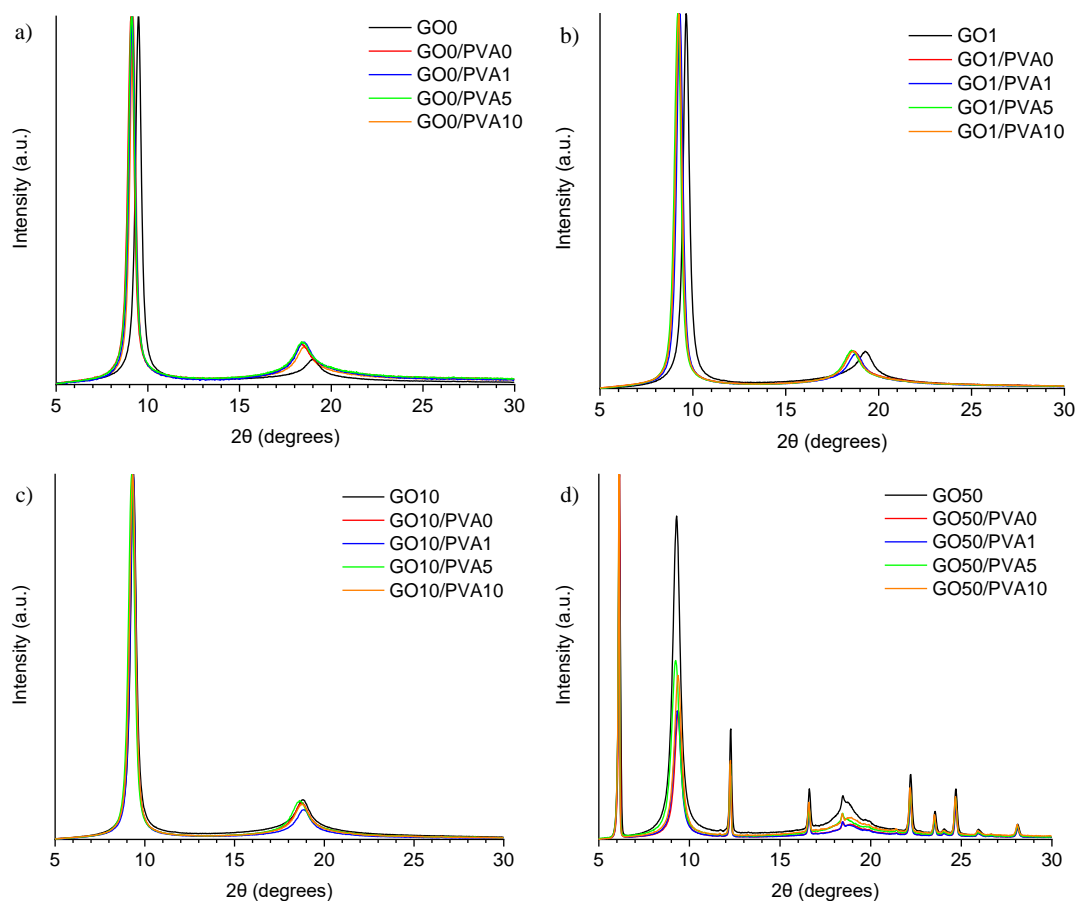
Figure 6.21 – XRD diffractograms of GOx/PVAy films for a) GO0 based films, b) GO1 based films, c) GO10 based films and d) GO50 based films.
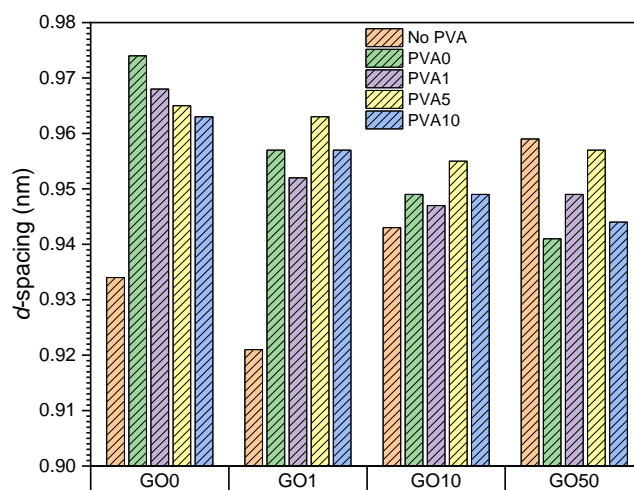
Figure 6.22 – Change in *d*-spacings for GOx/PVAy films (calculated from XRD) for GO0, GO1, GO10 and GO50 control films (Chapter 6.4).

The mechanical properties calculated from the stress-strain curves are displayed as bar charts in Figure 6.24. An increase in E from 2.75 ± 0.44 GPa for GO0 to 6.25 ± 3.28 GPa for GO0/PVA0 is observed. Despite this, the error in E for GO0/PVA0 is large and thus the influence of PVA0 on E is inconclusive. E increases for GO0/PVA1 (3.91 ± 0.76 GPa) compared to GO0. This is to be expected due to stiffening of the polymer,[36] previously discussed in Chapter 5.5.1 and suggests effective penetration of the PVA0 between the GO0 layers. For GO0/PVA5 and GO0/PVA10, $E = 5.17 \pm 1.15$ GPa and 5.04 ± 1.78 GPa, respectively, confirming an increase in E compared to GO0/PVA1. XRD confirmed that increasing the y content of PVAy (i.e. from PVA1 to PVA5 to PVA10) results in a reduction in d-spacing. Reduced d-spacing suggests improved packing and thus PVAy stiffening is more dominant and E increases.
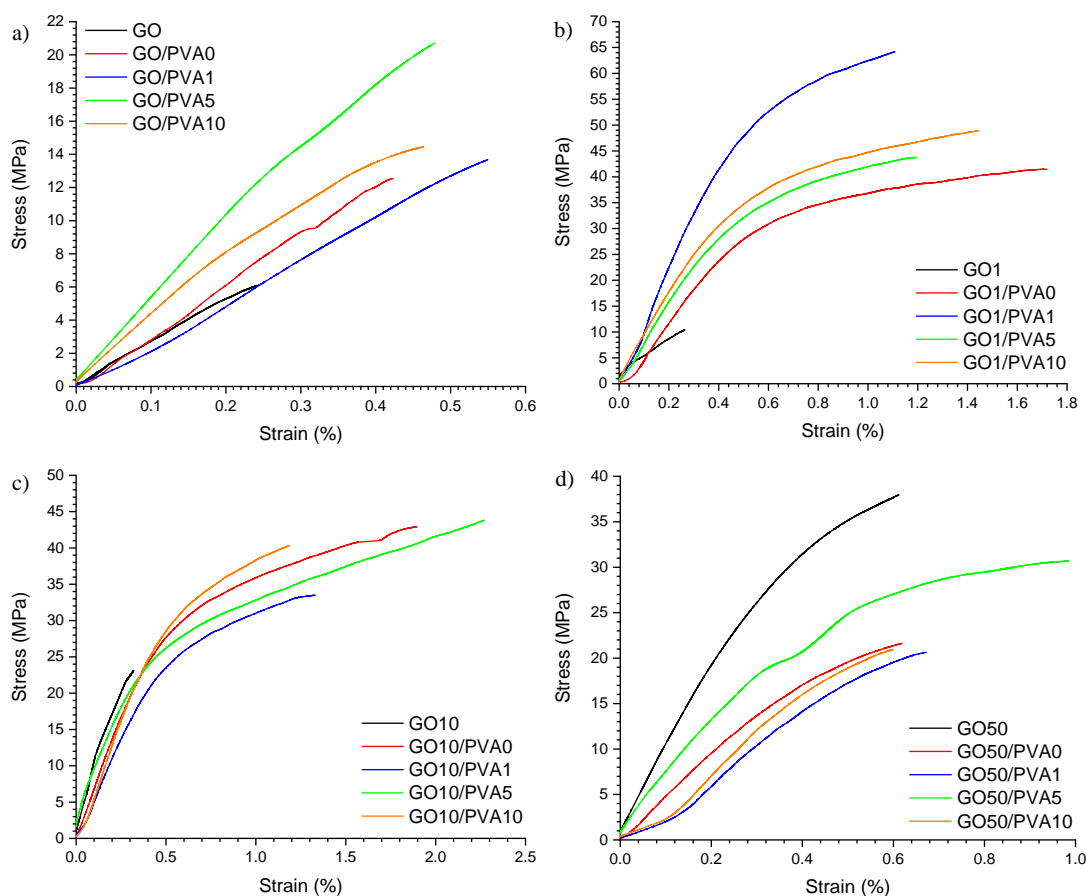
Figure 6.23 – Representative stress-strain curves for the GOx/PVAy films where a) GO0, b) GO1, c) GO10 and d) GO50 based films.

GO1 shows a significant increase for E upon addition of PVA0 from 3.12 ± 0.53 GPa for GO1 to 7.14 ± 0.29 GPa for GO1/PVA0, an increase of 229%. GO1/PVA1 further increases E to 12.24 ± 1.60 GPa, representing an increase of 392% and 171% compared to GO1 and GO1/PVA0, respectively. The UPy group (present on the GO1 and PVA1) forms strong interactions between the GO1 and PVA1 components, creating a 3D network of hydrogen bonding that increases PVAy stiffening. E is reduced for GO1/PVA5 and GO1/PVA10, down to 7.70 ± 0.24 GPa and 7.80 ± 0.26 GPa, respectively. The increasing y content on the PVAy results in a larger steric volume (UPy is much larger than hydroxyl pendant groups) of the PVAy component. This forces the GO1 nanoplatelets to separate and greater PVAy motion occurs. Separation of GO1/PVA5 and GO1/PVA10 is observed through the increased interlayer distance from XRD (GO1/PVA5 = 0.963 nm, GO1/PVA10 = 0.957 nm compared to GO1/PVA1 = 0.952 nm).
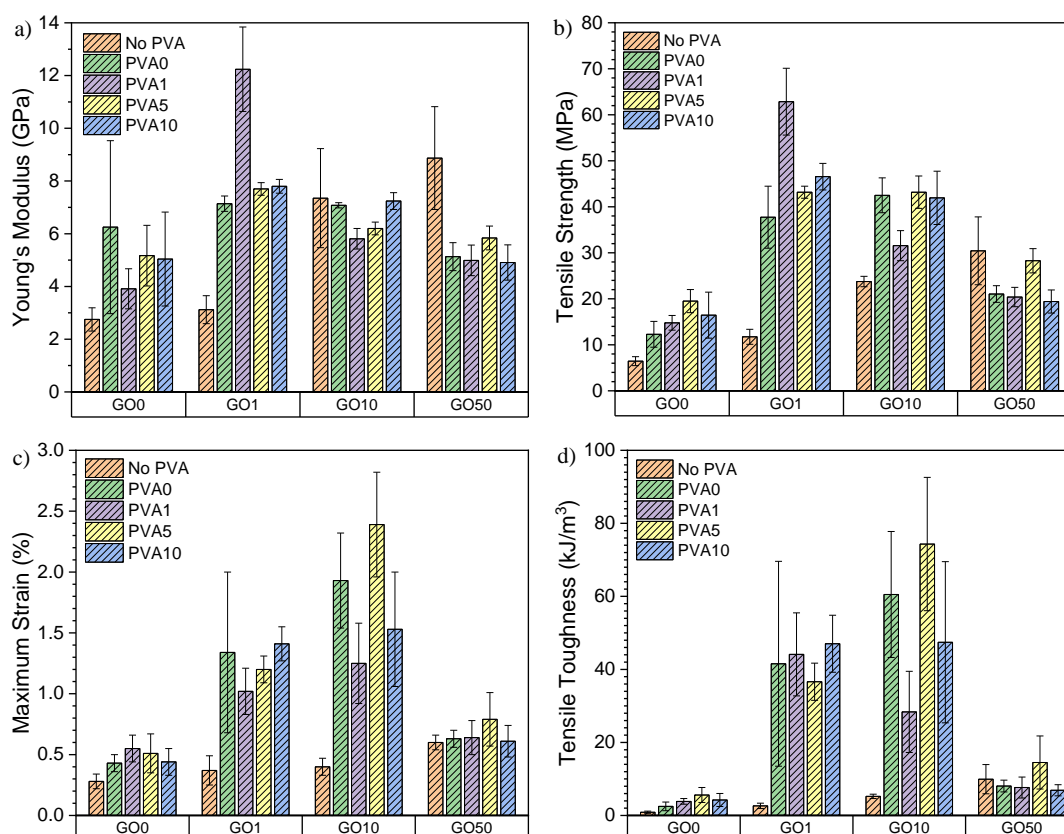
Figure 6.24 – Comparison of a) Young's modulus, b) tensile strength, c) maximum strain and d) tensile toughness of the different GOx/PVAy films.

The E of GO10 films ranges from 5.81 ± 0.39 GPa (GO10/PVA1) to 7.35 ± 1.88 GPa (GO10). The weight ratio of GOx:PVAy in these films = 95:5. As a result, increasing UPy content (x) in GOx (i.e. from GO1 to GO10) has a greater impact on the quantity of UPy groups in the structure compared to an increase to y in the PVAy (i.e. PVA1 to PVA10). It is therefore possible that in the GO10 films, the impact of changing the y content on the PVAy is not large enough to significantly affect E. The same is observed in the GO50 films where for all the GO50/PVAy films E is between 4.91 ± 0.67 GPa (GO50/PVA10) and 5.84 ± 0.45 GPa (GO50/PVA5). Interestingly, for GO50, $E = 8.87 \pm 1.95$ GPa, significantly higher than the GO50/PVAy films. It is likely the PVAy disrupts the strong hydrogen bonding between the GO50 nanoplatelets and thus reduces collaborative stiffening of the film.

In the case of GO0, σ increases from 6.45 ± 0.97 MPa for GO0 to 12.29 ± 2.80 MPa for GO0/PVA0, an increase of 191%. $\sigma = 14.78 \pm 1.59$ MPa for GO0/PVA1, 19.50 ± 2.52 MPa for GO0/PVA5 and 16.45 ± 5.00 MPa for GO0/PVA10. Critically, a significant increase to σ of 302% is observed between GO0 and GO0/PVA5. The GO0 nanoplatelets assemble into a porous structure. The pores localise stress and disrupt the dissipation of energy through the film. The PVAy occupies the pores within the film and bridges the GOx nanoplatelets. As a result, stress is dissipated over a larger area, resulting in an increase to σ. The GO1 film $\sigma = 11.74 \pm 1.62$ MPa however, addition of PVA0 yields an increase of 321% to 37.74 ± 6.75 MPa (GO1/PVA0). For GO1/PVA1 $\sigma = 62.85 \pm 7.27$ MPa, corresponding to a substantial increase of 535% over GO1. The UPy dimers between the GO1 and PVA1 create strong interfacial interactions that greatly increase the energy required to break the 3D network. The UPy content in GO1/PVA1 is optimal to maximise σ where the hydrogen bonding is most cooperative. GO1/PVA5 and GO1/PVA10 have $\sigma = 43.16 \pm 1.31$ MPa and 46.55 ± 2.89 MPa, respectively, most likely due to an increase in hydrogen bonding between PVAy chains hindering cooperative interactions with the GO1. Despite this, the σ still increases by close to 400% for both the GO1/PVA5 and GO1/PVA10 films when compared to GO1.

An increase to σ is recorded from 23.75 ± 1.13 MPa for GO10 to 42.50 ± 3.80 MPa for GO10/PVA0. No further increase is observed for GO10/PVA1 (31.55 ± 3.26 MPa), GO10/PVA5 (43.17 ± 3.52 MPa) or GO10/PVA10 (41.95 ± 5.79 MPa)

however, all have increased σ when compared to GO10. The increase in σ between GO10 and the GO10/PVAy films is due to the improved dissipation of stress as previously described. It is clear that increasing y content on the PVAy (i.e. PVA0 to PVA1, PVA5 and PVA10) does not increase σ. This suggests that hydrogen bonding between adjacent GO10 sheets dominates hydrogen bonding between the GO10 and PVAy.

Finally, σ decreases from 30.43 ± 7.37 MPa for GO50 to 21.03 ± 1.81 MPa, 20.39 ± 2.11 MPa, 28.27 ± 2.63 MPa and 19.41 ± 2.52 MPa for GO50/PVA0, GO50/PVA1, GO50/PVA5 and GO50/PVA10, respectively. GO50 had higher σ when compared to GO0, GO1 and GO10, suggesting the strongest hydrogen bonding between GOx sheets is present in the GO50 film. It is likely the PVAy disrupts the hydrogen bonding between the GO50 sheets, thus weakening interfacial interactions. As a result, stress cannot be dissipated between adjacent GO50 sheets resulting in a decrease in σ.

GO0 had $\varepsilon = 0.28 \pm 0.06\%$ with an increase of 154%, to $0.43 \pm 0.07\%$, recorded for GO0/PVA0. PVA0 hydrogen bonds to GO0 through pendant hydroxyl groups and the interactions to the GO0 allow the GO0 sheets to slide over each other as the PVA0 chains disentangle. GO0/PVA1, GO0/PVA5 and GO0/PVA10 recorded ε of $0.55 \pm 0.11\%$, $0.51 \pm 0.16\%$ and $0.44 \pm 0.11\%$ respectively, all showing an increase over the GO0 film. The increase to ε between GO0/PVA0 and GO0/PVA1, GO0/PVA5 and GO0/PVA10 is relatively small due to the lack of UPy functionalisation on the GO0 component.

For GO1/PVA0, $\varepsilon = 1.34 \pm 0.66\%$, a 362% increase over GO1 that measured $0.37 \pm 0.12\%$. In this case, the UPy on the GO1 binds to the hydroxyl groups of the PVA0 and the flexibility of the PVA0 enables extension through disentangling of the polymer chain. Similarly, for GO10/PVA0, $\varepsilon = 1.93 \pm 0.39\%$, compared to $0.40 \pm 0.07\%$ for GO10. ε is decreased for GO1/PVA1 ($1.02 \pm 0.19\%$) compared to GO1/PVA0 whilst GO10/PVA1 ($1.25 \pm 0.33\%$) decreases compared to GO10/PVA0. It is expected that ε would increase due to formation of UPy dimers between the GO1/GO10 and PVA1 components. The UPy six-carbon chain is longer than the hydroxyl groups present in PVA0 and so should extend further prior to failure. A

decrease in ε suggests the UPy dimers between the GO1 and PVA1 create anchor points that prevent the PVA1 chains from disentangling.

For GO10/PVA10, $\varepsilon = 2.39 \pm 0.43\%$ that corresponds to a 598% increase over the GO10 film ($0.40 \pm 0.07\%$). This represents the optimal GOx/PVAy composition for ε and is due to the cooperative effect of elongation of UPy dimers and disentangling of the PVA10 chains. This allows the GO10 sheets to slide over each other enabling high elongation. Critically, optimal UPy content is different for σ or ε properties.

For GO50, $\varepsilon = 0.60 \pm 0.06\%$ which increases slightly to $0.63 \pm 0.07\%$, $0.64 \pm 0.14\%$, $0.79 \pm 0.22\%$ and $0.61 \pm 0.13\%$ for GO50/PVA0, GO50/PVA1, GO50/PVA5 and GO50/PVA10, respectively. All these samples are within error and so the impact of the PVAy component is inconclusive. Despite this, it was previously discussed that the inclusion of PVAy in the GO50 films disrupts hydrogen bonding between the GO50 sheets. It is likely that increases to ε (due to the disentangling of PVAy) are negated by the disruption of hydrogen bonding and weakening of the interfacial interactions between GO50 sheets.

Tensile toughness is a strong indicator of the overall ability of the films to absorb energy prior to failure. Calculated from the area under the stress-strain curve, U_T depends on E, σ and ε. For GO0, $U_T = 0.89 \pm 0.31$ kJ/m^3 that increases 281%, to 2.50 ± 1.19 kJ/m^3, for GO0/PVA0. Subsequently, for GO0/PVA1, GO0/PVA5 and GO0/PVA10, $U_T = 3.86 \pm 0.79$ kJ/m^3, 5.61 ± 2.06 kJ/m^3 and 4.24 ± 1.79 kJ/m^3 respectively. PVAy aids in construction of a cooperative 3D network through occupation of pores within the GO0 structure. This enables dissipation of energy throughout the structure by eliminating localised stress points to increase σ and ε, resulting in an increase in U_T.

$U_T = 2.63 \pm 0.73$ kJ/m^3 for GO1 but critically, GO1/PVA10 yields a 1789% increase to 47.04 ± 7.81 kJ/m^3. This highlights the impact of strong UPy dimers between the GO1 and PVA10. The increased interfacial bonding strength, extension of the UPy dimer and disentangling of the PVA10 chains enable GO1/PVA10 to absorb and dissipate energy through multiple competing mechanisms. Maximum U_T was 74.33 ± 18.26 kJ/m^3 for GO10/PVA5, corresponding to a 1421% increase over GO10 and 6615% over GO0. GO10/PVA5 also had optimal ε and it is clear that the

UPy content on the GO10 and PVA5 yields strong cooperative interactions, producing a 3D network that effectively dissipates load.

Similarly to GO0, GO1, GO10 and GO50, σ and U_T of the GOx/PVAy films are lower than relative literature[37] with ionically[5, 6] and covalently[3, 4] cross-linked films reporting higher absolute values for σ and U_T. Despite this, E and ε are comparable in some cases. There is no widely accepted standard for tensile testing of films of this nature. Consequently, reported values of E, σ, ε and U_T can often be misleading. It is more valid to compare E, σ, ε and U_T to controls produced and tested using equivalent methodology as this provides a more realistic indication of the impact of any modifications. Functionalisation of GO and PVA with UPy for nacre-mimetic materials is highly novel and critically, in this work, increases to E, σ, ε and U_T are significant when compared to GO0, GO1 and GO10 controls. The increases to E, σ, ε and U_T (between GOx and GOx/PVAy films) eclipse those reported by Wang $et\ al.$,[37] Cui $et\ al.$[4] and Cheng $et\ al.$[3] however, when compared to the theoretical maximum E, σ and ε for GO, the films reported in this section achieve relatively poor mechanical properties.

6.7 Concluding remarks

In summary, it has been confirmed that GO can be functionalised with UPy using benign reaction conditions as confirmed by FTIR, Raman, XRD, SSNMR, XPS and titration. The resulting GOx powders can self-assemble into a uni-directional layered structure by vacuum-assisted filtration. These films represent the first example of UPy-functionalised GO nacre-like films reported in the literature. From static tensile testing, increases in E (323%), σ (470%), ε (214%) and U_T (1117%) between GO0 and GO50 were measured. Thus, it was proven that the UPy group promotes interfacial interactions between the GOx layers and provides reinforcement to the 3D film structure.

UPy reacted readily with PVA at RT, as confirmed by FTIR. The resulting PVAy dissolves in the GOx-DMSO dispersions and was found to self-assemble into a nacre-mimetic structure through vacuum-assisted filtration, thus producing the first GOx/PVAy films of their kind. The resulting films were found to display substantial increases in E, σ, ε and U_T of 392% (GO1/PVA1), 535% (GO1/PVA1), 598%

(GO10/PVA5) and 1789% (GO1/PVA10) that of the GOx analogues, respectively. Critically, the optimal UPy content for GOx and PVAy was different for E and σ (GO1/PVA1), ε and U_T (GO10/PVA5), confirming the energy dissipation mechanisms within the GOx/PVAy structures are complex and competing.

6.8 References

1.   L. Li and C. Ortiz, *Nature Materials*, 2014, **13**, 501-507.

2.   B. L. Smith, T. E. Schaffer, M. Viani, J. B. Thompson, N. A. Frederick, J. Kindt, A. Belcher, G. D. Stucky, D. E. Morse and P. K. Hansma, *Nature*, 1999, **399**, 761-763.

3.   Q. Cheng, M. Wu, M. Li, L. Jiang and Z. Tang, *Angewandte Chemie International Edition England*, 2013, **52**, 3750-3755.

4.   W. Cui, M. Li, J. Liu, B. Wang, C. Zhang, L. Jiang and Q. Cheng, *ACS Nano*, 2014, **8**, 9511-9517.

5.   S. Park, K.-S. Lee, G. Bozoklu, W. Cai, S. T. Nguyen and R. S. Ruoff, *ACS Nano*, 2008, **2**, 572-578.

6.   K. Shahzadi, I. Mohsin, L. Wu, X. Ge, Y. Jiang, H. Li and X. Mu, *ACS Nano*, 2017, **11**, 325-334.

7.   S. S. Abbas, G. J. Rees, N. L. Kelly, C. E. J. Dancer, J. V. Hanna and T. McNally, *Nanoscale*, 2018, **10**, 16231-16242.

8.   Y. Song, Y. Gao, H. Rong, H. Wen, Y. Sha, H. Zhang, H.-J. Liu and Q. Liu, *Sustainable Energy & Fuels*, 2018, **2**, 803-810.

9.   J. Wu, G. Huang, H. Li, S. Wu, Y. Liu and J. Zheng, *Polymer*, 2013, **54**, 1930-1937.

10.   S. Stankovich, R. D. Piner, S. T. Nguyen and R. S. Ruoff, *Carbon*, 2006, **44**, 3342-3347.

11.   H. Zhao, L. Wu, Z. Zhou, L. Zhang and H. Chen, *Physical Chemistry Chemical Physics*, 2013, **15**, 9084-9092.

12.   I. S. Blagbrough, N. E. MacKenzie, C. Ortiz and A. I. Scott, *Tetrahedron Letters*, 1986, **27**, 1251-1254.

13.   C. Gürtler and K. Danielmeier, *Tetrahedron Letters*, 2004, **45**, 2515-2521.

14.   W. J. Blank, Z. A. He and E. T. Hessell, *Progress in Organic Coatings*, 1999, **35**, 19-29.

15.   B. J. B. Folmer, R. P. Sijbesma, R. M. Versteegen, J. A. J. van der Dijt and E. W. Meijer, *Advanced Materials*, 2000, **12**, 874-878.

16.   A. Viinikanoja, J. Kauppila, P. Damlin, M. Suominen and C. Kvarnstrom, *Physical Chemistry Chemical Physics*, 2015, **17**, 12115-12123.

17.   S. Park, Y. Hu, J. O. Hwang, E. S. Lee, L. B. Casabianca, W. Cai, J. R. Potts, H. W. Ha, S. Chen, J. Oh, S. O. Kim, Y. H. Kim, Y. Ishii and R. S. Ruoff, *Nature Communications*, 2012, **3**, 638-646.

18.   H. R. Thomas, S. P. Day, W. E. Woodruff, C. Vallés, R. J. Young, I. A. Kinloch, G. W. Morley, J. V. Hanna, N. R. Wilson and J. P. Rourke, *Chemistry of Materials*, 2013, **25**, 3580-3588.

19.   P. L. Yap, S. Kabiri, D. N. H. Tran and D. Losic, *ACS Applied Materials and Interfaces*, 2019, **11**, 6350-6362.

20.   A. Marand, J. Dahlin, D. Karlsson, G. Skarping and M. Dalene, *Journal of Environmental Monitoring*, 2004, **6**, 606-614.

21.   S. Siggia and J. G. Hanna, *Analytical Chemistry*, 1948, **20**, 1084-1084.

22.   Y. Gao, L.-Q. Liu, S.-Z. Zu, K. Peng, D. Zhou, B.-H. Han and Z. Zhang, *ACS Nano*, 2011, **5**, 2134-2141.

23.   K. Hu, L. S. Tolentino, D. D. Kulkarni, C. Ye, S. Kumar and V. V. Tsukruk, *Angewandte Chemie International Edition England*, 2013, **52**, 13784-13788.

24.   K. Chen, X. Tang, Y. Yue, H. Zhao and L. Guo, *ACS Nano*, 2016, **10**, 4816-4827.

25.   S. Wan, F. Xu, L. Jiang and Q. Cheng, *Advanced Functional Materials*, 2017, **27**, 1605636-1605643.

26.   F. Barthelat and R. Rabiei, *Journal of the Mechanics and Physics of Solids*, 2011, **59**, 829-840.

27.   Y. H. Yang, L. Bolling, M. A. Priolo and J. C. Grunlan, *Advanced Materials*, 2013, **25**, 503-508.

28.   Y. Song, J. Gerringer, S. Qin and J. C. Grunlan, *Industrial & Engineering Chemistry Research*, 2018, **57**, 6904-6909.

29.   D. Feldman, *Journal of Macromolecular Science, Part A*, 2013, **50**, 441-448.

30.   S. H. M. Söntjens, R. P. Sijbesma, M. H. P. van der Genderen and E. W. Meijer, *Journal of the American Chemical Society*, 2000, **122**, 7847-7493.

31.   J. T. Chen, Y. J. Fu, Q. F. An, S. C. Lo, S. H. Huang, W. S. Hung, C. C. Hu, K. R. Lee and J. Y. Lai, *Nanoscale*, 2013, **5**, 9081-9088.

32. F. Ding, J. Liu, S. Zeng, Y. Xia, K. M. Wells, M.-P. Nieh and L. Sun, *Science Advances*, 2017, **3**, 1-9.

33. L. Medina, Y. Nishiyama, K. Daicho, T. Saito, M. Yan and L. A. Berglund, *Macromolecules*, 2019, **52**, 3131-3140.

34. K. W. Putz, O. C. Compton, M. J. Palmeri, S. T. Nguyen and L. C. Brinson, *Advanced Functional Materials*, 2010, **20**, 3322-3329.

35. X. Qi, D. Zhang, Z. Ma, W. Cao, Y. Hou, J. Zhu, Y. Gan and M. Yang, *ACS Nano*, 2018, **12**, 1062-1073.

36. P. Podsiadlo, A. K. Kaushik, E. M. Arruda, A. M. Waas, B. S. Shim, J. Xu, H. Nadivada, B. G. Pumplin, J. Lahann, A. Ramamoorthy and N. A. Kotov, *Science*, 2007, **318**, 80-83.

37. Y. Wang, T. Li, P. Ma, S. Zhang, H. Zhang, M. Du, Y. Xie, M. Chen, W. Dong and W. Ming, *ACS Nano*, 2018, **12**, 6228-6235.

7. Exfoliation and Self-assembly of α-Zirconium Phosphate Facilitated by a Poly(ether amine) in Water

7.1 Introduction

Reports of nacre-mimetic films using alpha-Zirconium phosphate (α-ZrP) are extremely limited (with only two examples published at the time of writing), but all are films supported on a substrate, none as standalone films. However, there is great potential to develop optically transparent films with improved scratch resilience over and above current polymer coatings. The films produced and described in both chapters 5 and 6 use GO as the nanoplatelet component and therefore result in black/brown coloured materials. This is not ideal for the target application. The use of nanoclays has enabled the production of numerous transparent films[1-3] however, α-ZrP remains wholly unexplored. The hypothesis is that through successful exfoliation and self-assembly of α-ZrP, transparent films can be produced achieving highly novel and scientifically interesting films.

Aqueous suspensions of α-ZrP are common but α-ZrP is not fully stable and requires additional agents to assist exfoliation. Commonly, small molecule amines[4-6] or larger poly(ether amine) (PEA)[7-9] moieties are employed. In both cases, oxygenated groups are present to facilitate solubility in aqueous media. Due to the nanoplatelet-polymer structure of nacre-mimetic materials, it is expected that with appropriate selection of an exfoliating agent it could also function as the 'mortar' component of any nacre-like material. If a PEA is used, it could enable exfoliation of α-ZrP whilst also assembling into the polymer component of the nacre-mimetic material. Favourable interactions between PEA and α-ZrP are proven due to the intercalating effect of the PEA and thus, self-assembly is possible. PEAs are commercially available and inexpensive with a wide range of molecular weight and structures possible.

In this work, Jeffamine M600 (referred to as PEA from hereon) with a molecular weight of ≈600 Da was used. This PEA offers a relatively small polymeric structure and therefore, is likely to provide more effective intercalation over larger alternatives. PEAs used in α-ZrP exfoliation typically contain a single amine group at one terminus of the polymer chain. The surface of the α-ZrP is known to have excellent ion exchange capabilities[10] and so a cation exchange reaction occurs to ionically bind

the α-ZrP to the PEA. The hydrophobic tail of the polymer then repels the adjacent α-ZrP nanoplatelets. By using a low molecular weight polymer, a greater number of amine groups are available for intercalation and thus, improved polymer-nanoplatelet interactions are produced. The PEA is also large enough that the collaborative effects of the polymer component of traditional nacre-mimetic materials are maintained.

In this chapter, an α-ZrP nanoplatelet is characterised using FTIR, Raman and XRD and the lateral dimensions and geometry measured using SEM. The α-ZrP is then exfoliated in water with PEA and freestanding nacre-mimetic materials are produced using a similar solution casting method as was described in Chapter 5. A uni-directional layered structure is confirmed from SEM imaging and the resulting films were analysed both chemically and mechanically.

7.2 Characterisation of α-ZrP nanoplatelets

The FTIR spectrum of the α-ZrP nanoplatelets is displayed in Figure 7.1. Symmetric P-O stretch vibrations are detected at 955 cm^{-1} and 1016 cm^{-1} with the asymmetric analogues observed at 1068 cm^{-1} and 1159 cm^{-1}. A P-O-H bend is detected at 1249 cm^{-1} whilst all the remaining peaks can be assigned to water in different conformations. The water bound in the interlayer space is detected through bending, symmetric and asymmetric vibrations at 1617 cm^{-1}, 3508 cm^{-1} and 3586 cm^{-1}, respectively. The broad peak at 3127 cm^{-1} is assigned to stretching of free water molecules, most likely adsorbed onto the α-ZrP nanoplatelets via hydrogen bonding. The FTIR spectrum of α-ZrP is widely reported and these assignments are in excellent agreement to that in previously published literature.[4, 6, 11]

The Raman spectrum of α-ZrP has also been recorded previously and so peaks can be assigned with a high level of confidence.[12, 13] The spectrum is displayed in Figure 7.2 and the peak data tabulated in Table 7.1. An intense peak is seen at 1053 cm^{-1}, assigned to a symmetric phosphate stretch with a 'scissor' stretch also present at 291 cm^{-1}. The asymmetric phosphate stretch is detected at 1082 cm^{-1} and 1140 cm^{-1} with a rotational vibration observed at 209 cm^{-1}. In-plane and out-of-plane stretching associated with the P-O-H group is present at 960 cm^{-1} and 985 cm^{-1}. A final rotational vibration of trapped water can be assigned to the peak at 416 cm^{-1}.
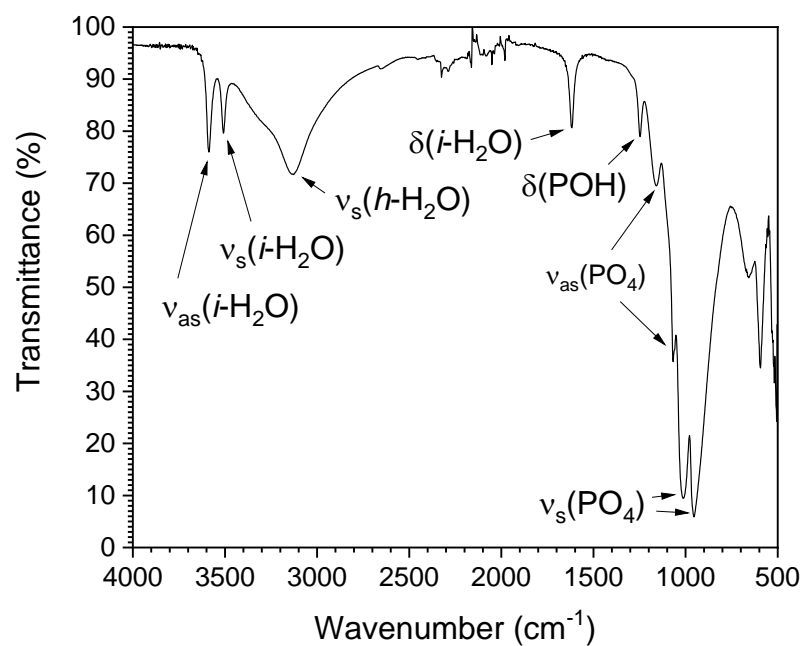
Figure 7.1 – FTIR spectrum of the α-ZrP nanoplatelets (*i-* and *h-* correspond to interlayer and hydrogen bonded, respectively).
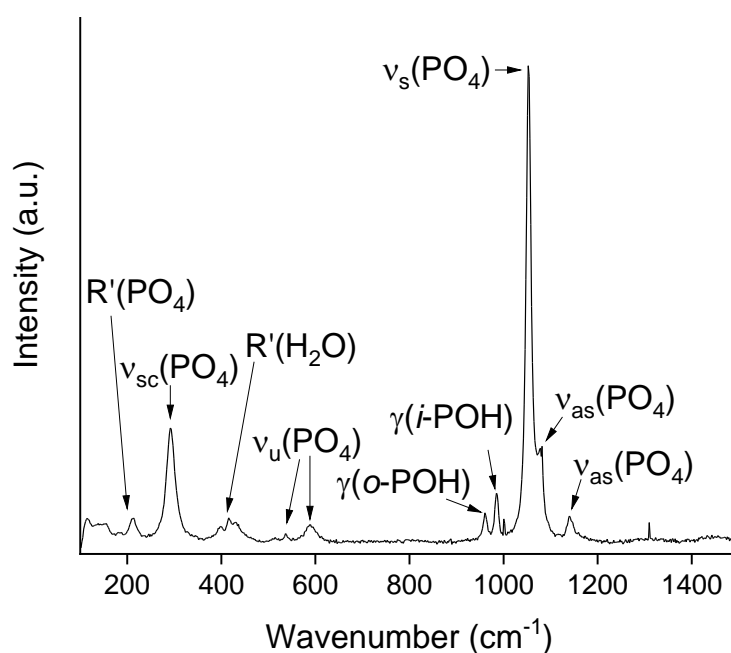
Figure 7.2 – Raman spectrum of α-ZrP nanoplatelets (*i-* and *o-* correspond to in-plane and out-of-plane, respectively).

Table 7.1 – Raman peak assignments for α-ZrP nanoplatelets.[12]

Wavenumber (cm^{-1})	Functional group	Mode	
209	PO_4	rotation	
291	PO_4	stretch	'scissor'
416	H_2O	rotation	
536	PO_4	stretch	'umbrella'
588	PO_4	stretch	'umbrella'
960	POH	stretch	in-plane
985	POH	stretch	out-of-place
1053	PO_4	stretch	symmetric
1082	PO_4	stretch	asymmetric
1140	PO_4	stretch	asymmetric

Due to the layered structure of Zr and PO_4 groups in the α-ZrP structure, multiple peaks are observed in the XRD diffractogram, each corresponding to a different unit cell morphology (Figure 7.3). Using the d-spacings calculated via XRD, the unit cell dimensions of monoclinic α-ZrP can be determined.[14] The unit cell dimensions depend on the crystallinity of the α-ZrP and therefore variations in crystallinity can be detected through changes in the intensity ratio of $hkl = 002$ and 204 peaks ($I_{002}:I_{204}$). More crystalline α-ZrP displays a more intense $hkl = 002$ peak due to a preferred orientation of particles within the structure. The $hkl = 204$ peak corresponds to a less crystalline morphology. The α-ZrP used in this work has an $I_{002}:I_{204}$ ratio of approximately 3:1.[15]

SEM imaging was completed to determine the lateral dimensions of the α-ZrP nanoplatelets (Figure 7.4). It can be seen the α-ZrP has rounded edges and a highly geometric shape as is observed in other works.[6] These nanoplatelets were reported to have lateral dimensions of 1.61 µm however, from an average of 250 platelets it was found to be 1.27 ± 0.43 µm. It was also determined the platelets were ≈50 nm thick.
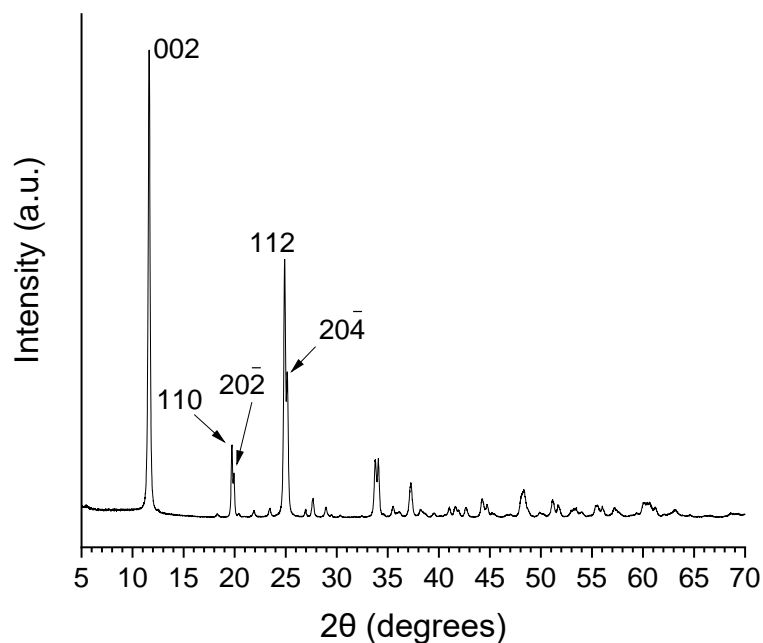
Figure 7.3 – XRD spectrum of the α-ZrP nanoplatelets with the relevant unit cell Miller indices annotated (*hkl*).
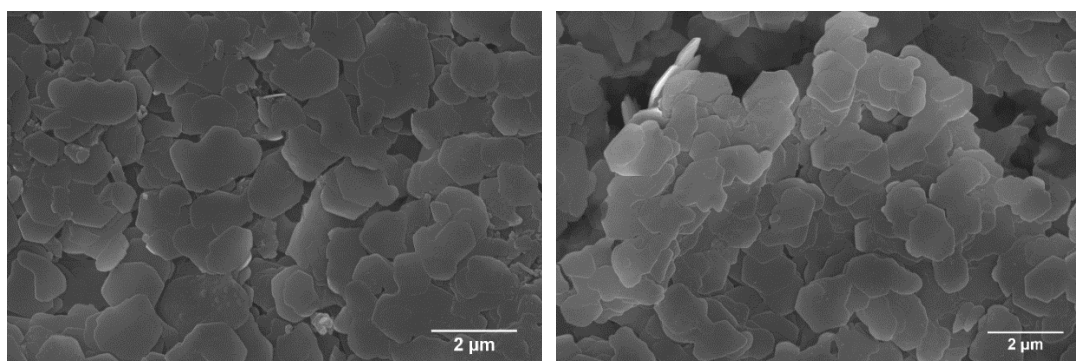
Figure 7.4 – Example SEM images of α-ZrP nanoplatelets.

7.3 Preparation and characterisation of α-ZrP nacre-mimetic films

Production of freestanding nacre-mimetic materials using α-ZrP as the nanoplatelet component have never been reported. Therefore, it was expected that significant optimisation would be required to produce films of this nature. Related examples have been reported where the films are supported by a substrate however,

these could not be separated post-production. In this work, a simple solution casting method was discovered which yielded freestanding α-ZrP-PEA films.

7.3.1 Solution casting of α-ZrP-PEA films using an aqueous medium

Nacreous freestanding films were produced using a similar method as described in Chapter 5. The α-ZrP nanoplatelets were first submerged in water before a 1 wt% solution of PEA in water was added to produce films of varying PEA content. Then, the mixtures were stirred for 2 hours. A PET substrate in a PS petri-dish was used as a mould and the resulting cast samples were dried at 40 °C in a fan-assisted oven. Drying under these conditions was completed in under 16 hours. This method was effective at producing homogeneous films with PEA content of 5 to 33 wt% (Figure 7.5). It was not possible to produce freestanding films outside of these parameters. At low PEA content (<5 wt%), the adhesive properties of the PEA polymer were unable to prevent a fragile powder-like product. At high PEA content (>33 wt%), the liquid properties of the PEA polymer dominate and the dried product is gel-like. The films become more transparent as the PEA content is increased. This is ideal for the targeted applications and is due to the transparent PEA dominating the opaque α-ZrP at higher PEA content. It is also likely that the high PEA content aids in the assembly of a uniform film structure that reduces random light scattering.

Figure 7.5 – Digital photographs of the α-ZrP-PEA films at a) 5, b) 9, c) 17, d) 23, e) 29 and f) 33 wt% PEA content.

The preparation conditions are critical and must be kept within tight control. For example, the use of a fan-assisted oven is essential to ensure the aqueous phase has evaporated quickly. Replicate experiments using an unassisted oven took many

days to dry, enabling settling of the solid phase and ultimately producing fragile, inhomogeneous films. These films could not be peeled from the substrate. Equally important is that stirring must be completed without excessive agitation of the dispersion. It was noted from multiple experiments that any bubbles produced during stirring were unable to break surface tension and would result in the presence of voids and defects in the films. Indeed, there were micro-bubbles still present in the successful films produced.
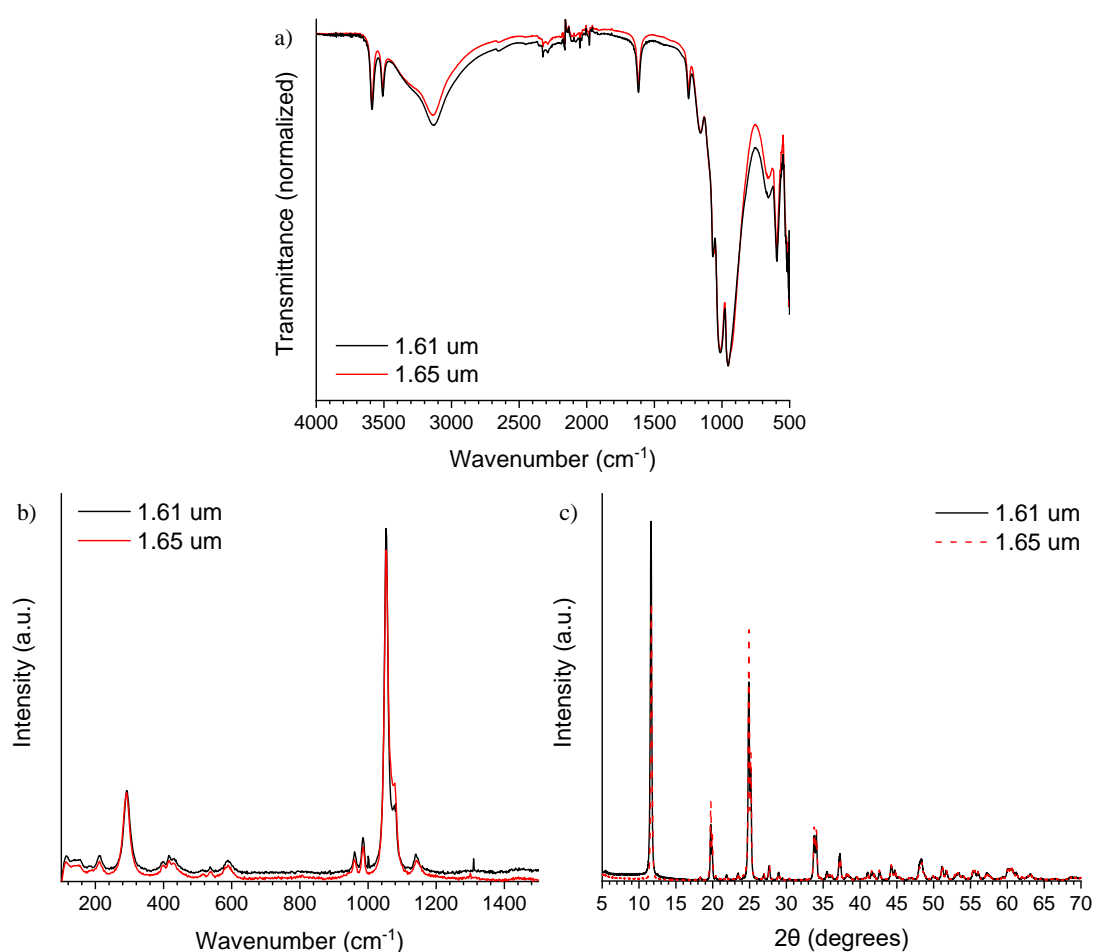
Figure 7.6 – Comparison of α-ZrP nanoplatelets of reported lateral dimensions of 1.61 and 1.65 µm where a) FTIR, b) Raman and c) XRD.

Interestingly, similar films could not be produced using an alternative α-ZrP nanoplatelet. In that case, the nanoplatelets were reported to have a lateral dimension

of 1.65 µm. Figure 7.6 shows comparisons between the two α-ZrP spectra from FTIR, Raman and XRD data. It can be seen that the signals are almost identical in each case suggesting similar chemical structures. The only observable change appears in the XRD spectra (Figure 7.6 c)) where the ratio of intensity between the $hkl = 002$ and $hkl = 112/204$ peaks shifts. It was previously discussed how the ratio of the $hkl = 002$ and $hkl = 204$ peaks can indicate the crystallinity of the α-ZrP. In the case of the 1.65 µm α-ZrP, the $I_{002}:I_{204} \approx 2:1$ confirming a reduction in crystallinity when compared to the 1.61 µm nanoplatelets ($I_{002}:I_{204} = 3:1$). It is clear that crystallinity has a significant impact on the exfoliation and self-assembly of the α-ZrP into a homogeneous nacre-mimetic film.
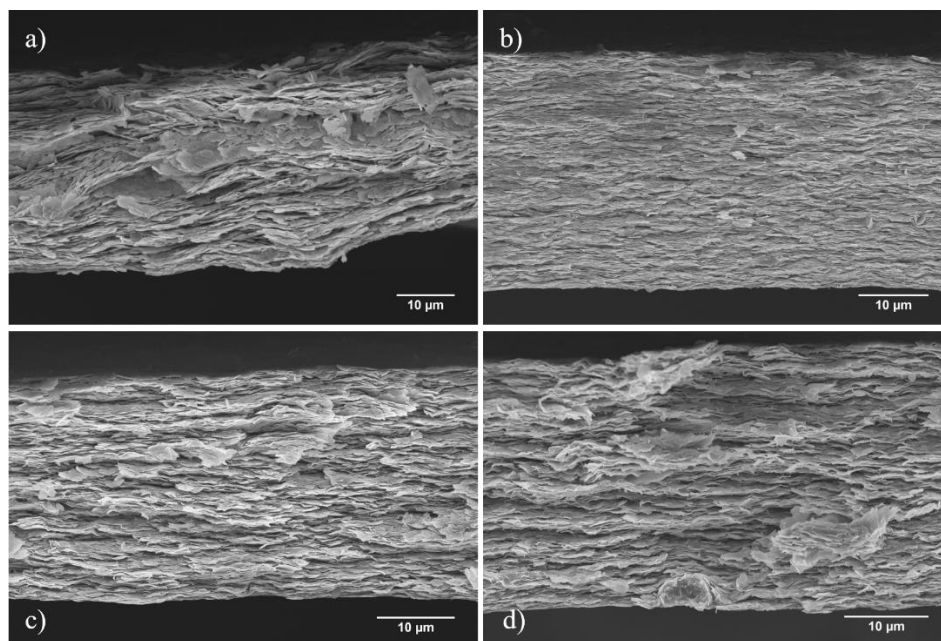
Figure 7.7 – Example cross-sectional SEM images of α-ZrP nacre-mimetic films where a) 9, b) 23, c) 29 and d) 33 wt% PEA content.

Cross-sectional SEM was completed to confirm the nacre-mimetic layered structure. Imaging of the 5 wt% PEA samples proved difficult despite multiple attempts however, at >9 wt% PEA, high quality images were collected (Figure 7.7). The layered morphology is observed in each film confirming successful self-assembly during drying. Interestingly, at the highest PEA content of 33 wt% (Figure 7.7 d)) the

platelets can be seen to have a more amorphous surface texture due to high adsorption of PEA onto the α-ZrP surface. At 9 wt% PEA (Figure 7.7 a)), defects in the layered morphology can be seen where regions of α-ZrP are misaligned from the bulk material. This is caused by an insufficient volume of PEA being unable to adequately exfoliate and coat the α-ZrP and is likely to affect the mechanical properties of these films.

7.3.2 Chemical and thermal characterisation of α-ZrP-PEA films

FTIR analysis provides little additional information regarding the chemical structure of the films (Figure 7.8). The peaks present in the starting material are detected in all cases in the films and due to the cationic exchange with the PEA polymer, shifts in wavenumber are not expected following sample preparation. Evolution of peaks associated with PEA are observed at 2873 cm^{-1}, 1251 cm^{-1} and 1031 cm^{-1}, corresponding to a C-H stretch, C-H bend and C-O stretch, respectively. Simultaneously, the intensity of the α-ZrP peaks decreases as PEA content increased. This is most notable for the 67:33 ratio where the multiplet of peaks between 1180 cm^{-1} and 760 cm^{-1} becomes less resolved as PEA peaks become detectable at similar intensity as the α-ZrP signals.
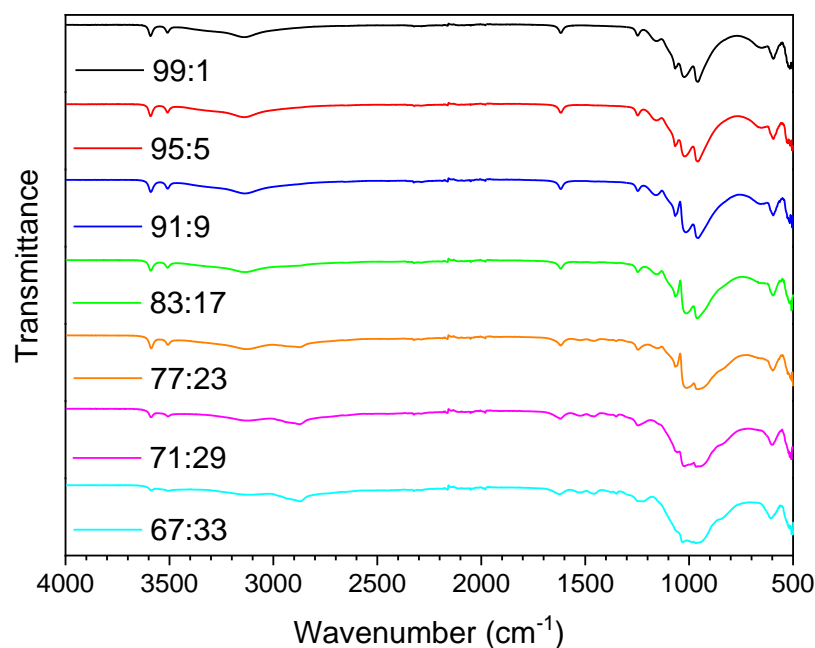
Figure 7.8 – FTIR spectra of the α-ZrP films at different PEA content. The labelled ratios correspond to α-ZrP:PEA.

XRD provides information on the effect of PEA content on the interlayer distances in the α-ZrP films (Figure 7.9). The strong peak at $2\theta \approx 12°$ is present in all cases and is consistent with the peak seen for α-ZrP powder. This peak is due to the layered structure within the α-ZrP platelets. With increased PEA content, a new peak evolves at $2\theta = 8\text{-}9°$ and is assigned to the homogeneous nacre-mimetic domains within the α-ZrP-PEA films. The peak intensity correlates with PEA content and is due to more effective exfoliation and self-assembly. Poorly exfoliated α-ZrP domains do not yield a peak within the XRD plot, symptomatic of poor homogeneity that is undetected by XRD. Increased PEA content produces a shift in 2θ derived from larger *d*-spacing (Table 7.2) due to larger volumes of PEA penetrating between the α-ZrP nanoplatelets. From a combination of SEM and XRD, it is clear that at low PEA content (<9 wt%), the self-assembly process is poor and produces mostly inhomogeneous films. In contrast, with higher PEA content (>9 wt%), the α-ZrP can be well exfoliated and PEA facilitates assembly of homogeneous nacre-like films with increased *d* spacing.
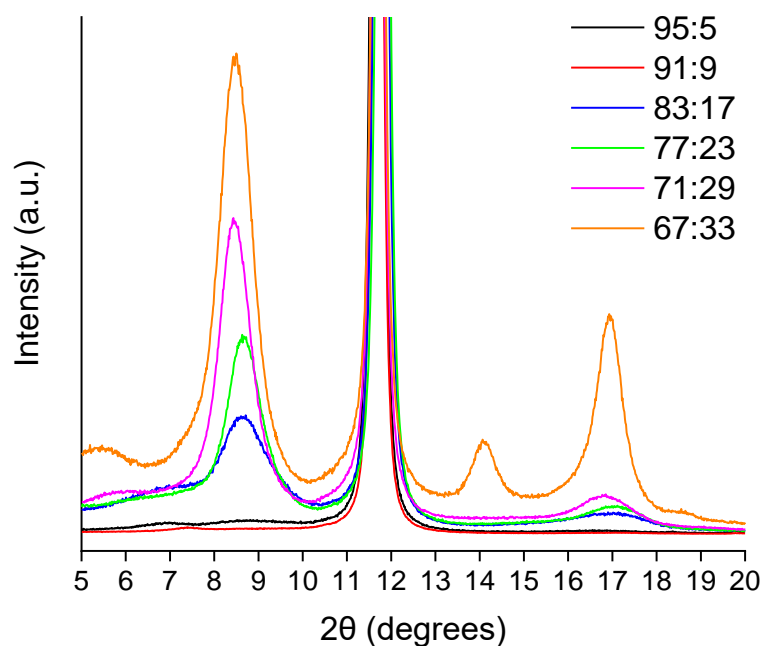
Figure 7.9 – XRD diffractogram for α-ZrP-PEA films of differing PEA content. The labelled ratios correspond to α-ZrP:PEA.

Table 7.2 – Calculated *d*-spacing for each α-ZrP:PEA ratio corresponding to the $2\theta =$ 8-9° peak.

Sample	95:5	91:9	83:17	77:23	71:29	67:33
d spacing (nm)	no peak	no peak	1.003	1.008	1.025	1.025

The thermal stability of the films was analysed using TGA analysis (Figure 7.10). Initially, interlayer water evaporates at temperatures of 100-200 °C. The films are stable up to 300 °C at which point the organic PEA begins to degrade.[16] The α-ZrP is much more stable and does not degrade, even at 800 °C.[17] Critically, with degradation only occurring at 300 °C, the films show high thermal stability and would remain stable in a wide range of applications.
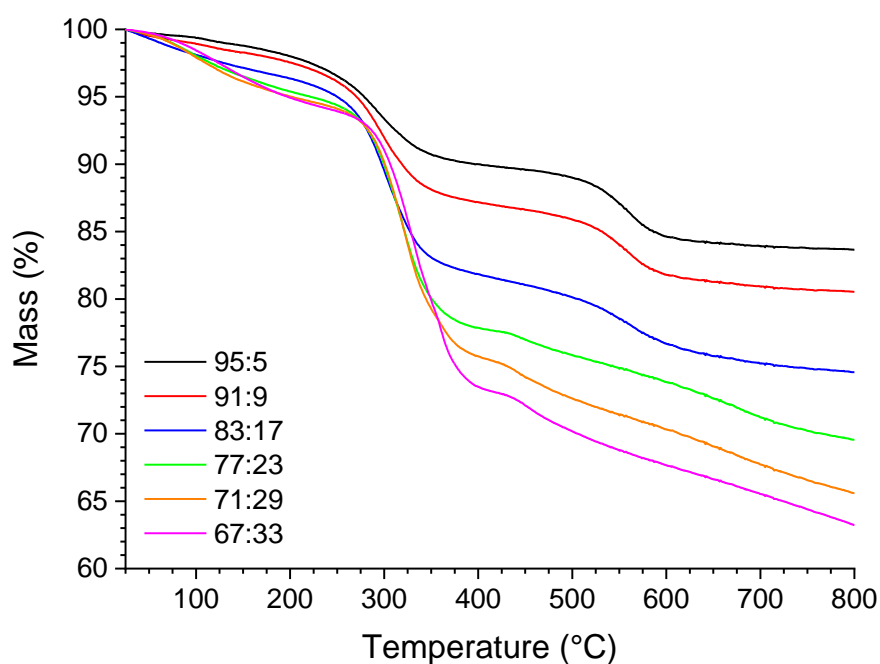
Figure 7.10 – TGA weight loss curves for different α-ZrP:PEA films.

7.3.3 Mechanical properties of α-ZrP-PEA films

The mechanical properties of the α-ZrP-PEA films were determined from both static tensile testing and nanoindentation. Previously, Waraich *et al*. completed

nanoindentation experiments on α-ZrP films supported on a polymer substrate[18] however, they were unable to complete static tensile tests. Due to the lack of previous literature on freestanding nacre-mimetic films based on α-ZrP, this work represents a benchmark for future studies. It should also be noted that neat α-ZrP films could not be produced and so property comparisons are made against the α-ZrP:PEA = 95:5 film as this represents the closest analogue. The mechanical properties recorded via tensile testing are outlined in Figure 7.11 and Table 7.3. Interesting trends are observed in each case and provide a strong insight into the effect of the PEA on the mechanical properties of the films at different ratios.
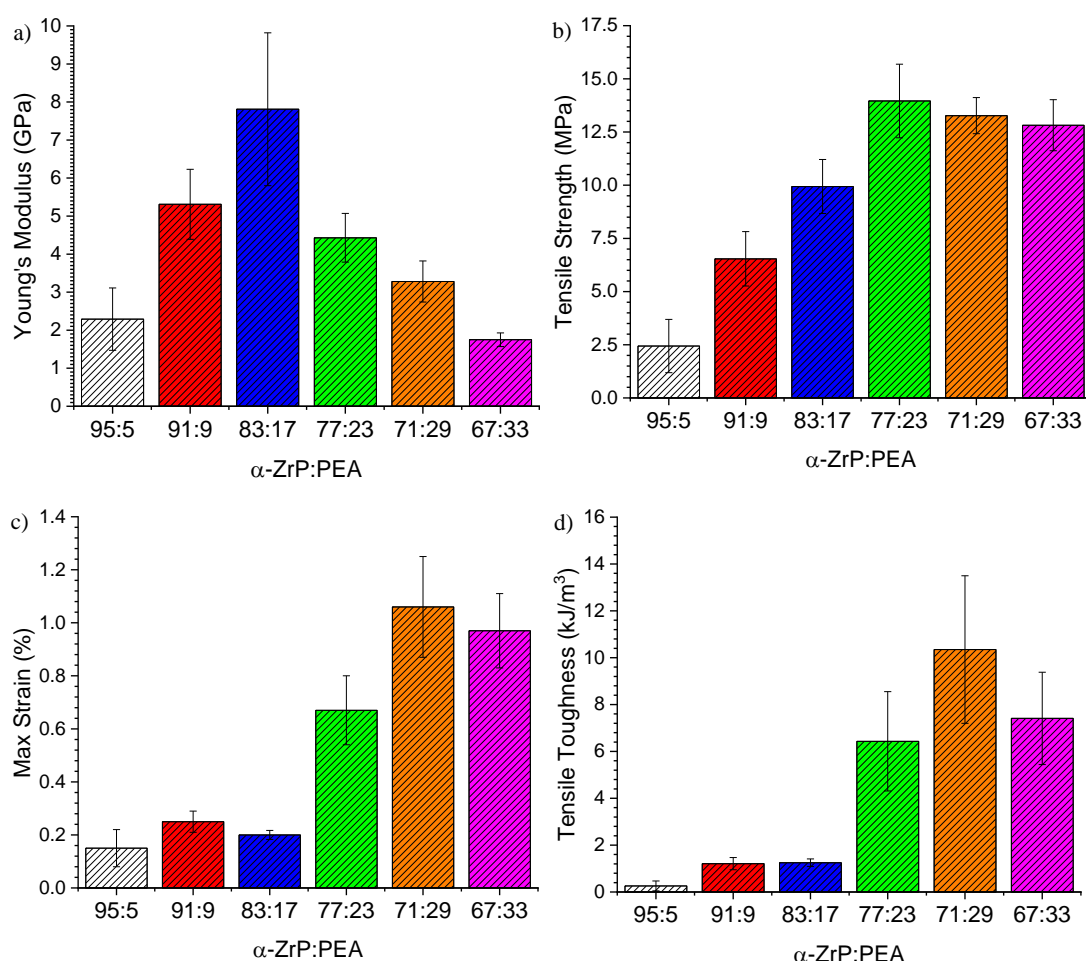
Figure 7.11 – Mechanical properties recorded for α-ZrP-PEA films of differing PEA content where a) Young's modulus, b) tensile strength, c) maximum strain and d) tensile toughness.

Table 7.3 – Mechanical data of α-ZrP-PEA films (±SD).

α-ZrP:PEA	Young's Modulus, E (GPa)	Tensile Strength, σ (MPa)	Maximum Strain, ε (%)	Tensile Toughness (kJ/m^3)
95:5	2.29 ± 0.82	2.44 ± 1.25	0.15 ± 0.07	0.26 ± 0.21
91:9	5.31 ± 0.92	6.54 ± 1.28	0.25 ± 0.04	1.21 ± 0.26
83:17	7.81 ± 2.01	9.94 ± 1.27	0.20 ± 0.02	1.25 ± 0.16
77:23	4.43 ± 0.64	13.96 ± 1.73	0.67 ± 0.13	6.43 ± 2.12
71:29	3.28 ± 0.54	13.27 ± 0.85	1.06 ± 0.19	10.35 ± 3.15
67:33	1.75 ± 0.18	12.82 ± 1.20	0.97 ± 0.14	7.41 ± 1.97

The PEA content that results in peak performance shifts with the mechanical property being measured (E = 83:17, σ = 77:23, ε and U_T = 71:29). This highlights the complex stress dissipation mechanisms occurring within the sample. The optimal value for E of 7.81 ± 2.01 GPa correlates to 341% of the 95:5 'control' sample. The stiffening effect of the polymer has been previously discussed in this thesis and in the broader literature.[1] It is clear the PEA is effectively constrained by the adjacent α-ZrP platelets, yielding a strong collaborative stiffening of the bulk material. At PEA content >17 wt%, the interlayer distance increases, as confirmed by XRD. This separation reduces the constraining effect of the α-ZrP nanoplatelets and results in a decrease in stiffening. A comparison to the theoretical maximum modulus is important. With an intrinsic E of 15.2 GPa,[19] the highest performing α-ZrP-PEA film (83:17) achieves 51% of the theoretical maximum modulus, further emphasising the high performance of these films.

Increases in σ, up to a maximum of 13.96 ± 1.73 MPa, were recorded for a 77:23 ratio. This represents a significant increase of 572% over the 95:5 sample. Typically, nacre-mimetic materials fail through platelet fracture or yielding of the soft interfaces (i.e. the polymer).[20] The interactions of the PEA towards the α-ZrP are essential to maximise resistance against soft interface yielding. At low PEA content, cleavage of the polymer from the α-ZrP surface causes failure of the sample. As the PEA content is increased, the quantity of α-ZrP-PEA binding sites increases, thus improving interfacial interactions. Above 77:23, the volume of PEA is sufficient to introduce polymer-polymer interactions. These interactions are significantly weaker

than the ionic binding between PEA and α-ZrP. As a result, yielding of the polymer results more easily and a reduction in tensile strength is observed.

For both ε and U_T, the 71:29 sample displayed optimal performance. Values of $1.06 \pm 0.19\%$ and $10.35 \pm 3.15 \text{ kJ/m}^3$ were recorded, representing an increase of 707% and 3981% over the 95:5 sample, respectively. The increases observed are substantial in both cases and is symptomatic of the increased contribution of the liquid-like polymer to the bulk properties. The 'soft' polymer elongates much more readily than the highly rigid nanoplatelet. With an increase in polymer content, this effect becomes more prominent (i.e. high strain is recorded before an alternative failure mechanism causes sample failure). The 71:29 sample is an optimal α-ZrP:PEA ratio as samples record relatively high extension prior to the polymer dominating properties. This is manifest by a reduction in ε for the 67:33 sample.

Optimal PEA weight content is different for E, σ, ε and U_T and these changes can be explained by the differences in α-ZrP and PEA interactions. For the 95:5 ratio, the PEA has little impact on the mechanical properties of the film however, sufficient exfoliation is achieved to facilitate production of freestanding films. As the PEA content is increased through 91:9 to 83:17, the interactions between α-ZrP and PEA increase. At 83:17, the value of E peaks due to the high stiffening effect and small interlayer distance between platelets. Further addition of PEA results in a reduction in the modulus of the film as the α-ZrP nanoplatelets are separated by an increased volume of PEA penetrating between the layers. Simultaneously, the quantity of binding sites between PEA and α-ZrP increases. This provides stronger interfacial interactions that result in an increase in σ. A further incremental increase in PEA promotes polymer-polymer interactions that hinder interfacial interactions between components and facilitate premature failure. Meanwhile, the high content 'soft' polymer provides an increase in ε (and consequently U_T). The material has a greater capacity to stretch and therefore records greater extension prior to failure. Ultimately, the reduced interfacial interactions and dominance of the liquid-like polymer component results in decrease to E, σ, ε and U_T when the α-ZrP:PEA = 67:33.

Nanoindentation experiments were completed and the data compared to previous literature findings. Representative nanoindentation curves, reduced Young's modulus (E_r) and hardness (H) are shown in Figure 7.12, with the calculated values

listed in Table 7.4. The maximum values for both E_r and H were recorded for a PEA content of 23 wt%. $E_r = 2.27 \pm 0.20$ GPa and $H = 58.4 \pm 9.2$ MPa were recorded, representing a 200- and 44-fold increase over the 95:5 sample, respectively. These increases highlight the significant impact of PEA on the collaborative energy dissipation mechanisms. The values are also comparable to those reported by Waraich *et al*. who employed chitosan as the polymer component.[18] Chitosan has been widely shown to produce very high mechanical properties due to the high hydrogen bonding potential towards nanoplatelet materials.[21-23] PEA has a much lower abundance of hydrogen bonding groups and so it is remarkable that comparable properties can be recorded using this polymer (PEA).
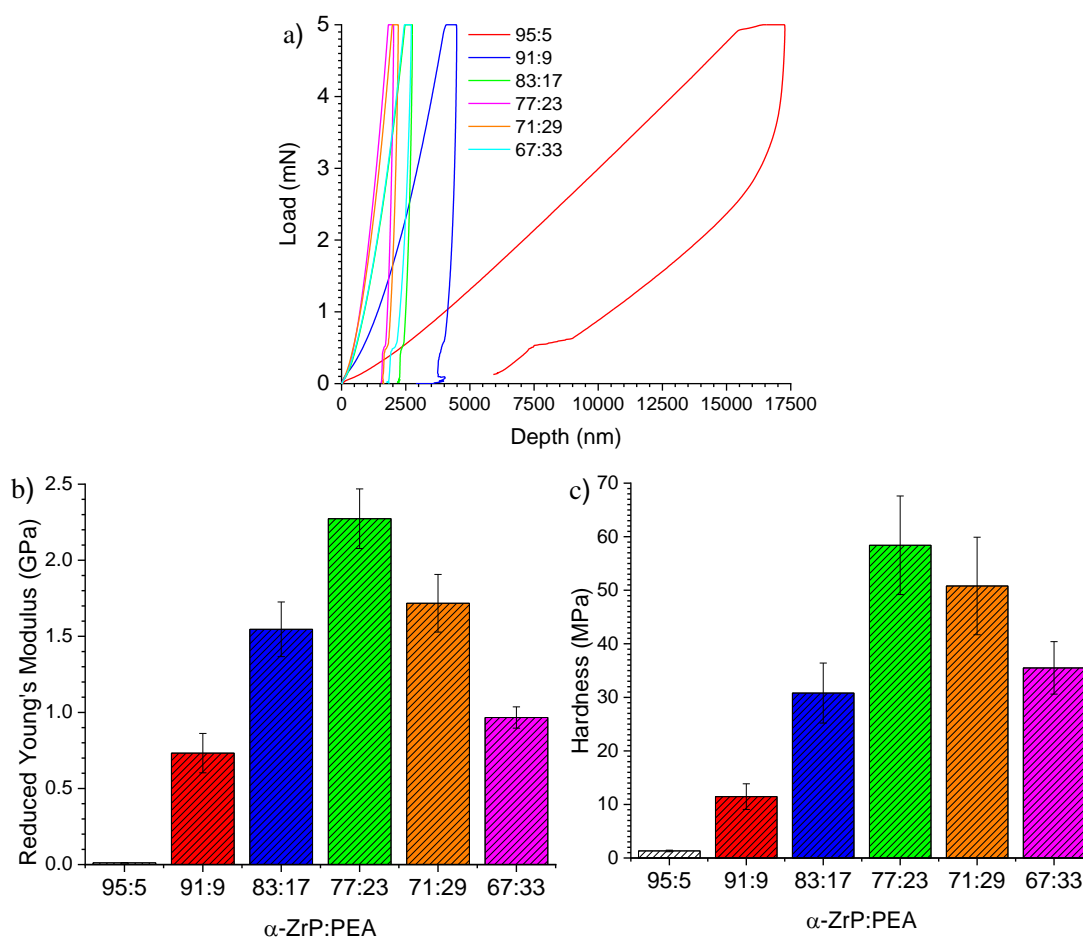
Figure 7.12 – Nanoindentation data for α-ZrP-PEA films a) representative depth versus load curves (the labelled ratios correspond to α-ZrP:PEA), b) reduced Young's modulus (E_r) and c) hardness (H).

Table 7.4 – Reduced Young's modulus and hardness values calculated from nanoindentation measurements (±SD).

α-ZrP:PEA	Reduced Young's modulus, E_r (GPa)	Hardness, H (MPa)
95:5	$0.01 \pm 6\text{x}10^{-4}$	1.32 ± 0.15
91:9	0.73 ± 0.13	11.46 ± 2.40
83:17	1.55 ± 0.18	30.80 ± 5.60
77:23	2.27 ± 0.20	58.40 ± 9.20
71:29	1.71 ± 0.19	50.80 ± 9.10
67:33	0.97 ± 0.07	35.50 ± 4.90

The significant increase in E_r and H is due to the dual functionality of the PEA polymer enabling exfoliation of the α-ZrP nanoplatelets whilst also encouraging uniform self-assembly upon drying. If the mode of deformation of interest is compression (as in nanoindentation), then it is critical that the morphology of the layered α-ZrP structure is as homogeneous and compact as possible. SEM imaging revealed defects in the films with low PEA content which result in poor mechanical properties. As the PEA content is increased, exfoliation is improved and the resulting films have a more homogeneous layered structure that allows the localised stress of the indenter tip to be dissipated more widely. Ultimately, this dissipation produces films of higher mechanical strength. At >23 wt% PEA, the liquid-like properties of the polymer become dominant and the indenter is able to compress the 'soft' polymer more easily and thus the mechanical properties are reduced.

At low PEA content, E_r and H are very low, confirming neat α-ZrP has little stability when a compressive force is applied. The difference in the mode of deformation between static tensile testing and nanoindentation has been discussed in Chapter 5.5.1 and results in significantly different modulus values. The tensile modulus (E) is significantly higher than the compressive modulus (E_r) suggesting an improved polymer stiffening effect under tensile load. This would be expected as the nanoindentation technique is able to compress α-ZrP and PEA into any pores or imperfections in the layered structure with little resistance, a phenomenon that cannot occur while the film is under tensile load.

7.3.4 Gas barrier properties of α-ZrP-PEA films.

The gas barrier properties of the films were measured however, it is likely the micro-bubbles resulted in small defects in the films that provided little resistance to oxygen or carbon dioxide permeation. In both cases, transmission rates were above the detection limits of the equipment. Despite this, water vapour transmission rates (WVTR) could be measured (Table 7.5) where the 91:9 film provides the greatest barrier recording a transmission rate per unit thickness of ~243 g mil/(m^2 24h). This value is approaching those reported for a range of polymer films including Nylon 6,6,[24, 25] poly(lactic acid),[25] orientated polystyrene,[26] and EVOH.[27]

Table 7.5 – WVTR data for different α-ZrP-PEA films.

Sample α-ZrP:PEA	Thickness μm	WVTR		
		g/(m^2 24h)	g μm/(m^2 24h)	g mil/(m^2 24h)
95:5	45	1956.687	88050.91	3466.57
91:9	48	128.860	6185.28	243.51
77:23	43	555.393	23881.89	940.23
71:29	37	274.660	10162.42	400.10
67:33	44	358.570	15777.10	621.14

7.4 Concluding remarks

To summarise, it has been proven in this work that α-ZrP nanoplatelets can be effectively exfoliated by a commercially available PEA (Jeffamine M600) and then self-assembled into a nacre-mimetic structure through a solvent casting approach. This work represents the first example of freestanding α-ZrP nacre-mimetic films reported in the literature. The PEA behaves as the polymer component, adhering the α-ZrP nanoplatelets together, and creating a 3D network that adequately dissipates energy and prevents localised failure. This is confirmed from static tensile testing where increases to E (341%), σ (572%), ε (707%), U_T (3981%), were recorded when compared to the α-ZrP:PEA = 95:5 film. Critically, the optimal ratio of α-ZrP:PEA was different for separate tensile properties (E = 83:17, σ = 77:23, ε and U_T = 71:29), proving the complexity of the interfacial interactions within the structure. Nanoindentation confirmed the films produced in this work record similar properties

to previous substrate-mounted literature examples with optimal E_r and $H = 2.27 \pm 0.20$ GPa and 58.4 ± 9.2 MPa, respectively. These values represent 200- and 44-fold increases over the 95:5 film confirming substantial increases to both E_r and H. Finally, gas barrier testing yielded similar WVTR to multiple polymer films.

7.5 References

1. P. Podsiadlo, A. K. Kaushik, E. M. Arruda, A. M. Waas, B. S. Shim, J. Xu, H. Nadivada, B. G. Pumplin, J. Lahann, A. Ramamoorthy and N. A. Kotov, *Science*, 2007, **318**, 80-83.

2. P. Das, J. M. Malho, K. Rahimi, F. H. Schacher, B. Wang, D. E. Demco and A. Walther, *Nature Communications*, 2015, **6**, 5967-5981.

3. S. Ming, G. Chen, J. He, Y. Kuang, Y. Liu, R. Tao, H. Ning, P. Zhu, Y. Liu and Z. Fang, *Langmuir*, 2017, **33**, 8455-8462.

4. T. Takei, Y. Kobayashi, H. Hata, Y. Yonesaki, N. Kumada, N. Kinomura and T. E. Mallouk, *Journal of the American Chemical Society*, 2006, **128**, 16634-16640.

5. X. Lin, D. Schmelter, S. Imanian and H. Hintze-Bruening, *Scientific Reports*, 2019, **9**, 16389-16404.

6. H. Huang, M. Li, Y. Tian, Y. Xie, X. Sheng, X. Jiang and X. Zhang, *Progress in Organic Coatings*, 2020, **138**, 105390-105400.

7. H.-J. Sue, K. T. Gam, N. Bestaoui, N. Spurr and A. Clearfield, *Chemistry of Materials*, 2004, **16**, 242-249.

8. M. Wong, R. Ishige, T. Hoshino, S. Hawkins, P. Li, A. Takahara and H.-J. Sue, *Chemistry of Materials*, 2014, **26**, 1528-1537.

9. M. Wong, R. Ishige, K. L. White, P. Li, D. Kim, R. Krishnamoorti, R. Gunther, T. Higuchi, H. Jinnai, A. Takahara, R. Nishimura and H. J. Sue, *Nature Communications*, 2014, **5**, 3589-3601.

10. J. Kerimo, D. M. Adams, P. F. Barbara, D. M. Kaschak and T. E. Mallouk, *Journal of Physical Chemistry B*, 1998, **102**, 9451-9460.

11. S. Wei, M. Lizu, X. Zhang, J. Sampathi, L. Sun and M. F. Milner, *High Performance Polymers*, 2012, **25**, 25-32.

12. R. C. T. Slade, J. A. Knowles, D. J. Jones and J. Roziere, *Solid State Ionics*, 1997, **96**, 9-19.

13. X. He, H. Xiao, H. Choi, A. Díaz, B. Mosby, A. Clearfield and H. Liang, *Colloids and Surfaces A: Physicochemical and Engineering Aspects*, 2014, **452**, 32-38.

14. A. Clearfield, L. Kullberg and A. Oskarsson, *The Journal of Physical Chemistry*, 1974, **78**, 1150-1153.

15. S. Ahrland and J. Albertsson, *Acta Chemica Scandinavica*, 1969, **23**, 1446-1447.

16. N. Bestaoui, N. A. Spurr and A. Clearfield, *Journal of Materials Chemistry*, 2006, **16**, 759-764.

17. X. Li, Z. Wang, L. Wu and T. Tsai, *RSC Advances*, 2016, **6**, 74903-74912.

18. S. M. Waraich, B. Hering, Z. Burghard, J. Bill, P. Behrens and H. Menzel, *Journal of Colloid and Interface Science*, 2012, **367**, 74-82.

19. J. E. Readman, A. Lennie, J. A. Hriljac, *Acta Crystallographica Section B*, **70**, 510-516.

20. F. Barthelat and R. Rabiei, *Journal of the Mechanics and Physics of Solids*, 2011, **59**, 829-840.

21. H. B. Yao, Z. H. Tan, H. Y. Fang and S. H. Yu, *Angewandte Chemie International Edition England*, 2010, **49**, 10127-10131.

22. S. Wan, J. Peng, Y. Li, H. Hu, L. Jiang and Q. Cheng, *ACS Nano*, 2015, **9**, 9830-9836.

23. B. Liang, Y. Shu, P. Wan, H. Zhao, S. Dong, W. Hao and P. Yin, *Composites Science and Technology*, 2019, **182**, 107747-107756.

24. L.-T. Lim, I. J. Britt and M. A. Tung, *Journal of Applied Polymer Science*, 1998, **71**, 197-206.

25. S. Farris, in *Engineering Properties of Packaging Films. In Innovative Packaging of Fruits and Vegetables: Strategies for Safety and Quality Maintenance*, eds. M. W. Siddiqui, M. S. Rahman and A. A. Wani, Apple Academic Press, Apple Academic Press, New Jersey, 2018, pp. 211-226.

26. S. L. Kamper and O. Fennema, *Journal of Food Science*, 1984, **49**, 1478-1481.

27. Z. Zhang, I. J. Britt and M. A. Tung, *Journal of Applied Polymer Science*, 2001, **82**, 1866-1872.

8. Conclusions and Recommendations for Future Work

8.1 Conclusions

Initial focus and experimentation began into the synthesis of a self-healing polymer based on poly(methyl methacrylate) (PMMA). The hypothesis was that through self-healing, the lifetime of a coating could be increased due to the ability of the material to heal damage. A maleimide-furan coupling (MFC) was employed due to the retro Diels-Alder (rDA) reaction temperature occurring above 100 °C. Synthesis of suitable functionalised methyl methacrylate (MMA) monomers were explored and a maleimide-based cross-linker was synthesised and ^{1}H NMR, ^{13}C NMR and FTIR confirmed the success of the reaction. Free-radical polymerisation (FRP) of the maleimide-based cross-linker and MMA was attempted however, the highly cross-linked nature of the product made traditional characterisation techniques challenging. Nonetheless, TGA confirmed the polymer was stable to >200 °C but no rDA/DA transition was observed from DSC studies. This could be due to masking of the transition by the T_g or as a result of undesired side reactions. Hot pressing of the polymer product was attempted yielding poor quality samples that could not be further tested.

Subsequently, greater control over the polymerisation process was investigated to improve the homogeneity of the polymer for improved thermal processing. Reversible addition-fragmentation chain-transfer (RAFT) polymerisation was selected due to the compatibility with a wide selection of monomers and selection of a suitable chain-transfer agent (CTA) was essential to achieving controlled polymerisation. From previous work 2-cyano-2-propyl dodecyl trithiocarbonate was identified as an ideal candidate for the control of MMA polymerisation. ^{1}H NMR confirmed the successful synthesis of the CTA before RAFT polymerisation of MMA was completed. The thermal stability of both the CTA and RAFT-PMMA were analysed by TGA confirming degradation of the polymer structure at temperatures as low as 125 °C. As a result, post-polymerisation removal of the CTA was essential for any future self-healing experiments. 1-ethylpiperidine hypophosphite (EPHP) was employed to initiate a radical-induced cleavage of the CTA with successful removal detected via ^{1}H NMR. Attempts to co-polymerise MMA and the maleimide-based

cross-linker proved unsuccessful due to poor solubility of the cross-linker in the reaction medium.

Due to the issues polymerising the maleimide-based cross-linker, an alternative approach was developed where the two components of the cross-linker were polymerised separately before combination at a later stage. Furfuryl methacrylate (FMA) is commercially available however, maleimide methacrylate (MiMA) required synthesis from precursor compounds. Successful synthesis of MiMA was confirmed by ^{1}H NMR and in agreement with previous studies. RAFT polymerisation of P(MMA-*co*-FMA) proved successful, confirmed by ^{1}H NMR and GPC, whilst kinetic analysis showed excellent control up to 9 hours. After 9 hours, cross-linking through the C-5 position of the furan ring was observed as M_n increased. TGA confirmed the poor thermal stability of the CTA and so the CTA was successfully removed using EPHP as confirmed by ^{1}H NMR. Polymerisation of MiMA proved challenging due to the evolution of multiple peaks in the GPC trace. It became clear that during polymerisation, the elevated temperature enabled the rDA reaction to proceed, thus de-protecting the maleimide group. Free maleimides are known to polymerise under radical conditions and hence, a permanently cross-linked polymer was produced. Cross-linking through the maleimide ring removes the potential for DA and rDA reactions.

Cu(0)-mediated living radical polymerisation (LRP) was utilised as it is known to be effective at RT. The polymer products are also more thermally stable as the terminal bromide degrades at a much higher temperature than the CTA. Cu(0)-mediated LRP of FMA proved successful however, conversion of the FMA monomer was low when compared to the RAFT equivalents. Despite this, FMA content in the final polymers was close to the targeted values. The use of Cu(0)-mediated LRP facilitated efficient polymerisation of MiMA into a P(MMA-*co*-MiMA) polymer with high conversion. GPC traces proved more Gaussian and a reduction in polydispersity confirmed that branching had been prevented. TGA analysis confirmed the polymers were stable to ≈300 °C. Despite the success of the Cu(0)-mediated LRP approach, the scalability towards industrial manufacture was low due to poor atom economy and reagent toxicity. As a result, alternative approaches were explored to achieving functional coatings.

Nacre-mimetic materials were targeted due to their high mechanical properties. As an alternative to self-healing, the lifetime of coatings can be improved by increasing resistance to damage. Chapters 5-7 explored this rationale. Initially, GO and a water-soluble polyurethane (wsPU) were investigated towards a covalently cross-linked network. GO paste was fully characterised through FTIR, Raman, XPS, TGA and SEM whilst the wsPU was characterised through FTIR, ^{1}H NMR, ^{13}C NMR, COSY NMR, DLS and the impact of UV curing on stiffness and hardness determined from nanoindentation measurements. Solvent casting was used to produce films that were subsequently UV cured. The films displayed a uni-directional layered arrangement of the GO nanoplatelets, confirmed by SEM. Defects in the film structure were observed suggesting poor exfoliation and penetration of the polymer between the GO platelets. Nonetheless, static tensile testing was completed showing a reduction in E and σ between neat GO and GO-wsPU films. An increase in ε was observed, most likely due to improved platelet sliding, facilitated by the flexible wsPU backbone. At high UV cure times, ε was reduced further, due to the increased rigidity of the wsPU. The acrylate cross-link density increased and thus polymer mobility was restricted. Nanoindentation measurements showed a reduction in reduced Young's modulus (E_r) and hardness (H) (from GO to GO-wsPU) due to structural defects reducing resistance to compression when compared to densely packed GO. Increases to Young's modulus (E), tensile strength (σ) and tensile toughness (U_T) were observed when substituting Et$_3$N for NaOH (and a reduction to maximum strain (ε)). This is due to the volatility of Et$_3$N preventing adequate pH control throughout the self-assembly process. Despite the increases, E, σ, ε and U_T were comparable to neat GO and defects were still observed in the SEM images. Ultimately, it was concluded that the micellar nature of the wsPU prevents adequate diffusion and distribution of the polymer between the GO sheets.

The mechanical properties of nacre-mimetic materials are governed by intermolecular interactions between the nanoplatelet and polymer components. As a result, investigations into improving non-covalent interactions within a GO-based film were completed through functionalisation of GO with a 4-fold hydrogen bonding synthon, 2-Ureido-4[1H]-pyrimidinone (UPy). It was confirmed, using FTIR and ^{1}H NMR, that UPy could be easily synthesised via a one-step reaction. The terminal isocyanate group of UPy allows for reaction with a number of functional groups, most

notably, hydroxyl, ketonic and carboxylic groups present on the GO surface. The reaction of GO and UPy (GOx) was confirmed using FTIR and followed by Raman, XRD, SSNMR, and XPS. The residual signals of starting material were detected for GO50 from XRD, SSNMR and XPS. This suggests that unreacted UPy dimerises with UPy groups that have grafted to the GO creating a strongly adsorbed UPy pendant group. An acid-base titration was employed to observe the degree of functionalisation and a previously unreported method established the effect of UPy functionalisation on the pH of the GO surface. It could be seen that increasing the UPy content (equally hexamethylene diisocyanate (HDI) content) reduced the acidity of the GO suggesting reaction with carboxylic acid groups, contradicting the data obtained from other techniques utilised in this section. The GOx was no longer stable when dispersed in water and so stability tests were completed in a range of solvents. DMSO was found to be the only solvent with good stability up to 96 hours and so was used to prepare nacre-like films. Due to the high boiling point and low volatility of DMSO, solvent casting was not suitable for film preparation however, a vacuum filtration approach was used allowing for fast production of freestanding films. The films were studied by SEM and XRD, their mechanical properties measured by static tensile testing and performance as a gas barrier. SEM confirmed a uni-directional layered structure with dense 'brick-like' GO structures observed at the highest UPy content. Despite this, tensile testing yielded the highest values for E, σ, ε and U_T for the GO50 film. Critically, as UPy content increased from 0 to 50 wt%, step-wise increases in E, σ, ε and U_T were recorded, thus confirming the beneficial effect of the UPy group promoting interfacial interactions within the structure. Ultimately, significant increases in E (323%), σ (470%), ε, (214%) and U_T (1117%) confirmed that interfacial interactions were significantly enhanced following functionalisation of GO with UPy. The gas barrier properties of the GO1 film were superior to the GO control for O_2, CO_2 and water vapour transmission, attributed to the reduced interlayer distance increasing the tortuosity of the permeation pathway. For GO10 and GO50, the interlayer distance increases and thus the barrier properties reduced. It was interesting to observe an increase in the barrier to water vapour for GO50, attributed to water capture by the UPy groups.

The impact of a polymer component on the properties of the GOx films was tested using poly(vinyl alcohol) (PVA) that was, in some cases, functionalised with

UPy (PVAy). The isocyanate group of the UPy group readily reacts with the hydroxyl groups of the PVA backbone and grafting was confirmed by FTIR. Step wise increases to the intensity of C=O stretches, proportional to UPy content, established that the degree of functionalisation could be controlled. At UPy content >10 wt%, the reaction mixture gelled and could not be solubilised in excess DMSO and so films were limited to PVAy of 0, 1, 5 and 10 wt% UPy. Nacre-mimetic films were produced using the vacuum filtration method and SEM imaging showed a distinct layered arrangement. Some structural defects were observed (GO50), suggesting incomplete exfoliation of the dispersion components prior to filtration. XRD confirmed increases in d-spacing between GO0 and GO1 films following addition of PVAy. This was due to penetration of PVAy between the GOx layers forcing them to separate. For GO10 and GO50, the interlayer distance remained largely consistent suggesting the polymer assembles in the pores created from the UPy spreading of the GO sheets. Tensile testing displayed significant increases in E, σ, ε and U_T over GOx films on inclusion of PVA0. For GOx/PVAy films, substantial increases were observed with maximum increases of 392% in E (GO1/PVA1), 535% in σ (GO1/PVA1), 598% in ε (GO10/PVA5) and 1788% in U_T (GO1/PVA10) when compared to GOx controls. This outcome confirmed that UPy has great potential as a tool for maximising the mechanical properties of nacre-mimetic films through formation of stronger interfacial interactions. UPy content can be used to tune the properties of the film, as confirmed by the difference in optimal GOx/PVAy ratio for E, σ, ε and U_T.

Finally, novel freestanding alpha-Zirconium phosphate (α-ZrP) based nacre-mimetic films were produced using a simple method through casting from water. Research into nacre-mimetic materials based on α-ZrP is very limited and so the academic interest in this topic is highly novel. The α-ZrP nanoplatelet has potential to produce transparent films that are highly desirable in multiple coating applications. The α-ZrP nanoplatelets were characterised using FTIR, Raman, XRD and SEM. The Raman spectra collected indicated the relative crystallinity of the platelets compared to that described previously in the literature. The α-ZrP was dispersed in water with the aid of a poly(ether amine) (PEA) that had dual-functionality as both an exfoliating agent for the α-ZrP platelets and the polymer component in the final structure. Nacre-like films were solvent cast as the layered structure self-assembled during the drying process. SEM was able to confirm the uni-directional layered arrangement of the

platelets and further characterisation was completed using FTIR, XRD, water vapour transmission, static tensile testing and nanoindentation. As the first example of freestanding nacre-mimetic films of this nature, the tensile data could not be compared directly with any previous literature. The beneficial effect of the PEA is clear from the tensile measurements. Optimal performance was recorded and increases of 341% in E (α-ZrP:PEA = 83:17), 572% in σ (77:23), 707% in ε (71:29) and 3981% in U_T (71:29) when compared to the 95:5 film. The difference between the optimal ratios for each property further indicates the tailor-ability of the films for varying applications. At the highest PEA content (67:33), reductions in E, σ, ε and U_T were recorded due to the impact of the liquid-like PEA dominating the structural rigidity of the α-ZrP, i.e. behaving more like a plasticiser. Nanoindentation measurements confirmed the films were comparable to similar, substrate-mounted examples in the literature with optimal E_r and H values of 2.27 ± 0.20 GPa and 58.40 ± 9.20 MPa, respectively. These correspond to a 200- and 44-fold increase over the 95:5 film. The transparent nature of the films for >17 wt% PEA further improves the potential of these films for real world applications.

8.2 Recommendations for future work

The use of the MFC for self-healing coatings with current technology has been proven to have limited potential for large-scale industrial production due to the multiple step process, purification requirements, poor atom economy and reagent toxicity. Despite this, with the development of a greener synthetic route and manufacture process, the viability of this method for future self-healing coatings may display greater promise. The 'zip' like approach does have the potential to provide an interesting insight into the coupling/decoupling mechanisms when using non-binary ratios of furan and maleimide pendant groups (e.g. 5 furan groups per maleimide). The ratio of these reversible cross-links should be explored to establish optimal conditions and maximise mechanical properties and self-healing functionality.

Nacre-mimetic materials have great potential for large-scale application. Unfortunately, the use of micellar polymers in preparation of nacre-mimetic materials has been proven to be a major technical challenge. The dispersion and distribution requirements necessary to produce a 'single-layer' polymer component is significant and ultimately resulted in defects that adversely affected the mechanical properties of

the films. Nonetheless, the UV cross-linking of a GO-PU structure has promise that should be studied further and UV cross-linking has not been widely explored in nacre-mimetic materials. Development of a UV active PU structure that is soluble in water would theoretically facilitate self-assembly of a homogeneous nacre-mimetic structure with potential for covalent cross-linking. The tunability of PUs makes them ideal for targeted applications and an in-depth study on the effect of PU structure, cross-link density and formulation would be interesting, both academically and industrially.

It has been proven in this project that there are significant benefits to improving the interfacial interactions between GO and PVA components in nacre-mimetic films. Despite this, the impact of PVAy content should be examined further. Previous research has shown that 95:5 is not always the optimal nanoplatelet:polymer ratio for increases in E, σ, ε and U_T. It would therefore be interesting to observe the impact of different PVAy content (i.e. >10 wt%) to determine whether the properties reported in this thesis can be improved on further. Research should also be completed towards the functionalisation of multiple polymer types and nanoplatelets with the UPy group to observe the impact on different nanoplatelet-polymer systems.

Arguably, the most promising discoveries described in this thesis were achieved when using α-ZrP. Unfortunately, the time constraints of the project did not allow for further investigations into the construction and optimisation of the freestanding films produced in Chapter 7. Solvent casting was used as a simple method to produce films on a short time scale, but critically from water. Further research is required to explore more scalable and industrially viable manufacturing approaches. Techniques such as spray coating and doctor blading could be ideal for production of large-scale films using α-ZrP. Further expansion could also include exploration of multiple PEAs. A single PEA was used in this work however, the range of commercially available analogues is vast and so a range of PEAs should be analysed for their effect on exfoliation, the self-assembly process and thus the mechanical properties possible of freestanding films. Polymers with different molecular weight backbones will present variable exfoliation and strengthening mechanisms and any correlation between these conditions would be an interesting study. Equally, PEAs with multiple terminal amines are available that could provide interesting self-assembly mechanisms when linked to adjacent α-ZrP sheets in a dispersion. With a

more comprehensive understanding of the PEA in the preparation of freestanding α-ZrP films, specific PEA structures could be developed and synthesised to target optimal performance.